Accelerating cavity and higher order mode coupler design for the Future Circular Collider

Dissertation
zur
Erlangung des akademischen Grades
Doktor-Ingenieur (Dr.-Ing.)
der Fakultät für Informatik und Elektrotechnik
der Universität Rostock

vorgelegt von
Shahnam Gorgi Zadeh, geboren am 11.09.1986 in Shiraz, Iran
aus Rostock, Deutschland

Eingereicht: Rostock, 05.11.2020
Verteidigt: Rostock, 15.03.2021

Gutachter:
Prof. Dr. rer. nat. Ursula van Rienen, Universität Rostock
Prof. Dr.-Ing. Herbert De Gersem, Technische Universität Darmstadt
Dr. Rama Calaga, CERN, Geneva, Switzerland

https://doi.org/10.18453/rosdok_id00003023

Abstract

The design study of the future circular collider includes a hadron collider (FCC-hh), an electron-positron collider (FCC-ee), and a hadron-lepton collider (FCC-he). The FCC-hh has been included in order to search for new physics beyond the standard model by colliding protons at unprecedented center-of-mass energy in the order of 100 TeV. The FCC-ee is planned to operate at different beam energies ranging from 45.6 GeV to 182.5 GeV to conduct precise measurements on the Z, W, H bosons and the top quark. Challenges for the superconducting radio frequency (SRF) cavity design for the FCC-ee result from operating at different RF voltages and beam currents. The objective of this thesis is to initiate the process of making a detailed design for the large and expensive RF system of the FCC-ee. This includes the determination of a suitable RF baseline for the FCC-ee cavities such as the RF frequency and the number of cells per cavity, taking into account the efficiency and cost of the RF system. Based on the considered baselines, multi-cell cavities are designed for operation at the W, H, and $t\bar{t}$ energies and a single-cell cavity to be operated at the Z energy. The middle cells and the end cells of the cavities are optimized separately, taking into account different objective functions. In the optimization of the cavities, the behavior of the fundamental mode and some dangerous higher order modes (HOM) are taken into account. Several higher order mode couplers, including coaxial HOM couplers and waveguide HOM couplers, are then parameterized and optimized to damp the dangerous HOMs of the designed cavities. In addition, a quad-ridged waveguide is introduced as a modified version of the conventional rectangular waveguide HOM coupler to lower the cutoff frequency of the waveguide, and thus improve its damping capability. The optimized cavities and HOM couplers are then combined, and several damping schemes are studied using different numerical methods. The numerical techniques required for the assessment of the performance of the cavities are presented. The behavior of the HOM damped cavities are studied for a single-cavity and for a four-cavity module. The total HOM power and the HOM power that propagates into each waveguide port are calculated from the time domain calculation and also from the eigenmode analysis. In addition, the HOM damped cavities are compared in terms of their beam impedance, and a suitable damping scheme is proposed for each case.

Zusammenfassung

Die Designstudie des Future Circular Collider umfasst einen Hadron-Collider (FCC-hh), einen Elektron-Positron-Collider (FCC-ee) und einen Hadron-Lepton-Collider (FCC-he). Der FCC-hh wurde aufgenommen, um nach neuer Physik jenseits des Standardmodells zu suchen, indem Protonen bei einer noch nie dagewesenen Schwerpunktsenergie in der Größenordnung von 100 TeV zur Kollision gebracht werden. Der FCC-ee soll bei verschiedenen Strahlenergien zwischen 45,6 GeV und 182,5 GeV arbeiten, um präzise Messungen an den Z-, W- und H-Bosonen und dem Top-Quark durchzuführen. Herausforderungen für das Design der supraleitenden Hochfrequenz (SRF)-Kavitäten für den FCC-ee ergeben sich aus dem Betrieb bei verschiedenen Hochfrequenz (HF)-Spannungen und Strahlströmen. Das Ziel dieser Arbeit ist es, die Erstellung eines detaillierten Designs für das große und teure HF-System des FCC-ee einzuleiten. Dazu gehört die Bestimmung eines geeigneten HF-Basisdesigns für die FCC-ee-Kavitäten, wie z.B. der HF-Frequenz und der Anzahl der Zellen pro Kavität, unter Berücksichtigung der Effizienz und der Kosten des HF-Systems. Auf Basis der berücksichtigten grundlegenden Lösungen werden mehrzellige Kavitäten für den Betrieb bei den Energien des W-, H- und $t\bar{t}$-Betriebs und eine einzellige Kavität für den Betrieb bei der Z-Energie ausgelegt. Die Mittel- und Endzellen der Kavitäten werden separat optimiert, wobei unterschiedliche Zielfunktionen berücksichtigt werden. Bei der Optimierung der Kavitäten wird das Verhalten der Grundmode und einiger gefährlicher Moden höherer Ordnung (engl. higher order modes - HOMs) berücksichtigt. Mehrere Koppler für die Moden höherer Ordnung, darunter koaxiale HOM-Koppler und Hohlleiter-HOM-Koppler, werden dann parametrisiert und optimiert, um die gefährlichen HOMs der entworfenen Kavitäten zu dämpfen. Darüber hinaus wird ein Quad-Ridged-Hohlleiter als modifizierte Version des konventionellen Rechteckhohlleiter-HOM-Kopplers eingeführt, um die Grenzfrequenz des Hohlleiters zu senken und damit sein Dämpfungsvermögen zu verbessern. Die optimierten Kavitäten und HOM-Koppler werden dann kombiniert, und mehrere Dämpfungsschemata werden mit Hilfe von verschiedenen numerischen Methoden untersucht. Die für die Beurteilung der Leistungsfähigkeit der Kavitäten erforderlichen numerischen Verfahren werden vorgestellt. Das Verhalten der HOM-gedämpften Kavitäten wird für ein Einkavitäten- und ein Vierkavitätenmodul untersucht. Die gesamte HOM-Leistung und die HOM-Leistung, die sich in jedem Hohlleitertor ausbreitet, werden mittels Zeitbereichs- und Eigenmodenanalyse berechnet. Darüber hinaus werden die HOM-gedämpften Kavitäten hinsichtlich ihrer Strahlkopplungsimpedanz verglichen und für jeden der Fälle ein geeignetes Dämpfungsschema vorgeschlagen.

Acknowledgment

I would like to thank all the people who directly or indirectly helped me to complete this thesis. Especially, I would like to thank:

- Prof. Ursula van Rienen for giving me the opportunity to work in her group, and for supervising and supporting me during my master's and Ph.D. study,
- Dr. Rama Calaga, my research advisor at CERN, for his guidance and thoughtful recommendations on this dissertation,
- Prof. Herbert De Gersem for the review of this thesis,
- Dr. Thomas Flisgen, for his support, helpful discussions, and reviewing my thesis,
- my former and present colleagues, among them Dawei Zheng, Dr. Dirk Hecht, Eden Tafa Tulu, Franziska Reimann, Gowrishankar Hallilingaiah, Hermann Pommerenke, Johann Heller, Kai Papke, Korinna Brackebusch, Piotr Putek, and Tomasz Galek, for providing a friendly working environment,
- my friends in Rostock, among them Alireza Koushki, Arash Ebrahimi, Hesam Khatibnezhad, Sahar Ghasemi, Sina Samarbakhsh, and the members of Admin's group for making my education time in Rostock memorable ones,
- all my friends that are scattered around the world, to name a few: Ahmad Pouya (who also helped me in editing this thesis), Hamid Eghbalpour, and Mojtaba Jafari, for the good memories that we share together,
- all my family, especially my parents and my sisters, for being the greatest source of emotional support and motivation for me.

Thesis Statements

of the dissertation

Accelerating cavity and HOM coupler design for the Future Circular Collider

by Shahnam Gorgi Zadeh

1. Particle accelerators have been widely used in recent decades in scientific research, especially in particle colliders. Colliding particles at high energies may give rise to the creation of new particles and phenomena at high energy levels.

2. After the discovery of the Higgs boson in 2012, CERN started the conceptual design study for a post-LHC collider called Future Circular Collider (FCC), which aims at colliding hadrons at 100 TeV center-of-mass collision energy. The FCC study covers three different types of particle collisions: hadron-hadron collision (FCC-hh accelerator), electron-positron collision (FCC-ee accelerator), and hadron-electron collision (FCC-he accelerator).

3. The aim of FCC-ee is to conduct precise measurements on the Z, W, and H bosons and the top quark in the beam energies ranging from 45.6 GeV to 182.5 GeV. The two limiting cases from the RF design point of view are the Z-pole, characterized by a low voltage and a current exceeding 1 A, and $t\bar{t}_2$, which requires a high voltage of 10.93 GeV. The H and W operating modes fall between these two extremes in terms of RF voltage and beam current.

4. In order to accelerate and keep the beam in the desired energy, the particles are accelerated through interaction with the resonating electromagnetic field in the RF cavities. Depending on the respective requirements of a given project, the shape of an accelerating cavity can generally be optimized for high accelerating field purposes, low surface losses, or low HOM impedance.

5. The RF design for Z favors a cavity with a lower number of cells, a lower frequency and a larger aperture to mitigate problems associated with a high beam current, while $t\bar{t}$ favors a higher frequency and a higher number of cells per cavity in order to achieve a higher acceleration per unit length.

6. The RF requirements of each operating mode of the FCC-ee are carefully studied, and the frequency and the number of cells per cavity for each energy option are determined, taking into account the cryogenic power losses, required input power per cavity and higher order mode (HOM) power losses.

7. Multi-cell cavities are considered for the W, H, and $t\bar{t}$ operations, and a single-cell cavity for the Z working point. The middle cells and end cells of the multi-cell cavities are optimized separately, taking into account the fundamental mode and some dangerous HOMs of the cavity.

8. HOM couplers are used to extract the energy of the HOMs from the the cavity. Based on the beam impedance of the designed cavities, three different coaxial HOM couplers are exploited and optimized.

9. Waveguide HOM couplers provide a broadband transmission with a high HOM power absorption rate at high frequencies. These couplers are optimized, and a modified version of waveguide couplers called quad-ridged waveguide couplers is introduced to reduce the cutoff frequency and size of the waveguide couplers.

10. The beam impedance of the cavity is obtained from the time-domain and eigenmode analysis of the HOM damped cavities. The required numerical techniques for the calculation of the beam impedance and the HOM power that propagates into the waveguide ports in time-domain and eigenmode analysis are presented.

11. The HOM power and the beam impedance of single-cavity and four-cavity modules using different damping schemes are studied, and the pros and cons are discussed.

Contents

List of Acronyms

ATLAS	A Toroidal LHC ApparatuS
BCS	Bardeen–Cooper–Schrieffer
BP	Beam pipe
BPA	Beam-pipe absorber
BS	Beamstrahlung
CEBAF	Continuous Electron Beam Accelerator Facility
CEM	Computational Electromagnetics
CEPC	Circular Electron Positron Collider
CERN	Conseil Européen pour la Recherche Nucléaire
CESR-B	Cornell Electron Storage Ring B-factory
CFL	Courant–Friedrichs–Lewy
CMS	Compact Muon Solenoid
cw	continuous wave
DQW	Double Quarter Wave
EM	Electromagnetic
ERL	Energy Recovery Linac
FCC	Future Circular Collider
FCC-ee	Future Circular electron-positron Collider
FCC-he	Future Circular hadron-electron Collider
FCC-hh	Future Circular hadron-hadron Collider
FEL	Free Electron Laser
FEM	Finite Element Method
FIT	Finite Integration Technique
FM	Fundamental Mode
FPC	Fundamental Power Coupler
GA	Genetic Algorithm
HL-LHC	High-Luminosity LHC
HOM	Higher Order Mode
ILC	International Linear Collider
IP	Interaction Point
JLab	Jefferson Lab
KEKB	KEK B-factory
LEP	Large Electron-Positron collider

LHC	Large Hadron Collider
MOR	Model Order Reduction
Nb	Niobium
Nb/Cu	Niobium-coated Copper
Nb_3Sn	Niobium-Tin
PDE	Partial Differential Equation
PEC	Perfect Electric Conductor
PERLE	Powerful Energy Recovery Linac Experiment
PMC	Perfect Magnetic Conductor
QRWG	Quad-ridged Waveguide
R&D	Research and Development
RF	Radio Frequency
RMS	Root Mean Square
RWG	Rectangular Waveguide
SM	Standard Model
SPL	Superconducting Proton Linac
SPS	Super Proton Synchrotron
SR	Synchrotron Radiation
SRF	Superconducting Radio Frequency
SSC	State Space Concatenation
TE	Transverse Electric
TEM	Transverse Electromagnetic
TM	Transverse Magnetic
UROS	University of Rostock
WG	Waveguide
XFEL	X-Ray Free Electron Laser
2DQW	Two Double-Quarter-Wave couplers
2DQW1QRWG	Two DQW and one QRWG coupler
2DQW1RWG	Two DQW and one RWG coupler
2H2P	Two Hook-type and two Probe-type couplers
3H1RWG	Three Hook-type and one RWG coupler
3H1QRWG	Three Hook-type and one QRWG coupler
3RWG	Three RWG couplers
4H	Four Hook-type couplers
5RWG	Five RWG couplers

List of Symbols

Symbol	Unit	Description
A	m	geometrical variable of middle cell and single-cell cavity
a	m	geometrical variable of middle cell and single-cell cavity
A_e	m	geometrical variable of end cell
a_e	m	geometrical variable of end cell
$\mathbf{A}_\mathrm{f}$	1/s	first-order state matrix
A_i	m^2	facet area of cell i in primary grid
$\tilde{A}_i$	m^2	facet area of cell i in dual grid
a_wg	m	width of a rectangular waveguide
B	m	geometrical variable of middle cell and single-cell cavity
b	m	geometrical variable of middle cell and single-cell cavity
$\underline{\mathbf{B}}$	Vs/m^2	phasor of the magnetic flux density
$\mathbf{B}(\mathbf{r}, t)$	Vs/m^2	magnetic flux density
$\mathbf{b}$	Vs/m^2	vector holding magnetic flux densities
$\hat{\tilde{\mathbf{b}}}$	Vs	vector holding magnetic grid fluxes
B_d	T	dipole magnetic field
B_e	m	geometrical variable of end cell
b_e	m	geometrical variable of end cell
$\mathbf{B}_\mathrm{f}$	$\sqrt{\mathrm{V}/(\mathrm{As})}$	first-order input matrix
$b_{p,m}$	$\sqrt{\mathrm{W}}$	time-dependent signal excited in mode m of port p
B_pk	T	peak magnetic field of FM on the surface of the cavity
$\underline{b}_{p,m}$	$\sqrt{\mathrm{W}}$	signal excited in mode m of port p in the frequency domain
B_s	T	magnetic field on the surface of the cavity
b_wg	m	height of a rectangular waveguide
$\mathbf{C}$	1	discrete curl operator for the primary grid
$\tilde{\mathbf{C}}$	1	discrete curl operator for the dual grid
c	m/s	speed of light in vacuum
c_1	1	optimization constraint on $E_\mathrm{pk}/E_\mathrm{acc}$
c_2	degree	optimization constraint on α
c_3	m	optimization constraint on R_i
$c_{\mathrm{d},i}$	m	ith geometrical parameter of the DQW coupler

Symbol	Unit	Description
$C_{\mathrm{h},i}$	F	capacitance i in the hook-type coupler's circuit model
$c_{\mathrm{h},i}$	m	ith geometrical parameter of the hook-type coupler
$C_{\mathrm{h},n}$	F	notch capacitance in the hook-type coupler's circuit
C_n	F	capacitance of the equivalent RLC circuit for mode n
$C_{\mathrm{p},3}$	F	capacitance in the probe-type coupler's circuit model
$c_{\mathrm{p},i}$	m	ith geometrical parameter of the probe-type coupler
$C_{\mathrm{p},n}$	F	notch capacitance in the probe-type coupler's circuit
C_{s}	1	scaling factor
$\underline{\mathbf{D}}$	$\mathrm{As/m^2}$	phasor of the electric flux density
$\mathbf{d}$	$\mathrm{As/m^2}$	vector holding electric flux densities
$\widehat{\widehat{\mathbf{d}}}$	As	vector holding electric grid fluxes
$\mathbf{D}(\mathbf{r}, t)$	$\mathrm{As/m^2}$	electric flux density
$\mathbf{D}_{\mathrm{A}}$	$\mathrm{m^2}$	diagonal matrix holding the areas of primary grid facets
$\tilde{\mathbf{D}}_{\mathrm{A}}$	$\mathrm{m^2}$	diagonal matrix holding the areas of dual grid facets
$d_{\mathrm{d},i}$	m	ith geometrical parameter of the DQW coupler
$d_{\mathrm{h},i}$	m	ith geometrical parameter of the hook-type coupler
$d_{\mathrm{p},i}$	m	ith geometrical parameter of the probe-type coupler
$\mathbf{D}_{\mathrm{s}}$	m	diagonal matrix holding the edge lengths of the primary grid
$\tilde{\mathbf{D}}_{\mathrm{s}}$	m	diagonal matrix holding the edge lengths of the dual grid
$\tilde{\mathbf{D}}_{\mathrm{V}}$	$\mathrm{m^3}$	diagonal matrix holding the volume of the dual grid cells
$\underline{\mathbf{D}}_Z$	Ω	complex diagonal matrix holding wave impedances
$\mathbf{D}_\varepsilon$	As/(Vm)	diagonal matrix holding the average permittivity of cells
$\mathbf{D}_\mu$	Vs/(Am)	diagonal matrix holding the average permeability of cells
$\mathbf{D}_\sigma$	A/(Vm)	diagonal matrix holding the average conductivity of cells
$\underline{\mathbf{E}}$	V/m	phasor of the electric field strength
$\mathbf{e}$	V/m	vector holding the electric field strengths
$\widehat{\mathbf{e}}$	V	vector holding the electric grid voltages
$\widehat{\mathbf{e}}'$	$\sqrt{\mathrm{VAs}}$	similarity transform of $\widehat{\mathbf{e}}$
E_0	eV	beam energy
$\mathbf{E}_0(\mathbf{r}, t)$	V/m	electric field strength
$\mathbf{E}_0(\mathbf{r})$	V/m	vector amplitude of the electric field
E_{acc}	V/m	accelerating field of the fundamental mode
$e_n^{(m)}$	1	relative electric field amplitude of mode m in cell n
$E_{\mathrm{p},i}$	V/m	peak axial electric field in the ith cell
E_{pk}	V/m	peak electric field of FM on the surface of the cavity
$E_{\mathrm{p,max}}$	V/m	maximum peak axial electric field among all cells

Symbol	Unit	Description
$E_{\mathrm{p,min}}$	V/m	minimum peak axial electric field among all cells
E_{s}	V/m	electric field on the surface of cavity
$E_z(\mathbf{r}, t)$	V/m	longitudinal component of the electric field strength
f_0	Hz	frequency of the operating mode
$f_{1/2}$	Hz	half bandwidth of the cavity at FM
$f(\mathbf{r}, t)$		source function in PDE
f_{cut}	Hz	cutoff frequency
$f_{\mathrm{d}i}$	Hz	frequency of the ith dipole mode
F_i		ith objective function
$\mathbf{F}_{\mathrm{lor}}(\mathbf{r}, t)$	$\mathrm{kg\,m/s^2}$	Lorentz force
$f_{mnp}^{(\mathrm{TE})}$	Hz	frequency of the TE mode in a pill-box cavity
$f_{mnp}^{(\mathrm{TM})}$	Hz	frequency of the TM mode in a pill-box cavity
f_n	Hz	frequency of mode n
$f_{\mathrm{p},0}$	Hz	lowest frequency in the passband
$\underline{F}_{p,m}$	$\sqrt{\mathrm{V/A}}$	weighting transfer function of mode m of port p
$f_{\mathrm{p},\pi}$	Hz	highest frequency in the passband
f_{rev}	Hz	revolution frequency
f_{s}	Hz	synchrotron frequency
f_{TE111}	Hz	frequency of the TE_{111} mode
f_{TM110}	Hz	frequency of the TM_{110} mode
G	Ω	geometry factor of the fundamental mode
$\underline{\mathbf{H}}$	A/m	phasor of the magnetic field strength
$\mathbf{h}$	A/m	vector holding sampled magnetic field strengths
$\widehat{\mathbf{h}}$	A	vector holding magnetic grid currents
$\mathbf{H}(\mathbf{r}, t)$	A/m	magnetic field strength
$\underline{\mathbf{H}}_{\mathrm{tan}}$	A/m	magnetic field tangential to the surface of the cavity
$H_z(\mathbf{r}, t)$	A/m	longitudinal component of the magnetic field strength
I_0	A	average beam current
I_{ex}	A	current of the exciting beam
$\mathbf{i}_{\mathrm{ext}}(t)$	A	input vector holding the modal port currents of the external ports
$\underline{\mathbf{i}}_{\mathrm{ext}}$	A	complex vector of the modal port currents of the external ports
$\underline{\mathbf{i}}_{\mathrm{ext},n}$	A	vector of the modal port currents at the frequency of mode n
$i_{\mathrm{ext},p,m}(t)$	A	modal port current of port mode m at the external port p
$\underline{I}_{\mathrm{fcc}}$	A	beam spectrum of FCC-ee at different beam energies

Symbol	Unit	Description
$I_{\mathrm{h},0}$	A	current source in the hook-type coupler's circuit model
$\hat{I}_n$	1	normalized Fourier spectrum of the beam current
$I_{\mathrm{p},0}$	A	current source in the probe-type coupler's circuit model
$\underline{\mathbf{J}}$	$\mathrm{A/m^2}$	phasor of the electric current density
$\mathbf{j}$	$\mathrm{A/m^2}$	vector containing electric grid current densities
j	1	complex unit
$\mathbf{J}(\mathbf{r},t)$	$\mathrm{A/m^2}$	electric current density
$\mathbf{j}_{\mathrm{cc}}$	$\mathrm{A/m^2}$	vector containing convection grid current densities
$\mathbf{J}_{\mathrm{cc}}(\mathbf{r},t)$	$\mathrm{A/m^2}$	convection electric current density
$\mathbf{j}_{\mathrm{imp}}$	$\mathrm{A/m^2}$	vector containing impressed grid current densities
$\mathbf{J}_{\mathrm{imp}}(\mathbf{r},t)$	$\mathrm{A/m^2}$	impressed electric current density
$\hat{\hat{\mathbf{j}}}$	A	vector containing electric grid currents
$\mathbf{J}_\sigma(\mathbf{r},t)$	$\mathrm{A/m^2}$	Ohmic electric current density
$\mathbf{j}_\sigma$	$\mathrm{A/m^2}$	vector containing Ohmic grid current densities
$\hat{\hat{\mathbf{j}}}_\sigma$	A	vector containing Ohmic grid currents
$\mathbf{K}$		stiffness matrix
k	1/m	wavenumber
k_{cc}	1	cell-to-cell coupling factor
$k_{\mathrm{d}i}$	1/m	wavenumber of the ith dipole mode
k_n	1/m	wavenumber of mode n
$k_\parallel$	V/C	total longitudinal loss factor
$k_{\parallel,0}$	V/C	longitudinal loss factor of FM
$k_{\parallel,\mathrm{HOM}}$	V/C	total longitudinal loss factor of HOMs
$k_{\parallel,n}$	V/C	longitudinal loss factor of mode n
$k_\parallel^{\mathrm{o}}$	V/C	original longitudinal loss factor
$k_\parallel^{\mathrm{s}}$	V/C	scaled longitudinal loss factor
L	m	half-cell length of the middle cell and single-cell cavity
$L[u(\mathbf{r},t)]$		differential operator L applied to $u(\mathbf{r},t)$
L_{active}	m	active length of the cavity
L_{bp}	m	length of the beam pipe
L_{cavity}	m	total length of the cavity
$l_{\mathrm{d},i}$	m	ith geometrical parameter of the DQW coupler
L_{e}	m	half-cell length of the end cell
$l_{\mathrm{h},i}$	m	ith geometrical parameter of the hook-type coupler
$L_{\mathrm{h},n}$	Vs/A	notch inductance in the hook-type coupler's circuit
L_i	m	edge length of cell i in the primary grid
$\tilde{L}_i$	m	edge length of cell i in the dual grid

Symbol	Unit	Description
L_n	Vs/A	inductance of the equivalent RLC circuit for mode n
L_{pb}	m	length of a pillbox cavity
$l_{\mathrm{p},i}$	m	ith geometrical parameter of the probe-type coupler
$L_{\mathrm{p},n}$	Vs/A	notch inductance in the probe-type coupler's circuit
L_{s}	m	length of the contour on the surface of the cavity
$\mathbf{M}$		mass matrix
M_{h}	Vs/A	coupling inductance in the hook-type coupler's circuit
M_p	1	maximum number of port modes of port p
M_{p}	Vs/A	coupling inductance in the probe-type coupler's circuit
$\mathbf{M}_\varepsilon$	As/V	matrix that maps the electric grid voltage to fluxes
$\mathbf{M}_\sigma$	A/V	matrix that maps the electric grid voltage to grid currents
$\mathbf{M}_\mu$	Vs/A	matrix that maps the magnetic grid voltage to fluxes
$\mathbf{n}$	1	normal unit vector
N_{cav}	1	the total number of cavities required to reach V_{RF}
N_{cell}	1	number of cells of the cavity
N_{e}	1	number of basis functions
N_{ext}	1	number of external terminals (all external port modes)
N_{f}	1	number of degrees of freedom
N_{h}	1	maximum considered harmonic number
N_{P}	1	number of grid nodal points
p	kg m/s	particle's momentum
P_{cryo}	W/m	static power loss per length
P_{ds}	W	power dissipated on the surface of the cavity
$P_{\mathrm{ds},0}$	W	power dissipated on the surface of the cavity by FM
P_{dynamic}	W	total dynamic power loss in cryogenic temperature
P_{ext}	W	external power loss
$P_{\mathrm{ext},n}$	W	external power loss of mode n
P_{HOM}	W	HOM power deposited in the cavity by the beam
$P_{\mathrm{HOM},n}$	W	HOM power of mode n
$P_{\mathrm{H-H}}$	W	HOM power for the H beam above 4.1 GHz
$P_{\mathrm{H-t\bar{t}_2}}$	W	HOM power for the $\mathrm{t\bar{t}_2}$ beam above 8.1 GHz
$P_{\mathrm{H-W}}$	W	HOM power for the W beam above 4.1 GHz
$P_{\mathrm{H-Z}}$	W	HOM power for the Z beam above 4.1 GHz
P_{in}	W	input power per cavity
P^*_{in}	W	minimum input power per cavity (at $Q^*_{\mathrm{L},0}$)
P_{loss}	W	power loss
$P_{\mathrm{L-H}}$	W	HOM power for the H beam up to 2.0 GHz

Symbol	Unit	Description
$P_{\mathrm{L-t\bar{t}_2}}$	W	HOM power for the $t\bar{t}_2$ beam up to 4.0 GHz
$P_{\mathrm{L-W}}$	W	HOM power for the W beam up to 2.0 GHz
$P_{\mathrm{L-Z}}$	W	HOM power for the Z beam up to 2.0 GHz
P_{mat}	W	power loss on lossy dielectric and magnetic materials
$P_{\mathrm{M-H}}$	W	HOM power for the H beam between 2.0 GHz to 4.1 GHz
$P_{\mathrm{M-t\bar{t}_2}}$	W	HOM power for the $t\bar{t}_2$ beam between 4.0 GHz to 8.1 GHz
$P_{\mathrm{M-W}}$	W	HOM power for the W beam between 2.0 GHz to 4.1 GHz
$P_{\mathrm{M-Z}}$	W	HOM power for the Z beam between 2.0 GHz to 4.1 GHz
P_p	W	power propagated into port p
$P_{p,m,n}$	W	external power loss of mode n via port mode m at port p
P_{s}	W	static power loss at cryogenic temperature for one cavity
P_{SR}	W	synchrotron radiation power loss
P_{static}	W	total static power loss at cryogenic temperature
$P_{\mathrm{tot-H}}$	W	total HOM power approximated for the H beam
$P_{\mathrm{tot-t\bar{t}_2}}$	W	total HOM power approximated for the $t\bar{t}_2$ beam
$P_{\mathrm{tot-W}}$	W	total HOM power approximated for the W beam
$P_{\mathrm{tot-Z}}$	W	total HOM power approximated for the Z beam
P_{wp}	W	total wall plug power
Q	1	quality factor
$\mathbf{q}$	As	vector containing electrical charges
q	As	electric charge
Q_0	1	intrinsic quality factor of the fundamental mode
Q_{b}	As	bunch charge
$Q_{\mathrm{ds},n}$	1	quality factor arising from surface losses of mode n
q_e	As	electric charge of a proton
Q_{ext}	1	external quality factor
$Q_{\mathrm{ext},n}$	1	external quality factor of mode n
$Q_{\mathrm{ext},p,n}$	1	Q_{ext} of mode n considering losses via port p
$Q_{\mathrm{ext},p,m,n}$	1	Q_{ext} of mode n considering losses via mode m of port p
$Q_{\mathrm{L},0}$	1	loaded quality factor of FM
$Q^*_{\mathrm{L},0}$	1	optimum loaded quality factor of FM
$Q_{\mathrm{L},n}$	1	loaded quality factor of the nth mode
$Q_{\mathrm{mat},n}$	1	quality factor arising from material losses of mode n
Q_n	1	quality factor of the nth mode
$\mathbf{r}$	m	position vector
R_0	Ω	residual resistance
r_{ah}	m	geometrical parameter of the quad-ridged WG

Symbol	Unit	Description
r_{aw}	m	geometrical parameter of the quad-ridged WG
R_{BCS}	Ω	BCS resistance
r_{bh}	m	geometrical parameter of the quad-ridged WG
R_{bp}	m	beam pipe radius
r_{bw}	m	geometrical parameter of the quad-ridged WG
$r_{\mathrm{d},i}$	m	ith geometrical parameter of the DQW coupler
R_{eq}	m	equator radius of an elliptical cell
$R_{\mathrm{ext},n}$	Ω	equivalent resistance of the HOM coupler for mode n
$r_{\mathrm{h},i}$	m	ith geometrical parameter of the hook-type coupler
R_{i}	m	iris radius of an elliptical cell
R_n	Ω	resistance of the equivalent RLC circuit for mode n
R_{pb}	m	radius of a pillbox cavity
$r_{\mathrm{p},i}$	m	ith geometrical parameter of the probe-type coupler
R_{res}		residual in FEM
R_{s}	Ω	surface resistance
R/Q	Ω	geometric shunt impedance
$R/Q_{\parallel}$	Ω	longitudinal shunt impedance
$R/Q_{\parallel,0}$	Ω	longitudinal shunt impedance of the operating mode
$R/Q_{\parallel,n}$	Ω	longitudinal shunt impedance of mode n
$R/Q_{\perp}$	Ω	transversal shunt impedance
$R/Q_{\perp,\mathrm{d}i}$	Ω	transversal shunt impedance of the ith dipole mode
$R/Q_{\perp,n}$	Ω	transversal shunt impedance of mode n
$R/Q_{\perp,\mathrm{TE111}}$	Ω	transversal shunt impedance of the TE_{111} mode
$R/Q_{\perp,\mathrm{TM110}}$	Ω	transversal shunt impedance of the TM_{110} mode
$R/Q_{\perp x,n}$	Ω	transversal shunt impedance of mode n in x-direction
$R/Q_{\perp y,n}$	Ω	transversal shunt impedance of mode n in y-direction
$\mathbf{S}$	1	discrete divergence operator for the primary grid
$\tilde{\mathbf{S}}$	1	discrete divergence operator for the dual grid
s	m	distance behind the exciting particle
$S_{i(j)k(l)}$	1	S-parameter between modes j and l of ports i and k, respectively
T	K	temperature
t	s	time
t_{b}	s	bunch spacing
T_{C}	K	critical temperature
U	J	stored energy
U_0	J	energy of the fundamental mode

Symbol	Unit	Description
$u(\mathbf{r}, t)$		unknown function in PDE
$u_j(t)$		unknown coefficient to be determined in FEM
U_{loss}	eV	beam energy loss per turn
U_n	J	energy of mode n
$\mathbf{v}$	m/s	particle's velocity
V_{400}	V	total RF voltage at 400 MHz
V_{800}	V	total RF voltage at 800 MHz
V_{cav}	V	accelerating voltage of the operating mode of one cavity
$\mathbf{v}_{\text{ext}}(t)$	V	output vector holding modal port voltages of the external ports
$\underline{\mathbf{v}}_{\text{ext}}$	V	complex vector of modal port voltages of the external ports
$\underline{\mathbf{v}}_{\text{ext},n}$	V	vector of modal port voltages at the frequency of mode n
$v_{\text{ext},p,m}(t)$	V	modal port voltage of port mode m at the external port p
$\tilde{V}_i$	m^3	volume of cell i in the dual grid
V_{loss}	V	RF voltage required to compensate the SR loss per turn
V_{RF}	V	total required RF voltage
V_{tot}	V	the total voltage provided by the RF system
$V_{\perp\text{x},n}$	V	transverse voltage of mode n in x-direction
$V_{\perp\text{y},n}$	V	transverse voltage of mode n in y-direction
$V_{\parallel,n}$	V	accelerating voltage of mode n
$\mathbf{w}$	V/C	wake function
$\mathbf{W}_i$	1	weight function in FEM
$\mathbf{W}(\mathbf{r}, s)$	V/C	wake potential
$w_{\parallel}$	V/C	longitudinal component of wake function
$\mathbf{w}_{\perp}$	V/C	transversal components of wake function
$\mathbf{x}$		eigenvector
x_0	m	offset from the axis in x-direction
$\underline{\mathbf{x}}_{\text{f}}$	$\sqrt{\text{VAs}}$	eigenvector arising from the first-order state-space model
$\mathbf{x}_{\text{f}}(t)$	$\sqrt{\text{VAs}}$	time-dependent first-order state vector
$\underline{\mathbf{x}}_{\text{f},n}$	$\sqrt{\text{VAs}}$	eigenvector of mode n in the first-order state-space model
y_0	m	offset from the axis in y-direction
z_0	m	center of Gaussian bunch distribution in z direction
Z_0	Ω	impedance of free space
Z_{h}	Ω	characteristic impedance of the transmission line connected to the hook-type coupler
$Z_{\text{h},i}$	Ω	characteristic impedance of the transmission line with the length $l_{\text{h},i}$ in the hook-type coupler's circuit

Symbol	Unit	Description
Z_{p}	Ω	characteristic impedance of the transmission line connected to the probe-type coupler
$Z_{\mathrm{p},i}$	Ω	characteristic impedance of the transmission line with the length $l_{\mathrm{p},i}$ in the probe-type coupler's circuit
$\underline{Z}_{p,m}(j\underline{\omega})$	Ω	complex termination impedance of mode m at port p
$\underline{Z}_{\mathrm{wave}}$	Ω	wave impedance
$\underline{Z}_{\mathrm{wave}}^{\mathrm{TE}}$	Ω	wave impedance of the TE modes
$\underline{Z}_{\mathrm{wave}}^{\mathrm{TM}}$	Ω	wave impedance of the TM modes
$Z_{\parallel}$	Ω	longitudinal impedance
$Z_{\parallel}^{\mathrm{o}}$	Ω	original longitudinal impedance
$Z_{\parallel}^{\mathrm{s}}$	Ω	scaled longitudinal impedance
$Z_{\parallel}^{\mathrm{th}}$	Ω	longitudinal impedance limit set by SR
$Z_{\perp}$	Ω/m	magnitude of the transversal beam impedance divided by the beam offset
$\mathbf{Z}_{\perp}$	Ω	transversal impedance
$Z_{\perp}^{\mathrm{th}}$	Ω/m	transversal impedance limit set by SR
α	degree	wall slope angle of the middle cell and single-cell cavity
α_{e}	degree	wall slope angle of the end cell
α_{c}	1	momentum compaction factor
α_{h}	degree	geometrical parameter of the hook-type coupler
α_{p}	degree	geometrical parameter of the probe-type coupler
α_{γ}	Np/m	attenuation constant
β	1	ratio of particle's velocity to the speed of light in vacuum
β_{xy}	m	beta function at the cavity region
β_{γ}	rad/m	phase constant
$\mathbf{\Gamma}$	m^2	arbitrary surface
$\underline{\gamma}$	1/m	propagation constant
ΔA	m	change in the variable A
ΔA_{cell}	1	field amplitude change in in each cell
δ_{d}	m^2/s	diffusion constant
Δf	1/s	detuning between the generator frequency and f_0
Δf^*	1/s	optimum value of Δf
Δf_{d}	1/s	deviation from the optimum detuning by, e.g., Lorentz force or microphonics effects
Δf_n	1/s	half-power bandwidth of mode n
$\delta_{m,n}$	1	Kronecker delta for index m and n
δ_{s}	m	skin depth

Symbol	Unit	Description
Δt	s	time step
Δx_i	m	edge length of the ith mesh cell in the x-direction
Δy_i	m	edge length of the ith mesh cell in the y-direction
Δz_i	m	edge length of the ith mesh cell in the z-direction
ε	As/(Vm)	permittivity
ε_0	As/(Vm)	permittivity of free space
ε_r	1	relative permittivity
η	1	net refrigerator efficiency factor
η_c	1	ideal Carnot efficiency factor
η_ff	1	field flatness coefficient
η_i	1	ith constant coefficient in the optimization
η_t	1	technical efficiency factor of the refrigeration machinery
λ	m	wavelength
$\underline{\lambda}$	1/s	eigenvalue arising from the first-order state-space model
λ_0	m	wavelength at FM frequency
λ_c	1	charge distribution
λ_e	1	eigenvalue
μ	Vs/(Am)	permeability
μ_0	Vs/(Am)	permeability of free space
μ_r	1	relative permeability
ν_s	1	synchrotron oscillation tune
$\boldsymbol{\varrho}$	As/m^3	vector containing sampled charged densities
$\underline{\rho}$	As/m^3	phasor of the electric charge density
$\rho(\mathbf{r}, t)$	As/m^3	electric charge density
ρ_b	m	bending radius
ρ_c	1	correlation coefficient
σ	A/(Vm)	conductivity
σ_z	m	RMS bunch length in the longitudinal direction
σ_z^o	m	original longitudinal bunch length
σ_z^s	m	scaled longitudinal bunch length
τ	s	time constant
τ_xy	s	transversal damping time
τ_z	s	longitudinal damping time
ϕ_0	1	initial phase of the RF voltage
ϕ_{400}	1	phase of the RF voltage at 400 MHz
ϕ_{800}	1	phase of the RF voltage at 800 MHz
ϕ_s	1	synchronous phase angle

Symbol	Unit	Description
$\varphi_0(\mathbf{r})$	1	initial phase
$\boldsymbol{\varphi}_j(\mathbf{r})$	1	basis function associated with the jth element in FEM
$\chi_{m,n}$	1	nth root of the mth order Bessel function
$\chi'_{m,n}$	1	nth root of the mth order Bessel function derivative
$\boldsymbol{\Omega}$	m^3	arbitrary domain
ω	1/s	angular frequency
$\underline{\omega}$	1/s	complex angular frequency
ω_0	1/s	angular frequency of FM
ω_{cut}	1/s	cutoff angular frequency
ω_n	1/s	angular frequency of mode n
$\Re$		real part of the complex number
$\Im$		imaginary part of the complex number
$\partial\boldsymbol{\Gamma}$	m	boundary of an arbitrary surface
$\partial\boldsymbol{\Omega}$	m^2	boundary of an arbitrary domain
$\partial\boldsymbol{\Omega}_{\mathrm{PEC}}$	m^2	PEC boundary condition
$\partial\boldsymbol{\Omega}_{\mathrm{PMC}}$	m^2	PMC boundary condition
∇	1/m	gradient operator
$\nabla_\perp$	1/m	gradient operator applied to transverse directions
$\nabla\cdot$	1/m	divergence operator
$\nabla\times$	1/m	curl operator
∇^2	$1/\mathrm{m}^2$	Laplace operator

1 Introduction

Since the beginning of the 20th century, particle accelerators have been widely used in a variety of applications such as medicine, industry, energy production, and scientific research. One application of particle accelerators are colliders in which two contra-rotating beams of particles are accelerated to high energies and then brought to collision. Detecting and analyzing the by-product of such collisions gives insights into the elementary particles and the physics involved. The existence of several fundamental particles was experimentally confirmed over the last few decades in different particle accelerators around the world. All known fundamental particles and three out of four fundamental forces are currently classified in the Standard Model (SM) of particle physics. In 2012, two Large Hadron[1] Collider (LHC) experiments, ATLAS [1] and CMS [2], detected the Higgs boson around a mass of $125\,\mathrm{GeV}/c^2$. The discovery of the Higgs boson experimentally validated the SM of particle physics. However, the SM is not a complete theory of fundamental interactions, and several important phenomena remained unexplained, e.g. the nature of dark matter and dark energy, matter-antimatter asymmetry, weakness of gravity force, the cause for the observed accelerating expansion of the universe, etc. Colliding particles at extremely high energies may give rise to the production of new particles and phenomena, and thus pave the way for answers to such questions.

At the moment, the world's largest and highest energy particle collider is the LHC, located in a tunnel with a circumference of around 27 km near Geneva. Until 2013, the center-of-mass proton-proton collision energy provided by the LHC was 7-8 TeV. No physics beyond the SM has yet been observed in the LHC. In 2015, the center-of-mass collision energy of the LHC was increased to 13-14 TeV. In order to extend the discovery potential of the LHC, current plans include an increase of its luminosity by a factor of ten by upgrading the LHC to the High-Luminosity LHC (HL-LHC) in the 2020s [3]. At the same time CERN launched the conceptual design study for a post-LHC collider called Future Circular Collider (FCC) in response to the request of the European Strategy for Particle Physics Update 2013 [4]. The FCC study covers three different types of particle collisions: hadron-hadron (hh) collision, electron-positron[2] (e^-e^+) collision and hadron-electron (he) collision. For each type of particle collision, a different accelerator configuration is required. The hadron collider option is referred to as FCC-hh, the lepton collider as FCC-ee, and

[1] Hadrons are composite particles, e.g. protons, that are made of quarks held together by gluons.
[2] In SM, the electron and positron are fundamental particles in the family of leptons.

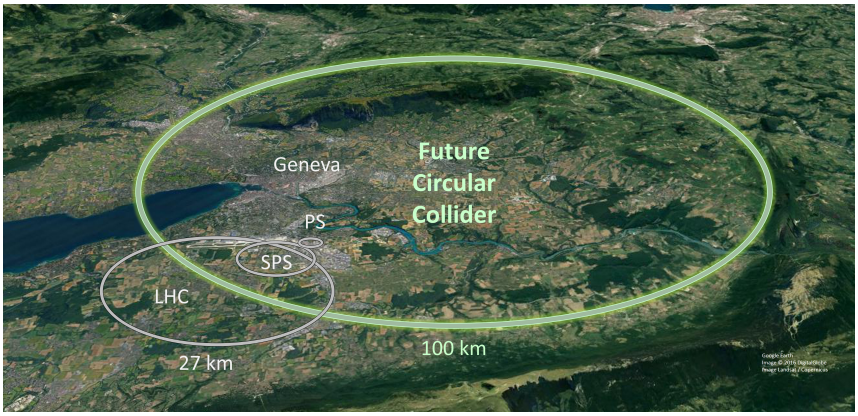

Figure 1.1: A schematic map of the FCC tunnel infrastructure (Image source: CERN [5]). The FCC tunnel requires a circumference of around 100 km (it is 97.75 km in the current baseline) to meet the physics goals.

the hadron-lepton collider as FCC-he.

As a design choice, the target value for the center-of-mass collision energy of FCC-hh is set to 100 TeV. At high energies, the beam rigidity of heavy particles such as hadrons increases significantly. Therefore, a strong dipole magnetic field B_d or a large bending radius ρ_b is required to bend the beam in the designated orbit. The beam rigidity, which is obtained by equating the Lorentz force with the centrifugal force, is defined as follows

$$B_\mathrm{d}\rho_\mathrm{b} = \frac{p}{q}, \tag{1.1}$$

where p and q are the particle's momentum and charge, respectively. For particle velocities close to the speed of light, the beam rigidity approximately equals E_0/c, where E_0 is the average particle's energy in the beam (also referred to as beam energy) and c is the speed of light in vacuum. For a proton beam of 50 TeV energy at relativistic velocity, the beam rigidity is around 1.67×10^5 Tm. The bending radius and the bending magnetic field have to be chosen in such a way that their product equals the beam rigidity. A large bending radius is costly (as it requires a larger collider), and a high bending magnetic field may go beyond the reach of available technology. Therefore, a compromise between civil engineering costs and dipole magnet capabilities should be achieved. Today, many researches are aiming at 16 T bending magnets based on Nb_3Sn superconductors [6, 7]. With a bending magnetic field slightly below 16 T and a dipole filling factor of about 0.8 in the arcs, the total length of the arcs will be 83.75 km. To accommodate the experiment systems, the injection and extraction systems, the radio frequency (RF) systems, and the collimation systems, additional straight sections with a total length of 14 km are considered. Thus, the total circumference of the ring adds up to 97.75 km [8]. Figure 1.1 shows a schematic map of the FCC tunnel.

The FCC-hh determines the tunnel infrastructure. Prior to the installation of the FCC-hh, the tunnel could accommodate a high-luminosity lepton collider (FCC-ee) for conducting precision studies on several fundamental particles. Finally, integration aspects for colliding electrons with protons are also considered within the framework of the FCC-he studies. The conceptual design report of FCC machines was published at the end of 2018 [9, 10, 11]. The focus of this thesis is on the RF system of FCC-ee.

1.1 The future circular lepton collider

The objective of FCC-ee is to provide lepton collisions in a wide range of beam energies from around 45 GeV to 182.5 GeV. The main center-of-mass energies of interest are the ones around the Z-pole ($\sim$ 91.2 GeV), at the W-pair production threshold ($\sim$ 160 GeV), at the ZH production peak ($\sim$ 240 GeV), at the top quark threshold ($\sim$ 350 GeV) and above ($\sim$ 365 GeV). The baseline operation energies are hereinafter, respectively, referred to as Z, W, H, $t\bar{t}_1$ and $t\bar{t}_2$. $t\bar{t}$ is also used to generally refer to the two highest energy options.

The performance of particle colliders is usually expressed by luminosity and center-of-mass collision energy. Luminosity is a quantity that measures the number of particle collisions produced in a collider per time per area. The higher the luminosity, the higher the amount of data produced in the detectors for study. In the case of a head-on collision in a circular collider, the luminosity is directly proportional to the product of the number of particles per bunch, to the revolution frequency, and to the number of bunches per beam, and it is inversely proportional to the transverse beam size [12]. Circular lepton colliders are the preferred choice for high luminosity lepton collisions at low energies (roughly below center-of-mass energy of 400 GeV) [13]. At high energies above 400 GeV, the circular colliders become less efficient due to synchrotron radiation (SR) loss. The SR loss scales inversely to the fourth power of the particle's mass. Therefore, light particles such as electrons lose a substantial amount of energy per turn due to SR, which has to be replenished by the RF system. For this reason, linear colliders are preferred for light particles at center-of-mass energies above 400 GeV. Figure 1.2 shows the luminosity as a function of center-of-mass energy for several proposed future lepton colliders. The Large Electron Positron collider (LEP), which is the highest energy lepton collider ever built so far, achieved a maximum luminosity of around $10^{32}\mathrm{cm}^{-2}\mathrm{s}^{-1}$ and a maximum beam energy of 104.5 GeV during its operation at CERN in the years between 1989 to 2000 [14]. In comparison to the LEP, FCC-ee aims to provide a much larger beam energy (maximum 182.5 GeV) and a several orders of magnitude higher luminosity (maximum $230 \times 10^{34}\mathrm{cm}^{-2}\mathrm{s}^{-1}$).

In the circular lepton colliders, the maximum achievable beam energy is limited

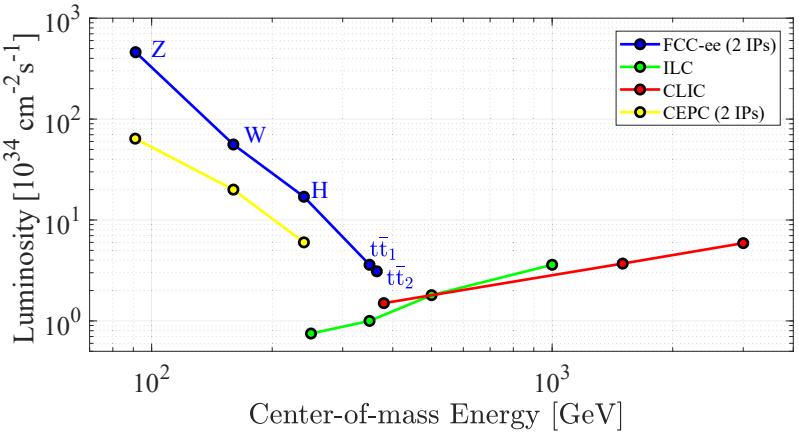

Figure 1.2: Expected luminosity of different lepton colliders as a function of center-of-mass energy. FCC-ee and CEPC [15] are circular colliders with two Interaction Points (IP) and ILC [16] and CLIC [17, 18] are linear colliders.

by the SR. The energy lost by an electron per turn is calculated by

$$U_{\text{loss}}\,[\text{keV}] = 88.46\frac{E_0^4\,[(\text{GeV})^4]}{\rho_{\text{b}}\,[\text{m}]}, \tag{1.2}$$

where E_0 is the particle's energy (here in GeV) and U_{loss} is the particle's energy loss per turn (here in keV). The particle's energy loss per turn depends on the fourth power of its energy. The beam energy loss per turn is 0.036 GeV for the Z energy and it reaches 9.2 GeV for the $\text{t}\bar{\text{t}}_2$. The RF voltage required to compensate the energy loss is subsequently obtained from

$$V_{\text{loss}} = \frac{U_{\text{loss}}}{q_e}, \tag{1.3}$$

where q_e is the elementary charge. In addition to the energy loss per turn, an over-voltage factor is typically considered in order to achieve a satisfactory beam lifetime [19, p. 93].

The total average radiation power of an electron beam is written as [20, p. 834]

$$P_{\text{SR}}\,[\text{kW}] = 88.46\frac{E_0^4\,[(\text{GeV})^4]\cdot I_0\,[\text{A}]}{\rho_{\text{b}}\,[\text{m}]}, \tag{1.4}$$

where I_0 is the average beam current. Additionally, some power is lost due to the interaction of the beam with the equipment in the ring. However, such losses are negligible compared to the SR power loss. As a design choice, the maximum SR power loss per beam for the FCC-ee is set to 50 MW (in total 100 MW for both beams). Therefore, the operation modes with lower beam energy are capable of

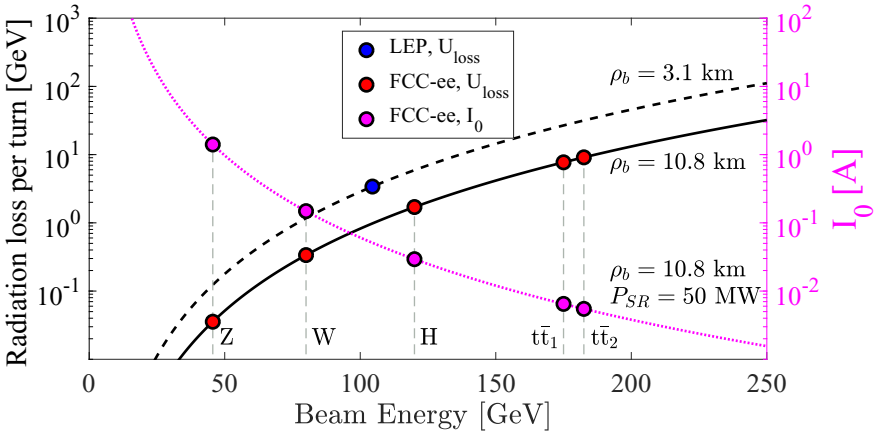

Figure 1.3: Radiation loss per turn for the FCC-ee and LEP as a function of beam energy is shown. For a given beam energy, the radiation loss in FCC-ee is lower than LEP due to the larger bending radius. Also shown is the beam current for the FCC-ee assuming 50 MW SR power loss per beam. For a fixed value of SR power loss, at lower energies higher beam current could be stored in the ring.

storing larger beam currents. A schematic graph of the synchrotron energy loss and the beam current as a function of beam energy for the FCC-ee is shown in Figure 1.3. Z and $t\bar{t}_2$ are the two limiting cases in terms of beam current and energy loss per turn. The Z energy option operates at a low energy but can store a high beam current of 1.39 A, and thus has the maximum luminosity among the FCC-ee operating points. On the other hand, the $t\bar{t}_2$ option has the largest SR loss and can subsequently store a low beam current of 5.4 mA. The other operating points fall between these two extremes in terms of voltage and current. Some baseline parameters of FCC-ee are listed in Table 1.1.

In order to keep the beam in the ring within the desired energy range, the lost energy has to be compensated by some accelerating mechanism. Electrostatic and electrodynamic particle accelerators are two basic classes of particle accelerators. In electrostatic accelerators, particles are accelerated in a static electric field. The maximum achievable energy gain in such accelerators is restricted by the high-voltage breakdown limits. Alternatively, a time-varying electromagnetic (EM) field that resonates in phase with the moving charged particles could be applied to achieve higher accelerating fields. Such resonating structures are referred to as RF cavities. Various forms of RF cavities are available depending on the velocity of particles to be accelerated [22, 23]. Rotationally symmetric elliptical cavities are typically used for the acceleration of charged particles close to the speed of light. A high accelerating field in the RF cavities is required to reduce the length of the RF section. The accelerating field of normal conducting cavities is mainly limited by the high losses on the surface of the cavity. The surface losses of the RF cavities could

Table 1.1: Machine parameters of the FCC-ee for different beam energies† [21].

	Z	W	H	$t\bar{t}_1$	$t\bar{t}_2$
Circumference [km]			97.756		
Bending radius [km]			10.76		
SR power / beam [MW]			50		
Beam energy [GeV]	45.6	80	120	175	182.5
Beam current [mA]	1390	147	29	6.4	5.4
Bunches / beam	16640	2000	328	59	48
Bunch population [10^{11}]	1.7	1.5	1.8	2.2	2.3
Average bunch spacing [ns]	19.6	163	994	2763	3396
Horizontal emittance [nm]	0.27	0.84	0.63	1.34	1.46
Vertical emittance [pm]	1.0	1.7	1.3	2.7	2.9
Arc cell phase advances [deg]	60/60	60/60	90/90	90/90	90/90
Momentum compaction [10^{-6}]	14.8	14.8	7.3	7.3	7.3
Horizontal β_x^* [m]	0.15	0.2	0.3	1.0	1.0
Vertical β_y^* [mm]	0.8	1.0	1.0	1.6	1.6
Horizontal size at IP σ_x^* [μm]	6.4	13.0	13.7	36.7	38.2
Vertical size at IP σ_y^* [nm]	28	41	36	66	68
Energy spread (SR/BS) [%]	0.038/0.132	0.066/0.131	0.099/0.165	0.144/0.196	0.150/0.192
Bunch length (SR/BS) [mm]	3.5/12.1	3.0/6.0	3.15/5.3	2.75/3.82	1.97/2.54
Energy loss / turn [GeV]	0.036	0.34	1.72	7.8	9.2
RF voltage [GV]	0.1	0.75	2.0	9.4	10.93
Long. damping time [turns]	1273	236	70.3	23.1	20.4
RF acceptance [%]	1.9	2.3	2.3	3.5	3.36
Energy acceptance [%]	±1.3	±1.3	±1.7	-2.8 +2.4	
Beam-beam parameter (x/y)	0.004/0.133	0.010/0.115	0.016/0.118	0.088/0.148	0.099/0.126
Synchrotron tune Q_z	-0.025	-0.0506	-0.0358	-0.0818	-0.0872
Horizontal tune Q_x	269.139	269.124	389.129	389.104	
Vertical tune Q_y	269.219	269.199	389.199	389.175	
Lifetime by rad. Bhabha [min]	68	59	38	37	40
Actual lifetime by BS [min]	>200	>200	18	24	18
Luminosity/IP [$10^{34}\,\mathrm{cm}^{-2}\mathrm{s}^{-1}$]	230	28	8.5	1.8	1.55

† Some parameters of the $t\bar{t}_1$ working point are changed in the conceptual design report [10, p. 283].

be substantially reduced by using superconducting radio frequency (SRF) cavities. This requires the operation of the cavities made of superconducting materials like niobium at extremely low temperatures (a few kelvin) to maintain the superconducting properties of the cavity walls. The advantage of superconducting cavities becomes clear in applications that require a high accelerating field in continuous wave (cw) or high duty factor operation because of significantly reducing the energy requirements [24, p. 6].

The RF cavities are usually equipped with auxiliary equipment such as input power coupler and higher order mode (HOM) couplers. The input coupler is con-

nected to the RF sources and excites the cavity at the accelerating mode[3] frequency. The energy lost by the beam in the ring is replenished by the power fed to the cavity through the input coupler. The availability of the RF sources at the desired frequency is an important consideration when selecting the frequency of the accelerating mode [25].

As a bunch of particles passes through the cavity (or experiences any variation in the cross-section of the vacuum chamber), it excites electromagnetic fields, which are referred to as wakefields. If not extracted, the wakefields can kick and disturb the following bunches or heat up the cavity walls. HOM couplers are used to extract such parasitic excited modes (that are referred to as HOMs) from the cavity, while leaving the accelerating mode intact. Today, various HOM damping methods are available, depending on the HOM power to be extracted and the strength of the damping required. Generally speaking, the higher the beam current, the stronger the excited wakefield. Therefore, large beam currents are more challenging for the design of the cavity and the HOM couplers. In the case of FCC-ee, the Z working point has the highest beam current and lowest voltage. Thus, it requires a dedicated cavity and HOM coupler design with a special focus on the HOM damping aspects of the cavity. Considering the beam energies of different operation modes of the FCC-ee, the $t\bar{t}_2$ option, on the other hand, needs the largest RF infrastructure. The very large RF voltage and the relatively low beam current of the $t\bar{t}_2$ working point demands a cavity design with more focus on the accelerating mode to lower the RF infrastructure requirements and subsequently reduce the respective RF cost. The possibility of merging the RF system of different operating modes of the FCC-ee also has to be carried out to lower the total cost of the RF system.

This thesis aims to take the first steps towards a detailed design for the large and expensive RF system of FCC-ee. First, this thesis will investigate a suitable baseline option for the RF system of FCC-ee. This includes the search for an appropriate RF frequency and number-of-cells per cavity for each working point of the FCC-ee, considering the HOM power, the power dissipated on the cavity walls, the input power, etc. RF cavities then have to be designed based on the requirements of each operation energy. After this, various HOM couplers have to be studied and optimized based on the HOM spectrum of the designed cavities. Finally, the performance of the HOM damped cavities has to be evaluated using various numerical techniques.

1.2 Overview

This thesis is based on the following structure: Chapter 1 provides an introduction to the FCC project. This chapter also includes the outline of this thesis. Chapter 2

[3]The accelerating mode of the elliptical cavity is also referred to as the fundamental mode (FM) as its field pattern corresponds to the fundamental mode of the cavity cells (the modes with the lowest frequency).

introduces the basic principles of this thesis. This includes an overview of Maxwell's equations and the behavior of EM fields in a closed structure. In particular, the RF cavities and the parameters that typically characterize them are presented. Furthermore, the basic principles of two commonly used numerical methods for the electromagnetic modeling are presented, namely the Finite Element Method (FEM) and the Finite Integration Technique (FIT).

Chapter 3 starts with a discussion of some of the figures of merit that are of importance in the determination of the RF layout. This includes the static and dynamic power loss in the cryomodules, which affects the total power required to run the superconducting cavities at the required low temperature, the input power, and the HOM power per cavity, which is limited by the capabilities of the available technology. Subsequently, various layout scenarios for different operating modes of the FCC-ee are studied, and a suitable frequency and number-of-cells per cavity for each option is determined. The layout of the FCC-ee is presented in the last section of Chapter 3. Based on the RF layout determined in Chapter 3, a cavity is designed for each energy option of the FCC-ee in Chapter 4. This includes multi-cell cavities for the W, H, and $t\bar{t}$ options and a single-cell cavity for the Z option. The middle cells and end cells of the multi-cell cavity are optimized separately, considering different objective functions. In Chapter 5, various HOM damping schemes are investigated. This includes coaxial HOM couplers and waveguide HOM couplers. Several coaxial HOM couplers are subsequently optimized based on the HOM spectrum of the cavities. A quad-ridged waveguide is also introduced, and its dimensions are optimized to allow efficient damping of the HOMs.

In Chapter 6, the HOM damped cavities are compared in terms of the HOM power and the longitudinal and transversal impedance of the cavities. In the first part of this chapter, two approaches for the calculation of the beam impedance of the cavity (i.e. from wake potential and from eigenmodes) are discussed. Two methods are then presented to approximate the HOM power that propagates into the waveguide ports connected to the HOM couplers. In section 6.1.3, the power propagated into the waveguide ports is obtained from the time domain calculation. Section 6.1.4, on the other hand, presents a numerical approach to calculate the coupling of each eigenmode of the cavity to the waveguide ports. Finally, the HOM damping aspects of the cavities designed for different energy options of the FCC-ee are studied. Chapter 7 concludes the thesis.

2 Theoretical background and numerical simulation methods

This chapter briefly presents the foundation of electromagnetic field theory and the underlying mathematical equations that describe the properties of RF structures. Next, the fundamental principles of the RF resonators is presented with a main focus on the SRF elliptical cavities. Finally, this chapter addresses the basic principles behind the numerical methods that are used in this thesis to solve Maxwell's equations in complex geometries with no analytical solution, including FEM and FIT.

2.1 Maxwell's equations

Maxwell's equations are a set of coupled partial differential equations, collected and completed by the 19th-century scientist James Clerk Maxwell [26], which form the foundation of electromagnetic theory. The representation of Maxwell's equations in their commonly known form was formulated by Oliver Heaviside (and independently by Gibbs). The integral formulation of Maxwell's equations is

$$\oint_{\partial\mathbf{\Gamma}} \mathbf{E}(\mathbf{r},t)\cdot \mathrm{d}\mathbf{l} = -\iint_{\mathbf{\Gamma}} \frac{\partial}{\partial t}\mathbf{B}(\mathbf{r},t)\cdot \mathrm{d}\mathbf{S}, \tag{2.1}$$

$$\oint_{\partial\mathbf{\Gamma}} \mathbf{H}(\mathbf{r},t)\cdot \mathrm{d}\mathbf{l} = \iint_{\mathbf{\Gamma}} \left(\frac{\partial}{\partial t}\mathbf{D}(\mathbf{r},t) + \mathbf{J}(\mathbf{r},t)\right)\cdot \mathrm{d}\mathbf{S}, \tag{2.2}$$

$$\oiint_{\partial\mathbf{\Omega}} \mathbf{D}(\mathbf{r},t)\cdot \mathrm{d}\mathbf{S} = \iiint_{\mathbf{\Omega}} \rho(\mathbf{r},t)\mathrm{dV}, \tag{2.3}$$

$$\oiint_{\partial\mathbf{\Omega}} \mathbf{B}(\mathbf{r},t)\cdot \mathrm{d}\mathbf{S} = 0, \tag{2.4}$$

where $\mathbf{E}(\mathbf{r},t)$ represents the electric field strength, $\mathbf{B}(\mathbf{r},t)$ the magnetic flux density, $\mathbf{H}(\mathbf{r},t)$ the magnetic field strength, $\mathbf{D}(\mathbf{r},t)$ the electric flux density, $\mathbf{J}(\mathbf{r},t)$ the electric current density and $\rho(\mathbf{r},t)$ the electric charge density. The spatial and time dependency of the introduced quantities is depicted by $\mathbf{r}$ and t, respectively. Equation (2.1) is referred to as Faraday's law of induction. It states that the line integral of the electric field strength along a closed boundary of an arbitrary surface $\partial\mathbf{\Gamma}$

equals the negative time derivative of the magnetic flux density integrated over the surface $\mathbf{\Gamma}$. Equation (2.2), known as Ampère's law with Maxwell's correction, states that the line integral of the magnetic field strength around a closed curve $\partial\mathbf{\Gamma}$ equals the sum of the surface integral of the electric current density and a time-varying electric flux density through the surface $\mathbf{\Gamma}$. Equation (2.3) is referred to as Gauss's law. It states that the net electric flux through any closed surface $\partial\mathbf{\Omega}$ of a domain $\mathbf{\Omega}$ is proportional to the net charge enclosed within the surface. Gauss's law for magnetism, Equation (2.4), states that the magnetic field is a solenoidal vector field, i.e. there are no magnetic charges analogous to electric charges.

In order to apply Maxwell's equations, it is necessary to relate electromagnetic fields that exist in material media by constitutive relations. The constitutive relations enable us to work only with free current and free charges without dealing explicitly with the magnetization vector or polarization vector in the media. For linear materials the constitutive relations are

$$\mathbf{D}(\mathbf{r},t) = \underbrace{\varepsilon_0\varepsilon_\mathrm{r}}_{\varepsilon}\mathbf{E}(\mathbf{r},t), \tag{2.5}$$

$$\mathbf{B}(\mathbf{r},t) = \underbrace{\mu_0\mu_\mathrm{r}}_{\mu}\mathbf{H}(\mathbf{r},t), \tag{2.6}$$

where $\varepsilon_0 \approx 8.854\times10^{-12}\,\mathrm{F/m}$ is the vacuum permittivity, ε_r the material-dependent relative permittivity, $\mu_0 \approx 4\pi\times10^{-7}\,\mathrm{H/m}$ the permeability of vacuum and μ_r the relative permeability of the material. For isotropic materials, ε and μ are scalars, while in anisotropic materials, they are second rank tensors. Throughout the rest of this thesis, we assume the materials under study are isotropic with a locally spatially constant ε and μ.

The electric current density is the sum of the current densities generated by different mechanisms

$$\mathbf{J}(\mathbf{r},t) = \mathbf{J}_\mathrm{imp}(\mathbf{r},t) + \underbrace{\sigma\mathbf{E}(\mathbf{r},t)}_{\mathbf{J}_\sigma(\mathbf{r},t)} + \underbrace{\delta_\mathrm{d}\nabla(\rho(\mathbf{r},t))}_{\mathbf{J}_\mathrm{cc}(\mathbf{r},t)}. \tag{2.7}$$

$\mathbf{J}_\mathrm{imp}(\mathbf{r},t)$ is the impressed current density which is externally supplied by a source, e.g. the beam current injected into the accelerating structure. $\mathbf{J}_\sigma(\mathbf{r},t)$ is the field-dependent Ohmic current density, referred to as conductive current density, with the electric conductivity σ, and $\mathbf{J}_\mathrm{cc}(\mathbf{r},t)$ represents the convection current density with the diffusion constant δ_d [27, p.12].

The integral forms of Maxwell's equations can conveniently be converted into their differential forms by using the divergence theorem [28, p. 45] and Stokes's theorem [28, p. 53] as follows

$$\nabla\times\mathbf{E}(\mathbf{r},t) = -\frac{\partial}{\partial t}\mathbf{B}(\mathbf{r},t), \tag{2.8}$$

$$\nabla \times \mathbf{H}(\mathbf{r},t) = \frac{\partial}{\partial t}\mathbf{D}(\mathbf{r},t) + \mathbf{J}(\mathbf{r},t), \tag{2.9}$$

$$\nabla \cdot \mathbf{D}(\mathbf{r},t) = \rho(\mathbf{r},t), \tag{2.10}$$

$$\nabla \cdot \mathbf{B}(\mathbf{r},t) = 0, \tag{2.11}$$

where $\nabla\times$ is the curl operator and $\nabla\cdot$ represents the divergence operator.

The force applied on a particle with charge q moving with velocity $\mathbf{v}$ in an electromagnetic field is referred to as Lorentz force and is calculated by

$$\mathbf{F}_{\text{lor}}(\mathbf{r},t) = q(\mathbf{E}(\mathbf{r},t) + \mathbf{v}(\mathbf{r},t) \times \mathbf{B}(\mathbf{r},t)). \tag{2.12}$$

Note that the force applied to the charged particle by the magnetic field is perpendicular to the direction of motion of the particle and depends on the particle's velocity, while the force applied by the electric field does not depend on the particle's velocity and has the same direction as the electric field strength. For this reason, the electric field is typically used for the acceleration of particles to high energies, and the magnetic field is usually used for changing the direction of the moving charged particles.

2.1.1 Helmholtz equation

Field vectors that are a function of space and vary sinusoidally with time can be equivalently written in vector phasor form that depends only on space. In other words, instantaneous values in the time domain can be replaced with phasor values in the frequency domain. Consider an electric field that varies sinusoidally with time

$$\mathbf{E}(\mathbf{r},t) = \mathbf{E}_0(\mathbf{r}) \cos[\omega t + \varphi_0(\mathbf{r})], \tag{2.13}$$

where $\mathbf{E}_0(\mathbf{r})$ is the vector amplitude of the electric field, ω the angular frequency and $\varphi_0(\mathbf{r})$ the initial phase. Equation (2.13) can be equivalently written as

$$\mathbf{E}(\mathbf{r},t) = \Re\{\underline{\mathbf{E}}(\mathbf{r})\mathrm{e}^{j\omega t}\}, \tag{2.14}$$

where $\Re$ represents the real part of the value in brackets and the complex-valued $\underline{\mathbf{E}}(\mathbf{r}) = \mathbf{E}_0(\mathbf{r})e^{j\varphi_0(\mathbf{r})}$ is the electric field phasor. The time derivative of a time-varying sinusoidal quantity in the time domain corresponds to an algebraic multiplication with $j\omega$ in the phasor domain. Maxwell's equations in time-harmonic form are then represented as

$$\nabla \times \underline{\mathbf{E}} = -j\omega\underline{\mathbf{B}}, \tag{2.15}$$

$$\nabla \times \underline{\mathbf{H}} = j\omega\underline{\mathbf{D}} + \underline{\mathbf{J}}, \tag{2.16}$$

$$\nabla \cdot \underline{\mathbf{D}} = \underline{\rho}, \tag{2.17}$$

$$\nabla \cdot \underline{\mathbf{B}} = 0, \tag{2.18}$$

The dependency of the phasors on the spatial coordinate $\mathbf{r}$ is not shown here for brevity. We will keep this notation throughout the rest of this thesis for the time-harmonic fields.

Maxwell's equations consist of a set of coupled first order partial differential equations. The equations for $\underline{\mathbf{E}}$ and $\underline{\mathbf{H}}$ could be combined to form a second order partial differential equation for each variable. For this purpose, the curl of equation (2.15) and (2.16) is taken

$$\nabla \times (\nabla \times \underline{\mathbf{E}}) = -j\omega\mu\nabla \times \underline{\mathbf{H}} = \omega^2\varepsilon\mu\underline{\mathbf{E}} - j\omega\mu(\underline{\mathbf{J}}_{\text{imp}} + \sigma\underline{\mathbf{E}} + \underline{\mathbf{J}}_{\text{cc}}), \tag{2.19}$$

$$\nabla \times (\nabla \times \underline{\mathbf{H}}) = j\omega\varepsilon\nabla \times \underline{\mathbf{E}} + \nabla \times \underline{\mathbf{J}} = \omega^2\varepsilon\mu\underline{\mathbf{H}} + \nabla \times (\underline{\mathbf{J}}_{\text{imp}} + \sigma\underline{\mathbf{E}} + \underline{\mathbf{J}}_{\text{cc}}), \tag{2.20}$$

where the equations (2.16), (2.15) and (2.7) are used to simplify the right hand side of the equations. The following vector identity is then used to further simplify the equations

$$\nabla \times (\nabla \times \mathbf{A}) = \nabla(\nabla \cdot \mathbf{A}) - \nabla^2\mathbf{A}, \tag{2.21}$$

where ∇^2 is the vector Laplacian operator. With this, the equations (2.19) and (2.20) can be written as

$$\nabla^2\underline{\mathbf{E}} - (-\omega^2\varepsilon\mu + j\omega\sigma\mu)\underline{\mathbf{E}} = \frac{1}{\varepsilon}\nabla\underline{\rho} + j\omega\mu(\underline{\mathbf{J}}_{\text{imp}} + \underline{\mathbf{J}}_{\text{cc}}), \tag{2.22}$$

$$\nabla^2\underline{\mathbf{H}} - \underbrace{(-\omega^2\varepsilon\mu + j\omega\sigma\mu)}_{\underline{\gamma}^2}\underline{\mathbf{H}} = -\nabla \times (\underline{\mathbf{J}}_{\text{imp}} + \underline{\mathbf{J}}_{\text{cc}}), \tag{2.23}$$

where $\underline{\gamma}$ is the propagation constant of the wave. The terms on the right hand side of the equations (2.22) and (2.23) represent the source of the fields. The real and imaginary part of the propagation constant have a different effect on the propagation of the wave

$$\underline{\gamma} = \alpha_\gamma + j\beta_\gamma = \sqrt{-\omega^2\mu\varepsilon + j\omega\mu\sigma}. \tag{2.24}$$

The real part α_γ is referred to as the attenuation constant and describes the attenuation rate of the wave. The imaginary part β_γ is referred to as the phase constant and represents the rate at which the phase changes as the wave propagates [29, p. 139].

In a non-excited, source-free and non-conducting medium, $\underline{\mathbf{J}}$, ρ and σ are zero. In such a case, equations (2.22) and (2.23) reduce to the so-called Helmholtz equations

$$\nabla^2\underline{\mathbf{E}} + \omega^2\mu\varepsilon\underline{\mathbf{E}} = \mathbf{0}, \tag{2.25}$$

$$\nabla^2\underline{\mathbf{H}} + \omega^2\mu\varepsilon\underline{\mathbf{H}} = \mathbf{0}. \tag{2.26}$$

Accordingly, the propagation constant is purely imaginary, and the phase constant is written as

$$\beta_\gamma = \omega\sqrt{\mu\varepsilon} = \frac{2\pi}{\lambda}, \tag{2.27}$$

where λ is the wavelength of a plane wave in the material. The phase constant β_γ is often also represented by the wave number k in the literature [29, p. 102].

2.2 Electromagnetic fields in a closed structure

The behavior of electromagnetic waves changes drastically near conducting structures. In fact, a perfect electric conductor (PEC) totally reflects back the incident EM waves. This principle could be used to create the so-called metallic waveguide (WG) structures. WGs are hollow conducting structures that are used to confine and guide the EM waves between their endpoints. The wave propagates through a WG by being repeatedly reflected at opposite walls of the WG. If both ends of the WG are terminated by a conductor, there will be a full reflection in the WG. In such a case, the waves traveling in opposite directions interfere with each other and establish a standing wave in the structure. The structure that supports standing waves is referred to as a resonator, and the standing fields are known as the eigenmodes of the resonator. The standing waves can oscillate in the resonator at fixed frequencies, referred to as eigenfrequency (or resonant frequency). The determination of the eigenmodes of a structure is a standard problem in computational sciences. The eigenmodes of a resonator in a non-excited source-free and lossless medium are determined by solving the Helmholtz equations presented in equations (2.25) and (2.26). The solutions of the Helmholtz equation must also satisfy the boundary conditions of the problem. The boundary conditions for a PEC imply that

$$\mathbf{n} \times \underline{\mathbf{E}} = \mathbf{0} \text{ and } \mathbf{n} \cdot \underline{\mathbf{H}} = 0 \text{ on } \partial\mathbf{\Omega}_{\text{PEC}}, \tag{2.28}$$

where $\mathbf{n}$ is the vector normal to the boundary $\partial\mathbf{\Omega}_{\text{PEC}}$. This indicates that the tangential component of the electric field and the normal component of the magnetic field on the surface of a PEC are zero. Free charges flow on the surface of a PEC in such a way as to enforce these boundary conditions. In a similar fashion, a perfect magnetic conductor (PMC) boundary condition could be defined over which

the tangential component of the magnetic field and the normal component of the electric field are zero

$$\mathbf{n} \cdot \underline{\mathbf{E}} = 0 \text{ and } \mathbf{n} \times \underline{\mathbf{H}} = \mathbf{0} \text{ on } \partial\mathbf{\Omega}_{\mathrm{PMC}}. \tag{2.29}$$

In this thesis, the conducting walls of the resonators are assumed to be of PEC and the interior domain of vacuum. The reason behind these assumptions is that the resonators studied in this thesis are made of superconducting materials with very high conductivity that are evacuated or filled with air.

2.2.1 RF cavities

A particle accelerator is a device that is used to accelerate particles to high velocities and energies. There are different particle accelerator designs, depending on the particle energy to be achieved, and the type of particles being accelerated. Today, RF cavities are one of the most widely used structures to accelerate charged particles. They consist of a hollow closed conductor in which the electromagnetic field can resonate. Charged particles passing through an RF cavity interact with the resonating electromagnetic field and, with the right phase, are accelerated along the cavity. The so-called pillbox cavity, which is an empty cylinder with conducting walls, is the simplest form of a cavity (see Figure 2.1(a)). This type of structure can sustain an infinite number of eigenmodes.

Traveling waves can be classified based on their field component in a given direction. Often that direction is the propagation direction of the wave, which is usually assumed to be the z-axis. A similar classification could be used for the standing-wave eigenmodes if they are considered as the superposition of two oppositely propagating waves in a given direction, e.g. along the z-axis (which is usually assumed to be the longitudinal direction of motion of particles in accelerator physics). The eigenmode is referred to as transverse electric (TE) mode if the z-component (longitudinal component) of the electric field is zero, i.e. $E_z(\mathbf{r}, t) = 0$. If the z-component of the magnetic field is zero, i.e. $H_z(\mathbf{r}, t) = 0$, the mode is referred to as transverse magnetic (TM) mode, and if both the electric and magnetic field are zero along the z-direction, the mode is known as the transverse electromagnetic (TEM) mode. If both the electric and magnetic fields have a non-zero component in the z-direction, the mode is referred to as hybrid mode. The field variation of the modes of a cylindrical cavity in space is usually designated by three subscript numbers attached to the mode type, i.e. TE_{mnp} and TM_{mnp} where m, n and p characterize the field distribution in the azimuthal $\hat{\boldsymbol{\varphi}}$, radial $\hat{\mathbf{r}}$ and longitudinal $\hat{\mathbf{z}}$ directions in a cylindrical coordinate system, respectively. Modes with an azimuthal order of zero $m = 0$ are referred to as monopole, $m = 1$ as dipole, $m = 2$ as quadrupole, and so on. The resonant frequency of the TM and TE modes in a pillbox cavity with a length of

L_{pb} and radius of R_{pb} are calculated from

$$f_{mnp}^{(\mathrm{TM})} = \frac{1}{2\pi\sqrt{\mu\varepsilon}}\sqrt{\left(\frac{\chi_{m,n}}{R_{\mathrm{pb}}}\right)^2 + \left(\frac{p\pi}{L_{\mathrm{pb}}}\right)^2}, \tag{2.30}$$

$$f_{mnp}^{(\mathrm{TE})} = \frac{1}{2\pi\sqrt{\mu\varepsilon}}\sqrt{\left(\frac{\chi'_{m,n}}{R_{\mathrm{pb}}}\right)^2 + \left(\frac{p\pi}{L_{\mathrm{pb}}}\right)^2}, \tag{2.31}$$

where $\chi_{m,n}$ and $\chi'_{m,n}$ are the n^{th} root of the m^{th} order Bessel functions and its first derivative, respectively.

As mentioned earlier, the electric field is used to accelerate particles to higher energies, while the magnetic field could be used to apply a transverse force to the traversing particle. The acceleration of particles could be achieved by using a TM mode; in fact, only the monopole TM modes have a nonzero longitudinal electric field at the center of the cavity, which is typically the path of the traversing particles [24, p. 41]. Among the infinite number of modes that can be excited in a pillbox cavity, the TM_{010} is a favorable mode for accelerating particles, as its electric field is purely longitudinal (see Figure 2.1(b)). Additionally, the magnetic field at the center of the cavity is zero for this mode, as shown in Figure 2.1(c). The dimensions of the pillbox cavity could be defined in such a way that the TM_{010} mode becomes the mode with the lowest frequency (the FM of the cavity). This helps to easily separate the operating FM from the other modes, and thus facilitates the damping of parasitic higher order modes.

The pillbox cavity is an idealized shape that cannot be directly used for particle acceleration as it does not have an aperture for the beam passage. In order to open a path for the incoming and outgoing beams, beam pipes are added on both sides of the cavity, as shown in Figure 2.1(d). The sharp corners of the resulting cavity are also rounded to lower the peak value of the electric and magnetic field on the surface of the cavity, and thus to lower the risk of problems associated with high surface fields such as field emission and thermal breakdown in superconducting cavities. A detailed explanation about the optimization of RF cavities will be given in Chapter 4. Note that adding the beam holes changes the geometry, so that resonating modes are no longer purely TE or TM. However, it is a common practice to identify modes as a TE or TM with their counterpart in a pillbox cavity if the E_z or H_z is negligibly small in the regions of interest.

In order to enhance the accelerating efficiency, one can concatenate several resonating cells and create a so-called multi-cell cavity [30, p. 22]. In such a case, the cells of the cavity behave like a set of coupled oscillators. Due to the multi-cell coupling, several modes of the same type exist in a multi-cell cavity that form the so-called passband of that mode type. By using a circuit model of the coupled resonators, the relative field amplitude in the cell number n of a mode m in a passband

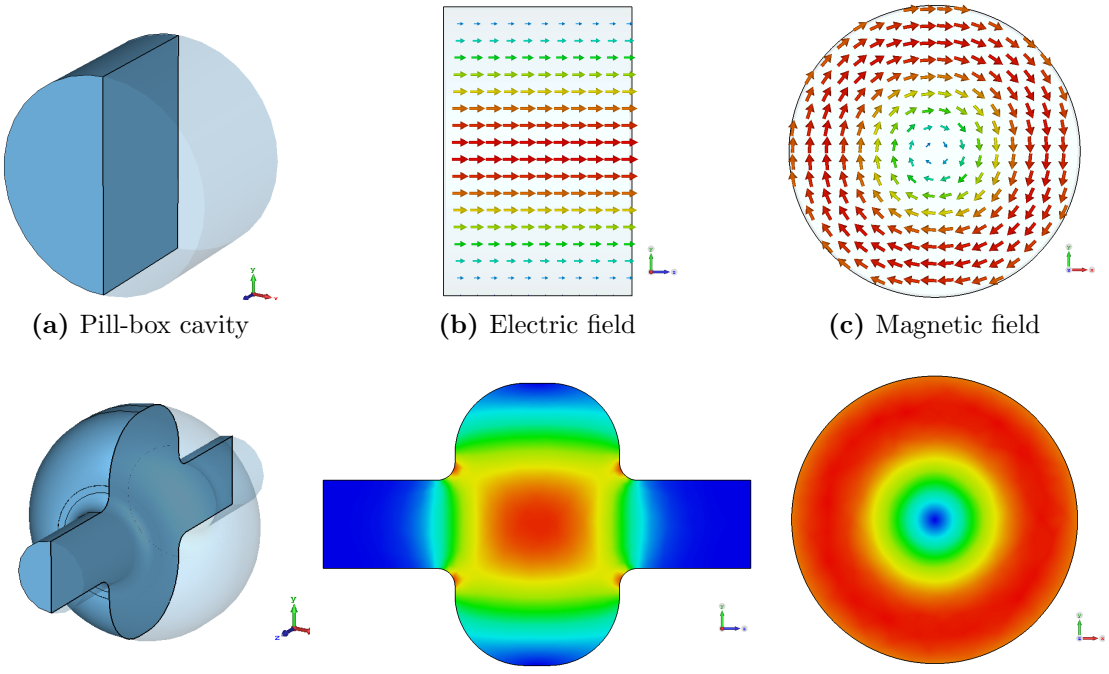

(a) Pill-box cavity **(b)** Electric field **(c)** Magnetic field

(d) Elliptical cavity **(e)** Absolute value of the electric field **(f)** Absolute value of the magnetic field

Figure 2.1: 3D model of a pillbox cavity (a) and a more realistic shape derived from the pillbox cavity with beam pipes and rounded edges (d). The electric and magnetic field distribution of the TM_{010} mode is also shown. The red color indicates a high magnitude of the electric and magnetic field, and the blue color corresponds to zero magnitude of the field.

of the multi-cell cavity is determined by

$$e_n^{(m)} = \sqrt{\frac{(2-\delta_{m,N_{\text{cell}}})}{N_{\text{cell}}}} \sin\left[m\pi\left(\frac{2n-1}{2N_{\text{cell}}}\right)\right], \tag{2.32}$$

where N_{cell} is the number of cavity cells, $\delta_{m,N_{\text{cell}}}$ is the Kronecker delta[1], and $n = 1,\ldots,N_{\text{cell}}$ and $m = 1,\ldots,N_{\text{cell}}$ represent the index for the cell and mode number, respectively [24, p. 132]. An example of the electric field distribution in the TM_{010} passband of a five-cell cavity is shown in Figure 2.2. Further details on the circuit model representation of monopole and dipole modes in a multi-cell cavity is given in [31, chapter 4]. Modes in one passband are usually designated by the longitudinal phase advance between the neighboring cells, which equals to $m\pi/N_{\text{cell}}$. As shown in Figure 2.2(a), the field amplitude of the π-mode is equal in all of the cells with

[1] $\delta_{m,n} = \begin{cases} 0, & \text{if } m \neq n, \\ 1, & \text{if } m = n. \end{cases}$

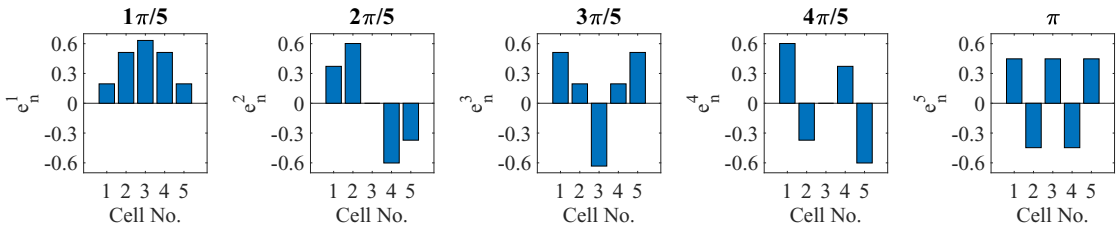

(a) Analytical

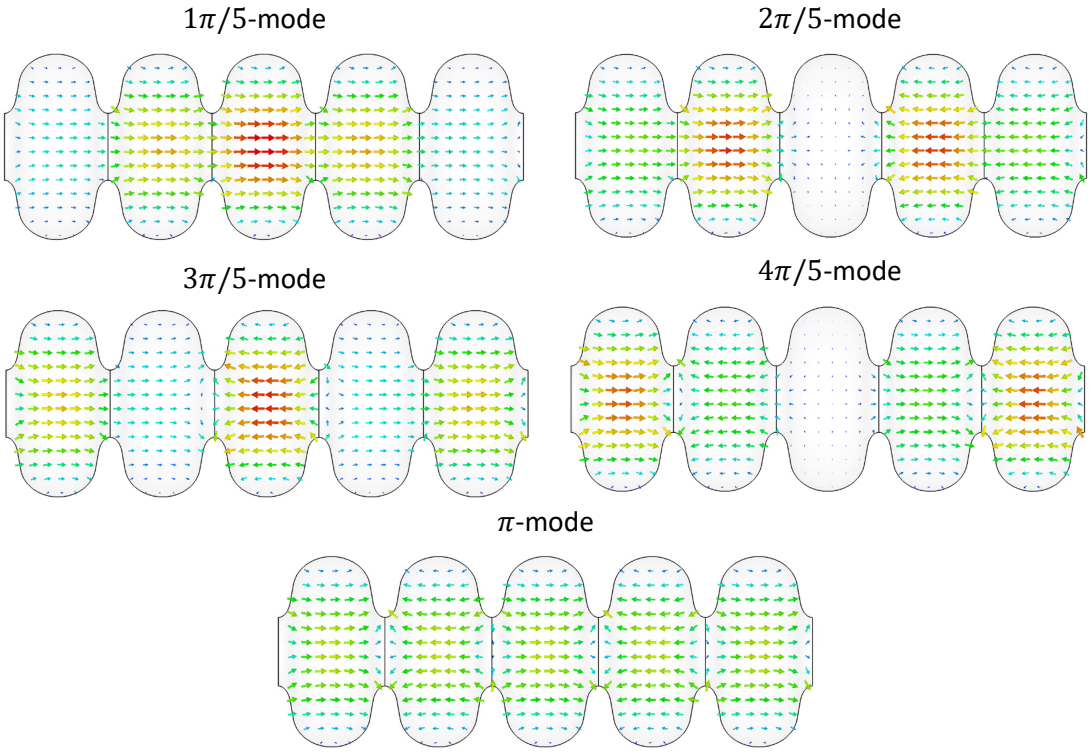

(b) Numerical

Figure 2.2: (a): Relative field distribution in the cells of a five-cell cavity calculated analytically using equation (2.32). (b): Electric field distribution of the modes in the TM_{010} passband of a five-cell cavity calculated numerically using PMC boundary condition at both ends in the longitudinal direction and PEC elsewhere.

opposite field direction between the neighboring cells. The $TM_{010} - \pi$ mode (where TM_{010} describes the mode-type in each cell, and π represents the phase difference between neighboring cells) is the most used mode for the acceleration of particles in RF cavities as the energy of the field is distributed equally among the cells, and thus each cell contributes equally to the acceleration of particles. Subsequently, the length of the cells is chosen such that the particles experience the same direction of

the electric field as they traverse the cavity (more details will be given in section 4.1).

2.2.2 Characteristic parameters

An RF cavity design is characterized by various figures of merit. Some of the most important parameters of the RF cavities are briefly presented in this section.

2.2.2.1 Operating frequency

The operating frequency f_0 of an RF cavity is the frequency of the eigenmode that is used for the acceleration of particles. The FM, or the lowest frequency mode, is typically used for the acceleration of particles in elliptical cavities (the TM_{010} mode). Note that in multi-cell elliptical cavities, the operating mode is not the mode with the lowest frequency, instead it is the highest-frequency mode of the first passband, i.e. the $\mathrm{TM}_{010} - \pi$ mode. The dimensions of the cavity are proportional to the wavelength of the operating mode λ_0. Thus, the size of the cavity scales inversely with the operating frequency. An operating frequency above several GHz gives rise to very tiny dimensions, which are difficult to fabricate with high precision [23]. Furthermore, in superconducting cavities, the surface losses approximately scale directly with the square of the frequency. For this reason, very high frequencies must be avoided for such cavities. An operating frequency below 100 MHz yields large cavities which would be expensive and difficult to manufacture and handle. Therefore, in practice, the operating frequency of the cavities ranges between several hundred MHz to a few GHz. The availability of appropriate RF sources is another factor which should be taken into account when choosing f_0.

2.2.2.2 Longitudinal and transversal voltage

The integrated force seen by a unit charge moving with the speed of light in an EM field along the z-axis is calculated by

$$\int_{z_{\min}}^{z_{\max}} (\underline{\mathbf{E}} + c\hat{\mathbf{z}} \times \underline{\mathbf{B}}) \mathrm{e}^{jk_n z} \mathrm{d}z = \int_{z_{\min}}^{z_{\max}} \left((\underline{E}_x - c\underline{B}_y)\hat{\mathbf{x}} + (\underline{E}_y + c\underline{B}_x)\hat{\mathbf{y}} + \underline{E}_z \hat{\mathbf{z}} \right) \mathrm{e}^{jk_n z} \mathrm{d}z. \tag{2.33}$$

The accelerating voltage is the effective voltage experienced by the charged particle in the longitudinal direction as it traverses the cavity, and for a mode n is calculated from

$$V_{\parallel,n}(x_0, y_0) = \int_{z_{\min}}^{z_{\max}} \underline{E}_z(x_0, y_0, z) \mathrm{e}^{jk_n z} \mathrm{d}z, \tag{2.34}$$

where k_n is the wave number ($k_n = \omega_n / \beta c$), and the integral is taken over the length of the investigated structure. The accelerating voltage for the FM of a cavity is

calculated from

$$V_{\mathrm{cav}} = \left|V_{\parallel,0}(0,0)\right| = \left|\int_{z_{\min}}^{z_{\max}} \underline{E}_z(0,0,z)\mathrm{e}^{jk_0 z}\mathrm{d}z\right|, \tag{2.35}$$

and the accelerating field is defined as

$$E_{\mathrm{acc}} = \frac{V_{\mathrm{cav}}}{L_{\mathrm{active}}}, \tag{2.36}$$

where L_{active} is the active length of the cavity in which the electric field is predominant. The active length of an elliptical cavity approximately equals the product of half the RF wavelength at FM frequency with the number of cells of the cavity (i.e. $L_{\mathrm{active}} = N_{\mathrm{cell}}\lambda_0/2$).

In a similar fashion, $V_{\perp\mathrm{x}}$ and $V_{\perp\mathrm{y}}$ are calculated by direct integration of the transverse force in the x and y directions, respectively, via:

$$V_{\perp\mathrm{x},n}(x_0,y_0) = \int_{z_{\min}}^{z_{\max}} \big(\underline{E}_x(x_0,y_0,z) - c\underline{B}_y(x_0,y_0,z)\big)\mathrm{e}^{jk_n z}\mathrm{d}z, \tag{2.37}$$

and

$$V_{\perp\mathrm{y},n}(x_0,y_0) = \int_{z_{\min}}^{z_{\max}} \big(\underline{E}_y(x_0,y_0,z) + c\underline{B}_x(x_0,y_0,z)\big)\mathrm{e}^{jk_n z}\mathrm{d}z. \tag{2.38}$$

The transverse voltages could also be calculated only from the electric field using Maxwell's equation through the Panofsky-Wenzel's theorem [32]. In such a case, equations (2.37) and (2.38) are, respectively, written as

$$V_{\perp\mathrm{x},n}(x_0,y_0) = \int_{z_{\min}}^{z_{\max}} \frac{j}{k_n}\frac{\partial \underline{E}_z(x,y_0,z)}{\partial x}\bigg|_{x_0} \mathrm{e}^{jk_n z}\mathrm{d}z - \left[\frac{j}{k_n}\underline{E}_x(x_0,y_0,z)\mathrm{e}^{jk_n z}\right]_{z_{\min}}^{z_{\max}}, \tag{2.39}$$

and

$$V_{\perp\mathrm{y},n}(x_0,y_0) = \int_{z_{\min}}^{z_{\max}} \frac{j}{k_n}\frac{\partial \underline{E}_z(x_0,y,z)}{\partial y}\bigg|_{y_0} \mathrm{e}^{jk_n z}\mathrm{d}z - \left[\frac{j}{k_n}\underline{E}_y(x_0,y_0,z)\mathrm{e}^{jk_n z}\right]_{z_{\min}}^{z_{\max}}. \tag{2.40}$$

If a PEC boundary condition at $z_{\min}$ and $z_{\max}$ is applied, the second terms, which depend on the tangential component of the electric field at both ends of the cavity, vanish and the transverse voltages could be derived solely from the longitudinal direction of the electric field, i.e. from $\underline{E}_z$. However, for a boundary condition different than PEC, both terms are required for the accurate calculation of the transverse voltage.

2.2.2.3 Impedance of a cavity

The geometric shunt impedance (also referred to as R/Q) relates the accelerating voltage to the stored energy in the cavity. The geometric shunt impedance in linac definition (two times the circuit definition) is

$$R/Q_{\parallel,n} = \frac{\left|V_{\parallel,n}(0,0)\right|^2}{\omega_n U_n}, \tag{2.41}$$

where U_n is the stored energy of mode n and is calculated from

$$U_n = \frac{1}{2}\iiint_\Omega \underline{\mathbf{H}}_n \cdot \underline{\mathbf{B}}_n \mathrm{d}V = \frac{1}{2}\iiint_\Omega \underline{\mathbf{D}}_n \cdot \underline{\mathbf{E}}_n \mathrm{d}V. \tag{2.42}$$

The geometric shunt impedance depends only on the geometry of the cavity. Increasing $R/Q_\parallel$ of a mode increases the particle's energy gain per unit of energy stored in that mode. The modal longitudinal loss factor, which relates the square of the charge to the energy deposited by the traversing point charge into the mode n of the cavity, is given by [33, p. 105]

$$k_{\parallel,n} = \frac{\left|V_{\parallel,n}(0,0)\right|^2}{4U_n} = \frac{\omega_n}{4} R/Q_{\parallel,n}. \tag{2.43}$$

The longitudinal loss factor is often expressed in V/pC.

Similar to equation (2.41), the transversal shunt impedance is calculated from

$$R/Q_{\perp,n} = \underbrace{\frac{\left|V_{\perp\mathrm{x},n}(0,0)\right|^2}{\omega_n U_n}}_{R/Q_{\perp\mathrm{x},n}} + \underbrace{\frac{\left|V_{\perp\mathrm{y},n}(0,0)\right|^2}{\omega_n U_n}}_{R/Q_{\perp\mathrm{y},n}}. \tag{2.44}$$

For a rotationally symmetric structure, the dipole modes are degenerate modes and can have any arbitrary azimuthal angle. This results in a different value of $V_{\perp\mathrm{x},n}$ and $V_{\perp\mathrm{y},n}$, depending on the chosen azimuthal angle. It can be shown that for the dipole modes, in a rotationally symmetric structure, the summation of the transverse shunt impedances in the x and y direction (as defined in equation (2.44)) is independent of the azimuthal angle of the mode and equals to the maximum value $R/Q_{\perp,n}$ can attain. Considering the Panofsky-Wenzel's theorem (from equations (2.39) and (2.40)), and assuming that the tangential component of the electric field is zero at both ends (PEC boundary condition), the transversal shunt impedance could be derived from the longitudinal voltage as follows

$$R/Q_{\perp,n} \approx \underbrace{\frac{\left|V_{\parallel,n}(x_0,0) - V_{\parallel,n}(0,0)\right|^2}{k_n^2 x_0^2 \omega_n U_n}}_{R/Q_{\perp\mathrm{x},n}} + \underbrace{\frac{\left|V_{\parallel,n}(0,y_0) - V_{\parallel,n}(0,0)\right|^2}{k_n^2 y_0^2 \omega_n U_n}}_{R/Q_{\perp\mathrm{y},n}}, \tag{2.45}$$

where the partial derivatives are approximated using the forward difference method with a step size of x_0 and y_0 in the x and y-directions, respectively. $R/Q_\perp$ is also referred to by R/Q_T.

The concept of impedance for a cavity is used to relate the beam current to the voltage induced in the cavity. The behavior of a resonating mode of the cavity close to the oscillation frequency could be modeled by a parallel RLC circuit [33, p. 79]. Thus, assuming that the eigenmodes are orthogonal to each other, the longitudinal impedance of the cavity close to the resonating angular frequency ω_n could be written as

$$Z_{\parallel,n}(\omega) = \frac{1}{2}\frac{R/Q_{\parallel,n}\cdot Q_n}{1 + jQ_n(\omega/\omega_n - \omega_n/\omega)}, \tag{2.46}$$

where Q_n is the quality factor of mode n. The factor $1/2$ is applied because the linac definition of the geometric shunt impedance is used. Similarly, the transverse impedance near a resonance frequency can be approximated from [34]

$$Z_{\perp,n}(\omega) = \frac{1}{2}\frac{k_n R/Q_{\perp,n}\cdot Q_n}{1 + jQ_n(\omega/\omega_n - \omega_n/\omega)}. \tag{2.47}$$

$Z_\parallel$ and $Z_\perp$ are also denoted by Z_L and Z_T, respectively.

2.2.2.4 Cell-to-cell coupling

Cell-to-cell coupling is a dimensionless coefficient which characterizes the spread of modes in a passband of the multi-cell cavity. The cell-to-cell coupling for the TM_{010} passband is defined as [23]

$$k_\mathrm{cc} = \left|2\frac{f_{\mathrm{p},\pi} - f_{\mathrm{p},0}}{f_{\mathrm{p},\pi} + f_{\mathrm{p},0}}\right| \cdot 100\,\%, \tag{2.48}$$

where $f_{\mathrm{p},0}$ and $f_{\mathrm{p},\pi}$ refer to the lowest and highest frequency in the passband, respectively. For the π-mode, which is the cavity's operating mode, the relative detuning of the cells changes the uniformity of the field amplitude in the cells via a proportionality factor of $\propto 1/k_\mathrm{cc}$ [35, 36, 37]. A uniform field energy distribution in the cells gives maximum accelerating efficiency. A large cell-to-cell coupling increases the robustness of the field profile in the cavity against geometrical perturbations.

2.2.2.5 Surface resistance

The relationship between the electric and magnetic field strength perpendicular to a given direction, e.g. z-direction, is described by means of the wave impedance and, in an unbounded medium, is obtained from [29, p. 140]

$$\underline{Z}_\mathrm{wave} = \frac{\underline{E}_{\perp,x}}{\underline{H}_{\perp,y}} = -\frac{\underline{E}_{\perp,y}}{\underline{H}_{\perp,x}} = \sqrt{\frac{j\omega\mu}{\sigma + j\omega\varepsilon}}. \tag{2.49}$$

For a normal conductor with $\omega\varepsilon \ll \sigma$, which implies that the displacement current is negligible compared to the conductive current, the wave impedance is simplified to

$$\underline{Z}_{\text{wave}} \approx \sqrt{\frac{j\omega\mu}{\sigma}} = \sqrt{\frac{\omega\mu}{2\sigma}} + j\sqrt{\frac{\omega\mu}{2\sigma}}. \tag{2.50}$$

The real part of the impedance is referred to as surface resistance and is given by [24, p. 79]

$$R_{\text{s}} = \sqrt{\frac{\mu\omega}{2\sigma}}. \tag{2.51}$$

Equation (2.51) shows that the surface resistance of a normal conducting material is proportional to the square root of frequency, i.e. $\propto \sqrt{f}$.

The resistance of a normal conductor gradually decreases as its temperature is lowered. For some remarkable materials, known as superconductors, the resistance to DC current suddenly drops to zero when the material is cooled below a so-called critical temperature T_{C}. The value of T_{C} varies for different materials, e.g. 9.2 K and 18.3 K for Nb and Nb_3Sn, respectively [38]. Superconducting materials have a low surface resistance when exposed to RF fields. The RF surface resistance of superconductors could be approximated by the following equation [24, p. 8]

$$R_{\text{s}} = \underbrace{A\frac{1}{T}f^2 \text{e}^{-\frac{\Delta(T)}{kT}}}_{R_{\text{BCS}}(T)} + R_0, \tag{2.52}$$

where A is a material dependent parameter, T the temperature, f the frequency, k the Boltzmann constant, 2Δ the temperature dependent energy gap of the superconductor material, and R_0 is the residual resistance, which is affected by the surface impurities and trapped magnetic flux. Note that the first term (R_{BCS}) decreases exponentially with the temperature and increases with the square of the frequency. R_0, on the other hand, seems to be not dependent on the temperature, and can be a few nΩ for a clean Nb surface.

The EM waves cannot penetrate deeper than a few skin depths into the conductors. The skin depth is the distance through which the amplitude of the wave is reduced to $1/e \approx 0.37$ of its initial value. The skin depth, for a good conductor, is calculated from [28, p. 320]

$$\delta_{\text{s}} = \sqrt{\frac{2}{\omega\mu\sigma}}. \tag{2.53}$$

At very high frequencies (in the range of tens of MHz and above), the induced current density is distributed on a thin layer near the surface of the conductor and is proportional to the tangential component of the magnetic field on the surface [39]. Therefore, the losses occur only near the surface of the conductor. The power

dissipated on the surface of a cavity is thus proportional to the surface resistance and is calculated by

$$P_{\mathrm{ds}} = \frac{1}{2} R_{\mathrm{s}} \iint_{\mathbf{\Gamma}} \left| \underline{\mathbf{H}}_{\mathrm{tan}} \right|^2 \mathrm{d}s, \tag{2.54}$$

where $\underline{\mathbf{H}}_{\mathrm{tan}}$ is the magnetic field tangential to the cavity surface.

At room temperature, the surface resistance of copper, a widely used normal conducting material, is in the range of a few mΩ (at several MHz frequency) while for a superconducting material it can reach some tens of nΩ. This leads to a significantly smaller power loss on the surface of superconducting cavities, which permits achieving a higher accelerating field. Superconducting cavities are superior to copper cavities in applications where high cw accelerating field (above a few MV/m) or high duty factor pulsed operation is required. Additionally, the beam pipe radius of superconducting cavities can be larger to reduce the effect of HOMs excited by the traversing beam. This leads to a reduction in $R/Q_{\parallel}$ of the FM, which, however, is compensated by large Q_0 of superconducting cavities (see next sub-subsection for the definition of Q_0). A detailed comparison between normal conducting and superconducting cavities is given in [40].

2.2.2.6 Quality factor

The quality factor is a dimensionless measure of power loss in a resonator, and represents the number of RF cycles required to dissipate the energy stored in the resonator

$$Q = \frac{\omega U}{P_{\mathrm{loss}}}. \tag{2.55}$$

Several mechanisms can contribute to the losses in a cavity, including dielectric and magnetic loss P_{mat}, conduction loss P_{ds} and external loss P_{ext}. The loaded quality factor Q_{L} of a mode n is defined as

$$\frac{1}{Q_{\mathrm{L},n}} = \frac{P_{\mathrm{ds},n} + P_{\mathrm{ext},n} + P_{\mathrm{mat},n}}{\omega_n U_n} = \frac{1}{Q_{\mathrm{ds},n}} + \frac{1}{Q_{\mathrm{ext},n}} + \frac{1}{Q_{\mathrm{mat},n}}. \tag{2.56}$$

The quality factor measuring the dissipated power on the surface walls of the cavity at the FM is an important figure of merit of the cavity and is referred to as unloaded quality factor or intrinsic quality factor and is denoted by Q_0

$$Q_0 = \frac{\omega_0 U_0}{P_{\mathrm{ds},0}} = \frac{\omega_0 \iiint_{\Omega} \underline{\mathbf{H}}_0 \cdot \underline{\mathbf{B}}_0 \mathrm{d}V}{R_{\mathrm{s}} \iint_{\Gamma} \left| \underline{\mathbf{H}}_{\mathrm{tan},0} \right|^2 \mathrm{d}s}, \tag{2.57}$$

where the index 0 refers to the FM. The intrinsic quality factor depends both on the material properties and the geometry of the cavity. The geometry-dependent part of the intrinsic quality factor is referred to as geometry factor

$$G = Q_0 \cdot R_{\mathrm{s}} = \frac{\omega_0 \iiint_{\Omega} \underline{\mathbf{H}}_0 \cdot \underline{\mathbf{B}}_0 \mathrm{d}V}{\iint_{\Gamma} \left| \underline{\mathbf{H}}_{\mathrm{tan},0} \right|^2 \mathrm{d}s}. \tag{2.58}$$

The quality factor is inversely proportional to the surface resistance. The value of Q_0 for copper cavities is in the order of 10^4 while it can reach 10^{10} for superconducting cavities. Since the considered superconducting cavities are evacuated, the dielectric and magnetic losses are only present when the lossy material in HOM absorbers is taken into account. In this thesis, such materials are not considered. The external losses comprise the EM energy that propagates out of the cavity via beam pipes or couplers. This can be modeled by terminating the couplers and beam pipes with WG ports, which resemble a non-reflective boundary condition. The smallest quality factor in equation (2.56) is the dominant value in Q_{L}. For superconducting cavities, due to very high Q_0, the Q_{ext} is mostly the dominant value, i.e. $Q_{\mathrm{L}} \approx Q_{\mathrm{ext}}$. For the HOMs with very small external loss, referred to as trapped modes, the value of Q_{ext} could become comparable to Q_0. Such modes could be detrimental to the operation of the cavity, as they can cause beam instability or deposit a significant power on the cavity wall.

From an *RLC* circuit model, the quality factor of a resonance mode could also be represented via the resonance bandwidth

$$Q_{\mathrm{L,n}} = \frac{f_n}{\Delta f_n}, \tag{2.59}$$

where Δf_n is the half-power bandwidth of the resonance mode.

2.3 Simulation methods to solve Maxwell's equations

Maxwell's equations could be solved analytically only for simple geometries such as spheres and cylinders. Complex electromagnetic problems could be tackled with a wide variety of numerical techniques, known as computational electromagnetics (CEM). In the majority of such methods, the computational domain is discretized into a structured or unstructured grid, composed of elements (or mesh cells). Maxwell's equations are then solved for each element in the grid, which, when combined for the entire mesh, approximates the solution in the whole computational domain.

The accuracy of numerical solutions is affected by several sources of error, such as modeling error, discretization error, iterative error, truncation error, and round-off error [41, p. 8-10]. The modeling error arises when converting the physical problem into a mathematical model under certain idealistic assumptions. These assumptions are sometimes made to simplify the model, for example, treating the boundary of superconducting cavities as PEC in solving the Helmholtz equation. The discretization error is the difference between the exact solution of the partial differential equation (PDE) and the exact solution of its discrete form. Such error

can arise from inaccurate fitting of the geometry with the mesh cells, also known as geometry modeling error. In order to tackle this problem, various forms of mesh cells are presented in the literature, such as triangular and quadrilateral meshes in 2D, and tetrahedron, pyramid, prism, and hexahedron mesh cells in 3D [42, p. 94]. Another important source of the discretization error corresponds to the assumptions made on the field's variation across each element during the discretization of a continuous problem. Such errors arise when the behavior of the field in the mesh cells does not precisely match with the physical problem; for example, a piecewise linear approximation of field in space and time can lead to large errors when using coarse mesh and large time steps, respectively. The discretization error typically decreases when a finer mesh is used, which, on the other hand, demands higher computational expenses. The numerical discretization of the PDE gives rise to a system of algebraic equations that are usually solved by iterative methods. The difference between the exact solution of the discrete form of the PDE and the iterative solution is referred to as iterative error. The truncation error arises when an infinite sum is truncated and approximated by a finite sum. The round-off error is the difference between the exact value of a number and its rounded-off value. This error occurs when storing numbers in digital computers with a finite precision. If no care is taken, small round-off errors can be amplified in certain numerical manipulations, e.g. avoid division by very small numbers, or adding or subtracting very large and very small numbers.

FEM and FIT are two widely used numerical methods for solving Maxwell's equations. In this thesis, the time domain calculations and the eigenmode computation within the framework of the State-Space Concatenation (SSC) method is carried out with FIT. The rest of the frequency domain calculations are done with FEM-based solvers. The basics of these two methods are briefly outlined in this section. A detailed description of FEM and FIT methods are given in [42, Ch. 6] and [27, Ch. 2.3], respectively.

2.3.1 Finite Element Method

The finite element method is a numerical method for finding an approximate solution of a PDE. A differential equation can be generally written in the form

$$L[u(\mathbf{r},t)] = f(\mathbf{r},t), \tag{2.60}$$

where L is an operator, $f(\mathbf{r},t)$ the source and $u(\mathbf{r},t)$ the unknown function (scalar or vector) in a domain $\mathbf{\Omega}$. For example, in a non-excited, source-free and non-conducting medium, the curl-curl equation (2.19) can be written as

$$\underbrace{\nabla\times\nabla\times\underline{\mathbf{E}}-\omega^2\varepsilon\mu\underline{\mathbf{E}}}_{L[\mathbf{u}(\mathbf{r})]} = \underbrace{\mathbf{0}}_{\mathbf{f}(\mathbf{r})} \quad \text{in } \mathbf{\Omega}, \tag{2.61}$$

where $\underline{\mathbf{E}}$ is the unknown function under the following boundary conditions

$$\mathbf{n}\times\underline{\mathbf{E}} = \mathbf{0} \quad \text{on } \partial\Omega_{\mathrm{PEC}}, \tag{2.62}$$

$$\mathbf{n} \times (\nabla \times \underline{\mathbf{E}}) = \mathbf{0} \quad \text{on } \partial\Omega_{\mathrm{PMC}}. \tag{2.63}$$

In the first step of FEM, the solution domain of equation (2.60) is subdivided into a collection of mesh cells. The unknown function is then expanded into a finite number N_e of basis functions $\varphi_j(\mathbf{r})$, i.e.

$$u(\mathbf{r}, t) \approx \sum_{j=1}^{N_e} u_j(t)\varphi_j(\mathbf{r}), \tag{2.64}$$

where $u_j(t)$ is the unknown coefficient to be determined. The basis functions are usually low order polynomials that are associated with a mesh entity such as node or edge and have small local support, i.e. nonzero in a few adjacent elements and zero elsewhere. In electromagnetic problems, the degrees of freedom in each element could be associated with the nodes or edges of the elements using nodal basis functions or edge basis functions, respectively. When dealing with vector quantities, such as electric field or magnetic field, nodal basis functions lead to nonphysical solutions, usually called spurious modes. Edge elements have turned out to be more suitable than nodal basis functions in the modeling of electric and magnetic fields as they provide solutions free from the spurious modes. The basis functions of edge elements are defined in a way to have a continuous tangential field component across element boundaries, while leaving the normal component free to jump across boundaries [42, p. 115]. Expanding the electric field in terms of basis functions yields

$$\underline{\mathbf{E}} \approx \sum_{j=1}^{N_e} \underline{E}_j \boldsymbol{\varphi}_j(\mathbf{r}), \tag{2.65}$$

where $\underline{E}_j$ is a scalar associated with the jth edge and N_e is the number of edges.

In the next step the residual of the PDE is formed, i.e. $R_{\mathrm{res}} = L[u(\mathbf{r}, t)] - f(\mathbf{r}, t)$. The aim is to make the residual as small as possible by properly choosing $u_j(t)$. Reducing the residual to zero at all points in the domain is not usually feasible (it would be the exact solution), therefore it is set to zero in a weighted average sense (referred to as the weak form of the governing equations). The weak form of equation (2.61) is obtained by taking its dot product with the weight function $\mathbf{W}_i$ and integrating it over the computational domain $\boldsymbol{\Omega}$

$$\iiint_{\boldsymbol{\Omega}} \left[\mathbf{W}_i \cdot \nabla \times \nabla \times \underline{\mathbf{E}} - \omega^2 \mu\varepsilon \mathbf{W}_i \cdot \underline{\mathbf{E}}\right] \mathrm{d}\Omega = 0. \tag{2.66}$$

By using a vector identity[2], the left hand side of the upper equation can be rewritten as

$$\iiint_{\boldsymbol{\Omega}} \left[(\nabla \times \mathbf{W}_i) \cdot (\nabla \times \underline{\mathbf{E}}) - \nabla \cdot \big(\mathbf{W}_i \times (\nabla \times \underline{\mathbf{E}})\big) - \omega^2 \mu\varepsilon \mathbf{W}_i \cdot \underline{\mathbf{E}}\right] \mathrm{d}\Omega = 0. \tag{2.67}$$

[2] $\mathbf{A} \cdot (\nabla \times \mathbf{B}) = (\nabla \times \mathbf{A}) \cdot \mathbf{B} - \nabla \cdot (\mathbf{A} \times \mathbf{B})$

The second term of the upper equation could be simplified using the divergence theorem[3] and the triple product identity[4] as follows

$$\begin{aligned}\iiint_{\mathbf{\Omega}} -\nabla\cdot\big(\mathbf{W}_i\times(\nabla\times\underline{\mathbf{E}})\big)\mathrm{d}\Omega &= \oiint_{\partial\mathbf{\Omega}} -\mathbf{n}\cdot\big[\mathbf{W}_i\times(\nabla\times\underline{\mathbf{E}})\big]\mathrm{d}\Gamma \\ = \iint_{\partial\mathbf{\Omega}_{\mathrm{PMC}}} \mathbf{W}_i\cdot\big[\mathbf{n}\times\nabla\times\underline{\mathbf{E}}\big]\mathrm{d}\Gamma &- \iint_{\partial\mathbf{\Omega}_{\mathrm{PEC}}} (\mathbf{n}\times\mathbf{W}_i)\cdot(\nabla\times\underline{\mathbf{E}})\mathrm{d}\Gamma,\end{aligned} \tag{2.68}$$

where the integral over the boundary is separated for the PEC and PMC regions. The first term on the right-hand side of equation (2.68) vanishes due to the Neumann boundary condition on the PMC region according to (2.63). The test functions also have to vanish on the parts of the boundary where the value of the unknown function is fixed by the Dirichlet boundary condition. Therefore, based on equation (2.62), the tangential components of the test functions are set to zero on PEC boundaries [43, p. 29]

$$\mathbf{n}\times\mathbf{W}_i = \mathbf{0} \quad \text{on } \partial\Omega_{\mathrm{PEC}}. \tag{2.69}$$

As a result, equation (2.67) turns into the following equation

$$\iiint_{\mathbf{\Omega}} \big((\nabla\times\mathbf{W}_i)\cdot(\nabla\times\underline{\mathbf{E}})\big)\mathrm{d}\Omega = \omega^2\mu\varepsilon \iiint_{\mathbf{\Omega}} \mathbf{W}_i\cdot\underline{\mathbf{E}}\,\mathrm{d}\Omega. \tag{2.70}$$

In the next step, $\underline{\mathbf{E}}$ is replaced with its approximate value using equation (2.65). A common approach in the weighted residual method is to take the test functions identical with the basis functions, i.e. $\mathbf{W}_i(\mathbf{r}) = \boldsymbol{\varphi}_i(\mathbf{r})$, which is known as Galerkin's method. Integrating equation (2.70) over all mesh elements yields the following generalized eigenvalue problem

$$\mathbf{K}\mathbf{x} = \lambda_e\mathbf{M}\mathbf{x}, \quad \mathbf{x}\neq\mathbf{0}, \tag{2.71}$$

with the unknowns $\mathbf{x}$ and λ_e. The scalar λ_e is the eigenvalue of the matrix pair $(\mathbf{K}, \mathbf{M})$ and contains information of the resonant frequency of the eigenmode i.e. equals $\omega^2\mu\varepsilon$. The non-zero vector $\mathbf{x}$ is the eigenvector corresponding to the eigenvalue λ_e and contains information on the field distribution in the structure, i.e. contains the scalar coefficient $\underline{E}_j$ [44]. The matrices $\mathbf{K}$ and $\mathbf{M}$ are referred to as stiffness matrix and mass matrix, respectively. The elements of the matrices $\mathbf{K}$ and $\mathbf{M}$ are, respectively, given by

$$K_{ij} = \iiint_{\mathbf{\Omega}} (\nabla\times\boldsymbol{\varphi}_i(\mathbf{r}))\cdot(\nabla\times\boldsymbol{\varphi}_j(\mathbf{r}))\mathrm{d}\Omega, \tag{2.72}$$

and

$$M_{ij} = \iiint_{\mathbf{\Omega}} \boldsymbol{\varphi}_i(\mathbf{r})\cdot\boldsymbol{\varphi}_j(\mathbf{r})\mathrm{d}\Omega. \tag{2.73}$$

[3] $\iiint_\Omega(\nabla\cdot\mathbf{A})\mathrm{d}\Omega = \oiint_{\partial\Omega}(\mathbf{A}\cdot\hat{\mathbf{n}})\mathrm{d}\Gamma$
[4] $\mathbf{A}\cdot(\mathbf{B}\times\mathbf{C}) = -\mathbf{B}\cdot(\mathbf{A}\times\mathbf{C})$

The matrices $\mathbf{K}$ and $\mathbf{M}$ are symmetric because of the Galerkin's method assumption. The system matrices are usually sparse due to the small local support of the chosen basis functions. Numerical software packages, such as [45], could then be used to solve the generalized eigenvalue problem for modes around the frequency of interest.

2.3.2 Finite Integration Technique

The FIT, introduced by T. Weiland in 1977 [46], discretizes the integral form of Maxwell's equations on a given mesh and transforms them into a set of matrix equations. The FIT method makes use of two computational grids, primary grid and dual grid. Every edge and facet of the primary grid intersect with a facet and edge of the dual grid, respectively. The integral-state variables of FIT are defined on the geometrical entities (edges, surfaces, and volumes) of the primary and dual grid as follows

$$\begin{aligned} \widehat{e}_i &= \int_{L_i} \mathbf{E}(\mathbf{r},t)\cdot \mathrm{d}\mathbf{l}, & \widehat{h}_i &= \int_{\tilde{L}_i} \mathbf{H}(\mathbf{r},t)\cdot \mathrm{d}\mathbf{l}, & \widehat{\widehat{\rho}}_i &= \iiint_{\tilde{V}_i} \rho(\mathbf{r},t)\mathrm{d}V, \\ \widehat{\widehat{d}}_i &= \iint_{\tilde{A}_i} \mathbf{D}(\mathbf{r},t)\cdot \mathrm{d}\mathbf{S}, & \widehat{\widehat{b}}_i &= \iint_{A_i} \mathbf{B}(\mathbf{r},t)\cdot \mathrm{d}\mathbf{S}, & \widehat{\widehat{j}}_i &= \iint_{\tilde{A}_i} \mathbf{J}(\mathbf{r},t)\cdot \mathrm{d}\mathbf{S} \end{aligned} \tag{2.74}$$

where $\widehat{e}$ is the electric grid voltage, $\widehat{h}$ the magnetic grid voltage, $\widehat{\widehat{d}}$ the electric grid flux, $\widehat{\widehat{b}}$ the magnetic grid flux, $\widehat{\widehat{j}}$ the electric grid current and $\widehat{\widehat{\rho}}$ the electric grid charges distributed in the computation domain. The quantities L_i and A_i are the edge and facet of the primary grid cells, while $\tilde{L}_i$, $\tilde{A}_i$, and $\tilde{V}_i$ are the edge, facet, and volume of the dual grid cells, respectively. In this thesis, only hexahedral meshes are used for FIT calculations. The location of field variables on the primary and dual grid of a hexahedral cell is shown in Figure 2.3. The quantities $\widehat{e}$ and $\widehat{\widehat{b}}$ are defined on the edges and facets of the primary grid cells, respectively. Analogously, $\widehat{h}$, $\widehat{\widehat{d}}$, $\widehat{\widehat{j}}$ and $\widehat{\widehat{\rho}}$ are defined on the edges, facets, facets and volumes of the dual grid cells, respectively. Combining equations in (2.74) with Maxwell's equations (2.1) - (2.4) in closed loops and closed surfaces results in a set of matrix-vector equations referred to as Maxwell's grid equations:

$$\mathbf{C}\widehat{\mathbf{e}} = -\frac{\mathrm{d}}{\mathrm{d}t}\widehat{\widehat{\mathbf{b}}}, \tag{2.75}$$

$$\tilde{\mathbf{C}}\widehat{\mathbf{h}} = \frac{\mathrm{d}}{\mathrm{d}t}\widehat{\widehat{\mathbf{d}}} + \widehat{\widehat{\mathbf{j}}}, \tag{2.76}$$

$$\tilde{\mathbf{S}}\widehat{\widehat{\mathbf{d}}} = \mathbf{q}, \tag{2.77}$$

$$\mathbf{S}\widehat{\widehat{\mathbf{b}}} = \mathbf{0}. \tag{2.78}$$

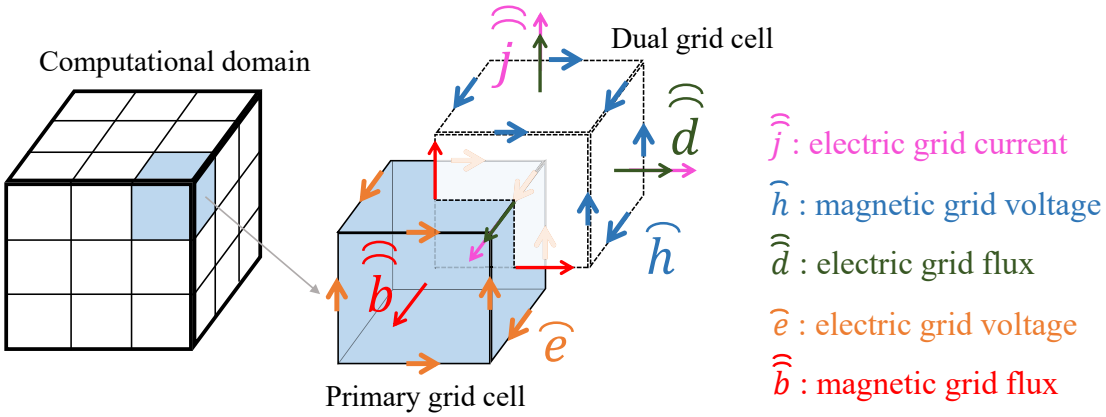

Figure 2.3: Topological FIT grid and state variables on hexahedral mesh.

The matrices $\mathbf{C}$ and $\tilde{\mathbf{C}} = \mathbf{C}^{\mathrm{T}}$ are the discretized curl operators in the primary and dual grid, respectively. The curl matrices are sparse matrices with the dimension $3N_{\mathrm{p}} \times 3N_{\mathrm{p}}$, where N_{p} is the number of nodal grid points. Similarly, the matrices $\mathbf{S} \in \mathbb{R}^{N_{\mathrm{p}} \times 3N_{\mathrm{p}}}$ and $\tilde{\mathbf{S}} \in \mathbb{R}^{3N_{\mathrm{p}} \times N_{\mathrm{p}}}$ represent the discretized divergence operators on the primary and dual grid, respectively. Both the curl and divergence matrices contain only $\{-1, 0, 1\}$ as their entries. Further details on the properties of the curl and divergence matrices are available in [47, p. 59].

The Maxwell's grid equations (2.75) - (2.78) are exact (free of approximation) representations of Maxwell's equation. The approximations are introduced by expressing the integral-state variables on a given mesh entity (edge, facet, or volume) as the product of the variable sampled in the middle of the mesh entity (referred to as sample-state variable) and the size of the respective mesh entity. A list of FIT approximate equations on a given grid is presented in Table 2.1. The Maxwell's grid equations for the sample-state variables are thus obtained by replacing the equations of Table 2.1 into equations (2.75) - (2.78)

$$\mathbf{C}\mathbf{D}_{\mathrm{s}}\mathbf{e} \approx -\mathbf{D}_{\mathrm{A}}\frac{\mathrm{d}}{\mathrm{d}t}\mathbf{b}, \tag{2.79}$$

$$\tilde{\mathbf{C}}\tilde{\mathbf{D}}_{\mathrm{s}}\mathbf{h} \approx \tilde{\mathbf{D}}_{\mathrm{A}}\frac{\mathrm{d}}{\mathrm{d}t}\mathbf{d} + \tilde{\mathbf{D}}_{\mathrm{A}}\mathbf{j}, \tag{2.80}$$

$$\tilde{\mathbf{S}}\tilde{\mathbf{D}}_{\mathrm{A}}\mathbf{d} \approx \tilde{\mathbf{D}}_{\mathrm{V}}\boldsymbol{\varrho}, \tag{2.81}$$

$$\mathbf{S}\mathbf{D}_{\mathrm{A}}\mathbf{b} \approx \mathbf{0}. \tag{2.82}$$

Combining equations (2.79) and (2.80) in the frequency domain yields the FIT formulation of the discrete curl-curl equation

$$\left(\tilde{\mathbf{C}}\mathbf{M}_{\mu}^{-1}\mathbf{C} + j\omega\mathbf{M}_{\sigma} - \omega^2\mathbf{M}_{\varepsilon}\right)\mathbf{D}_{\mathrm{s}}\mathbf{e} = -j\omega\tilde{\mathbf{D}}_{\mathrm{A}}(\mathbf{j}_{\mathrm{imp}} + \mathbf{j}_{\mathrm{cc}}), \tag{2.83}$$

where according to equation (2.7), the current density is replaced by different current sources, i.e. $\mathbf{j} = \mathbf{j}_{\mathrm{imp}} + \mathbf{j}_{\sigma} + \mathbf{j}_{\mathrm{cc}}$. For a given frequency, equation (2.83) gives a linear system of equations of the form $\mathbf{A}\mathbf{x} = \mathbf{b}$, where the terms on the right-hand-side are the excitation and $\mathbf{x}$ is the unknown (here it is $\mathbf{e}$). In a source-free and lossless medium, equation (2.83) is transformed to an eigenvalue problem

$$\mathbf{M}_{\varepsilon}^{-1}\tilde{\mathbf{C}}\mathbf{M}_{\mu}^{-1}\mathbf{C}\,\widehat{\mathbf{e}} = \omega^2\,\widehat{\mathbf{e}}, \tag{2.84}$$

where the unknowns ω^2 and $\widehat{\mathbf{e}}$ are the eigenvalue and the eigenvector, respectively. The system matrix of the eigenvalue problem could be made symmetric by the transformation $\widehat{\mathbf{e}}' = \mathbf{M}_{\varepsilon}^{1/2}\widehat{\mathbf{e}}$ which results in [48]

$$\mathbf{M}_{\varepsilon}^{-1/2}\tilde{\mathbf{C}}\mathbf{M}_{\mu}^{-1}\mathbf{C}\mathbf{M}_{\varepsilon}^{-1/2}\,\widehat{\mathbf{e}}' = \omega^2\,\widehat{\mathbf{e}}'. \tag{2.85}$$

Table 2.1: A list of FIT approximations on a given grid. The vectors $\mathbf{e}$, $\mathbf{h}$, $\mathbf{d}$, $\mathbf{b}$, $\mathbf{j}$ and $\boldsymbol{\varrho}$ collect the sample-state quantities of the respective integral-state quantities evaluated in the middle of mesh entities. The diagonal matrices $\mathbf{D}_{\mathrm{s}}$ and $\tilde{\mathbf{D}}_{\mathrm{s}}$ contain the edge lengths, $\mathbf{D}_{\mathrm{A}}$ and $\tilde{\mathbf{D}}_{\mathrm{A}}$ the surface area of the primary and dual grid cells, respectively. Similarly, $\tilde{\mathbf{D}}_{\mathrm{V}}$ contains the volume of the dual grid cells. The material matrices $\mathbf{D}_{\varepsilon}$, $\mathbf{D}_{\mu}$, and $\mathbf{D}_{\sigma}$ contain the average permittivity, permeability and, conductivity in the mesh cells, respectively.

$\widehat{\mathbf{e}} \approx \mathbf{D}_{\mathrm{s}}\mathbf{e}$	$\widehat{\tilde{\mathbf{d}}} \approx \tilde{\mathbf{D}}_{\mathrm{A}}\mathbf{d}$	$\mathbf{d} \approx \mathbf{D}_{\varepsilon}\mathbf{e}$	$\widehat{\tilde{\mathbf{d}}} \approx \underbrace{\tilde{\mathbf{D}}_{\mathrm{A}}\mathbf{D}_{\varepsilon}\mathbf{D}_{\mathrm{s}}^{-1}}_{\mathbf{M}_{\varepsilon}}\widehat{\mathbf{e}}$
$\widehat{\mathbf{h}} \approx \tilde{\mathbf{D}}_{\mathrm{s}}\mathbf{h}$	$\widehat{\tilde{\mathbf{b}}} \approx \mathbf{D}_{\mathrm{A}}\mathbf{b}$	$\mathbf{b} \approx \mathbf{D}_{\mu}\mathbf{h}$	$\widehat{\tilde{\mathbf{b}}} \approx \underbrace{\mathbf{D}_{\mathrm{A}}\mathbf{D}_{\mu}\tilde{\mathbf{D}}_{\mathrm{s}}^{-1}}_{\mathbf{M}_{\mu}}\widehat{\mathbf{h}}$
$\mathbf{q} \approx \tilde{\mathbf{D}}_{\mathrm{V}}\boldsymbol{\varrho}$	$\widehat{\tilde{\mathbf{j}}} \approx \tilde{\mathbf{D}}_{\mathrm{A}}\mathbf{j}$	$\mathbf{j}_{\sigma} \approx \mathbf{D}_{\sigma}\mathbf{e}$	$\widehat{\tilde{\mathbf{j}}}_{\sigma} \approx \underbrace{\tilde{\mathbf{D}}_{\mathrm{A}}\mathbf{D}_{\sigma}\mathbf{D}_{\mathrm{s}}^{-1}}_{\mathbf{M}_{\sigma}}\widehat{\mathbf{e}}$

Maxwell's grid equations can be discretized in time by forward or backward finite difference methods which yield explicit and implicit time-updating schemes, respectively. In each time-step of the explicit methods, the state variables at the new time could be computed from the state variables at the previous times by using simple matrix-vector multiplications without the need to solve algebraic equations. In the implicit methods, on the other hand, the latter variables are determined by solving a system of equations at each time step. The implicit time-updating schemes are more demanding computationally, but they are unconditionally stable, while the explicit methods are conditionally stable, and they have to satisfy certain conditions such as the Courant–Friedrichs–Lewy (CFL) condition [49]. The leap-frog scheme is a commonly used explicit time-updating scheme which samples electric and magnetic grid voltages at times separated by a half of time step and recursively updates

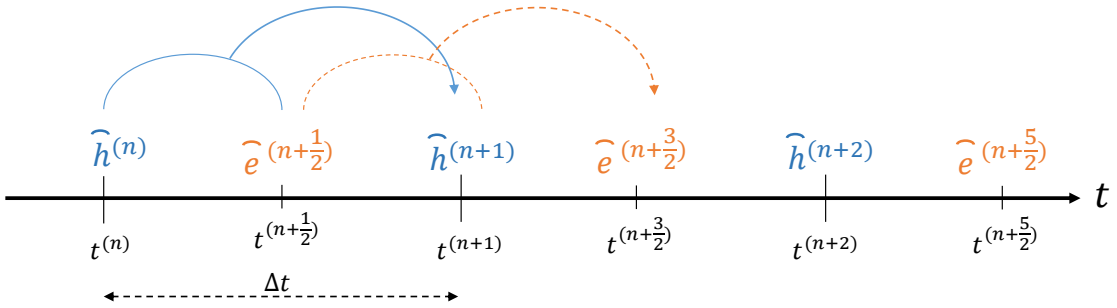

Figure 2.4: Leap-frog's time-updating scheme.

equations (2.75) and (2.76) as follows [50]

$$\begin{aligned} \widehat{\mathbf{h}}^{(n+1)} &= \widehat{\mathbf{h}}^{(n)} - \Delta t\, \mathbf{M}_{\mu}^{-1}\, \mathbf{C}\, \widehat{\mathbf{e}}^{(n+1/2)} \\ \widehat{\mathbf{e}}^{(n+3/2)} &= \widehat{\mathbf{e}}^{(n+1/2)} + \Delta t\, \mathbf{M}_{\varepsilon}^{-1} \big(\tilde{\mathbf{C}} \widehat{\mathbf{h}}^{(n+1)} - \widehat{\mathbf{j}}^{(n+1)} \big), \end{aligned} \tag{2.86}$$

where Δt is the time step. This time-updating scheme is also used in the wakefield solver of CST Studio Suite® [51]. A graphical representation of the leap-frog scheme is shown in Figure 2.4. The CFL stability condition requires the time step Δt to fulfill the following inequality [47, p. 55]

$$\Delta t \leq \min_i \frac{\sqrt{\varepsilon_i \mu_i}}{\sqrt{\frac{1}{\Delta x_i^2} + \frac{1}{\Delta y_i^2} + \frac{1}{\Delta z_i^2}}} \tag{2.87}$$

where i runs over all the mesh cells and Δx_i, Δy_i, and Δz_i are the edge lengths of the ith mesh cell. The CFL condition implies that the signal can travel at most one mesh cell per time-step to maintain the numerical stability [42, 66].

3 RF layout for FCC-ee

As discussed in Chapter 1, FCC-ee optimally demands different RF systems for each operating energy. This chapter starts by introducing some important parameters that are taken into account when designing the RF layout, such as the dissipated power in cavities, the required input power per cavity, and the HOM power. Each operating mode is then carefully studied, and the frequency and number of cells per cavity for each energy option is determined. The chapter ends with a staging and base-line plan for the development of the collider energy from the Z-pole to the $t\bar{t}_2$ energy.

3.1 Quantities of interest

3.1.1 Dissipated power

The power consumption of the cryogenic system is one of the cost drivers in the operation of FCC-ee. There are two sources of heat loss in the cryomodule, i.e. static losses and dynamic losses. The static heat losses are present when the module is at its designed operational temperature, and the losses exist even when the cavities are not powered. The static losses are caused by the non-ideal thermal insulation of the cold sections of the cryomodule e.g. via heat conduction and radiation through supports and pipes. Static heat loss is in the range of a few watts per meter [52, 53]. The dynamic heat loss arises from the power loss of induced RF currents into the cavity walls when cavities are operated at their nominal fields. Using equations (2.41) and (2.57), the power dissipated on the cavity walls by the FM is calculated from

$$P_{\mathrm{ds},0} = \frac{V_{\mathrm{cav}}^2}{R/Q_{\parallel,0} \cdot Q_0}, \tag{3.1}$$

where Q_0 is the intrinsic quality factor and $R/Q_{\parallel,0}$ is the geometric shunt impedance of the FM (linac definition). This dynamic power loss into the helium bath is the largest heat load in the cryomodule when its cavities are powered to their operating EM field [54].

A typical value of Q_0 for normal conducting copper cavities is in the order of 10^4, while for superconducting cavities, it can be in the order of 10^{10}. However, the actual energy saved with the superconducting cavities is less dramatic as the dissipated RF losses are lost at cryogenic temperature, and, therefore, the wall plug power required

to maintain the cryogenic temperature has to be taken into account. The total wall plug power (also referred to as AC power) can be approximated from [55]

$$P_{\mathrm{wp}} \approx N_{\mathrm{cav}} \frac{P_{\mathrm{ds},0} + P_{\mathrm{s}}}{\eta} = N_{\mathrm{cav}} \frac{P_{\mathrm{ds},0} + P_{s}}{\eta_{\mathrm{c}} \eta_{\mathrm{t}}}, \tag{3.2}$$

where P_{s} is the static power loss in cryogenic temperature for one cavity, η is the net refrigerator efficiency, η_{c} is the ideal Carnot efficiency:

$$\eta_{\mathrm{c}} = \frac{T}{300 - T}, \tag{3.3}$$

and η_{t} is the technical efficiency of the refrigeration machinery, which is typically between 0.2 to 0.3 (20% to 30%) [24, p. 7]. In this study, η_{t} is taken to be 0.3 at $T = 4.5\,\mathrm{K}$ and 0.2 at $T = 2\,\mathrm{K}$ [56]. The total wall plug power in (3.2) is calculated by multiplying the wall plug power for one cavity with the total number of cavities. The integer number N_{cav} is calculated by dividing the total required RF voltage by the voltage of one cavity, i.e.

$$N_{\mathrm{cav}} = \frac{V_{\mathrm{RF}}}{V_{\mathrm{cav}}} = \frac{V_{\mathrm{RF}}}{E_{\mathrm{acc}} \cdot L_{\mathrm{active}}}. \tag{3.4}$$

Note that in the numerator of equation (3.2), only the dynamic heat loss of the FM is considered. HOMs, if not properly damped, can also contribute to the dynamic heat losses and thus increase the total wall plug power of the cavities. For this reason, HOM couplers are used to decrease the external quality factor of HOMs and subsequently decrease the HOM power loss on the cavity walls.

The total wall plug power needed for removing dynamic and static RF heat losses out of cavities could be written as:

$$P_{\mathrm{wp}} \approx \frac{1}{\eta} \underbrace{V_{\mathrm{RF}} \frac{E_{\mathrm{acc}} \cdot L_{\mathrm{active}}}{R/Q_{\parallel,0} \cdot Q_0}}_{P_{\mathrm{dynamic}}} + \frac{1}{\eta} \underbrace{\frac{L_{\mathrm{cavity}} \cdot V_{\mathrm{RF}}}{L_{\mathrm{active}} \cdot E_{\mathrm{acc}}} P_{\mathrm{cryo}}}_{P_{\mathrm{static}}}. \tag{3.5}$$

The static power loss is proportional to the product of the length of the cold section of one cavity (L_{cavity}) with the total number of cavities (N_{cav}) and the static power loss per length (P_{cryo}). The value of P_{cryo} is around $8\,\mathrm{W/m}$ at $500\,\mathrm{MHz}$ and varies approximately as [57]

$$P_{\mathrm{cryo}} \approx \frac{8\,\mathrm{W/m}}{\sqrt{f_0/500\,\mathrm{MHz}}} \tag{3.6}$$

where f_0 is the operational frequency in MHz. The static loss P_{static} has an inverse relationship with E_{acc}, because for lower E_{acc} more cavities are needed to reach the total voltage V_{RF}, and thus the static loss increases. The dynamic losses, on the other hand, have a direct relationship with E_{acc}. Furthermore, the value of Q_0 in the denominator of (3.5) depends on E_{acc} and varies based on the material, temperature

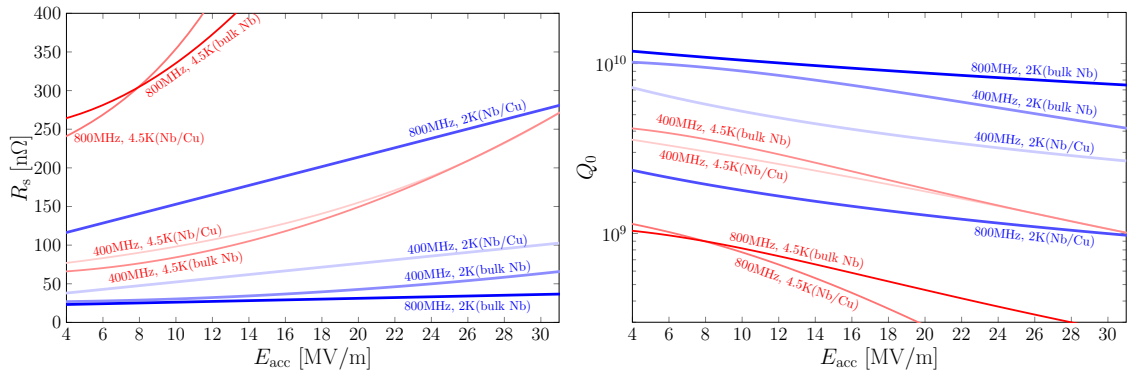

(a) R_s **(b)** Q_0

Figure 3.1: Surface resistance of bulk Nb and Nb/Cu at different frequencies and temperatures. Empirical formulas are used in each case to approximate the surface resistance [60]. In the approximation of R_s, B_{pk}/E_{acc} of 4.2 mT/(MV/m) is assumed. The quality factor is calculated by $Q_0 = G/R_s$ where a value of 274 Ω is assumed for G.

and frequency of operation. The surface resistance and the equivalent intrinsic quality factor (for a typical cavity with $B_{pk}/E_{acc} = 4.2\,\mathrm{mT/(MV/m)}$ and $G = 274\,\Omega$) for different materials and operational conditions are shown in Figure 3.1.

Considering the material properties and operational costs, throughout the rest of this chapter, Niobium-coated Copper (Nb/Cu) operating at 4.5 K is assumed for the 400 MHz cavities, and bulk Niobium at a temperature of 2 K is considered for the 800 MHz cavities. Alternative SRF materials with a higher critical temperature and smaller R_s than niobium (such as Nb_3Sn) have shown promising results in laboratories [58, 59]. Since such cavities are still under development and more R&D has to be carried out on such types of materials, they are not considered in this study.

3.1.2 Input RF power

The input power coupler should provide the necessary RF power to the cavity in order to compensate for the energy lost by the beam, e.g. due to SR. In the FCC-ee design, the maximum SR power loss is assumed to be 50 MW per beam. This power has to be provided by the input couplers. The generator power for superconducting cavities can be written as [61, p. 39]:

$$P_{in} = \frac{V_{cav}^2}{4(R/Q_{\parallel,0})Q_{L,0}}\left(\left[1+\frac{(R/Q_{\parallel,0})Q_{L,0}I_0}{V_{cav}}\cos\phi_s\right]^2+\left[\frac{\Delta f}{f_{1/2}}+\frac{(R/Q_{\parallel,0})Q_{L,0}I_0}{V_{cav}}\sin\phi_s\right]^2\right) \tag{3.7}$$

where $Q_{\mathrm{L},0}$ is the loaded quality factor of FM, Δf is the difference between the generator frequency f and f_0, i.e. $\Delta f = f_0 - f$, I_0 is the average beam current and $f_{1/2}$ is the half bandwidth of the cavity at fundamental mode frequency and is defined as:

$$f_{1/2} = \frac{f_0}{2Q_{\mathrm{L},0}} \tag{3.8}$$

where f_0 is the frequency of the accelerating mode. The angle ϕ_s is the synchronous phase angle, defined with respect to the on-crest operation, and is calculated from

$$\phi_\mathrm{s} = \arccos\left(\frac{V_\mathrm{loss}}{V_\mathrm{RF}}\right). \tag{3.9}$$

The impedance between the generator and the combined beam-cavity system should be matched in order to minimize the reflected power. Therefore, maximum power can be transferred to the cavity and thus to the beam. Making the second bracket of (3.7) zero by detuning the cavity minimizes the required power

$$\Delta f^* = \frac{-(R/Q_{\parallel,0}) f_0 I_0 \sin\phi_\mathrm{s}}{2V_\mathrm{cav}}. \tag{3.10}$$

The optimum coupling, i.e. the optimum loaded quality factor, could be derived by differentiating the resulting equation with respect to $Q_{\mathrm{L},0}$ and equating it to zero:

$$Q^*_{\mathrm{L},0} = \frac{V_\mathrm{cav}}{(R/Q_{\parallel,0}) I_0 \cos\phi_\mathrm{s}}. \tag{3.11}$$

The input coupler has to compensate the energy lost in the cavity walls by the RF field, the energy lost by the beam due to SR and other parasitic losses due to impedances. Since superconducting cavities are used, the loss on the cavity walls is negligible compared to the SR loss. Therefore, the minimum input power per cavity can be simply approximated by dividing the total SR loss by the number of cavities:

$$P^*_\mathrm{in} \approx \frac{V^2_\mathrm{cav}}{(R/Q_{\parallel,0})(Q^*_{\mathrm{L},0})} = V_\mathrm{cav} I_0 \cos\phi_\mathrm{s} = \frac{P_\mathrm{SR}}{N_\mathrm{cav}}, \tag{3.12}$$

where P_SR represents the losses by SR.

3.1.3 HOM power

A beam traversing the cavity interacts with the surrounding enclosure and deposits electromagnetic energy in the cavity. This beam-cavity interaction can limit the current handling capability of the accelerator. The HOM power deposited by the beam in a single pass is given by:

$$P_\mathrm{HOM} = k_{\parallel,\mathrm{HOM}} Q_\mathrm{b} I_0, \tag{3.13}$$

where Q_b is the bunch charge and I_0 is the average beam current. The value of $k_{\parallel,\mathrm{HOM}}$ represents the longitudinal loss factor of the excited higher order modes and is given by

$$k_{\parallel,\mathrm{HOM}} = k_{||} - k_{||,0}, \tag{3.14}$$

where $k_{\parallel,0}$ is the loss factor of the FM, and $k_{||}$ is the total longitudinal loss factor, which could be calculated by numerical solvers such as ABCI [62]. For an exciting bunch with the length σ_z, the loss factor $k_{\parallel,0}$ of the FM can be obtained by

$$k_{||,0} = \frac{\omega_0}{4}\frac{R}{Q}_{\parallel,0} \mathrm{e}^{-(\omega_0\sigma_z/c)^2}, \tag{3.15}$$

where ω_0 is the angular frequency of the FM, and c is the speed of light [63]. The loss factor depends on the cavity structure and on the bunch shape. As shown in Figure 3.2, smaller cavities (higher FM frequency) and more transitions in the vacuum chamber cross-section along the beam path (higher number of cells) lead to larger $k_{||}$. The total longitudinal loss factor is, on the other hand, inversely proportional to the square root of the bunch length.

The total longitudinal loss factor for a Gaussian bunch can be expressed by the integral [33]:

$$k_{||}(\sigma_z) = \frac{1}{2\pi}\int_{-\infty}^{\infty} Z_{||}(\omega)\mathrm{e}^{-(\omega\sigma_z/c)^2}\mathrm{d}\omega. \tag{3.16}$$

Assume all the geometrical parameters of a cavity to be scaled by a factor of C_s; the longitudinal impedance spectrum of the cavity in the frequency domain scales by $1/C_\mathrm{s}$, i.e. $Z^\mathrm{o}_{||}(\omega) = Z^\mathrm{s}_{||}(\omega/C_\mathrm{s})$, where $Z^\mathrm{o}_{||}$ and $Z^\mathrm{s}_{||}$ are the longitudinal impedance of the original and the scaled cavity, respectively. The loss factors of the scaled and the original geometry are related, as

$$\begin{aligned} k^\mathrm{o}_{||}(\sigma^\mathrm{o}_z) &= \frac{1}{2\pi}\int_{-\infty}^{\infty} Z^\mathrm{o}_{||}(\omega)\mathrm{e}^{-(\omega\sigma^\mathrm{o}_z/c)^2}\mathrm{d}\omega \\ &= \frac{1}{2\pi}\int_{-\infty}^{\infty} Z^\mathrm{s}_{||}(\frac{1}{C_\mathrm{s}}\omega)\mathrm{e}^{-(\omega\sigma^\mathrm{o}_z/c)^2}\mathrm{d}\omega \\ &= \frac{C_\mathrm{s}}{2\pi}\int_{-\infty}^{\infty} Z^\mathrm{s}_{||}(\omega')\mathrm{e}^{-(C_\mathrm{s}\omega'\sigma^\mathrm{o}_z/c)^2}\mathrm{d}\omega' \\ &= \frac{C_\mathrm{s}}{2\pi}\int_{-\infty}^{\infty} Z^\mathrm{s}_{||}(\omega')\mathrm{e}^{-(\omega'\sigma^\mathrm{s}_z/c)^2}\mathrm{d}\omega', \end{aligned} \tag{3.17}$$

where we assumed that the bunch length is also scaled by a factor of C_s, i.e. $\sigma^\mathrm{s}_z = C_\mathrm{s}\sigma^\mathrm{o}_z$. For this reason, the following relationship exists between the loss factor of the original and the scaled cavity:

$$k^\mathrm{s}_{||}(C_\mathrm{s}\sigma^\mathrm{o}_z) = \frac{1}{C_\mathrm{s}}k^\mathrm{o}_{||}(\sigma^\mathrm{o}_z). \tag{3.18}$$

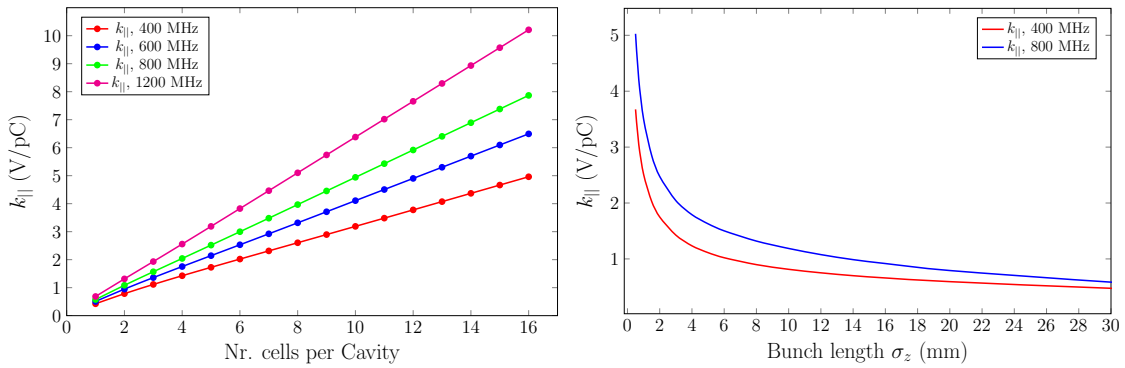

(a) Number of cells per cavity vs $k_{||}$

(b) Bunch length vs $k_{||}$

Figure 3.2: Dependency of the longitudinal loss factor on the (a) number of cells (with a bunch length of 3 mm), and (b) bunch length (for a four-cell cavity with an aperture radius of 120 mm at 400 MHz). The longitudinal loss factor in a cavity is inversely proportional to the square root of the bunch length, i.e. $k_{||} \propto \sigma_z^{-0.5}$ [33, p.250].

In other words, if all the geometrical parameters of the cavity and the bunch length scale by a factor of C_s, the longitudinal loss factor scales by a factor of $1/C_s$. Since the dimensions of the cavity are scaled by C_s, the loss factor per unit length scales by $1/C_s^2$.

3.2 High energy vs. high current set-ups

The FCC-ee should operate at different energy levels. The beam current for each case is scaled inversely to the fourth power of energy to be within the 50 MW SR limit according to (1.4). The two limiting cases are the Z-pole, characterized by low voltage and a current exceeding 1 A, and $t\bar{t}_2$ which requires a high voltage of 10.93 GV [64]. The beam requirements for each case would optimally necessitate different cavity designs. The high current of the Z option can lead to a high HOM power and various beam instabilities. Its design, therefore, favors a cavity with a lower number of cells, a lower frequency and a large aperture (which translates into lower R/Q). The RF design of $t\bar{t}$, on the other hand, favors a higher frequency and a higher number of cells per cavity in order to achieve a higher acceleration per unit length. The $t\bar{t}$ option requires the longest accelerating structure. The H and W operating modes fall between these two extremes in terms of voltage and current. The H option has the second highest energy to be achieved. Its RF cavity requirements are similar to $t\bar{t}$ as it has to achieve a high voltage of 2 GV with a relatively low beam current. The W option falls between Z and H in terms of total voltage and beam current. The determination of the RF frequency and the number of cells per cavity for each FCC-ee working point is the first step in designing the

RF cavities.

3.2.1 Choice of frequency

There are different arguments for the choice of high or low frequency for the RF system. The frequency of SRF cavities is usually chosen between 200 MHz to 3 GHz. Below 200 MHz, the size of the cavities becomes prohibitive in particular for multi-cell cavities. Above 3 GHz, the R_{BCS} dominates the surface resistance ($R_{\mathrm{BCS}} \gg R_0$) and increases with f^2 (at $T = 2\,\mathrm{K}$ [65]), therefore the power dissipation per unit length in the cavity increases linearly with frequency f (see Table 3.1). In linear colliders, frequencies above 1 GHz are preferred, as the length of the RF section highly influences the length of the total accelerating facility. Therefore, a shorter RF structure significantly reduces the total cost of the project [66, 67]. Additionally. the impedance thresholds for beam stability are more relaxed in linear accelerators in contrast to the storage rings, as each bunch crosses through the cavities once. For this reason, multi-cell cavities at frequencies above 1 GHz are a favorable choice for large linear accelerators, e.g. the nine-cell cavities at 1.3 GHz designed for ILC and XFEL [65, 68].

Table 3.1: Scaling of some RF parameters per unit length with respect to frequency for a typical superconducting cavity [31, p. 193].

Parameters	Scaling per unit length
Quality factor (Q_0)	f^{-2}
Cavity dimensions	f^{-1}
Geometry factor (G)	f^0
Power dissipation on the surface (P_{ds})	f^1
$R/Q_{\parallel}$	f^1
R_s	f^2
Longitudinal loss factor[a]	f^2
Transversal kick factor[a]	f^3

[a] Assuming that the bunch length is scaled by the same factor as the geometrical parameters

In circular accelerators, on the other hand, cavities with large apertures are preferred to facilitate the suppression of HOMs and wakefield effects. The HOM power is smaller at lower frequencies, as the longitudinal and transverse wake loss scale with the second and third power of frequency, respectively [65]. As indicated in Table 3.1, the effect from wakefields and the heat on the surface favor low frequencies, and the accelerating efficiency favors a high frequency regime.

High cw RF power sources are mostly available at frequencies below 1 GHz [69]. In circular lepton colliders, high cw power is required to compensate for the SR loss across the ring. In FCC-ee, a power of 50 MW per beam has to be compensated by the RF sources. For this reason, we limit our choice to the frequencies below 1 GHz and perform a comparison between two designs, one at 400.79 MHz and the other at 801.58 MHz (for simplicity, we refer to these designs as 400 MHz and 800 MHz RF systems when comparing them in the rest of this thesis). The frequencies are chosen as a multiple of the RF frequency of LHC (which can serve as a potential injector for FCC-hh [70]). The actual circumference of the ring will, in the end, have a slight influence on the exact RF frequency, as it has to be a multiple of the revolution frequency. In addition to power sources, the design of the high power fundamental power coupler is easier at low frequencies. Considering the existing fundamental power couplers, there is a trend line for the achievable cw power given by [71]

$$P_{\mathrm{cw}} \approx \frac{2 \times 10^5}{f} \tag{3.19}$$

where P_{cw} is the cw power in kW and f is the frequency in MHz. At 400 MHz and 800 MHz, this results in a 500 kW and 250 kW power limit, respectively.

Another crucial parameter for the design of the RF system is the heat loss in the cryomodules. Figure 3.3 shows a comparison between the dynamic and static losses of a four-cell cavity at 400 MHz and a four-cell cavity at 800 MHz. The materials considered for the 400 MHz and 800 MHz cavities are Nb/Cu at 4.5 K and bulk Niobium at 2 K, respectively. The respective surface resistance of each material is shown in Figure 3.1(a), and some characteristic parameters of the used cavities are listed in Table 3.2.

Plotting the power loss with respect to the accelerating electric field allows us to locate an optimum E_{acc}. Furthermore, it shows the extra power required for operation at a higher or lower accelerating field. At very low accelerating fields, the static power loss is the dominant loss, as the number of cavities required to reach the total voltage is higher (static power loss depends on the length of the RF structure regardless of the accelerating field E_{acc}). According to (3.5), the dynamic power loss is directly proportional to E_{acc} and inversely proportional to Q_0, which degrades at high accelerating fields, as shown in Figure 3.1 (b). Therefore, in contrast to the static loss, the dynamic power loss is the dominant loss at high E_{acc}. The power loss at the cryogenic temperature is below 10 kW for the Z-pole even at high E_{acc} for both 400 MHz and 800 MHz systems (see Figure 3.3 (a)). On the other hand, the use of 400 MHz cavities for $\mathrm{t\bar{t}_2}$ leads to a significantly high power loss at high values of E_{acc} (see Figure 3.3 (d)).

In Figure 3.4, the efficiency of the refrigerating system is considered to calculate the wall plug power ($1/\eta$ of 219 and 745 is assumed for the 400 MHz and 800 MHz cryogenic systems, respectively). The total number of cavities and the input power per cavity are also shown in the same plots. Here we assume that the same RF

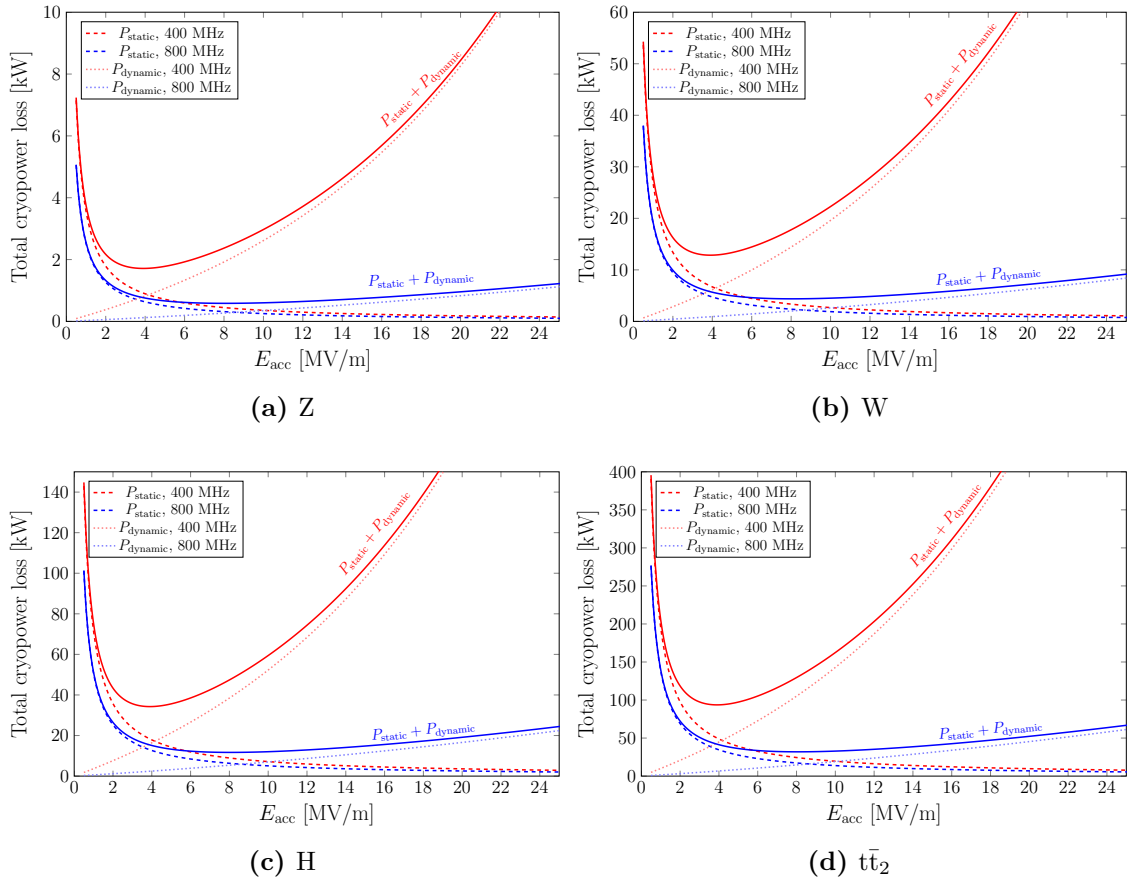

(a) Z **(b)** W

(c) H **(d)** $t\bar{t}_2$

Figure 3.3: Dynamic and static power loss of the cavities at different operating modes of FCC-ee. A four-cell cavity at 400 MHz and a four-cell cavity at 800 MHz is assumed for each case. In the calculation of the static power loss, an extra length of twice the wavelength of FM ($2\lambda_0$) is considered for each cavity, i.e. $L_{cavity} = L_{active} + 2\lambda_0$.

system is used for both beams in the $t\bar{t}$ operation. This requires a change of machine layout for the $t\bar{t}$ working point (which will be further explained in Section 3.3.2).

For the Z-pole working point, one of the limiting factors is the input power per cavity. As shown in Figure 3.4 (a), the required P^*_{in} increases drastically at high E_{acc}. The number of cavities has an inverse relation to E_{acc}. At an equal accelerating field, the number of cavities required at 400 MHz is half of that at 800 MHz, but with double input power per cavity. We set an upper limit of 1 MW at 400 MHz for the power couplers (this requires R&D for the input couplers to either increase the power limit of the couplers or to have two input couplers per cavity [71]). With an upper limit of 1 MW at 400 MHz on the input power (and 500 kW at 800 MHz), the 400 MHz is a more efficient option, as the required number of cavities at 400 MHz is half of that at 800 MHz. This also fixes the E_{acc} of each cavity at low values (a few

Table 3.2: Relevant RF cavity parameters used in the calculations of this chapter.

		1-Cell	2-Cell	3-Cell	4-Cell	5-Cell	6-Cell
f_0 [MHz]				400.79			
l_{active} [m]		0.374	0.748	1.122	1.496	1.870	2.244
$R/Q_{\parallel,0}$ [Ω]		82.9	192.9	301.9	411	520.3	629.5
G [Ω]		261.5	274.3	273.6	273.2	272.9	272.8
$k_{\parallel}$ [V/pC] [a]	Z/W	0.13/0.20	0.35/0.56	0.53/0.83	0.72/1.08	0.90/1.31	1.09/1.55
	H/$t\bar{t}_2$	0.21/0.33	0.61/1.05	0.90/1.52	1.17/1.91	1.42/2.27	1.66/2.60
$k_{\parallel}$ [V/pC] [b]	Z/W	0.27/0.30	0.82/0.92	1.20/1.35	1.53/1.70	1.83/2.03	2.12/2.34
	H/$t\bar{t}_2$	0.29/0.37	0.89/1.29	1.30/1.85	1.65/2.30	1.96/2.70	2.27/3.07
f_0 [MHz]				801.58			
l_{active} [m]		0.187	0.374	0.561	0.748	0.935	1.122
$R/Q_{\parallel,0}$ [Ω]		82.9	192.9	301.9	411	520.3	629.5
G [Ω]		261.5	274.3	273.6	273.2	272.9	272.8
$k_{\parallel}$ [V/pC] [a]	Z/W	0.18/0.27	0.46/0.70	0.72/1.07	0.99/1.44	1.26/1.81	1.53/2.19
	H/$t\bar{t}_2$	0.29/0.43	0.76/1.25	1.16/1.85	1.54/2.39	1.93/2.90	2.32/3.40
$k_{\parallel}$ [V/pC] [b]	Z/W	0.36/0.40	1.00/1.12	1.50/1.66	1.96/2.16	2.41/2.63	2.86/3.10
	H/$t\bar{t}_2$	0.39/0.50	1.08/1.50	1.61/2.20	2.09/2.82	2.56/3.38	3.02/3.93

[a] $k_{\parallel}$ is calculated for the BS bunch lengths of Table 1.1

[b] $k_{\parallel}$ is calculated for the SR bunch lengths of Table 1.1

MV/m depending on the number of cells per cavity). The high HOM power of Z provides another reason to stay at a lower frequency (400 MHz), which is discussed in the next subsection. This frequency is also considered for the FCC-hh and thus offers a good perspective for the reuse of part of the infrastructure for the Hadron machine.

A similar argument is valid for the W option. By limiting the maximum input power to 1 MW at 400 MHz (and to 500 kW at 800 MHz), the required E_{acc} is around 10 MV/m for the four-cell cavity. With a fixed value of E_{acc}, the required number of cavities at 400 MHz is half that of the cavities required at 800 MHz. At E_{acc} of 10 MV/m, the value of P_{wp} at 400 MHz is around 1.5 MW higher than that at 800 MHz. Roughly speaking, the cost of 2.2 MW of power is around 400 k€/year [72]. In comparison to other costs, the cost of an extra 1.5 MW of power is not significant, considering that the W machine is planned to be operated for a short time only (one or two years). Staying at 400 MHz enables us to use a large part of the hardware and RF infrastructure used at the previous stage (the Z-pole working point).

In comparison to the Z and W options, the input power constraint is relaxed for H. If we use the same number of cavities at 400 MHz and 800 MHz, and operate

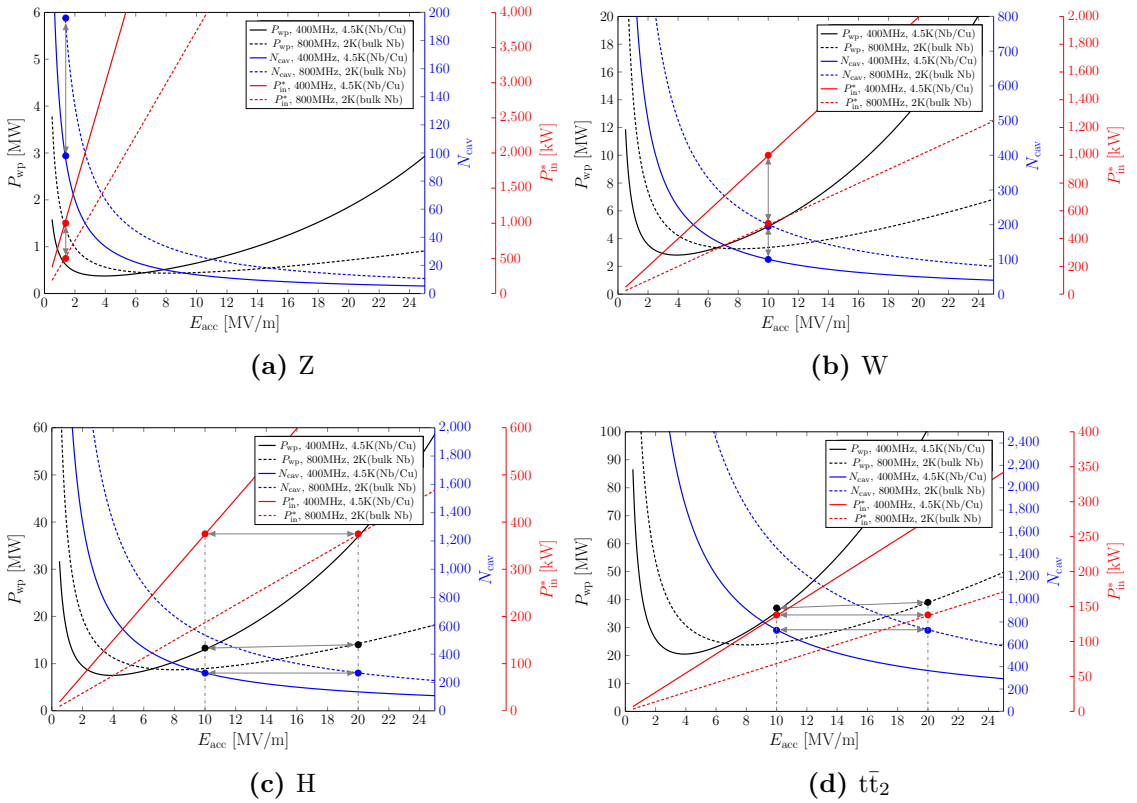

(a) Z **(b)** W

(c) H **(d)** $t\bar{t}_2$

Figure 3.4: The wall plug power, the total number of cavities, and the required input power per cavity for different operating modes of FCC-ee. Four-cell cavities at 400 MHz and 800 MHz is assumed for each case. One RF system is considered to be used for both beams in the $t\bar{t}$ working point. The number of cells for each case is determined in Subsection 3.2.2.

the 800 MHz cavities at a double accelerating field, the P_{wp} would be of the same order at both frequencies (see Figure 3.4 (c)). However, providing the high input power of around 400 kW is more challenging at 800 MHz. Furthermore, the cost of a cryomodule with 400 MHz NB/Cu cavities is around 20 % lower than that of a cryomodule with bulk Nb cavities at 800 MHz [73]. The HOM power and impedance constraints favor a lower frequency for the H option. Therefore, we use the same cavities as used for W, and add more 400 MHz cavities to provide the necessary voltage for the H option.

Several hundreds of cavities are required for the $t\bar{t}$ operation. This leads to a very large RF section in the ring. As shown in Figure 3.4 (d), the number of cavities, the input power and the P_{wp} for the 400 MHz cavities operated at $E_{acc} = 10$ MV/m is roughly equal to those at 800 MHz using $E_{acc} = 20$ MV/m. The input power is around 150 kW for the considered four-cell cavities, which is within the range

of available technology for both frequencies. The relatively low beam current of $t\bar{t}$ relaxes the constraints on the HOM power and impedance budget, and thus provides more freedom for the choice of a higher frequency or a higher number of cells per cavity (which will be discussed in the following sections). Note that having a high number of cells per cavity at 400 MHz leads to an unwieldy cavity size. The use of the 800 MHz RF system for the $t\bar{t}$ results in a more compact RF power system and a shorter straight section along the ring. The increase in the cost of the cryomodule at 800 MHz (compared to 400 MHz) can be compensated by increasing the number of cells per cavity, e.g. by using five-cell cavities instead of four-cell cavities. Thus, the total RF voltage of $t\bar{t}$ option could be achieved by reusing the cavities of the H option (to provide 2 GV per beam) and then adding 800 MHz cavities for the remaining voltage.

3.2.2 Choice of number of cells

A high number of cells per cavity decreases the total number of cavities and thus reduces the total cost by demanding a lower number of auxiliary equipment such as input or HOM couplers. However, there are various parameters that limit the use of a high number of cells per cavity. The sensitivity of the field profile of the FM in each cell ΔA_{cell} to the geometrical perturbations increases with $N_{\text{cell}}^{3/2}$ as follows [35, p. 22]

$$\Delta A_{\text{cell}} \propto N_{\text{cell}}^{3/2}/k_{\text{cc}} \tag{3.20}$$

where k_{cc} is the cell-to-cell coupling and N_{cell} is the number of cells per cavity. Large values of N_{cell} make the field-flatness less stable with respect to the geometrical perturbations.

In addition to the FM, the HOM damping requirements also restrict the use of a high number of cells. The HOM damping in SRF cavities is typically carried out by installing dampers on the exterior of the structure. A high number of cells increases the risk of trapping HOMs in the cavity (as the field decays before reaching to the dampers). This is more critical in superconducting cavities, as an HOM with small R/Q can have a large Q_{ext} and consequently, a high beam impedance. If we neglect the intrinsic losses, the Q_{ext} of a given mode scales linearly with the number of cells, assuming that the external loss depends only on the energy propagating out of the beam tubes, and that the field amplitude of the mode is equal in all cells [74, p. 15]. Furthermore, the loss factor of the cavity increases with respect to the number of cells, as shown in Figure 3.2 (a). A higher loss factor means that more power is deposited into the cavity by the beam (see equation (3.13)); for this reason, the power handling capacity of the HOM couplers should be increased proportionally.

There are three main reasons for the selection of a single-cell cavity for the Z option: the input power limit, the HOM power and the impedance considerations. The HOM power of different operating modes of the FCC-ee for both the BS and

SR bunch length is plotted in Figure 3.5. The HOM power of a single-cell cavity at 400 MHz in the Z option is around 3 kW for the BS bunch length (when bunches are in collision). The high HOM power of the Z option limits the use of more cells per cavity. A single-cell cavity also helps to lower the longitudinal and transversal impedance of the cavity (which is crucial for the Z option due to its Ampère level beam current, which will be discussed in Chapter 6). By using one cell per cavity for the Z energy, and assuming that each cavity will be operated with an electric field of 10 MV/m, 27 cavities are necessary to provide the total voltage of 100 MV. As a result, an input power of around 1870 kW is required for each cavity to compensate the total 50 MW SR loss (see Figure 3.6 (a)). However, as indicated earlier, we set an upper limit of 1 MW for the input power; therefore, the number of cavities should be increased to lower the input power fed into each cavity. This also indicates that using multi-cell cavities with the aim of decreasing the total number of cavities is not practical for the Z option, as we are restricted by the input power limit. For all of the above reasons, a 400 MHz cw RF system comprised of single-cell Nb/Cu cavities is considered for the Z option.

The HOM power and input power restrictions are more relaxed for the W and H options, and as a result, a higher number of cells per cavity could be used. The possible options are two to four cells per cavity. Due to their overall size, five-cell cavities (or more) are not considered at 400 MHz. Because of the high HOM power and input power per cavity, the W option favors fewer cells per cavity (see Figures 3.5 (b) and 3.6 (b)), while the H option favors more cells per cavity, as it is more cost-efficient in terms of the total number of cavities (see Figure 3.6 (c)). However, we try to use a similar RF system for different energy levels of FCC-ee to lower the infrastructure cost. In this thesis, a four-cell cavity at 400 MHz will be considered for both the W and H options, and the pros and cons will be studied. Four-cell cavities were also used in the LEP at CERN in the 1990s [75].

Assuming an accelerating field of 10 MV/m in the four-cell cavities, the total number of cavities required for the W energy is 100 (50 cavities per beam) with an input power of around 1 MW for each cavity (see Figure 3.6 (b)). The exact number of cavities will ultimately be fine-tuned based on the number of cavities used in each cryomodule. For the W beam current, the HOM power of the four-cell cavity is around 3 kW (for the BS bunch length). Furthermore, the impedance of the four-cell cavity is close to the stability threshold set by the SR, and increasing the number of cells would deteriorate it (as will be discussed in Chapter 6). The same four-cell cavity design will also be used for the H option. The lower beam current and smaller input power do not restrict the use of the four-cell cavities for the H working point.

As discussed in the previous subsection, having FM at 800 MHz could provide an efficient and compact RF system for the $t\bar{t}$ option. Due to the lower beam current of $t\bar{t}$, increasing the number of cells does not create a crucial problem in HOM damping. As shown in Figure 3.5 (d) and 3.6 (d), both the five-cell and six-cell cavities have

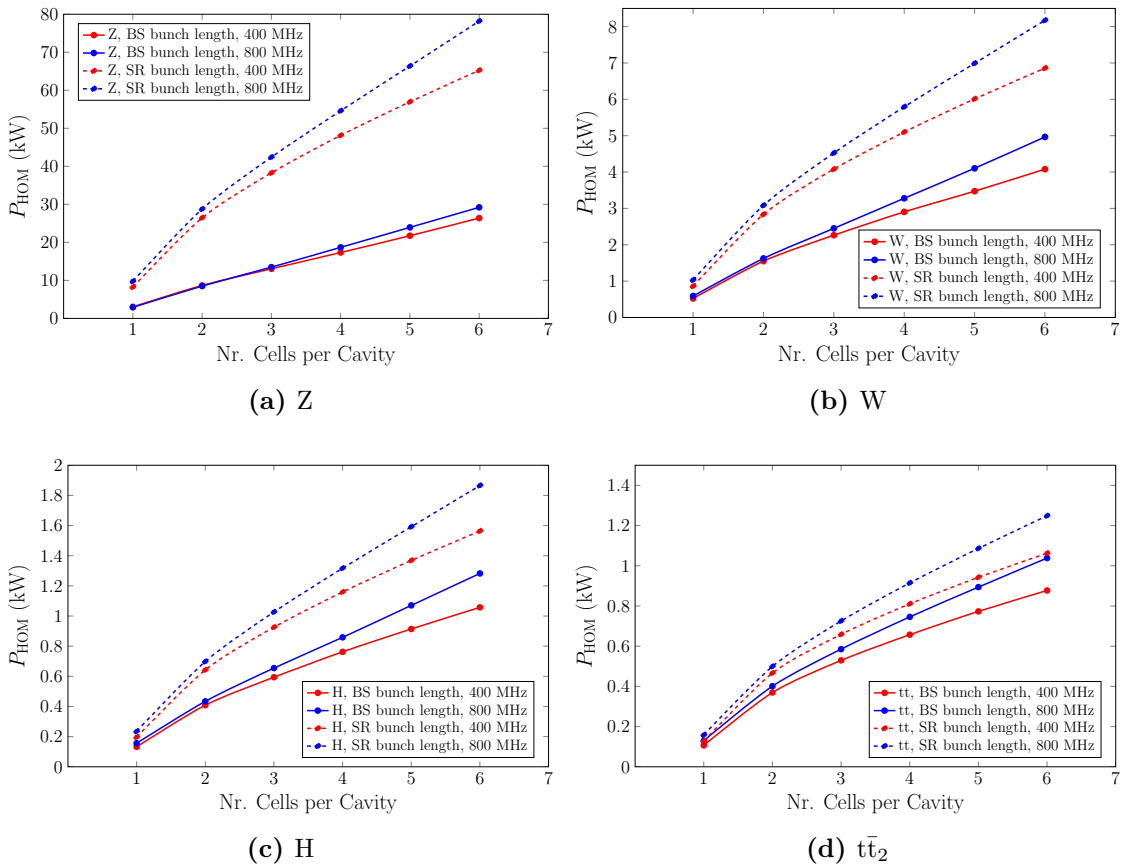

(a) Z **(b)** W

(c) H **(d)** $\mathrm{t\bar{t}_2}$

Figure 3.5: HOM power loss vs. the number of cells per cavity for different operating modes of FCC-ee. An aperture radius of 150 mm is chosen for the single-cell cavity and an iris radius of 120 mm is chosen for the 400 MHz multi-cell cavities (at 800 MHz the dimensions of the cavities are scaled by half).

an HOM power and input power that is within a permitted range, i.e. the HOM power is around 1 kW and the input power is between 150 kW to 200 kW (the plots are for cavities operated at 400 MHz and $E_{\mathrm{acc}} = 10\,\mathrm{MV/m}$ which roughly has the same value of P_{wp}, N_{cav} and P_{in} as an 800 MHz cavity operated at $E_{\mathrm{acc}} = 20\,\mathrm{MV/m}$, as was shown in Figure 3.4). A six-cell cavity can save around 17 % of the total number of cavities compared to a five-cell design (the total number of cells stays constant). However, a six-cell cavity has a higher impedance and its field profile is more sensitive to the geometrical perturbations according to (3.20). Here we make a more conservative choice and select a five-cell cavity at 800 MHz for the $\mathrm{t\bar{t}}$ operation. In several other projects such as LHeC and PERLE, five-cell 800 MHz cavities are envisaged [76, 77, 78, 79], and thus a five-cell cavity for $\mathrm{t\bar{t}}$ provides a good synergy with other existing projects.

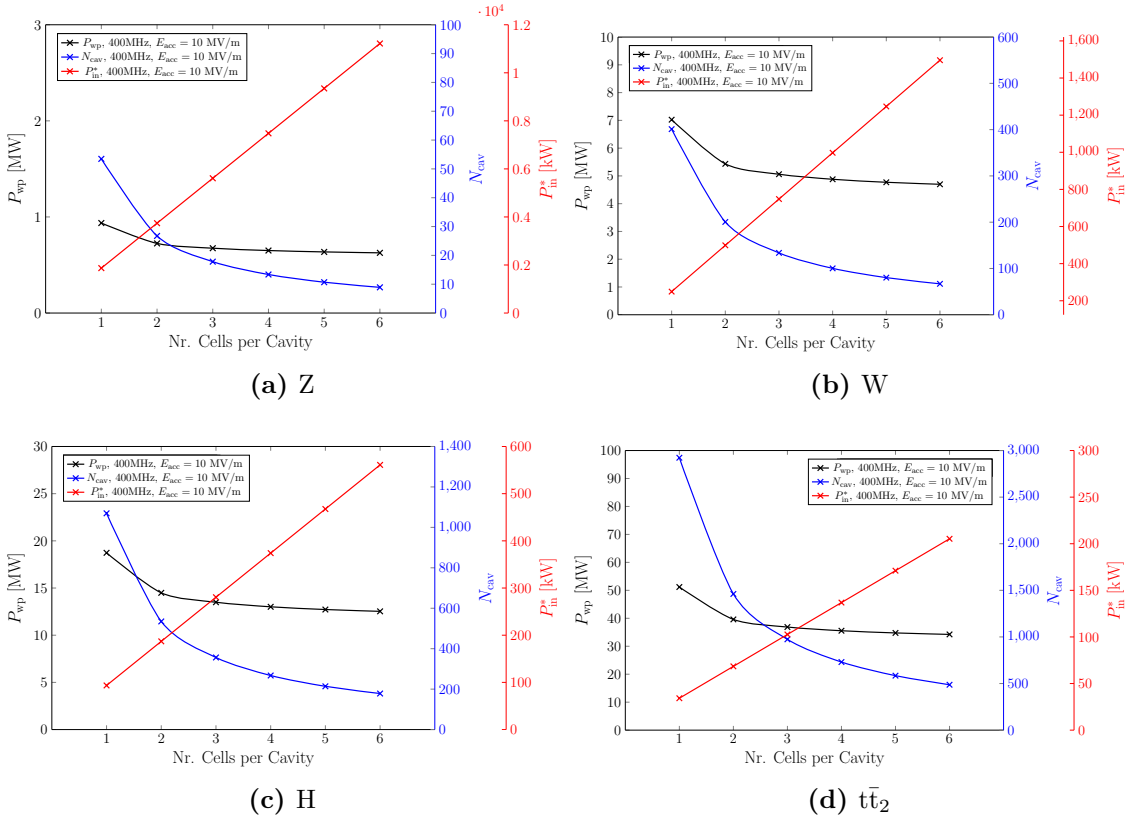

Figure 3.6: Wall plug power, number of cavities, and input power for different operating modes of FCC-ee. An aperture radius of 150 mm is chosen for the single-cell cavity and an iris radius of 120 mm is considered for the 400 MHz multi-cell cavities.

3.3 RF layout

3.3.1 Fundamental power coupler

Assuming optimal detuning, the input power of one cavity is plotted in Figure 3.7 as a function of $Q_{\mathrm{L},0}$ for different FCC-ee working points (by using (3.7)). The minimum point of each curve indicates the optimum loaded quality factor $Q^*_{\mathrm{L},0}$. Any deviation from $Q^*_{\mathrm{L},0}$ leads to an increase in the input power required to maintain the accelerating field in the cavity. In addition to this, Lorentz force detuning or microphonics effects can detune the cavity, which makes the second bracket of (3.7) nonzero. This leads to an additional power taken from the generator system. For example for the W working point, if we assume $R/Q_{\parallel,0} = 411.0\,\Omega$ and $V_{\mathrm{cav}} = 14.42\,\mathrm{MV/m}$, then $\Delta f^* = -0.748\,\mathrm{kHz}$, $Q^*_{\mathrm{L},0} = 5.265 \times 10^5$ and $f_{1/2} = 380.6\,\mathrm{Hz}$; subsequently equation (3.7) can be written as

$$P_{\mathrm{in}} = 240232 \times \left(4.0 + \left[\frac{\Delta f_{\mathrm{d}}}{380.6}\right]^2\right), \tag{3.21}$$

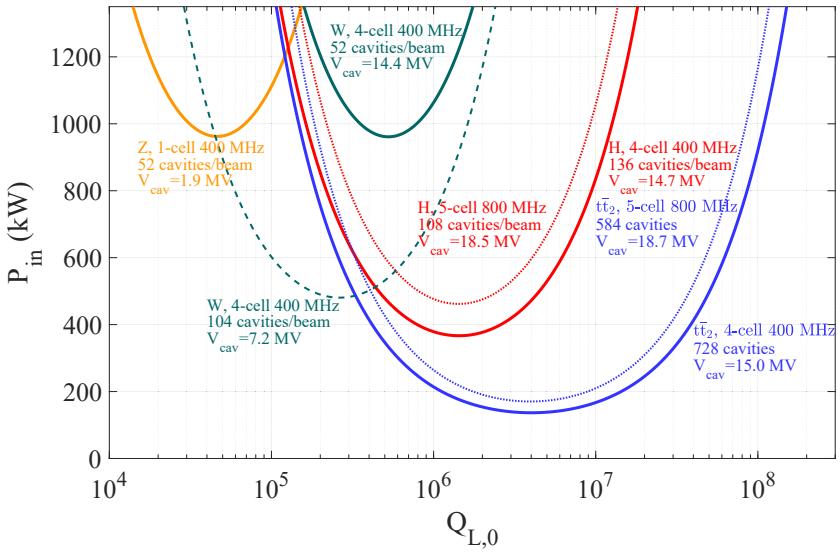

Figure 3.7: Input power as a function of $Q_{\mathrm{L},0}$ with optimal detuning for different energy options.

where Δf_{d} is the deviation from the optimum detuning created by, e.g., Lorentz force or microphonics effects. In such a case, a Δf_{d} of 100 Hz increases the input power by around 1.7%.

For the same cell-shape and E_{acc}, increasing the number of cells per cavity does not change the optimum loaded quality factor, as V_{cav} in the numerator and $R/Q_{\parallel,0}$ in the denominator of equation (3.11) change roughly by the same factor when the number of cells is changed. Under the same assumptions, the value of P^*_{in} increases linearly with the number of cells per cavity according to (3.12).

Due to the large beam current, the single-cell cavities of the Z option demand a low $Q^*_{\mathrm{L},0}$ of around 4.6×10^4 with a P^*_{in} of 962 kW (assuming 52 cavities are used per beam). With 52 four-cell cavities per beam, the W option requires the same amount of P^*_{in} at $Q^*_{\mathrm{L},0} \approx 5.3 \times 10^5$. The input power requirements could be reduced by using more cavities and operating them at a lower voltage, e.g. if 104 cavities are used per beam, both P^*_{in} and $Q^*_{\mathrm{L},0}$ are decreased by half. Since the cavities of the W option will also be reused for the H and $\mathrm{t\bar{t}}$ options, a variable input coupler [80, 81] with an adjustable $Q_{\mathrm{L},0}$ by around one order of magnitude is required. However, it is a challenging design as in the LHC, an adjustable $Q_{\mathrm{L},0}$ by a factor of three took several years to develop. The remaining four-cell cavities which will be added for the H working point can have either a fixed input coupler with a $Q_{\mathrm{L},0}$ located between the optimum loaded quality factor of the H and $\mathrm{t\bar{t}}$ working points, or a variable input coupler with an adjustable $Q_{\mathrm{L},0}$ by a factor of around 2.5. A fixed input coupler with $Q^*_{\mathrm{L},0} \approx 4 \times 10^6$ could be used for the five-cell cavities at 800 MHz in the $\mathrm{t\bar{t}}$ working point.

3.3.2 Multi-harmonic system for $t\bar{t}$

The $t\bar{t}$ working point demands the largest RF structure in FCC-ee. Due to the low beam loading and small number of bunches of $t\bar{t}$ (which partially fill the arc), the same RF structure could be used for both beams. Therefore, we use the same cavities as in H, re-align the cavities of both beams, and then add new 800 MHz cavities to reach the voltage needed for the $t\bar{t}$ operation (see Figure 3.9 (a)). This requires the use of a double frequency system for the $t\bar{t}$, i.e. up to 4 GV is produced at 400 MHz and the rest at 800 MHz. Since both beams pass through the same cavities, we double the value of the beam current for the $t\bar{t}$ calculations.

The Touschek lifetime[1] can be increased in storage rings by either increasing the energy acceptance or increasing the bunch length [82, p. 453]. Usually, a higher harmonic system is added to manipulate the bunch length (shorten or lengthen it) by varying the amplitude and phase of the harmonic cavities [83]. In order to get zero slope of the total voltage at the center of the bunch, the voltage of the harmonic system should be a fraction of the main RF system. In the case of $t\bar{t}$, however, this cannot be used as the voltage is dominated by the 800 MHz RF system (most of the voltage is provided at 800 MHz). For this reason, varying the phase angle does not provide a zero slope, as shown in Figure 3.8. However, a nonzero phase difference ($\phi_0 \neq 0$) reduces the over-voltage (the peak of the RF voltage compared to the SR loss). The synchronous phase at each frequency should be determined in a way that the SR loss is compensated, and maximum over-voltage is obtained. The over-voltage helps to increase the energy acceptance and thus increases the Touschek lifetime and in general the lifetime of the beam [19, p. 93].

The total voltage is a summation of the voltages at 400 MHz and 800 MHz

$$\begin{aligned} V_{\text{tot}} &= V_{400}\cos(\underbrace{\omega_{400}t}_{\phi_{400}}) + V_{800}\cos(\underbrace{2\omega_{400}t+\phi_0}_{\phi_{800}}) \\ &= 4\cos(\phi_{400}) + 6.93\cos(2\phi_{400}+\phi_0). \end{aligned} \tag{3.22}$$

The value of V_{tot} for different values of ϕ_0 is plotted in Figure 3.8. In order to get the highest over-voltage, the phase difference has to be zero ($\phi_0 = 0$), i.e.

$$\phi_{800} = 2\phi_{400}. \tag{3.23}$$

The synchronous phase is determined such that the total voltage equals the synchrotron loss

$$V_{400}\cos(\phi_{400}) + V_{800}\cos(\phi_{800}) = V_{\text{loss}}. \tag{3.24}$$

Combining equation (3.23) with (3.24) and solving the resulting equation yields the synchronous phase at 400 MHz and 800 MHz.

[1] Touschek lifetime is the time required for the beam to decay to half of its initial intensity value, where the loss occurs from the scattering between two particles in the bunch.

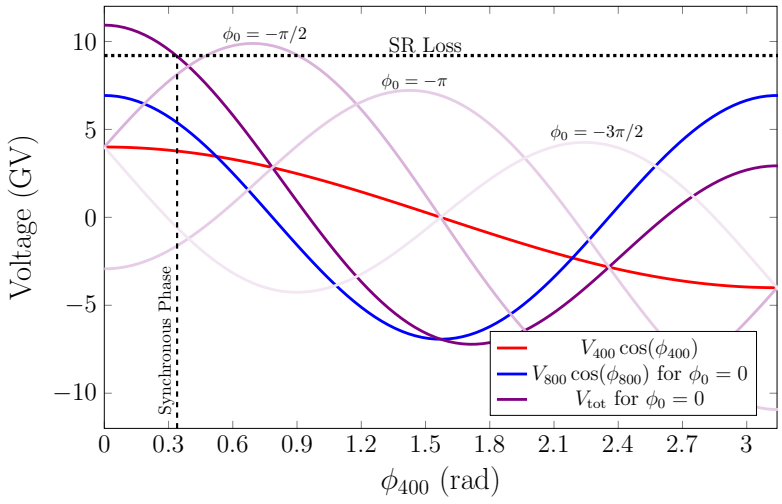

Figure 3.8: The total voltage of the $t\bar{t}$ is a summation of 4 GV at 400 MHz and 6.93 GV at 800 MHz. Zero phase difference ($\phi_0 = 0$) between the two frequencies provides the highest over-voltage (which corresponds to $V_{\text{RF}} = 10.93$ GV).

3.3.3 FCC-ee installation plan

As discussed in the previous sections, a single-cell cavity at 400 MHz is considered for the Z working point, a four-cell cavity at 400 MHz is chosen for the W and H working points, and a double frequency system including four-cell cavities at 400 MHz and five-cell cavities at 800 MHz is considered for the $t\bar{t}$. The detailed RF parameters of this scenario are given in Table 3.3.

Table 3.3: RF parameters of the considered scenario for FCC-ee.

	Z	W	H	$t\bar{t}_1$		$t\bar{t}_2$	
Total beam voltage [GV]	0.1	0.75	2.0	9.4		10.93	
Beam Voltage [GV]	0.1	0.75	2.0	4.0	5.4	4.0	6.93
f_0 [MHz]	400.79	400.79	400.79	400 .79	801.58	400.79	801.58
No. of cells / cavity	1	4	4	4	5	4	5
No. of cavities[a]	52 × 2	52 × 2	136 × 2	272	296	272	372
No. of cryomodules[a]	13 × 2	13 × 2	34 × 2	68	74	68	93
E_{acc} [MV/m]	5.1	9.6	9.8	9.8	19.5	9.8	19.9
P^*_{in} [kW]	962	962	367	176	175	150	158
$Q^*_{\text{L},0}$ [10^6]	0.046	0.53	1.44	2.99	3.65	3.51	4.23
Δf^* [kHz]	-11.2	-0.75	-0.08	-0.025	-0.097	-0.02	-0.075
P_{HOM} (SR/BS) [kW]	8.25/3.04	5.09/2.89	1.16/0.76	0.70/0.53	0.95/0.74	0.81/0.66	1.09/0.89
T Operation [K]	4.5	4.5	4.5	4.5	2.0	4.5	2.0
Material	Nb/Cu	Nb/Cu	Nb/Cu	Nb/Cu	Nb	Nb/Cu	Nb
P_{static} [kW]	0.87×2	1.39×2	3.64×2	7.28	3.15	7.28	3.96
P_{dynamic} [kW]	0.74×2	9.31×2	25.51×2	51.03	21.44	51.03	28.29
P_{wp} [MW]	0.35×2	2.34×2	6.38×2	12.76	18.32	12.76	24.02

[a] The ×2 indicates that a factor 2 has to be considered to account for the total number of cavities and the total power loss of two beams. Note that one RF structure will be used for both beams in the $t\bar{t}$ operation.

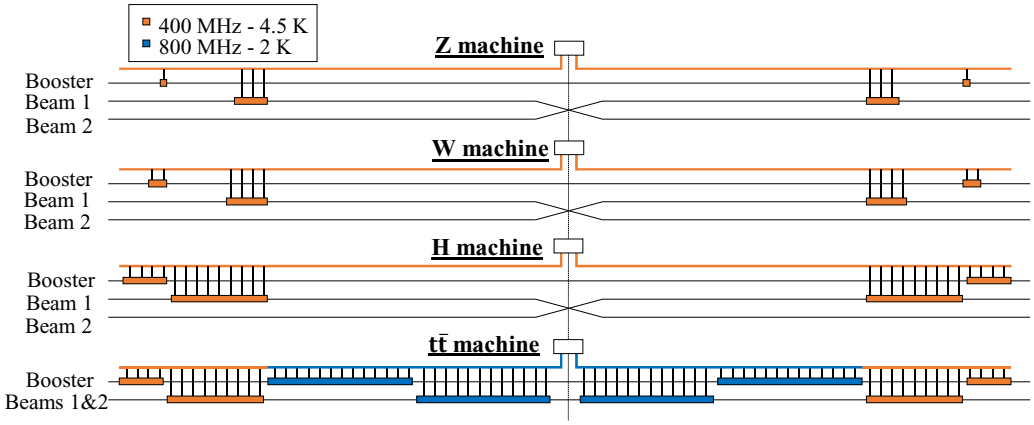

(a) Machine development after each operation. The picture shows only the RF section of the 100 km ring. Both beams are re-aligned for the $t\bar{t}$ machine (picture is adapted from [10, p. 466]).

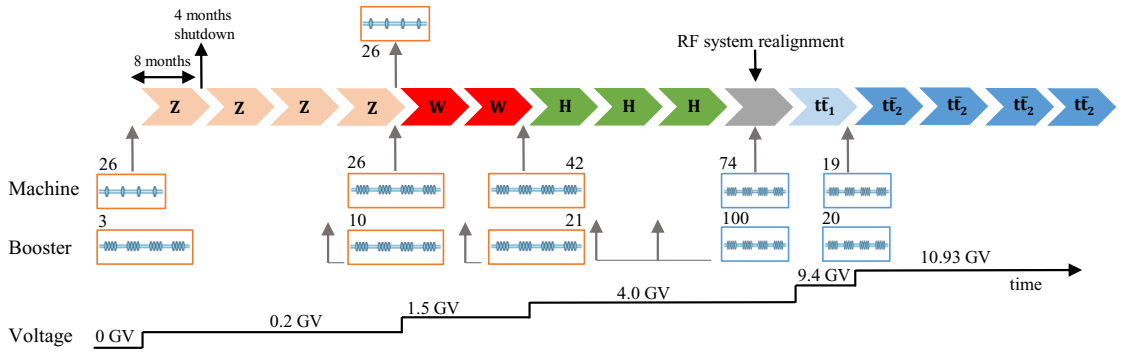

(b) Development of the machine voltage from 0 GV to 10.93 GV (picture is adapted from [10, p. 416]).

Figure 3.9: Staging and development plan of the RF system of FCC-ee as of December 2018. Arrows in (b) indicate an eight-month operation followed by a four-month gap for the hardware upgrade.

In order to investigate the physics of interest and obtain the required data at each energy step, it is planned to operate the machine four years at the Z energy, one or two years at the W energy, three years at the H energy and five years at the $t\bar{t}$ energy (one year at $t\bar{t}_1$ and four years at $t\bar{t}_2$) [10]. This requires an upgrade of the hardware of the machine after each phase of operation. As depicted in Figure 3.9 (b), 26 modules containing single-cell 400 MHz cavities are installed for the Z working point. After four years, the modules are replaced with 26 modules containing four-cell 400 MHz cavities for the operation at the W energy. After that, 42 modules will be installed to provide the voltage for the operation at the H energy. Both beams are then aligned, and five-cell 800 MHz cavities are added to the cavities used for the H energy to provide a total of 10.93 GV for the $t\bar{t}$ working point.

The luminosity of the beam degrades due to a rather short beam lifetime (around one hour or less). In order to keep the luminosity within the permitted range, a booster ring located next to the collider ring, is essential to provide continuous top-up injection into the collider ring. The injection system of the FCC-ee is envisaged to comprise a 6 GeV linac of a length of 239 m, a damping ring with a circumference of 242 m, a pre-booster to increase the energy from 6 GeV to 20 GeV, which could be the existing Super Proton Synchrotron (SPS), and a top-up booster to ramp up the beam energy from 20 GeV to the full beam energy (from 45.6 GeV to 182.5 GeV) [84]. Due to a rather low beam current in the injection system, multi-cell cavities could be used for all energy options. Therefore, the same type of multi-cell cavities as used for the collider ring is considered for the booster, i.e. four-cell cavities at 400 MHz and five-cell cavities at 800 MHz. More details of the booster's RF system are given in [85].

4 Geometrical cavity design

As discussed in the previous chapter, single-cell Nb/Cu cavities at 400 MHz are considered for the Z running, four-cell Nb/Cu cavities at 400 MHz are considered for the W, H and $t\bar{t}$ working points, and five-cell Nb cavities at 800 MHz are selected for the $t\bar{t}$ running. In this chapter, a four-cell cavity is designed for the operation in the W, H, and $t\bar{t}$ running at 400 MHz. The middle cell and the end cell of the cavity are designed separately. Both the middle cell and end cell designs are also scaled to 800 MHz and are used to make a five-cell cavity for the $t\bar{t}$ option. In the end, a single-cell cavity at 400 MHz is designed for the Z option. Since the beam current of the Z running is in the range of 1 A, special attention is given to the HOM characteristics of the single-cell cavity.

4.1 Middle cell optimization

Elliptical cavities are composed of two elliptical arcs connected by a straight line. A typical elliptical cavity parametrization is shown in Figure 4.1. Seven parameters uniquely determine the shape of elliptical cavities, i.e. A, B, a, b, L, R_{eq} and R_{i}. The optimization of the cavity consists of the proper choice of these parameters in order to serve a certain goal. Not all parameters are freely variable in the process of the optimization. In the design of the middle cells of high β cavities (particle velocities close to the speed of light), the half-cell length of the middle cell (L) is

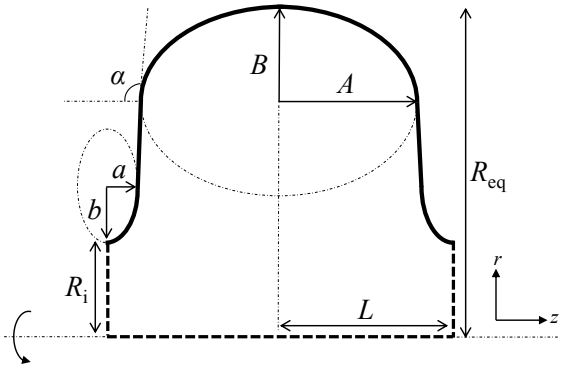

Figure 4.1: Middle cell parametrization of an elliptical cavity. The geometry is axisymmetric around the centerline, and here only the upper part of the cross-section is shown.

taken as a quarter of the wavelength of the FM

$$L = \beta\lambda_0/4, \tag{4.1}$$

where λ_0 is the wavelength at the FM frequency, and β is the ratio of particle velocity to the speed of light. The length of the middle cells is determined such that as the particle moves from one cell to the next, the direction of the oscillating electric field changes, and the particle always receives an accelerating force in the same direction. For particle velocities close to the speed of light, the value of β roughly equals one; therefore, the half-cell length of the middle cell of a 400.79 MHz cavity is set to 187 mm for maximum acceleration.

Between the seven parameters, the frequency of FM is more sensitive to the variations in the R_{eq} [86]. A small change in the R_{eq} changes the volume of the cavity in the equator part. The energy of the magnetic field of the TM_{010} mode is maximal around the equator, while the energy of the electric field is minimal (see Figure 2.1). According to Slater's theorem [87], the frequency of an eigenmode changes roughly proportional to the subtraction of the electric field energy from the magnetic field energy in the volume added or removed from the cavity [44]. For that reason, the equator radius R_{eq} is typically used for tuning the frequency to the desired value, e.g. 400.79 MHz.

Generally speaking, the shape of an accelerating cavity can be optimized for high accelerating field purposes, low surface losses, or low HOM impedance. Depending on the requirements of a given project, the objective functions are established. In order to operate the cavities at a high accelerating field (and decrease the total number of cavities in large-scale projects such as ILC), the surface electric and magnetic field should be reduced to provide room for increasing the accelerating field. A low surface loss decreases the cryogenic power required to maintain cryogenic temperature, which again should be taken into account for large accelerator complexes. In the design of cavities for high current machines, priority is given to strong HOM damping in the cavity in order to secure beam stability. The iris radius R_{i} (also referred to as aperture radius) is a geometrical parameter that has a major influence with regard to all three objectives [88]. A small iris radius provides room to lower the surface electric and magnetic field and decreases the surface losses at the cost of high HOM impedance. On the other hand, a large iris radius increases the cell-to-cell coupling and lowers the HOM impedance at the cost of higher surface fields and surface losses. Therefore, R_{i} is chosen on the basis of some considerations such as the permitted HOM damping and the target accelerating field.

In the parametrization of Figure 4.1, the wall slope angle α is a dependent variable, and its value is determined by other geometrical parameters. If α is smaller than 90°, the shape is called reentrant [89, 90]. A higher α is preferred for chemical treatment, cleaning procedures, and the mechanical stability of the cavity. A lower α, on the other hand, distributes the magnetic field over a larger surface area. This leads to a reduction in surface current density and lowers the surface losses.

In the design of the cavity for FCC-ee, the optimization of the cavities for minimal loss is crucial, as it comprises the major part of the total power required for maintaining the cryogenic temperature. This minimization is, in particular, important for the H and $t\bar{t}$ systems as they demand a large number of cavities, and a slight improvement in the cryolosses can save a considerable amount of energy on the large scale. Here we separate the design of the middle cell and the end cell. The middle cells define the major part of the losses in a multi-cell cavity. Therefore, they are mainly designed from the viewpoint of minimal losses. In addition to the losses, the connection of the cavity to the beam pipe and obtaining sufficient HOM damping should also be taken into account in the design of the end cells. These additional considerations might increase the losses in the end cell, but since the end cell is being designed separately from the middle cells, the relative increase in total losses would be small for the multi-cell cavity. In addition to this, the ease of computation is another reason for treating the middle cell and the end cell separately.

4.1.1 Method of optimization

For any cell shape, the ratio of the peak electric field on the surface to the acceleration field ($E_{\mathrm{pk}}/E_{\mathrm{acc}}$), and the ratio of the peak magnetic field on the surface to the acceleration field ($B_{\mathrm{pk}}/E_{\mathrm{acc}}$) can be used as indicators of a good cavity choice. A low $E_{\mathrm{pk}}/E_{\mathrm{acc}}$ is needed to overcome field emission at high fields. The field emission limits the accelerating field in SRF cavities. In the presence of a high surface electric field in SRF cavities, electrons are emitted from the cavity walls. The emitted electrons absorb energy from the electric field and lower the stored energy in the cavity, and thus deteriorate the Q_0 of the cavity [91, p. 162].

Minimization of $B_{\mathrm{pk}}/E_{\mathrm{acc}}$ helps to reduce surface losses and avoid quench or thermal break down. At the operating temperature of 2 to 4.2 K, the critical surface magnetic field for Niobium is around 200 mT [91, p. 45]. In the cavity optimizations, one approach is to consider $B_{\mathrm{pk}}/E_{\mathrm{acc}}$ as the main objective function while keeping $E_{\mathrm{pk}}/E_{\mathrm{acc}}$ below a certain value. The argument behind this approach is that the critical magnetic field is a hard limiting factor (e.g. it causes thermal breakdown and cavity quench), whereas E_{pk} is a soft limit, as the field emission can be reduced by maintaining better cleanliness [92]. In a different approach, a balance between $B_{\mathrm{pk}}/E_{\mathrm{acc}}$ and $E_{\mathrm{pk}}/E_{\mathrm{acc}}$ could be obtained. For example in [77], by analyzing more than 1000 half-cell structures, a Pareto front between $B_{\mathrm{pk}}/E_{\mathrm{acc}}$ and $E_{\mathrm{pk}}/E_{\mathrm{acc}}$ was obtained.

Low surface losses are another crucial criterion in cell shape design. The surface loss given in (3.1) can be rewritten in the form

$$P_{\mathrm{ds},0} = \frac{V_{\mathrm{cav}}^2 \cdot R_{\mathrm{s}}}{G \cdot R/Q_{\parallel,0}}, \tag{4.2}$$

where $G \cdot R/Q_{\parallel,0}$ depends only on the shape of the cavity. The cell shape optimization

can be carried out for minimal losses (by maximizing $G \cdot R/Q_{\parallel,0}$) or a minimum surface magnetic field (minimum $B_{\mathrm{pk}}/E_{\mathrm{acc}}$). As shown in [90, 93, 94], optimizing the middle cells for either low surface losses or a low surface magnetic field yields a similar geometry which can practically serve both goals.

Here we try to minimize $B_{\mathrm{pk}}/E_{\mathrm{acc}}$ with constraints on iris radius, $E_{\mathrm{pk}}/E_{\mathrm{acc}}$ and wall angle. The optimization of the cell shape can be formulated as

$$\begin{aligned} \underset{A,B,a,b}{\text{minimize}} \quad & B_{\mathrm{pk}}/E_{\mathrm{acc}} \\ \text{subject to} \quad & E_{\mathrm{pk}}/E_{\mathrm{acc}} \leq c_1, \\ & \alpha \geq c_2, \\ & R_{\mathrm{i}} = c_3, \\ & \underset{R_{\mathrm{eq}}}{\text{minimize}} \ \left| f_0 - 400.79 \text{ MHz} \right|. \end{aligned} \tag{4.3}$$

Any constraints on the wall slope angle, $E_{\mathrm{pk}}/E_{\mathrm{acc}}$, and iris radius can be applied, depending on the requirements of the project, and all the other geometrical parameters of the cavity can be determined via the optimization. Different cavities can be compared based on the constraints of this optimization i.e. with regard to the values of $E_{\mathrm{pk}}/E_{\mathrm{acc}}$, α and R_{i}.

The following part closely follows the optimization method proposed in [95] for the solution of the optimization problem of equation (4.3). In the optimization, SuperLANS [96, 97], a 2D axisymmetric finite element based code, was used for simulating the electromagnetic fields and calculating relevant secondary parameters. Since the middle cell is symmetric, only half of the cell is modeled (in order to save computational time), and the boundary conditions are applied in a way to obtain the π-mode field pattern in the cell for the first TM mode (see Figure 2.2 (b)), i.e. the PEC boundary condition is applied to the symmetry plane crossing the middle of the cavity and also to the surface of the cavity, and the PMC boundary condition is applied to the iris.

The length of the cavity and the iris radius are set fixed in the optimization. For each set of A, B, a and b in the optimization, the value of R_{eq} is changed to tune the FM frequency to 400.79 MHz. This requires an inner 1D optimization loop inside the main optimization problem. We implemented a wrapper code of SuperLANS (called TunedCell) that receives A, B, a, b, L, R_{i} and the desired frequency as the input, solves the 1D optimization problem and yields the optimum R_{eq} and the secondary parameters of the tuned cavity. Therefore, in the main optimization problem, only four variables are freely varied, i.e. A, B, a and b. It is also a common practice to normalize $B_{\mathrm{pk}}/E_{\mathrm{acc}}$, $E_{\mathrm{pk}}/E_{\mathrm{acc}}$ and α to a certain value so that all objectives have a similar order of magnitude [95].

Based on the prior knowledge of the problem [98] we know that by using a larger $E_{\mathrm{pk}}/E_{\mathrm{acc}}$ and a smaller wall slope angle, there is more freedom in decreasing

$B_{\mathrm{pk}}/E_{\mathrm{acc}}$, and the optimal point in equation (4.3) is located at the boundaries set by the constraints. Initially, we try to find a point on or close to the boundary constraints, i.e. a point that has $E_{\mathrm{pk}}/E_{\mathrm{acc}} \approx c_1$ and $\alpha \approx c_2$. The Monte Carlo method [99] is used to search randomly in the four-dimensional space and to find a point with small $B_{\mathrm{pk}}/E_{\mathrm{acc}}$ that is close to the constraint boundaries. For this purpose, the optimization problem shown in equation (4.3) is reformulated as follows

$$\begin{aligned} &\underset{A,B,a,b}{\text{minimize}} \quad B_{\mathrm{pk}}/E_{\mathrm{acc}}\Big(\eta_1 + \eta_2\big|\min(c_1 - E_{\mathrm{pk}}/E_{\mathrm{acc}}, 0)\big| + \eta_3\big|\min(\alpha - c_2, 0)\big|\Big), \\ &\text{subject to} \quad R_{\mathrm{i}} = c_3 \quad \text{and} \quad \underset{R_{\mathrm{eq}}}{\text{minimize}} \ \big|f_0 - 400.79\ \mathrm{MHz}\big|, \end{aligned} \tag{4.4}$$

where the function $\min(x, y)$ returns the lowest number of its arguments, and η_1, η_2 and η_3 are constants that are chosen arbitrarily, e.g. $\eta_1 = 0.01$, $\eta_2 = 2$ and $\eta_3 = 1$. The values of η_2 and η_3 are penalty coefficients and $\big|\min(c_1 - E_{\mathrm{pk}}/E_{\mathrm{acc}}, 0)\big|$ and $\big|\min(\alpha - c_2, 0)\big|$ are penalty functions that add a penalty-like term to the objective function as a measure of constraint violation. If the constraints of $E_{\mathrm{pk}}/E_{\mathrm{acc}}$ and α are not violated, the penalty functions are zero.

This routine was implemented in MATLAB [100]. For each sample of the Monte Carlo method, TUNEDCELL was called for the optimization of the FM frequency by changing R_{eq} and calculating relevant secondary parameters of the tuned cavity. The secondary values were read by MATLAB, post-processed, and the next sample point was created by the Monte Carlo method. The process was continued until the constraint boundaries were reached, and the value of $B_{\mathrm{pk}}/E_{\mathrm{acc}}$ could not be improved further.

In the next step, starting from the point obtained from the Monte Carlo method, a gradient-based method was used to minimize $B_{\mathrm{pk}}/E_{\mathrm{acc}}$ while remaining on the subspace over which the values of $E_{\mathrm{pk}}/E_{\mathrm{acc}}$ and α do not change. In order to move in this subspace, the following system of equations is solved

$$\begin{aligned} &\frac{\partial\left(\frac{B_{\mathrm{pk}}}{E_{\mathrm{acc}}}\right)}{\partial A}\cdot\Delta A + \frac{\partial\left(\frac{B_{\mathrm{pk}}}{E_{\mathrm{acc}}}\right)}{\partial B}\cdot\Delta B + \frac{\partial\left(\frac{B_{\mathrm{pk}}}{E_{\mathrm{acc}}}\right)}{\partial a}\cdot\Delta a + \frac{\partial\left(\frac{B_{\mathrm{pk}}}{E_{\mathrm{acc}}}\right)}{\partial b}\cdot\Delta b = \Delta\left(\frac{B_{\mathrm{pk}}}{E_{\mathrm{acc}}}\right), \\ &\frac{\partial\left(\frac{E_{\mathrm{pk}}}{E_{\mathrm{acc}}}\right)}{\partial A}\cdot\Delta A + \frac{\partial\left(\frac{E_{\mathrm{pk}}}{E_{\mathrm{acc}}}\right)}{\partial B}\cdot\Delta B + \frac{\partial\left(\frac{E_{\mathrm{pk}}}{E_{\mathrm{acc}}}\right)}{\partial a}\cdot\Delta a + \frac{\partial\left(\frac{E_{\mathrm{pk}}}{E_{\mathrm{acc}}}\right)}{\partial b}\cdot\Delta b = \Delta\left(\frac{E_{\mathrm{pk}}}{E_{\mathrm{acc}}}\right) = 0, \\ &\frac{\partial\alpha}{\partial A}\cdot\Delta A + \frac{\partial\alpha}{\partial B}\cdot\Delta B + \frac{\partial\alpha}{\partial a}\cdot\Delta a + \frac{\partial\alpha}{\partial b}\cdot\Delta b = \Delta\alpha = 0. \end{aligned} \tag{4.5}$$

Here $\Delta\left(\frac{B_{\mathrm{pk}}}{E_{\mathrm{acc}}}\right)$ is a small negative value added to decrease $B_{\mathrm{pk}}/E_{\mathrm{acc}}$. Equation (4.5) is composed of three linear equations with four unknowns. The changes in geometrical

values ΔA, ΔB, Δa and Δb have to be determined such that the changes in $E_{\mathrm{pk}}/E_{\mathrm{acc}}$ and α are zero and $B_{\mathrm{pk}}/E_{\mathrm{acc}}$ changes by a small negative value, i.e. $\Delta\left(\frac{B_{\mathrm{pk}}}{E_{\mathrm{acc}}}\right)$. At each point, the partial derivatives of the objective functions with respect to the geometrical parameters are calculated using the forward difference method with a step size of 0.005 mm. This requires four additional calls of the TunedCell function per point.

Equation (4.5) represents an underdetermined system of linear equations. The problem is solved with the conventional least-norm method [101, p. 408]. In this method, a solution is chosen that has the smallest norm, i.e. the length of the vector of increment is minimal. During optimization we allow a small deviation from c_1 and c_2 for the values of $E_{\mathrm{pk}}/E_{\mathrm{acc}}$ and α. In the next iteration, however, this deviation from the desired value can be restrained by choosing an appropriate value for $\Delta\alpha$ and $\Delta\left(\frac{E_{\mathrm{pk}}}{E_{\mathrm{acc}}}\right)$ to compensate this difference. Sometimes the assigned value for $\Delta\left(\frac{B_{\mathrm{pk}}}{E_{\mathrm{acc}}}\right)$ demands a large geometrical change in which the local derivative is no longer valid. This might lead to a geometry that deteriorates $B_{\mathrm{pk}}/E_{\mathrm{acc}}$ and deviates significantly from the constraints. In such a case, the magnitude of $\Delta\left(\frac{B_{\mathrm{pk}}}{E_{\mathrm{acc}}}\right)$ should be reduced to create a smaller incremental vector. Thus, the right-hand sides of the equation (4.5) are changed dynamically to keep the solution on the boundary constraints and decrease $B_{\mathrm{pk}}/E_{\mathrm{acc}}$. This algorithm is carried out until a further decrease of $B_{\mathrm{pk}}/E_{\mathrm{acc}}$ is infeasible. In order to reduce the risk of falling into a local optimum, the Monte Carlo method is applied again, starting from the optimal point obtained from the proposed gradient-based method. This procedure is repeated several times until no improvement is observed in the objective function.

4.1.2 Choice of Constraints

The results of the optimization for different constraints on α, R_{i} and $E_{\mathrm{pk}}/E_{\mathrm{acc}}$ are depicted in Figure 4.2, together with some well-known cavity designs. As shown in Figure 4.2 (a) and 4.2 (b), a lower α results in a higher $G \cdot R/Q_{\parallel,0}$ and a smaller $B_{\mathrm{pk}}/E_{\mathrm{acc}}$. As stated earlier, the minimization for $B_{\mathrm{pk}}/E_{\mathrm{acc}}$ yields a geometry with high $G \cdot R/Q_{\parallel,0}$. The wall angle α has small influence on the cell-to-cell coupling as shown in Figure 4.2 (c). An increase in the limit of $E_{\mathrm{pk}}/E_{\mathrm{acc}}$ results in a geometry with lower $B_{\mathrm{pk}}/E_{\mathrm{acc}}$ and higher cell-to-cell coupling. The longitudinal loss factor is mainly affected by the aperture radius while the wall slope angle has small influence on it (see Figure 4.2 (d)). A large R_{i} increases the cell-to-cell coupling and reduces the longitudinal loss factor at the cost of a higher $B_{\mathrm{pk}}/E_{\mathrm{acc}}$ and higher surface losses. This trade-off should be considered in the final choice of the R_{i}. A list of optimized cavities with a different aperture radius R_{i}, $E_{\mathrm{pk}}/E_{\mathrm{acc}}$ and α is shown in Table 4.1.

In addition to the FM, the HOM spectrum plays an important role in designing the cavity. Each HOM can be characterized by its R/Q and its external quality factor

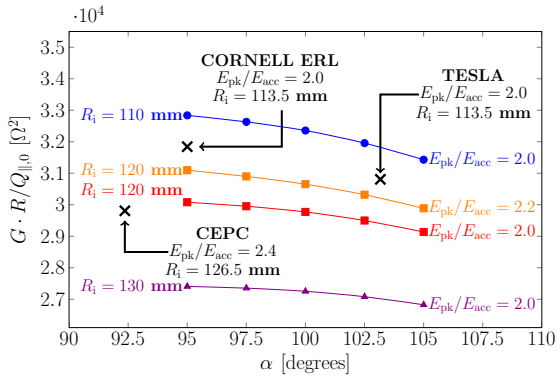

(a) $G \cdot R/Q_{\parallel,0}$ for different α

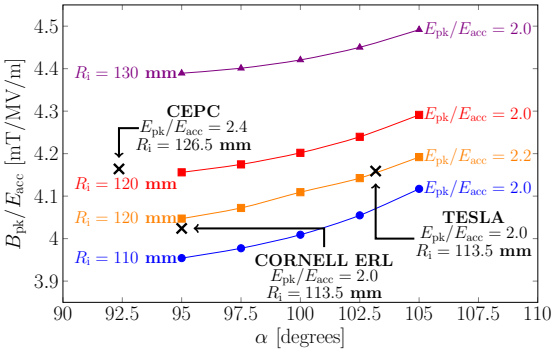

(b) $B_{\mathrm{pk}}/E_{\mathrm{acc}}$ for different α

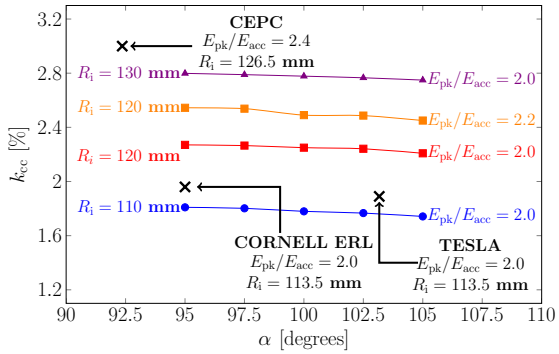

(c) Cell-to-cell coupling for different α

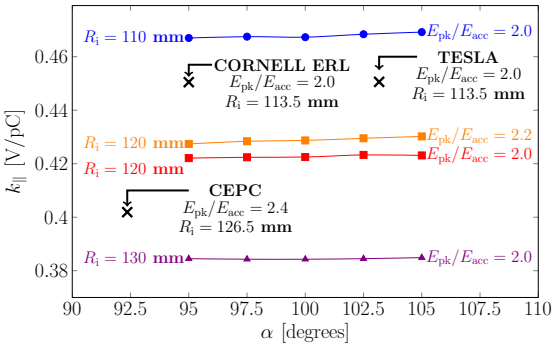

(d) Longitudinal loss factor (σ_z=3 mm) for different α

Figure 4.2: Middle cell optimization for different values of $E_{\mathrm{pk}}/E_{\mathrm{acc}}$, α and R_{i}. The dimensions of the CEPC [63], TESLA [65] and CORNELL ERL [93] cavities are scaled to 400.79 MHz for comparison. For each point in the graphs, the optimization problem of equation (4.3) is solved for the $\mathrm{TM}_{010}-\pi$ mode. Each curve in (b) represents a Pareto front that depends on the constraints of the optimization problem (4.3).

Q_{ext}. The Q_{ext} shows the extent by which HOMs are damped, and highly depends on the used damping method. The R/Q solely depends on the shape of the cavity. The dependency of the frequency and R/Q of two monopole (TM_{010} and TM_{011}) and two dipole modes (TE_{111} and TM_{110}) with respect to the optimization constraints of problem (4.3) are shown in Figure 4.3. The longitudinal shunt impedance $R/Q_{\parallel}$ is calculated for the monopole modes and the transversal shunt impedance $R/Q_{\perp}$ for the dipole modes, using equations (2.41) and (2.44), respectively[1].

During the initial design study, a high value of the transversal impedance was observed in the first dipole band. For this reason, special attention is paid to the

[1]Equation (2.45) is not used for the calculation of $R/Q_{\perp}$ because the PMC boundary condition is used at both ends of the cavity along the iris radius.

Table 4.1: A list of optimized middle cells with a different aperture radius, $E_{\mathrm{pk}}/E_{\mathrm{acc}}$ and α. The cavities are tuned to 400.79 MHz and the length of the half-cell is 187 mm for all cases.

A [mm]	B [mm]	a [mm]	b [mm]	R_i [mm]	R_{eq} [mm]	α [°]	$\frac{E_{\mathrm{pk}}}{E_{\mathrm{acc}}}$ -	$\frac{B_{\mathrm{pk}}}{E_{\mathrm{acc}}}$ [$\frac{\mathrm{mT}}{\mathrm{MV/m}}$]	$R/Q_{\parallel,0}$ [Ω]	G [Ω]	k_{cc} [%]
141.60	113.74	31.51	48.76	100	326.754	100	2.0	3.84	127	275.6	1.36
138.82	114.07	37.16	59.53	110	329.64	100	2.0	4.01	118.2	274.2	1.78
135.44	114.90	43.50	71.19	120	333.182	100	2.0	4.20	109.5	272.3	2.25
130.69	110.99	50.68	84.28	130	336.83	100	2.0	4.42	101.1	270	2.78
125.25	107.99	59.18	102.22	140	341.431	100	2.0	4.67	92.9	267.3	3.38
119.11	108.15	68.12	115.95	150	347.14	100	2.0	4.95	85.2	263.4	4.0
110.86	102.18	79.62	140.62	160	353.43	100	2.0	5.28	77.8	259	4.7
149.60	108.48	25.99	36.97	100	323.546	97.5	2.2	3.75	128.2	280.7	1.55
146.55	102.75	30.17	43.40	110	325.464	97.5	2.2	3.90	119.5	279.6	2.01
143.46	100.33	34.59	49.08	120	328.30	97.5	2.2	4.07	110.9	278.6	2.54
140.25	105.71	39.62	52.65	130	332.70	97.5	2.2	4.27	102.7	277.1	3.07
135.56	95.43	45.92	69.82	140	335.893	97.5	2.2	4.47	94.4	276.0	3.81
131.50	94.18	50.76	70.88	150	340.206	97.5	2.2	4.69	87.1	274.4	4.50
126.64	93.75	57.26	80.24	160	345.606	97.5	2.2	4.93	80.0	272.7	5.29
152.91	104.32	26.79	39.07	100	321.268	95	2.2	3.72	129.3	281.0	1.57
149.91	103.50	30.74	43.70	110	323.989	95	2.2	3.87	120.3	279.9	2.02
146.42	101.87	35.17	49.65	120	327.13	95	2.2	4.05	111.5	278.7	2.54
142.51	99.75	40.01	56.14	130	330.706	95	2.2	4.24	103.1	277.4	3.13
138.15	97.08	45.28	63.76	140	334.768	95	2.2	4.45	95.0	276.0	3.79
133.30	95.22	51.07	71.49	150	339.514	95	2.2	4.67	87.3	274.4	4.51
127.93	94.32	57.50	80.64	160	345.067	95	2.2	4.92	80.1	272.6	5.29

damping of the first two dipole modes in order to maintain the beam stability limit. The following considerations were taken into account for the choice of the optimization constraints: first, a high value of $R/Q_{\parallel}$ for the TM_{010} mode and a low value of $R/Q_{\perp}$ for the TE_{111} and TM_{110} modes are aimed for. Second, there should be sufficient distance between the frequency of the FM and the frequency of the first dipole mode in order to facilitate the HOM coupler design. Third, the distance between the frequency of the TE_{111} and TM_{110} modes should be minimized so that both modes can be sufficiently damped by means of a coaxial HOM coupler. As shown in Figure 4.3 (a), the wall slope angle has only a minor influence on the parameters mentioned. The frequency of the TM_{011} mode, which is the first higher order monopole mode, increases for larger α. Therefore, a wall slope angle of $\alpha = 100°$ is chosen to push the frequency of the TM_{011} mode well above the cutoff frequency of the beam pipe, and also to facilitate the fabrication of the SRF cavity.

The $E_{\mathrm{pk}}/E_{\mathrm{acc}}$ has a major influence on the frequency of TE_{111} and TM_{011} modes, as shown in Figure 4.3 (b). We choose $E_{\mathrm{pk}}/E_{\mathrm{acc}} = 2.0$ to obtain a low value of the

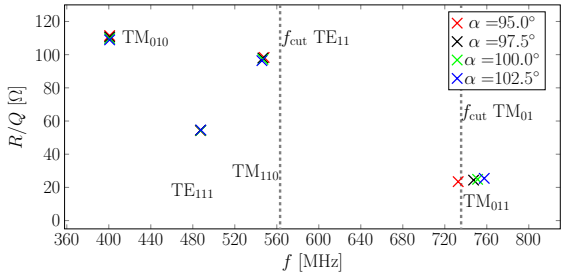

(a) Dependency of R/Q on α when $E_{\mathrm{pk}}/E_{\mathrm{acc}}$ = 2.0 and R_{i}=120 mm

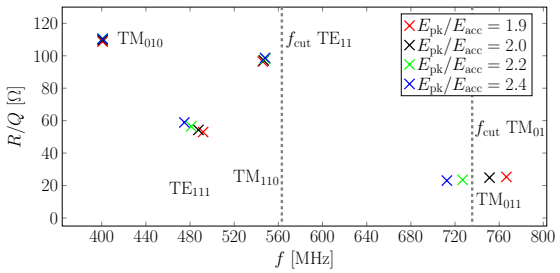

(b) Dependency of R/Q on $E_{\mathrm{pk}}/E_{\mathrm{acc}}$ when α = 100° and R_{i}=120 mm

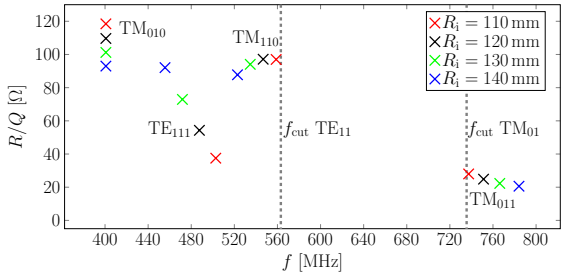

(c) Dependency of R/Q on R_{i} when $E_{\mathrm{pk}}/E_{\mathrm{acc}}$ = 2.0 and $\alpha = 100°$

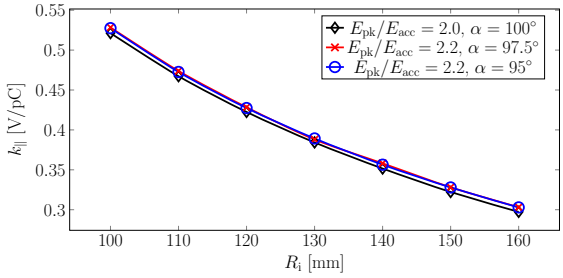

(d) Dependency of the loss factor on R_{i}

Figure 4.3: Dependency of the frequency and R/Q of the first two monopole and dipole modes of the cavity on the constraints of (4.3). The longitudinal shunt impedance $R/Q_{\parallel}$ is calculated for the TM_{010} and TM_{011} modes and the transversal shunt impedance $R/Q_{\perp}$ for the TE_{111} and TM_{110} modes, using (2.41) and (2.44), respectively. The vertical dashed lines represent the cutoff frequencies of the TE_{11} and TM_{01} modes of a cylindrical beam pipe with a radius of 156 mm. The TE_{111} and TM_{110} modes in the cavity couple to the TE_{11} mode, and the monopole mode TM_{011} couples to the TM_{01} mode of the cylindrical beam pipe. The drastic change in the $R/Q_{\perp}$ of the TE_{111} mode in (c) arises from the non-zero tangential electric field values at both ends of the cell (the second bracket in (2.39) and (2.40) is not zero because of the PMC boundary condition). In a multi-cell cavity or in the presence of beam pipes this dependency is not observed.

surface electric field and to reduce the frequency difference between the TE_{111} and TM_{110} modes. The selection of the iris radius is another crucial parameter in the optimization problem. A high value of the iris radius decreases the $R/Q_{\parallel}$ of the FM and brings the frequency of the TE_{111} mode closer to the TM_{010} mode. Furthermore, it decreases the loss factor, as depicted in Figure 4.3 (d). A value between 120 to 130 mm seems to be a reasonable range for the iris radius parameter. In the following design we consider $R_{\mathrm{i}} = 120\,\mathrm{mm}$.

Considering the above arguments, a geometry corresponding to $E_{\mathrm{pk}}/E_{\mathrm{acc}} = 2.0$, $\alpha = 100°$ and $R_{\mathrm{i}} = 120\,\mathrm{mm}$ is selected for further study of the cavity. The geomet-

rical parameters of this cavity are given in Table 4.1.

4.2 End cell optimization

Adding the beam pipes to the cavity cells changes the frequency and field pattern of the modes. Special care should be taken in designing the end cells to compensate for this effect on the FM and to facilitate HOM damping. The parametrization of one possible form of the end cell is shown in Figure 4.4. In such a parametrization, the inner side of the end cell is identical with the optimized middle cells. The outer half-side of the end cell is used for the tuning of the end cell, and here it is labeled with the subscript e. The equator radius R_{eq} of the end cell is set equal to that of the middle cells. The length of the cell is the third effective parameter on the frequency of the fundamental mode, after R_{eq} and A [86]. In the middle cells, the cell length was fixed and R_{eq} was used for frequency tuning. In the end cell we keep R_{eq} fixed, and vary L_{e} of the end cell for frequency tuning. The parameter A_{e} together with B_{e}, a_{e}, b_{e} and R_{bp} are used as free parameters in the end cell optimization.

The end cell shown in Figure 4.4 was simulated using SuperLANS software. A wrapper code based on SuperLANS was implemented. All the geometrical parameters (except L_{e}) and the desired frequency were used as inputs, and the code consequently supplied the optimum L_{e} and the secondary parameters as outputs. The whole program was controlled by Matlab. In order to generate a π-mode-type field pattern in the end cell, the PMC boundary condition is applied to the boundary along R_{i}, and the PEC boundary condition is applied on the surface of the cavity. The fundamental cutoff frequency of the beam pipe with the radius R_{bp} is above the FM frequency of the cavity. This keeps the field of the FM mainly inside the cavity

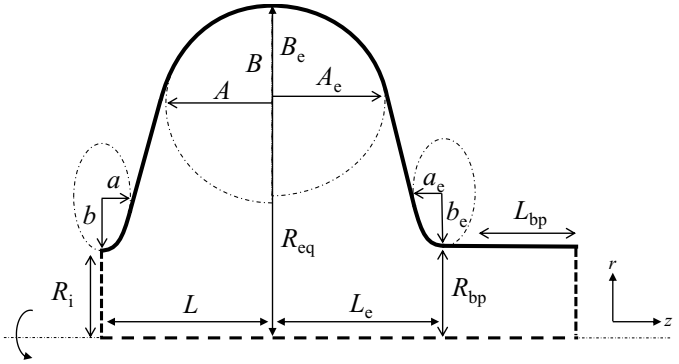

Figure 4.4: End cell parametrization of an elliptical cavity (parametrization is adapted from [93]). The inner side of the end cell is identical with the optimized middle cells, and the outer half-side, which is connected to the beam pipe, is changed in the end cell optimization. Note that the geometry is axisymmetric around the centerline, and only the upper part of the cross-section is shown.

with small leakage into the beam pipe. The beam-pipe length is extended such that the field of the FM attenuates before reaching the boundaries of the beam pipe, i.e. $L_{\mathrm{bp}} = 4R_{\mathrm{bp}}$, which attenuates the FM field to below -70 dB for any R_{bp} smaller than 156 mm (assuming $f_0 = 400.79$ MHz). Therefore, the boundary condition at the end of the beam pipe has no significant influence on the field and frequency of the FM.

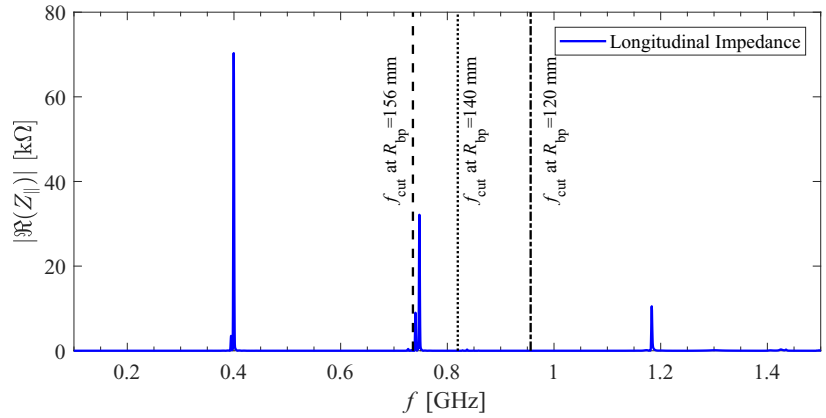

(a) Longitudinal impedance and the cutoff frequency of the TM_{01} mode of a cylindrical waveguide.

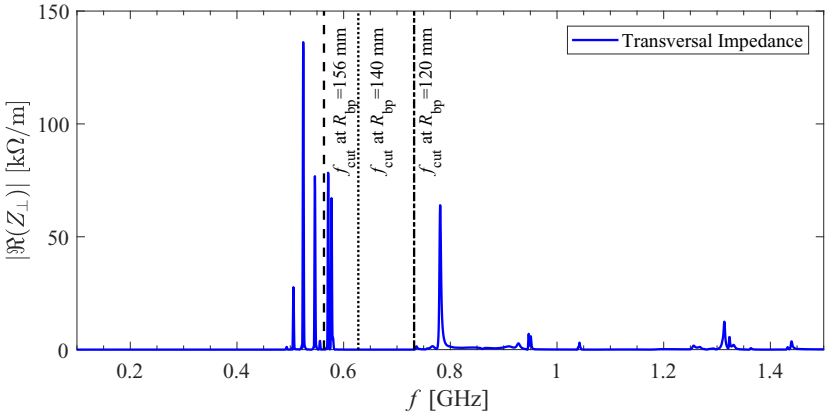

(b) Transversal impedance and the cutoff frequency of the TE_{11} mode of a cylindrical waveguide.

Figure 4.5: Longitudinal and transversal impedance of a four-cell cavity with identical cells are shown in blue. The cutoff frequency of the TM_{01} and TE_{11} mode of a cylindrical waveguide with different aperture radius is plotted in black vertical lines. The impedances are calculated for a bare cavity, and the peaks are not fully resolved.

Before optimizing the end cell, a suitable value for the beam-pipe radius R_{bp} has to be selected. The longitudinal and transversal impedance of a four-cell cavity with four identical cells, as designed in the previous section, is shown in Figure 4.5.

Changing only the end half-cells does not significantly change the location of the impedance peaks in a multi-cell cavity. Choosing a beam-pipe radius of 156 mm allows us to bring the cutoff frequency of the TM_{01} mode of the beam pipe below the frequency of the higher order monopole mode with the highest longitudinal impedance, and thus facilitates its damping. This radius also brings the cutoff frequency of the TE_{11} mode of the beam pipe below some HOMs in the first dipole band, as depicted in Figure 4.5 (b). This facilitates the use of a coaxial HOM coupler for the damping of the first dipole band. However, having different aperture radii for the end cells and middle cells can increase the risk of having modes trapped inside the cavity, as the oscillating frequency for a certain mode in the middle cells and end cells may become very different and, consequently, the coupling between cells for that particular mode may get weak. Therefore, special attention should be paid to the HOMs with high R/Q when choosing the other geometrical parameters of the end cells to prevent such HOMs from being trapped in the cavity.

Thanks to the computational efficiency of 2D axisymmetric codes, a parameter sweep in the four-dimensional space over the four parameters A_e, B_e, a_e and b_e of the end cell is carried out. For each geometry in the parameter sweep, the length L_e, of the end cell is varied by the aforementioned wrapper code to tune the frequency to 400.79 MHz. The objective of the parameter sweep is to seek for a geometry that has a high E_acc at the end cell while the location of E_pk is kept on the inner side of the end cell. This ensures that the value of E_pk is equal to that of the middle-cells. Furthermore, the maximum magnetic field B_pk on the surface of the outer half-cell should not significantly exceed the same value in the inner half-cell (maximum exceedance 1 %). As R_bp is larger than R_i, it is difficult to have the location of E_pk and B_pk on the inner side of the end cell at the same time. The E_pk constraint can be more easily met because, unlike the middle cells, the electric field around the iris region of the outer half-cell penetrates into the beam pipe, and this reduces the value of the E_pk. The maximum value of the magnetic field B_pk, on the other hand, is located around the equator region, and having a larger R_bp reduces the surface area over which the magnetic field is distributed, which might result in a higher value of B_pk. For this reason, we allow the maximum value of the magnetic field on the outer half-cell to slightly exceed the same value in the inner half-cell. Since L_e is changed for tuning the frequency, we define E_acc at the end cell as the ratio of the accelerating voltage to the length of the middle cells, i.e. $E_\mathrm{acc} = V_\mathrm{cav}/(2L)$.

The frequency of the first mode in the TM_{011}-type passband (which typically has the highest $R/Q_\parallel$ among HOMs) in the two inner cells, which constitute the middle cells of the four-cell cavity, is 736 MHz and 725 MHz under the PMC and the PEC boundary condition on the iris line, respectively (see Figure 4.6 (a)-(b)). To prevent these modes from getting trapped in the cavity, in addition to the above constraints, a geometry is chosen for the end cell the second monopole mode frequency of which is close to 736 MHz (under PMC boundary condition on the iris line). Note that, as stated earlier, PMC is also used for the FM mode calculation.

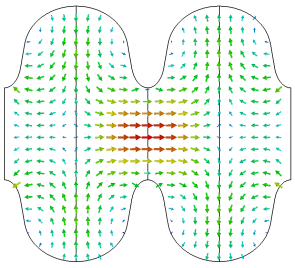

(a) $f = 736\,\text{MHz}$ and PMC is applied on both ends

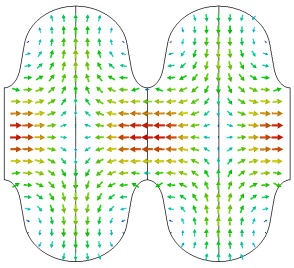

(b) $f = 725\,\text{MHz}$ and PEC is applied on both ends

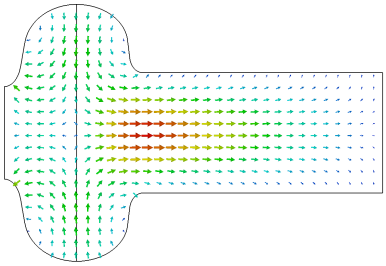

(c) $f = 735\,\text{MHz}$ and PMC is applied on both ends

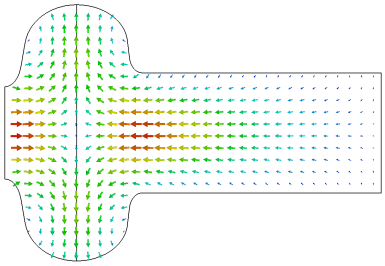

(d) $f = 725\,\text{MHz}$ and PEC is applied on the left and PMC on the right

Figure 4.6: Field distribution of the first TM_{011}-type mode in the two inner cells (a)-(b) and the end cell (c)-(d) under different boundary conditions. At the end of the beam pipe in (c) and (d) PMC boundary condition is applied, while in the inner side that connects to the middle cells different boundary conditions are used.

Therefore, two monopole modes are calculated with the same simulation set-up, i.e. the first monopole mode corresponds to the FM and the second monopole mode to the TM_{011}.

In order to avoid discarding geometries that have desirable peak field values and TM_{011} mode frequency, simply because their wall angle is below 100°, the lower limit for the wall slope angle of the outer part of the end cell is set to 95°. Thus, the optimum L_e, the location of E_pk and B_pk, the value of E_pk/E_acc and B_pk/E_acc, the frequency of the second monopole mode, and the wall angle of the outer half-cell of the end cell is calculated for each sample in the parameter sweep.

After running the parameter sweep, the results are filtered in accordance with the aforementioned constraints, and the geometrical parameters listed in Table 4.2 are chosen for the end cell. The electric and magnetic field over the surface of the end cell is shown in Figure 4.7. As aimed for, the E_pk location is on the inner side of the end cell, and the maximum value of the magnetic field on the outer half cell is only 0.5 % higher than that on the inner cell. The frequency of the TM_{011} mode under PMC and PEC boundary conditions is 735 MHz and 725 MHz, respectively, as shown in Figure 4.6 (c) and (d).

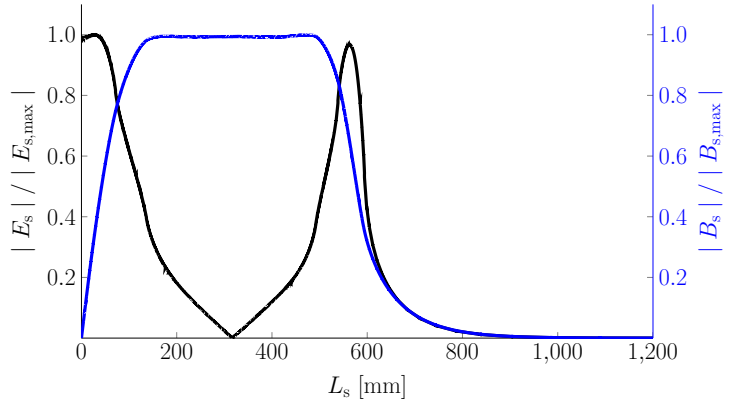

Figure 4.7: The normalized electric and magnetic field over the surface of the end cell. L_s is the contour length on the surface of the cavity.

Table 4.2: End cell parameters.

A_e [mm]	B_e [mm]	a_e [mm]	b_e [mm]	R_bp [mm]	R_eq [mm]	L_e [mm]	α_e [°]
133	102	34	46	156	333.182	171.532	96.9

4.3 Multi-cell cavity

4.3.1 Four-cell cavity at 400.79 MHz

In this section, the middle cell and the end cell designed in Sections 4.1 and 4.2 are combined to create a multi-cell cavity. Six half-cells of the middle-cell type, and two outer parts of the end cells are connected to each other to form a four-cell cavity at 400.79 MHz (for the W, H and $\mathrm{t\bar{t}}$ options). A picture of the cavity with the electric and magnetic field on the surface of the cavity and the electric field on the longitudinal axis is shown in Figure 4.8.

Field flatness is an important figure of merit in multi-cell cavities that shows how uniformly the energy is distributed over cells. Having a high field flatness means that particles receive an equal amount of energy in each cell. Furthermore, it allows to uniformly increase the field level of the whole cavity without reaching the maximum surface limit too early in one cell. The field flatness in a cavity with N_cell number of cells can be defined as [102]

$$\eta_\mathrm{ff} = 100 \cdot \left(1 - \frac{E_\mathrm{p,max} - E_\mathrm{p,min}}{\frac{1}{N_\mathrm{cell}} \sum_{i=1}^{N_\mathrm{cell}} E_{\mathrm{p},i}}\right) \tag{4.6}$$

where $E_{\mathrm{p},i}$ is the peak axial electric field of the i-th cell, and $E_\mathrm{p,max}$ and $E_\mathrm{p,min}$ are the maximum and minimum peak axial electric field considering all cells, respectively.

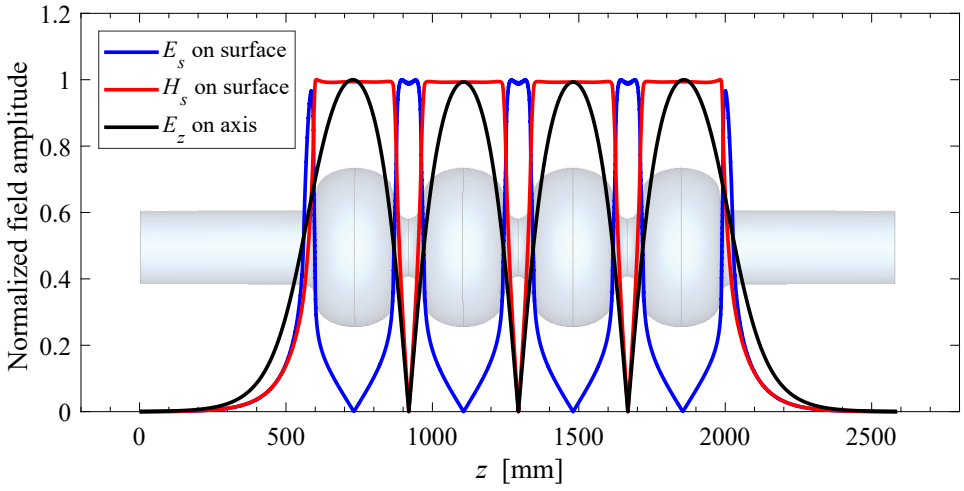

Figure 4.8: Four-cell cavity with the FM frequency at 400.79 MHz. The surface electric field, the surface magnetic field and the electric field along the longitudinal axis of the cavity are plotted. The magnitude of the fields is normalized in each case. The maximum value of the electric field is concentrated around the iris region of the cells, while the maximum value of the magnetic field is located around the equator of the cells.

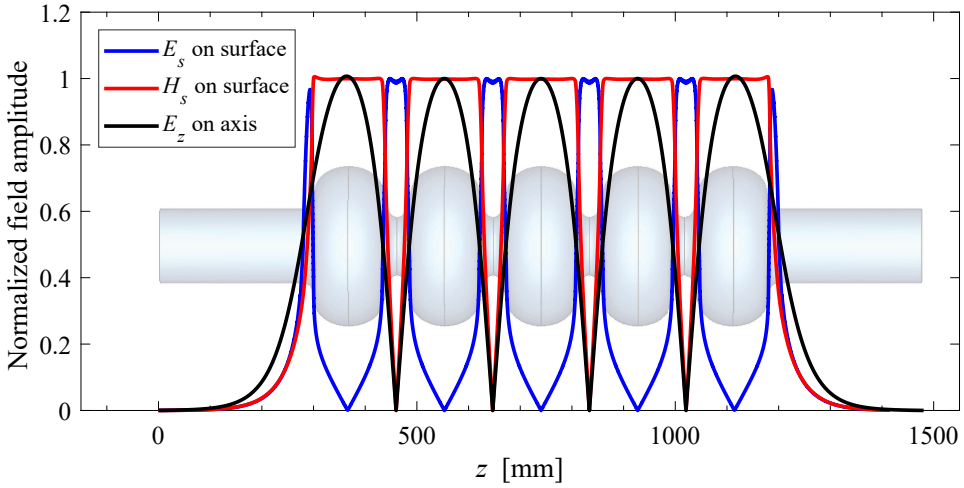

Figure 4.9: Five-cell cavity with the FM frequency at 801.58 MHz. The magnitude of the fields is normalized in each case.

For the designed end cell, a high value of field flatness of the FM is obtained automatically because both middle cells and end cells were exactly tuned to 400.79 MHz for the $TM_{010} - \pi$ mode. A list of the parameters of the four-cell cavity is given in Table 4.3.

4.3.2 Five-cell cavity at 801.58 MHz

The geometrical parameters of the middle cell and end cell given in Table 4.1 and 4.2 are scaled by half to create a cavity at 801.58 MHz. Eight re-scaled half middle-cells and two outer parts of the end cells are combined in order to create a five-cell cavity for the $t\bar{t}$ working point. The surface electric field, the surface magnetic field, and the longitudinal field on the axisymmetrical axis of the five-cell cavity are shown in Figure 4.9. The advantage of designing middle cells and end cells becomes clear here. The number of middle cells can be varied while the frequency and the field flatness of the FM of the cavity remains almost the same. The RF parameters of the five-cell cavity and two other five-cell cavities designed for the PERLE project [78] are given in Table 4.3.

Table 4.3: RF parameters of the proposed four-cell (FCC_{UROS4}) and five-cell (FCC_{UROS5}) cavities. The cavities are compared with two five-cell cavities designed for operation in PERLE [78, p. 61].

Parameters	FCC_{UROS4} *	FCC_{UROS5} *	$CERN_2$	$JLab_2$
Frequency, f_0 [MHz]	400.79	801.58	801.58	801.58
Number of cells, N_{cell}	4	5	5	5
$R/Q_{\parallel,0}$ [Ω]	411.3	520.6	393	523.9
G [Ω]	273.2	272.9	283	274.6
$G \cdot R/Q_{\parallel,0}$ [Ω^2]	112367	142072	111219	143862
$B_{\text{pk}}/E_{\text{acc}}$ (middle cell) [$\frac{\text{mT}}{\text{MV/m}}$]	4.2	4.2	4.92	4.2
$E_{\text{pk}}/E_{\text{acc}}$ (middle cell)	2.0	2.0	2.4	2.26
Cavity active length, L_{active} [mm]	1465.1	919.5	935	917.9
Radius of the middle cells, R_i [mm]	120	60	80	65
Beam pipe radius, R_{bp} [mm]	156	78	80	65
Wall angle of middle cell, α [°]	100	100	102.5	90
k_{cc} of the middle cell [%]	2.25	2.25	5.75	3.21
k_{cc} of the cavity [%]	1.92	2.04	5.19	2.93
Field flatness, η_{ff} [%]	99	99	96	99
$k_{\parallel}$ ($\sigma_z = 2$ mm) [V/pC]	2.27	3.37	2.63	2.74
f_{cut} TE_{11} for R_{bp} [GHz]	0.563	1.126	1.10	1.35
f_{cut} TM_{01} for R_{bp} [GHz]	0.7355	1.471	1.43	1.77
$N_{\text{cell}}^2/k_{\text{cc}}$	833	1225	481	853

* The designed cells are adapted to a four-cell cavity at 400.79 MHz and a five-cell cavity at 801.58 MHz.

4.4 Single-cell cavity design for Z

A single-cell elliptical cavity is depicted in Figure 4.10. In cavities, part of the EM field of the FM leaks into the beam pipes. For this reason, the cell and the beam pipes have to be considered together for the simulation and optimization of the single-cell design, similar to the procedure for the end-cell design. This differs from the optimization of the middle cells (as shown in Section 4.1), where only middle cells with appropriate boundary conditions are simulated. Since the electric field of FM penetrates the beam pipe, the concentration of the electric field around the iris region is smaller in a single-cell cavity. Therefore, the $E_{\mathrm{pk}}/E_{\mathrm{acc}}$ would be smaller compared to a similar middle-cell geometry. This relaxes one of the constraints that we had in the middle-cell optimization. In the design of the middle cells, the half-length of the cell was set fixed in accordance with (4.1). This length allows the particle to absorb the maximum energy as it traverses the consecutive cells. In a single-cell cavity, this restriction is not mandatory as the particle passes only through one cell. Therefore, the length of the cavity can be varied freely in the course of cell-optimization. This adds one more degree of freedom to the shape optimization of single-cell cavities.

As indicated in the previous chapter, the number of Z cavities is limited by the high input power per cavity. For this reason, no high accelerating fields are required as the Z cavities will be operated at a low E_{acc} (at 5.1 MV/m in accordance with Table 3.3). Due to the small number of cavities and the low accelerating field, the wall-plug power of the Z cavities is small (below 1 MW, refer to Table 3.3). The high beam current of the Z running demands strong HOM damping requirements. For this reason, the design of the Z cavities does not only require an optimization of $E_{\mathrm{pk}}/E_{\mathrm{acc}}$, $B_{\mathrm{pk}}/E_{\mathrm{acc}}$ and $G \cdot R/Q_{\parallel,0}$, but special attention should be paid to the HOM damping aspects right from the early design stages of the cavity, in particular with regard to the modes in the first dipole band. As indicated in Figure 4.3 (c-d), a higher iris radius decreases the loss factor $k_{||}$. Furthermore, a high iris radius

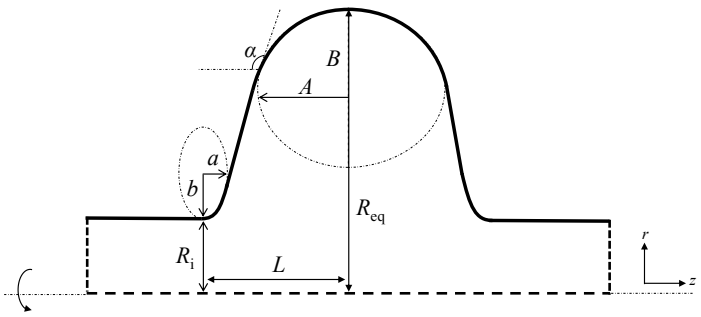

Figure 4.10: Single-cell parametrization of an elliptical cavity. The beam pipes should be considered during the optimization of the single-cell cavity. The geometry is axisymmetrical around the centerline, and only the upper part of the cross-section is shown.

pushes the frequency of the TM_{011} mode (the first higher order monopole mode) above the cutoff frequency of the beam pipe and untraps this mode. The first two dipole modes (the TE_{111} and TM_{110} modes), on the contrary, remain trapped in the cavity even with a reasonably enlarged iris radius.

Coaxial couplers, WG couplers, and beam-pipe absorbers are usually used for the damping of HOMs. As the coaxial and WG couplers can be placed close to the cells, where the HOMs are generally created, they provide better damping of the trapped modes. Coaxial HOM couplers are optimized to have a notch at the FM and a high transmission at frequencies that require strong damping. If the difference between the frequencies of the TE_{111} and TM_{110} modes is small, the design of a coaxial narrow-band HOM coupler for their damping can be simplified. Therefore, as an objective function, the difference between the frequencies of the first two dipole modes (the TE_{111} and TM_{110} modes) is minimized, i.e. $\mid f_{\mathrm{d1}} - f_{\mathrm{d2}} \mid$ where subscripts d1 and d2, respectively, refer to the first and second dipole modes (not counting the degenerate modes). Furthermore, the following term is minimized in order to minimize the sum of the transverse impedances of the TE_{111} and TM_{110} modes: $k_{\mathrm{d1}} R/Q_{\perp,\mathrm{d1}} + k_{\mathrm{d2}} R/Q_{\perp,\mathrm{d2}}$ (see equation (2.47)).

To avoid a steep transmission curve near the FM notch of the coaxial HOM couplers there should be a sufficient distance between the frequency of the FM and the first dipole mode (which is typically the TE_{111} mode). This also benefits the design of WG HOM couplers. In order to cover the entire HOM spectrum with the WG couplers, the dimensions of the WG are determined such that the frequency of the first mode of the WG (the TE_{01} mode) is located between the FM and the first dipole mode of the cavity. If f_{d1} is very close to f_0, a WG with a larger cross-section and a longer length is required to lower the cutoff frequency of its TE_{01} mode and to provide sufficient distance for decaying the FM leaked into the WG, respectively. A larger WG complicates the design of the cryomodule as it occupies more space in the module, especially at 400.79 MHz. Therefore, the distance between f_{d1} and f_0 should be maximized (this is equivalent to minimizing $-\mid f_0 - f_{\mathrm{d1}} \mid$).

The problem is a constrained multi-objective optimization with constraints on geometrical parameters. The wall slope angle of the cavity should not deliver a reentrant cavity, and the frequency of the FM has to be tuned to 400.79 MHz. Thus, the constrained multi-objective optimization problem is formulated as

$$\begin{aligned} \underset{R_{\mathrm{i}},L,A=B,a=b}{\text{minimize}} \quad & \Big(\underbrace{-\mid f_0 - f_{\mathrm{d1}} \mid}_{F_1}, \underbrace{\mid f_{\mathrm{d1}} - f_{\mathrm{d2}} \mid}_{F_2}, \underbrace{k_{\mathrm{d1}} \frac{R}{Q}_{\perp,\mathrm{d1}} + k_{\mathrm{d2}} \frac{R}{Q}_{\perp,\mathrm{d2}}}_{F_3}, \\ & \underbrace{-G \cdot R/Q_{\parallel,0}}_{F_4}, \underbrace{E_{\mathrm{pk}}/E_{\mathrm{acc}}}_{F_5}, \underbrace{B_{\mathrm{pk}}/E_{\mathrm{acc}}}_{F_6} \Big) \\ \text{subject to} \quad & \underset{R_{\mathrm{eq}}}{\text{minimize}} \ \mid f_0 - 400.79 \text{ MHz} \mid \quad \text{and} \quad \alpha \geq 90^\circ. \end{aligned} \tag{4.7}$$

The optimization variables are R_{i}, L, A, B, a and b. For each geometry, R_{eq} is used to tune the frequency of the FM to 400.79 MHz. As shown in [86], B and b have only a minor influence on the chosen objective functions (except on $E_{\mathrm{pk}}/E_{\mathrm{acc}}$). Therefore, the number of variables and thus the search space could be reduced by setting $a = b$ and $A = B$. The geometrical constraints chosen for the optimization are given in Table 4.4. In order to solve the optimization problem and to find any existing Pareto front, a genetic algorithm (GA) method [103] that is available in the optimization toolbox of MATLAB is used.

Table 4.4: Geometrical constraints in the optimization problem of equation (4.7).

Parameter	R_{i} [mm]	L [mm]	$A = B$ [mm]	$a = b$ [mm]
Lower bound	145	120	40	10
Upper bound	160	190	140	70

For each individual of the GA, the geometrical data were created by MATLAB and saved in a text file readable by SUPERLANS and SLANS2. SLANS2 is a generalization of SUPERLANS code, developed for the calculation of the multipole modes in axisymmetric structures [96]. The executable files of SUPERLANS and SLANS2 were then called by MATLAB to calculate the monopole mode and the two dipole modes, respectively. Next, the calculated secondary parameters were read by MATLAB to evaluate the objective functions. A 1D optimization problem for tuning f_0 was solved for each individual of GA. The population size and the maximum number of generations were set to 100 and 75, respectively. After running the optimization problem, the favorable individual had an R_{i} close to 156 mm (which is the aperture radius of the end cell designed in section 4.2 for the multi-cell cavities). Using a similar aperture radius in different machines is favorable, as it permits the reuse of some equipment such as flanges. For this reason, the dimensions of the chosen individual were rounded to the nearest integer, its R_{i} was set to 156 mm and the R_{eq} varied to tune f_0. The GA algorithm was run again using the chosen geometry as one of the individuals in the first generation. The chosen individual was also among the best points of the second run of the optimization.

A scatter plot is used in Figure 4.11 to demonstrate the trade-off between the six objective functions in the Pareto front approximation after 75 generations. The ith element on the main diagonal shows the histogram distribution of the objective function F_i. The number below the main diagonal in the ith row and the jth column where $i > j$, shows the correlation coefficient between F_i and F_j. The graph above the main diagonal at position (i, j) where $i < j$ displays the values of F_i (y-axis) and F_j (x-axis) for the individuals in the last generation. The reason for the positive correlation between F_1 and F_2 is that f_{d1} is more sensitive to the geometrical changes

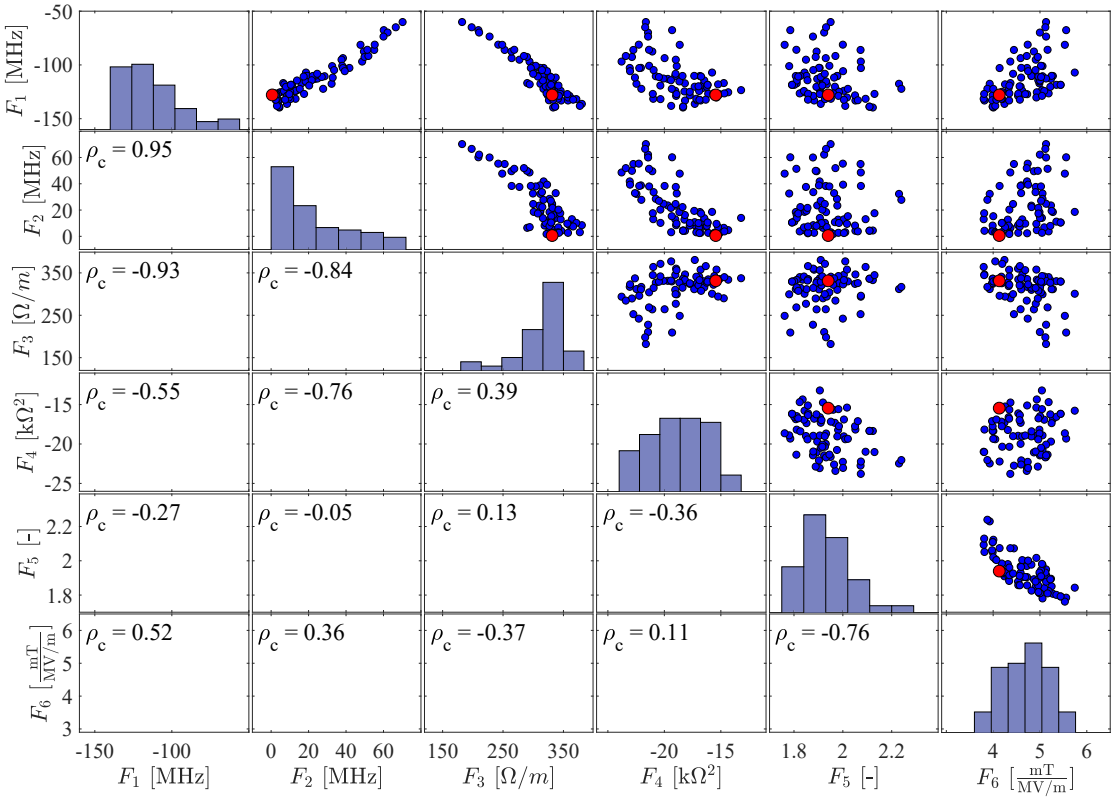

Figure 4.11: A scatter plot for each pair of objective functions of the individuals in the last generation of the GA. The numbers below the main diagonal are the correlation coefficients between the objective functions. The six objective functions cannot be minimized at the same time. The scatter plot shows the dependencies between the six objective functions, and the compromise one has to make for improving each objective function. The selected geometry is highlighted by red color.

than f_{d2}. Therefore, the further f_{d1} gets from f_0 (which is fixed to 400.79 MHz), the closer it gets to f_{d2}. Here, a high aperture radius decreases the transverse impedance of both dipole modes, but it significantly reduces the frequency of the TE_{111} mode (brings it close to the FM frequency). Therefore, F_1 and F_2 are inversely correlated with F_3. The RF parameters of the selected geometry (denoted by $\mathrm{FCC}_{\mathrm{UROS1}}$) and four other storage ring single-cell cavity designs (CESR-B [104], HL-LHC [105], LHC [106], and $\mathrm{FCC}_{\mathrm{PR19}}$ [86]) are given in Table 4.5.

To have less constraints on the coaxial HOM coupler design for the damping of the TE_{111} and TM_{110} modes, F_2 of the selected individual from the GA is close to zero. For the chosen geometry, $G \cdot R/Q_{\parallel,0}$ is sacrificed in favor of other objective

Table 4.5: A comparison of the chosen cavity in the last generation of the GA, denoted by $\mathrm{FCC}_{\mathrm{UROS1}}$, with some storage ring single-cell cavities. The dimensions of the CESR-B and HL-LHC cavities are scaled and tuned such that $f_0 = 400.79\,\mathrm{MHz}$. The $\mathrm{FCC}_{\mathrm{PR19}}$ is a single-cell cavity proposed for FCC by S. Gorgi Zadeh and M. Kranjčević which is optimized with respect to a different set of objective functions, including the robustness of the cavity against geometrical perturbations. In the calculation of E_{acc} the actual cavity length ($2L$) is considered.

Variable	$\mathrm{FCC}_{\mathrm{UROS1}}$	CESR-B	HL-LHC	LHC	$\mathrm{FCC}_{\mathrm{PR19}}$
R_{i} [mm]	156.0	150.0	150.0	150.0	153.704
L [mm]	120.0	150.0	140.0	160.0	137.1
A [mm]	70.0	103.750	104.0	104.0	53.582
B [mm]	70.0	103.750	104.0	104.0	53.582
a [mm]	25.0	25.0	25.0	25.0	36.683
b [mm]	25.0	25.0	25.0	25.0	36.683
R_{eq} [mm]	350.574	341.856	338.512	344.398	363.346
RF parameters	$\mathrm{FCC}_{\mathrm{UROS1}}$	CESR-B	HL-LHC	LHC	$\mathrm{FCC}_{\mathrm{PR19}}$
$f_{\mathrm{TE}_{111}}$ [MHz]	529.61	513.20	523.53	502.95	526.80
$f_{\mathrm{TM}_{110}}$ [MHz]	528.76	542.65	543.36	542.03	526.94
$R/Q_{\parallel,0}$ [Ω]	79.0	89.5	90.6	88.1	78.2
$R/Q_{\perp,\mathrm{TE}_{111}}$ [Ω]	2.3	5.5	4.6	6.3	3.2
$R/Q_{\perp,\mathrm{TM}_{110}}$ [Ω]	27.8	24.1	26.7	21.2	26.8
α [°]	102.8	104.9	99.0	109.5	109.2
$\frac{E_{\mathrm{pk}}}{E_{\mathrm{acc}}}$ [-]	1.9	2.0	2.0	2.0	1.8
$\frac{B_{\mathrm{pk}}}{E_{\mathrm{acc}}}$ $\left[\frac{\mathrm{mT}}{\mathrm{MV/m}}\right]$	4.1	4.2	4.0	4.4	4.7
$G \cdot R/Q_{\parallel,0}$ [kΩ^2]	15.5	21.8	21.3	22.2	15.0
$k_{\parallel}$ [V/pC] ($\sigma_z = 12.1\,\mathrm{mm}$)	0.116	0.141	0.136	0.146	0.119

functions. However, this is not crucial for the Z cavities as they will be operated at low E_{acc}, and thus the dynamical losses on the surface of the cavity would be small (see Figure 3.3). A low $R/Q_{\parallel,0}$, on the other hand, helps to decrease the detuning needed to counteract the reactive beam loading, which is considerably large for the Z-pole running (see (3.10)). The EM field profile on the surface and on the longitudinal axis of the $\mathrm{FCC}_{\mathrm{UROS1}}$ cavity is shown in Figure 4.12 (a). A comparison between the shape of the $\mathrm{FCC}_{\mathrm{UROS1}}$ cavity and the other single-cell cavities is demonstrated in

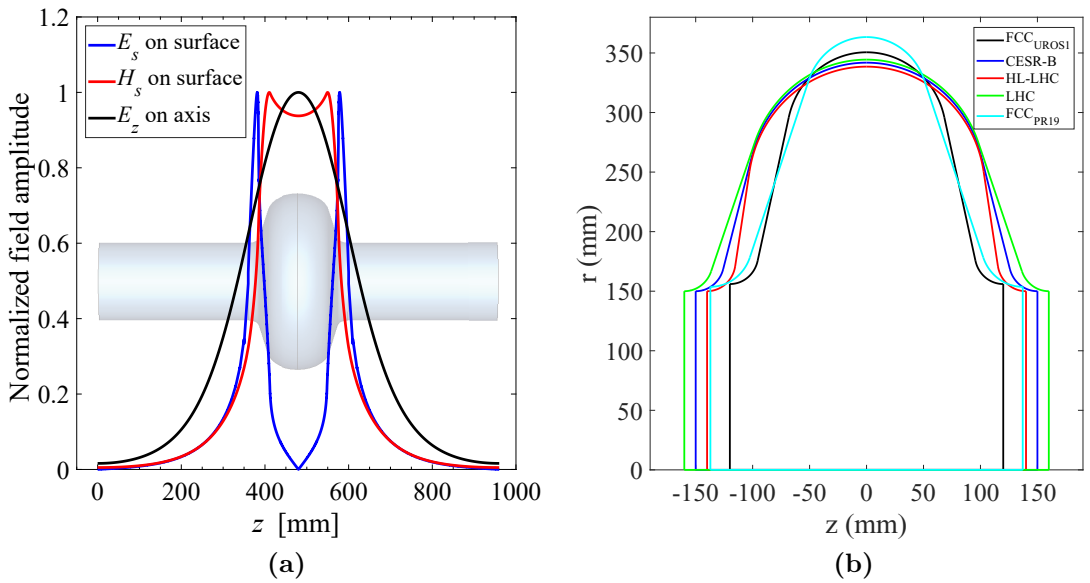

Figure 4.12: Field plot of the designed single-cell cavity (a) and a comparison between the surface profile of the designed cavity and some storage ring single-cell cavities (b).

Figure 4.12 (b). In comparison with the other designs, the $\text{FCC}_{\text{UROS1}}$ cavity has a larger R_{i} which results in a smaller loss factor, as shown in Table 4.5. A small equator size in the $\text{FCC}_{\text{UROS1}}$ and FCC_{PR19} designs results in a small value of $G \cdot R/Q_{\parallel,0}$. The longitudinal and transversal impedances of the single-cell cavities are shown in Figure 4.13. $\text{FCC}_{\text{UROS1}}$ and FCC_{PR19} have an analogous HOM spectrum due to rather similar objective functions used in their optimization. No longitudinal mode is trapped in the $\text{FCC}_{\text{UROS1}}$ and FCC_{PR19} cavities, and they have a rather small value of longitudinal impedance around 0.8 GHz (where typically the first higher order monopole passband exists). As shown in Figure 4.13 (b), the modes in the first dipole passband of the $\text{FCC}_{\text{UROS1}}$ and FCC_{PR19} cavities are coalesced, while for the other designs the TE_{111} and TM_{110} modes are distinctly separated and need special treatment during the HOM coupler design.

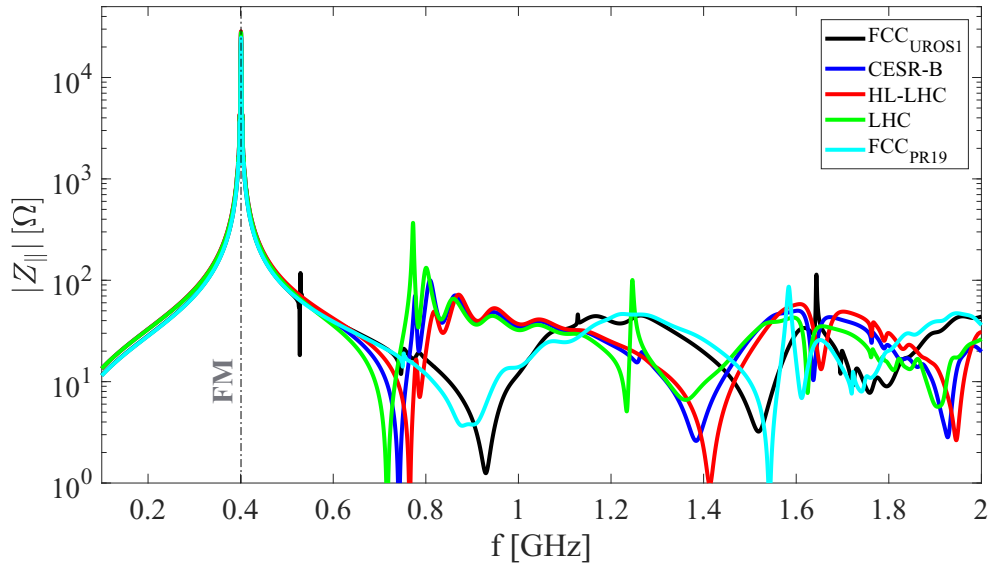

(a) Longitudinal impedance

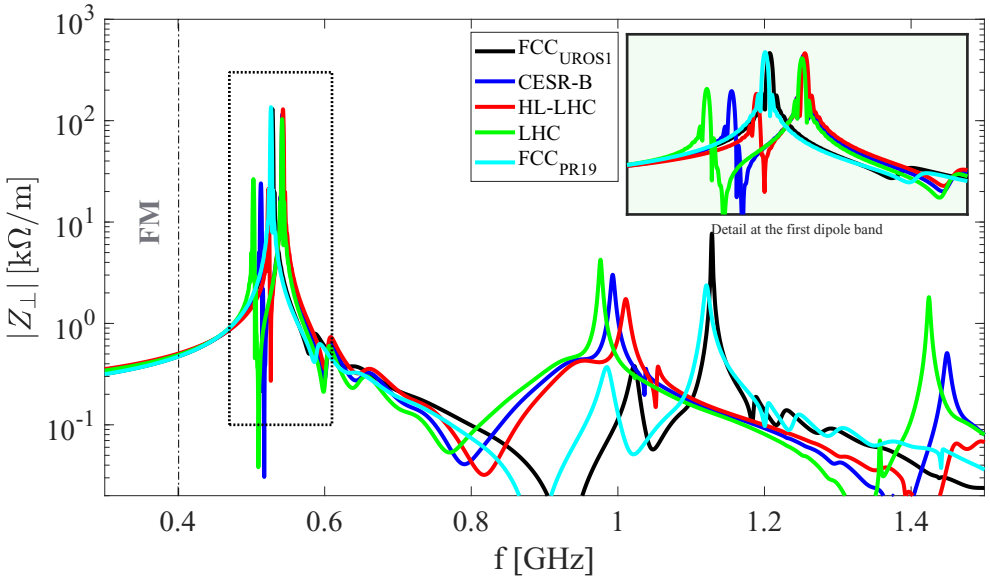

(b) Tranvsersal impedance

Figure 4.13: A comparison between the longitudinal and transversal impedance of the single-cell cavities. The impedances are calculated from a wake potential with a simulated wakelength of 200 m.

5 HOM coupler design

Chapter 4 outlined the design of a four-cell cavity at 400.79 MHz, a five-cell cavity at 801.58 MHz and a single-cell cavity at 400.79 MHz. When a bunch of charged particles passes through an accelerating cavity, it deposits electromagnetic energy into the surrounding structure. The resulting electromagnetic field, which is described by wake potential in the time domain and higher order modes in the frequency domain [23], can limit the operation of the accelerating cavity. These excited HOMs can interact with the following bunches and harm the beam stability by deflecting the beam. Extracting the HOM power from the SRF cavity is a challenging task as the power has to be removed at cryogenic temperature. Thus, efficient HOM damping mechanisms should be used to extract the energy of the HOMs from the cavity. In the first part of this chapter different conventional damping methods are briefly introduced. The HOM spectrum of the designed cavities is also studied and a suitable HOM damping mechanism is proposed for each case.

5.1 Different HOM damping mechanisms

Usually, one fundamental power coupler (or input coupler) and several HOM couplers are attached to the accelerating cavity. The role of the HOM couplers is to extract the energy of the HOMs from the cavity, while the input coupler has to feed power into the cavity and should optimally couple with the FM with a Q_{L} given in (3.11). Ideally, there should be no coupling between the FM and the HOM couplers. In other words, the FM should only have losses on the surface of the cavity and its damping by the HOM couplers should be zero. Conversely, the Q_{ext} of the HOMs should be as low as possible. Therefore, in superconducting cavities with a Q_0 in the order of 10^{10}, the external quality factor Q_{ext} usually determines the loaded quality factor Q_{L}.

In the vicinity of each resonance mode, the RF behavior of the cavity can be modeled by a parallel *RLC* circuit (see Figure 5.1 (a)). The resistive part determines the losses in the cavity, and the capacitor and the inductor determine the resonating behavior of the resonance mode with an oscillating frequency calculated by

$$\omega_n = \frac{1}{\sqrt{L_n C_n}}, \tag{5.1}$$

where L_n and C_n are the corresponding capacitance and inductance of mode n. The role of the HOM coupler is to add an extra mean of loss for the HOMs in the cavity

by adding $R_{\text{ext},n}$ (see Figure 5.1 (b)). The value of the $R_{\text{ext},n}$ should be as small as possible to make the losses in the cavity wall (in R_n) negligible compared to the losses in the HOM coupler (in $R_{\text{ext},n}$) [107].

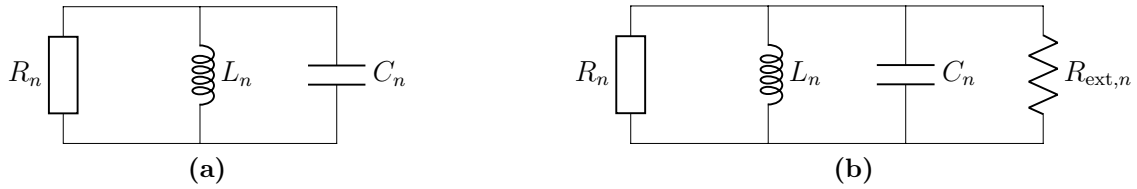

Figure 5.1: The cavity near a resonance mode can be described by a parallel RLC circuit. The HOM coupler adds an extra mean of loss to the HOMs ($R_{\text{ext},n}$).

The HOM coupler acts like a filter in the cavity; it has to efficiently couple with the HOMs and does not absorb the energy of the FM. Several damping mechanisms are designed and manufactured in the accelerator facilities based on the HOM damping requirements. The conventional HOM damping mechanisms are: beam pipe absorber (BPA), waveguide damper, and coaxial dampers. The dampers are typically placed on the exterior of the cavity in accordance with their different designs. Recent literature suggest on-cell dampers as a possible strong damping choice in single-cell cavities [74, 108]. Such dampers are waveguides that directly connect to the cell and absorb the energy of HOM at the site of origin inside the cell. Since such dampers are not fully explored yet and require more study, they are not considered in this thesis. In the following subsection, the aforementioned conventional damping methods are briefly introduced.

5.1.1 Beam pipe absorber

In this damping technique, part of the beam pipe is covered with dissipative material and the HOM fields are directed toward the absorbing load. The absorbers should have a broadband behavior and are made from materials such as ceramic tiles or lossy ferrites. The beam pipe absorbers designed for CESR and KEKB are shown in Figure 5.2 (a-b). These absorbers are capable of damping several kW of HOM power and are water-cooled at the room temperature outside the cryostat [109, 110].

In this damping method, the end cell of the cavity should be designed such that all HOM frequencies can pass the cutoff frequency limit of the beam pipe and propagate toward the absorbing load. Several beam pipe designs such as beam pipes with grooves or flutes are proposed in the literature to push the frequency of all of the HOMs above the cutoff frequency of the beam pipe [111, 112, 93]. A BPA has the advantage that it is rotationally symmetric and can damp the HOMs with different polarizations. Unlike the coaxial couplers, the BPA does not introduce any transversal kick to the beam. This damping scheme does not require additional ports on the

cavity or beam pipe, and thus mechanically has a simpler design than waveguide and coaxial couplers, and is also more robust against geometrical perturbations.

The BPA suffers from a few drawbacks. Most absorbers are made of brittle materials that can contaminate the cavities [113]. Furthermore, if the load of the BPA is above several hundreds of watts, the absorber is placed outside the cryostat to lower the cryostat load. This makes the placement of several cavities in one cryostat impractical, as a cold to warm transition is needed between the cavities [74]. Thus, the BPA increases the total length of the RF structure. Since a large number of cavities is required for the RF system of FCC-ee, the use of BPAs means a significant increase in the RF installation length. For this reason, this option is excluded in the following study. However, the BPA can be placed at the end of the cryomodules to damp the HOMs that leave the module via the end beam pipes.

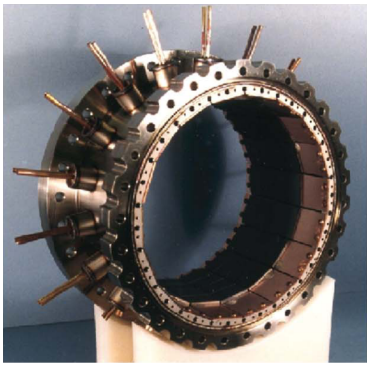

(a) BPA for CESR. Figure reproduced from [109]: ©[1999] IEEE.

(b) BPA for KEKB. Figure reproduced from [110].

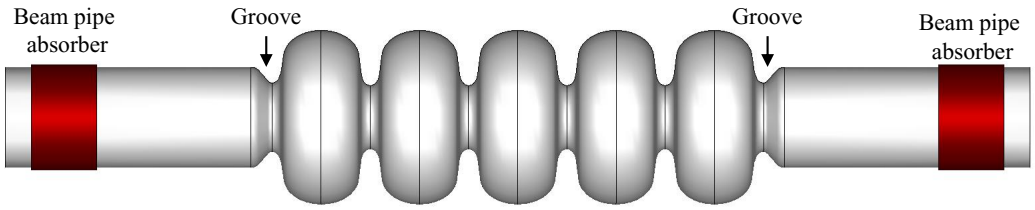

(c) A cavity with grooved beam pipe and beam pipe absorbers.

Figure 5.2: Room temperature BPAs capable of damping several kilowatts of HOM power as designed for CESR (a) and KEKB (b). The transition from the end cell to the beam pipe should be specially designed to allow the HOM to propagate through the beam pipe and get absorbed by the absorbers (c).

5.1.2 Waveguide HOM coupler

Waveguide HOM couplers transmit the HOM power via waveguides to an absorbing material at room or cryogenic temperature [114]. If the HOM power is small, the absorber can be installed in the helium bath. For example, in CEBAF the anticipated HOM power in the five-cell cavities was less than 1 mW. Placing the absorber in the helium vessel created less loss than the static heat loss that would have been generated if the absorbers had been installed at the room temperature. For this reason, the absorbers were installed in the helium bath at the end of the waveguide at 2 K [115, 116]. The Ampère class cavities designed at JLab for operation in ERLs and FELs were equipped with six waveguide couplers, i.e. five HOM couplers and one fundamental power coupler (see Figure 5.3). Each HOM absorber is capable of dissipating up to 4 kW (20 kW for the cavity). Due to the high HOM power in these cavities, the absorbers are installed at room temperature [117].

Waveguide couplers have a simple design and are less sensitive to geometrical perturbations than coaxial couplers. An FM rejection filter is not required, as the waveguide dimensions are specified such that the cutoff frequency of the first mode is above the FM of the cavity. Above the cutoff frequency, waveguides offer a broadband damping and are capable of damping a few kW of HOM power at room temperature. Furthermore, operational problems such as multipacting are less likely to occur in the waveguide HOM couplers in comparison to the coaxial couplers. The bulky shape of the waveguide couplers complicates the cryomodule design, as they take up a lot of space and also introduce a high heat load into the cryostat.

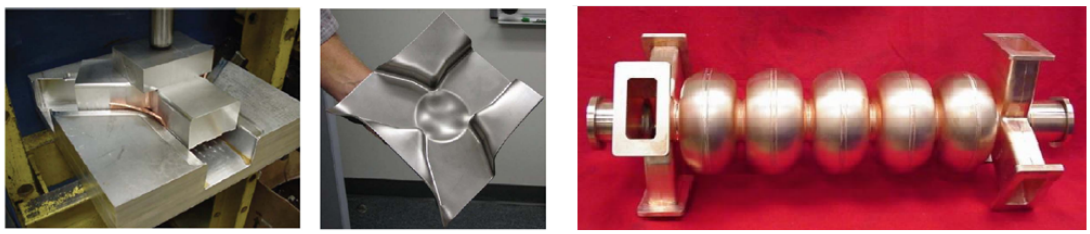

Figure 5.3: Niobium sheets are deep drawn (left) to form half of a three folded rectangular WG coupler (middle) [74] (©IOP Publishing. Reproduced with permission. All rights reserved). In the right picture, the WG coupler is electron-beam welded to a multi-cell cavity (figure is reproduced from [118] with author's permission).

5.1.3 Coaxial HOM coupler

Coaxial couplers work in a similar way to the waveguide couplers, i.e. they couple to the HOMs and do not couple to the FM. The TEM mode of a simple coaxial transmission line has no lower cutoff frequency, therefore the energy of the FM would be absorbed by such a coupler. Thus, the coaxial couplers are specifically designed

to include means of rejecting the FM. Furthermore, these couplers are designed to deliver high transmission behavior in frequencies where dangerous HOMs exist (modes with high beam impedance). Such couplers act like filters that have a low transmission at the FM frequency and a high transmission elsewhere. The compact design of such couplers has made them a favorable choice in many accelerating complexes.

However, some operational limitations must be dealt with when using coaxial HOM couplers. Multipacting is more likely to occur in the coaxial couplers than the other two damping methods. When the coaxial couplers are cooled down to the operating temperature, the notch at FM might be detuned and this could exceed the operational limits of the coupler. Such couplers are more sensitive to geometrical perturbations and manufacturing tolerances. The cooling down of such couplers is more challenging than of the other two damping methods [113].

To tackle the aforementioned problems, various coaxial couplers have been designed in the accelerating community. Figure 5.4 shows some of these couplers. Figure 5.4 (a) shows the coaxial hook-type coupler designed for the LHC [119]. This coupler has a narrow-band behavior and was specifically designed to damp the TE_{111} and TM_{110} modes of the LHC cavities. The hook-type coupler was used in combination with a probe-type coupler to cover a broad frequency range. The probe-type coupler is shown in Figure 5.4 (b), and was used in the LHC cavities for the damping of the HOMs at high frequencies (above the first dipole passband) [119]. The LHC couplers were designed for the handling of an HOM power of around 1 kW [113]. The HOM couplers were cooled with liquid helium ducted through the tubes of the coupler. Figure 5.4 (c) depicts a demountable version of the HOM coupler designed for the TESLA cavities. This design is a rescaled and modified version of the HOM coupler designed for the LEP cavities [107]. A welded version of the HOM coupler proposed for the TESLA cavities is shown in 5.4 (d). The advantages and disadvantages of each concept (welded or demountable) are discussed in [121]. A coaxial coupler that includes two notches for the FM rejection is proposed in [122]. The addition of a second notch increases the bandwidth at the FM and thus makes the rejection less sensitive to geometrical perturbations. This second notch leads to a more complex HOM coupler design, as shown in Figure 5.4 (e). The HOM coupler of the Double Quarter Wave (DQW) crab cavity used in the HL-LHC is shown in Figure 5.4 (f). The DQW coupler is detachable from the cavity and is internally cooled by liquid helium.

5.2 HOM Coupler optimization

The design and optimization of the coaxial HOM couplers is not a straight forward and intuitive procedure. The conventional approach to the simplification of the design is the modeling of the cavity and the coupler by a lumped element circuit.

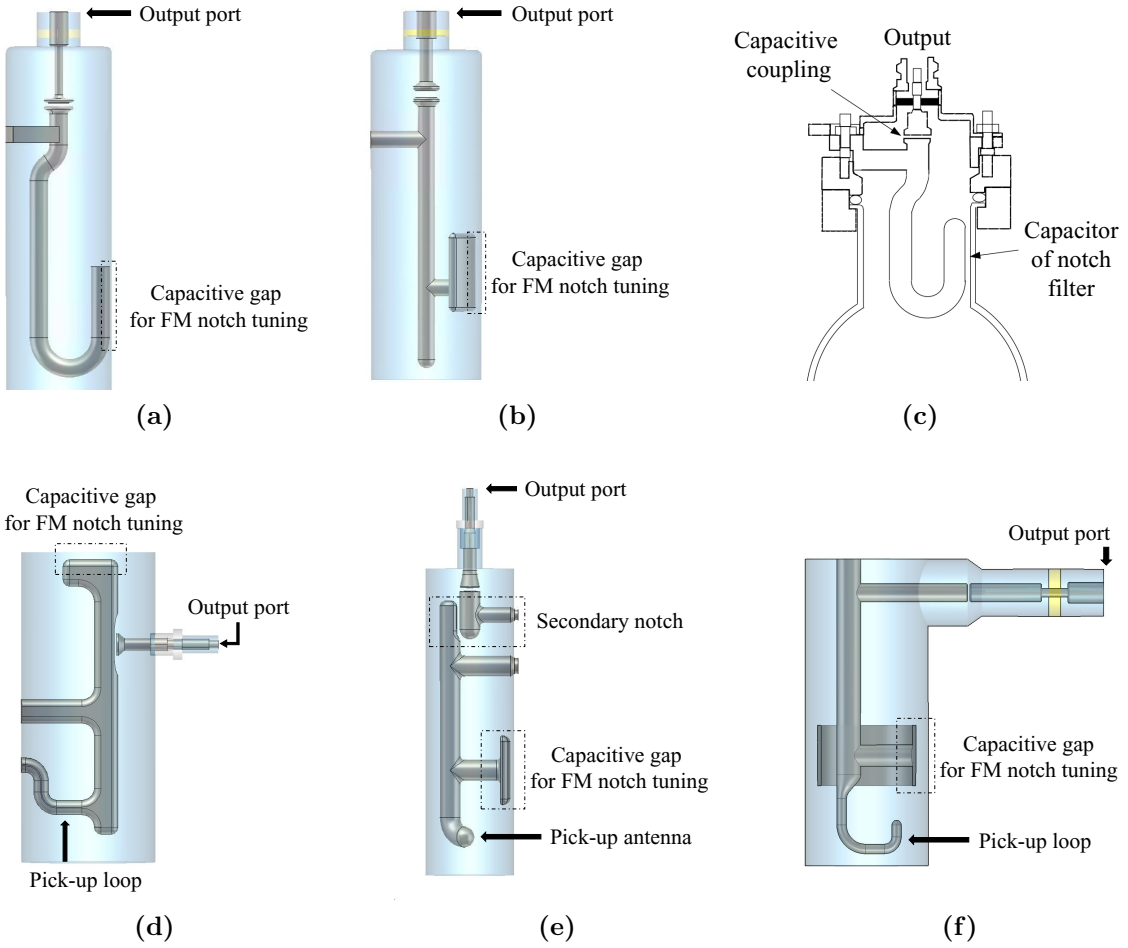

Figure 5.4: (a): Coaxial hook-type coupler developed for the LHC and specifically designed to damp the first dipole band [119, 120]. (b): Coaxial probe-type coupler designed for the LHC with a broad-band transmission behavior [119, 120]. (c): Demountable version of the TESLA coupler [121] (figure adapted from [65]: CC BY 3.0). (d): Welded version of the TESLA coupler [121]. (e) Double notch HOM coupler proposed for the Superconducting Proton Linac (SPL) [122]. (f) Cross-section of the DQW HOM coupler designed for the crab cavities of the HL-LHC [123].

The principles of filter design are then used to obtain the necessary transmission characteristics in the circuit model. In the end a 3D geometry is created on the basis of the circuit model and then fine-tuned. This approach provides an intuitive notion of the role of each segment of the coupler, e.g. straight rods can be modeled by coaxial transmission lines, the distance between surfaces can be modeled by capacitors and the inductive effect of straight sections that connect the inner conductor to the outer conductor can be modeled by inductors. The circuit model helps to optimize the circuit elements with conventional circuit simulators much faster than the 3D

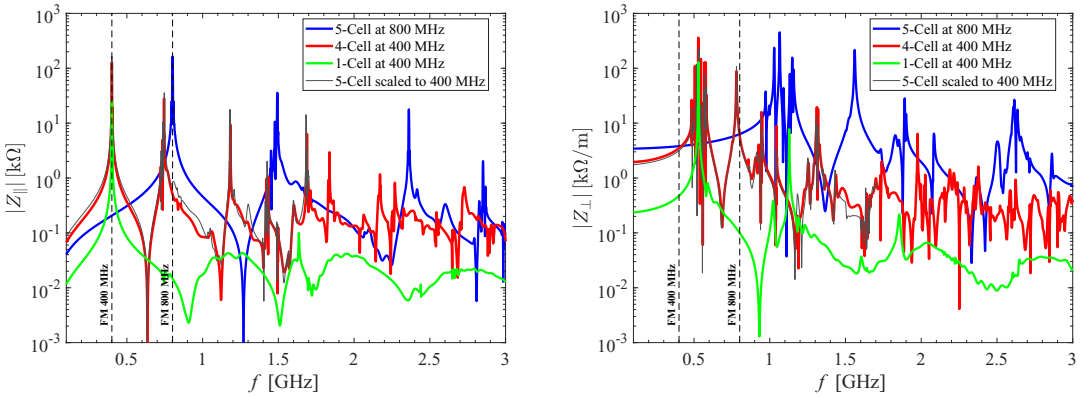

(a) Longitudinal impedance **(b)** Transversal impedance

Figure 5.5: The longitudinal and transversal impedance of the single-cell, four-cell and five-cell cavities. The impedance is calculated for the bare cavity (without couplers) and the peaks are not fully resolved due to the truncated wake potential. In addition, the impedance of the five-cell cavity is scaled from 800 MHz to 400 MHz for comparison.

electromagnetic solvers. A circuit modeling is also useful to identify which part in the 3D geometry is most effective in a certain frequency range. However, the circuit model has some disadvantages. The 3D design cannot be easily created from the lumped model and vice versa, especially in complicated geometries. Furthermore, the practical geometrical limitations, such as the size of the couplers, are not taken into account in the circuit model. A circuit modeling can provide a good starting point for the coupler design, and then the geometry can be fine-tuned using 3D electromagnetic solvers such as CST Microwave Studio® [51].

In the following subsections, the geometries of the hook-type, probe-type, DQW and waveguide HOM couplers are optimized to achieve high transmission at frequencies where a high level of longitudinal and transversal impedance exists in the cavities. The longitudinal and transversal impedance of the single-cell, four-cell and five-cell cavities that were optimized in the previous chapter are shown in Figure 5.5. In addition, the impedance of the five-cell cavity is scaled to 400 MHz for comparison with the other designs. The frequency of the FM is at 400.79 MHz for the single-cell and four-cell cavity, and it is at 801.58 MHz for the five-cell cavity. A high value of longitudinal impedance exists at the FM frequency as shown in Figure 5.5 (a). The other peaks correspond to the HOMs with high impedance values. These modes have to be damped using HOM couplers.

The impedance spectrum of the four-cell cavity is similar to the rescaled five-cell cavity. Therefore, the HOM couplers will be optimized on the basis of the spectrum of the four-cell cavity, and then the geometry of the couplers will be scaled to 800 MHz for the five-cell cavity. Note that at this stage the couplers are mainly

designed and evaluated from the damping point of view, and the mechanical and practical limitations such as multipacting or RF heating are not considered. The longitudinal impedances of the HOMs of the four-cell and rescaled five-cell cavity have a high value at around 745 MHz. There are several dipole modes from 485 MHz to 580 MHz with high transversal impedance. The largest transversal impedance of the four-cell cavity is located at around 530 MHz. Due to the large aperture radius, the dangerous monopole modes of the single-cell cavity are untrapped. This effect results in a small longitudinal impedance at high frequencies. The highest transversal impedance of the single-cell cavity is located at 529 MHz, which is close to the peak value of the transversal impedance of the four-cell and the rescaled five-cell cavity. Therefore, the HOM couplers designed to damp the first dipole passband of the four-cell cavity could also be used for the damping of the respective passband in the single-cell cavity.

5.2.1 Hook-type LHC coupler

The hook-type LHC coupler was designed to damp the TE_{111} and TM_{110} modes of the LHC cavities. The hook-type coupler and its equivalent circuit model are shown in Figure 5.6. This coupler has a loop as the coupling element. The HOM coupler can either couple via the magnetic field (inductive or loop coupling) or the electric field (electric or probe coupling) to the field inside the cavity. The electric coupling of the probe with the field inside the cavity induces a displacement current on the probe's surface which is represented by a current source in the equivalent circuit model of the coupler. In the magnetic coupling, a voltage is induced by the changing magnetic field that traverses the loop. In the case of loop-coupling, the induced voltage is represented by a voltage source in the equivalent circuit model. The gap capacitance $C_{\mathrm{h,n}}$ and the coupling loop $L_{\mathrm{h,n}}$ form the notch filter by resonating at the FM frequency of the cavity. At the resonance frequency, this series resonator is short circuited right at the beginning of the coupler and thus the energy of FM is not transmitted by the coupler to the load. The notch filter is interlinked with two other resonators that are coupled by the inductive element M_{h}. These two resonators are tuned to increase the impedance seen by the current source at the TE_{111} and TM_{110} mode frequencies, and thus to increase the extracted HOM power by the coupler at these two frequencies. In [124] the derivation of the parameters of the circuit model based on the damping requirements is studied extensively and thus will not be discussed here. The circuit parameters of the hook-type coupler designed for the HL-LHC cavities are given in [125]. The design presented in [125] is selected here as a reasonable starting point, and rescaled from 800 MHz to 400 MHz (the geometry is scaled by a factor of 2).

To optimize the HOM couplers, the whole computational domain should include the cavities and the HOM couplers. However, this is computationally expensive. The computational domain and subsequently the simulation time could be reduced

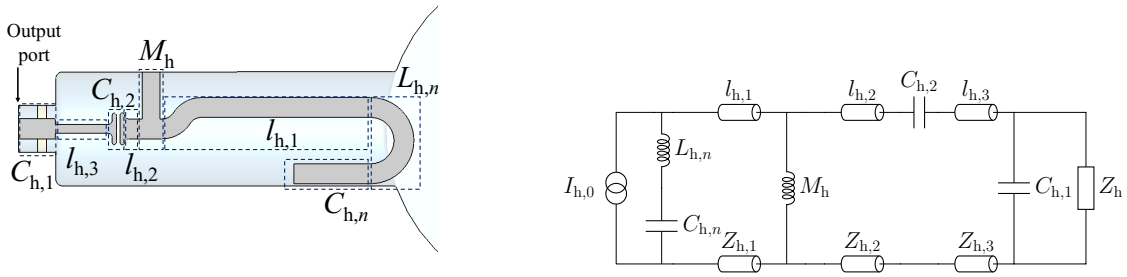

(a) Side view of the hook-type coupler

(b) Equivalent circuit of the hook-type coupler

Figure 5.6: Side view of the hook-type HOM coupler with its equivalent circuit model for electric coupling [125, 105, 126]. The straight rods of the coupler are modeled by coaxial transmission lines with a length of $l_{\mathrm{h},i}$ and a characteristic impedance of $Z_{\mathrm{h},i}$. Z_h is the characteristic impedance of the transmission line connected to the coupler (its standard value is $50\,\Omega$).

by considering only the couplers connected to the beam pipe. To achieve this, the geometry is cut at the intersection of the beam pipe with the cavity, and the intersection is terminated with a waveguide port (the cavity is not considered in the simulations). The TE_{111} and TM_{110} modes in the cavity cells couple to the TE_{11}-type of modes in the beam pipe. The FM of the cavity, on the other hand, couples to the TM_{01} mode in the beam pipe. The loop of the hook-coupler is oriented to be parallel to the magnetic field of the TM_{01} mode to exclude the magnetic coupling of the FM with the loop. The first three modes of the waveguide port connected to the beam pipe are shown in Figure 5.7. The transmission between two ports is studied: one port at the beam pipe which excites a field pattern resembling the fields inside the cavity and an output port at the end of the coupler (see Figure 5.6). Hereinafter in this chapter, we label the port at the beam pipe as port number 1 and the output port at the end of the coupler as port number 2. Since the first mode of the coaxial output port is a TEM mode (with no cutoff frequency), and the second mode lies at much higher frequency ranges, we only study the transmission between the modes of port 1 with the first mode of port 2.

The circuit model of the cavity is helpful to develop the general structure of the HOM coupler. Since all the details of the HOM coupler cannot be represented accurately by the lumped element circuit, the real 3D model should be used for the fine-tuning of the coupler. In this thesis we tune the HOM coupler by directly optimizing the geometry. The geometry of the hook-coupler is parameterized as shown in Figure 5.8. It is not possible to vary all parameters freely in the course of optimization and several practical limitations have to be taken into account. The diameter of the rod $r_{\mathrm{h},2}$ should be as large as possible to facilitate the fabrication of the hollow rod that can be internally cooled by liquid helium. To provide sufficient room inside the outer cylinder for the variation of other elements, the diameter $r_{\mathrm{h},6}$

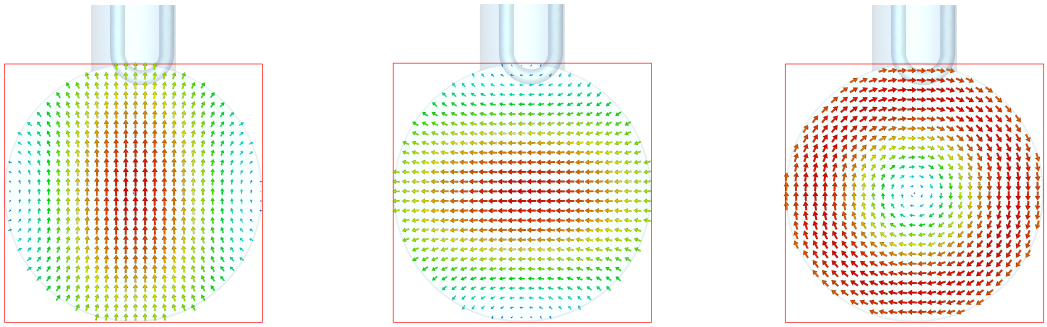

(a) TE_{11} mode **(b)** TE_{11} mode **(c)** TM_{01} omde

Figure 5.7: The first three modes of a circular waveguide. The electric field of the TE_{11} mode is shown in (a) and (b), and the magnetic field of the TM_{01} mode is shown in (c). The TE_{11} mode is a degenerated mode and thus has two polarizations.

is fixed at a moderate value of 103 mm. The ratio of $r_{h,5}$ and $r_{h,3}$ should yield a fixed impedance of 50 Ω to match with the impedance of the load (or impedance of the RF cables). The length $l_{h,6}$ plays no significant role as it is terminated with a matched load. The combination of $c_{h,1}$ and $d_{h,2}$ correspond to the $C_{h,n}$ element in the circuit model. By varying the capacitive behavior, the notch effect could be tuned to 400.79 MHz according to (5.1).

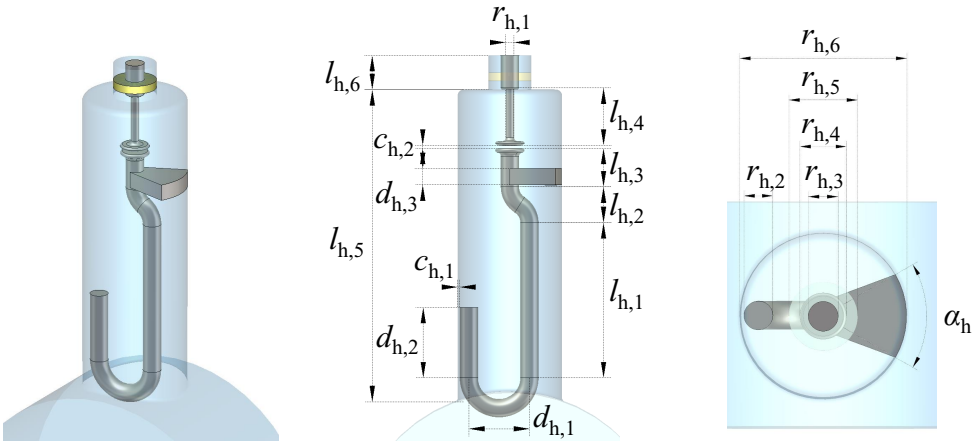

Figure 5.8: Parametrization of the hook-type LHC coupler.

In order to tune the HOM coupler, first the influence of each geometrical parameter on the transmission between ports is studied. The investigation of the transmission between ports is performed with the S-parameters [127]. Two S-parameters are of interest here: $S_{1(3),2(1)}$, which is the S-parameter between the third mode of port 1 and the first mode of port 2 (TM_{01}-TEM coupling) and $S_{1(2),2(1)}$, which is the S-parameter between the second mode of port 1 and the first mode of port 2

(TE_{11}-TEM coupling). Since the TE_{11} mode has two polarizations, the polarization that yields a higher transmission is studied.

Figure 5.9 shows the dependency of the S-parameters on some geometrical variables. The local sensitivity analysis is carried out by a one-dimensional parameter sweep over the values given in Table 5.1 (the final geometrical results after optimization). In the parameter sweep, one parameter is varied at a time while keeping the other parameters at their nominal values. The sensitivity of the S-parameters may change at different nominal values or by simultaneous variation of the geometrical parameters. Nonetheless, the one-at-a-time sensitivity analysis provides an understanding of the model mechanism, and also helps to identify the input variables with a major or minor impact on the outputs.

The main goal is to have a high value of $S_{1(2),2(1)}$ at frequencies between 485 MHz to 580 MHz with the peak at 530 MHz. The value of $S_{1(3),2(1)}$ should be as low as possible at 400.79 MHz. Some parameters change the behavior of the S-parameters globally (in the frequency domain), such as $l_{\mathrm{h},1}$, $d_{\mathrm{h},1}$ and $r_{\mathrm{h},6}$. When the length of the antenna (coaxial part of the coupler) is varied in the sensitivity analysis, the value of $l_{\mathrm{h},5}$ is varied by the same amount to maintain the penetration depth of the antenna into the beam pipe. Similarly, when $r_{\mathrm{h},6}$ is varied, $d_{\mathrm{h},1}$ is increased to keep the value of $c_{\mathrm{h},1}$ constant. The length of $l_{\mathrm{h},1}$ plays a major role in bringing the peaks of the $S_{1(2),2(1)}$ curve close to the frequency of interest without significantly changing the notch effect. A longer $d_{\mathrm{h},1}$ increases the inductive part of the notch and thus lowers the frequency of the notch (according to (5.1)). The parameter study was carried out with the frequency domain solver of CST Studio Suite®. Note that as mentioned earlier, the value of $r_{\mathrm{h},6}$ is fixed at 103 mm, therefore in the first step the other two parameters that have global influence, namely $l_{\mathrm{h},1}$ and $d_{\mathrm{h},1}$, are determined. After fixing the parameters with global influence, the parameters with local effects are changed.

Some parameters that have local effects are $c_{\mathrm{h},1}$, $d_{\mathrm{h},2}$, $r_{\mathrm{h},2}$, $l_{\mathrm{h},4}$, $c_{\mathrm{h},2}$ and α_{h}. The values of $c_{\mathrm{h},2}$, $l_{\mathrm{h},4}$ and α_{h} play a significant role in shaping the peaks of the $S_{1(2),2(1)}$ curve over the frequency range of interest. The values of the $c_{\mathrm{h},1}$ and $d_{\mathrm{h},2}$ parameters are used in the end to fine-tune the notch to 400.79 MHz. The geometrical parameters of the tuned coupler are given in Table 5.1.

Table 5.1: Geometrical parameters of the optimized hook-type coupler.

Parameter	$r_{\mathrm{h},1}$	$r_{\mathrm{h},2}$	$r_{\mathrm{h},3}$	$r_{\mathrm{h},4}$	$r_{\mathrm{h},5}$	$r_{\mathrm{h},6}$	$d_{\mathrm{h},1}$	$d_{\mathrm{h},2}$	$d_{\mathrm{h},3}$
Unit	[mm]	[mm]	[mm]	[mm]	[mm]	[mm]	[mm]	[mm]	[mm]
Value	8.0	18.0	18.4	28.8	42.4	103	59.8	69.4	8.0
Parameter	$l_{\mathrm{h},1}$	$l_{\mathrm{h},2}$	$l_{\mathrm{h},3}$	$l_{\mathrm{h},4}$	$l_{\mathrm{h},5}$	$l_{\mathrm{h},6}$	$c_{\mathrm{h},1}$	$c_{\mathrm{h},2}$	α_{h}
Unit	[mm]	[mm]	[mm]	[mm]	[mm]	[mm]	[mm]	[mm]	[°]
Value	153	35.34	38	55.58	307.93	33.6	2.0	3.0	60

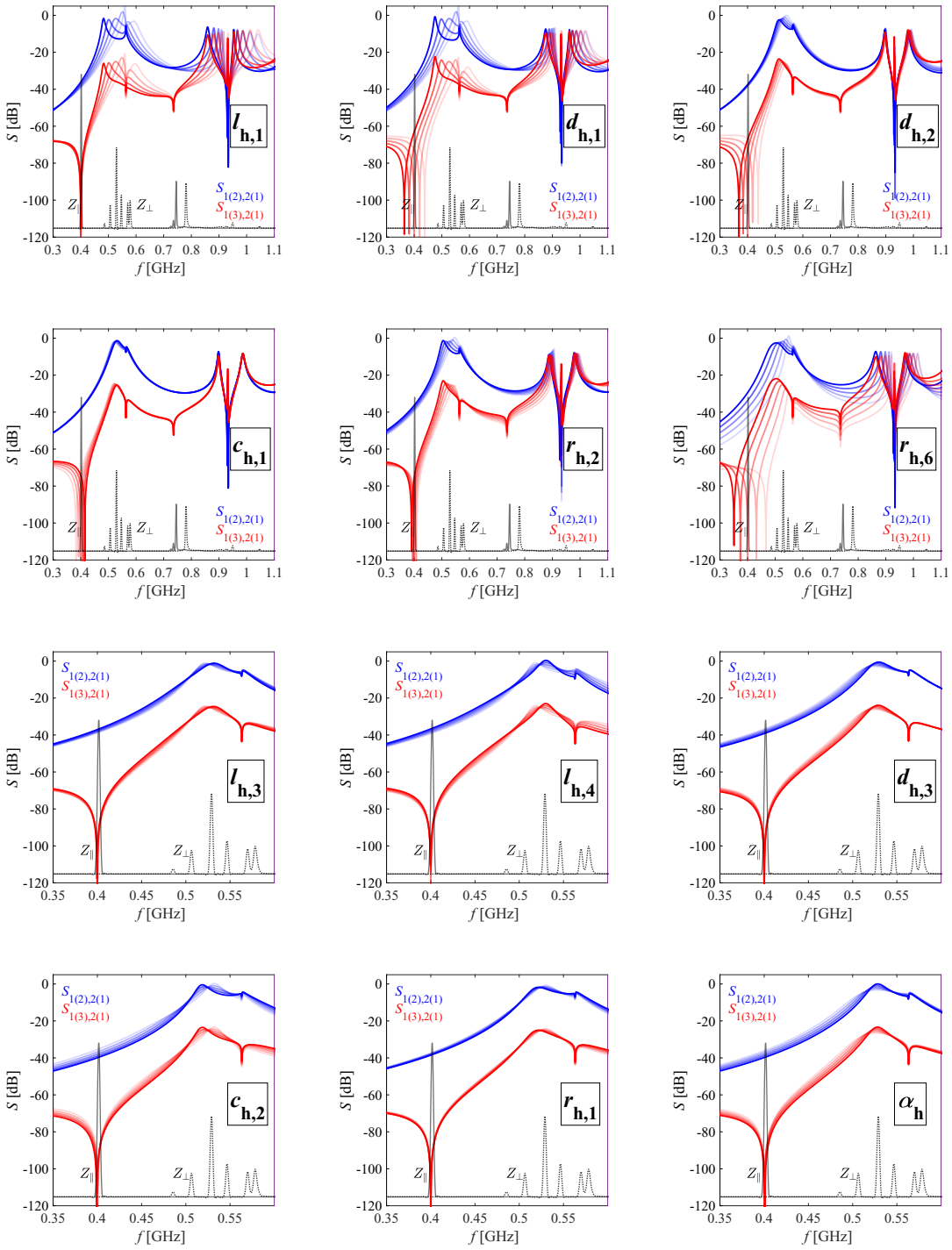

Figure 5.9: Dependency of the S-parameters on the geometrical parameters of the hook-type coupler as depicted in Figure 5.8. All the geometrical parameters (except $d_{\mathrm{h},1}$) are varied from −20% (light color) to 20% (dark color) around the nominal values given in Table 5.1. Due to the lack of space, $d_{\mathrm{h},1}$ is varied from −10% to 10%. The longitudinal and transversal impedance of the four-cell cavity are shown as black curves for reference.

5.2.2 Probe-type LHC coupler

The probe-type coupler was used as a broad-band damper in the accelerating cavities of the LHC to cover large frequency ranges from roughly 700 MHz to 1300 MHz [124]. The probe-type coupler and its equivalent circuit are shown in Figure 5.10. This coupler uses a probe to couple with the electric field of the cavity which is modeled by a current source. If the real part of the impedance seen by the current source is increased, a higher amount of HOM power is absorbed by the HOM coupler.

The coupler is composed of three resonant circuits that cover a wide frequency range. The first resonant circuit is composed of $l_{\mathrm{p},1}$, $L_{\mathrm{p},n}$ and $C_{\mathrm{p},n}$. The transmission line $l_{\mathrm{p},1}$ functions like a quarter-wave impedance transformer that increases the real part of the impedance seen by the field of the cavity. The $L_{\mathrm{p},n}$ and $C_{\mathrm{p},n}$ parameters provide the notch effect to reject the FM. The straight section $l_{\mathrm{p},2}$ resembles a half-wave transformer that connects via M_{p} to the third resonant circuit $l_{\mathrm{p},3}$, $C_{\mathrm{p},3}$ and $l_{\mathrm{p},4}$. The derivation of the circuit parameters is given in detail in [124] and thus is not discussed here. A rescaled version of the model presented in [125] is used here as the initial design for further study and optimization. Instead of optimizing the probe coupler on the basis of the circuit model, the geometry is directly parameterized and optimized. A parameterized model of the probe coupler is shown in Figure 5.11. Again, the transmissions between the first three modes of port 1 (two TE_{11} modes and one TM_{01} mode) and the TEM mode of port 2 are studied.

The sensitivity of the S-parameters with respect to the geometrical parameters, around the values given in Table 5.2, is shown in Figure 5.12. As can be seen, this coupler is not suitable for damping the first dipole passband. The aim here is to have a high transmission (high $S_{1(3)2(1)}$) at the first monopole HOM passband, which is located at around 745 MHz, and also to have a notch at 400.79 MHz.

Similar to the hook-type coupler, the diameter of the rods $r_{\mathrm{p},1}$, $r_{\mathrm{p},2}$ and $r_{\mathrm{p},8}$ should be large enough to ease the fabrication of the inner tubes for internal cooling. The outer diameter of the cylinder $r_{\mathrm{p},7}$ is fixed at 103 mm here too. For any change in the values of $l_{\mathrm{p},1}$, $l_{\mathrm{p},2}$, $l_{\mathrm{p},3}$, $l_{\mathrm{p},4}$ and $c_{\mathrm{p},1}$, the value of $l_{\mathrm{p},7}$ was changed automatically to maintain the same penetration depth of the coupler into the beam pipe. The values of $d_{\mathrm{p},1}$, $c_{\mathrm{p},2}$ and α_{p} change the capacitance $C_{\mathrm{p},n}$ as shown in Figure 5.10, and thus have a high impact on the notch at FM frequency. Similarly, the parameter $r_{\mathrm{p},8}$ affects the inductive part of the FM filter, i.e. $L_{\mathrm{p},n}$. Tuning the notch to the FM frequency with $r_{\mathrm{p},8}$ is not suitable because it also affects the peak values around the first monopole passband. Therefore, the notch is tuned by varying the capacitive part of the FM filter. The values of $r_{\mathrm{p},3}$ and $r_{\mathrm{p},6}$ should deliver a 50 Ω coaxial line impedance. The parameter $l_{\mathrm{p},5}$ has no impact on the results, as the coupler is terminated with a waveguide port with matched impedance.

Some of the variables that have global influence on the S-parameters are $l_{\mathrm{p},1}$, $l_{\mathrm{p},2}$ and $r_{\mathrm{p},5}$. First, these variables are varied with the parameter sweep tool of CST Studio Suite® to obtain a high $S_{1(3)2(1)}$ transmission at around 745 MHz. Then the

variables with local influence such as $r_{\mathrm{p},1}$, $r_{\mathrm{p},2}$, $l_{\mathrm{p},4}$ and $c_{\mathrm{p},1}$ are used for the fine-tuning. The values of $d_{\mathrm{p},1}$ and $c_{\mathrm{p},2}$ are changed last in order to tune the notch at 400.79 MHz. The list of parameters of the optimized coupler is given in Table 5.2.

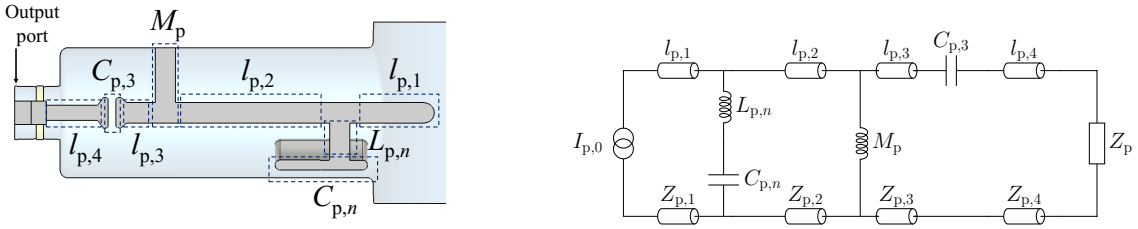

(a) Side view of the probe-type coupler **(b)** Equivalent circuit of the probe-type coupler

Figure 5.10: Side view of the probe-type HOM coupler with its equivalent circuit model for electric coupling [125, 105, 126]. The straight rods of the coupler are modeled by coaxial transmission lines with a length of $l_{\mathrm{p},i}$ and a characteristic impedance of $Z_{\mathrm{p},i}$. Z_{p} is the characteristic impedance of the transmission line connected to the coupler.

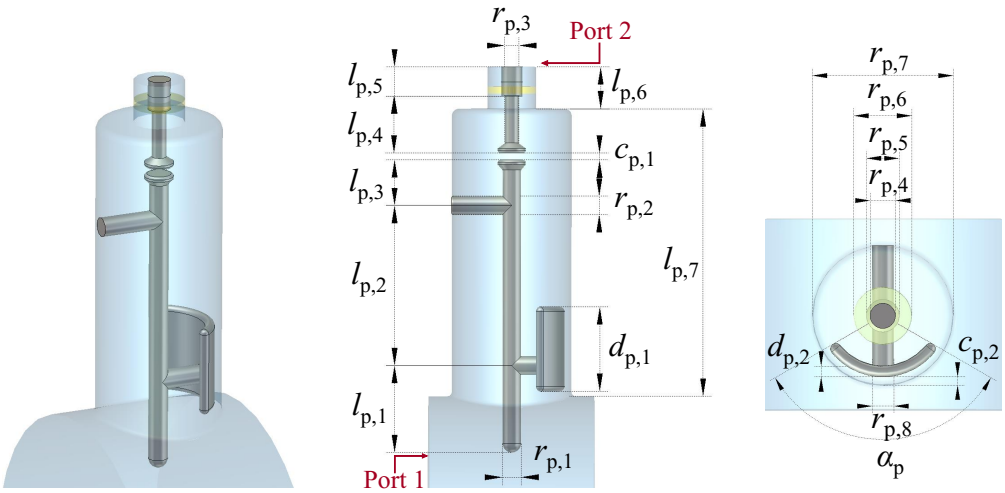

Figure 5.11: Parametrization of the probe-type LHC coupler.

Table 5.2: Geometrical parameters of the optimized probe-type coupler.

Parameter	$r_{\mathrm{p},1}$,$r_{\mathrm{p},2}$,$r_{\mathrm{p},8}$	$r_{\mathrm{p},3}$	$r_{\mathrm{p},4}$	$r_{\mathrm{p},5}$	$r_{\mathrm{p},6}$	$r_{\mathrm{p},7}$	$d_{\mathrm{p},1}$	$d_{\mathrm{p},2}$	α_{p}
Unit	[mm]	[mm]	[mm]	[mm]	[mm]	[mm]	[mm]	[mm]	[°]
Value	16.0	12.0	18.4	24	42.4	103	72.5	8.0	120
Parameter	$l_{\mathrm{p},1}$	$l_{\mathrm{p},2}$	$l_{\mathrm{p},3}$	$l_{\mathrm{p},4}$	$l_{\mathrm{p},5}$	$l_{\mathrm{p},6}$	$l_{\mathrm{p},7}$	$c_{\mathrm{p},1}$	$c_{\mathrm{p},2}$
Unit	[mm]	[mm]	[mm]	[mm]	[mm]	[mm]	[mm]	[mm]	[mm]
Value	74.8	137.6	39	49	25	36	247	6.0	6.0

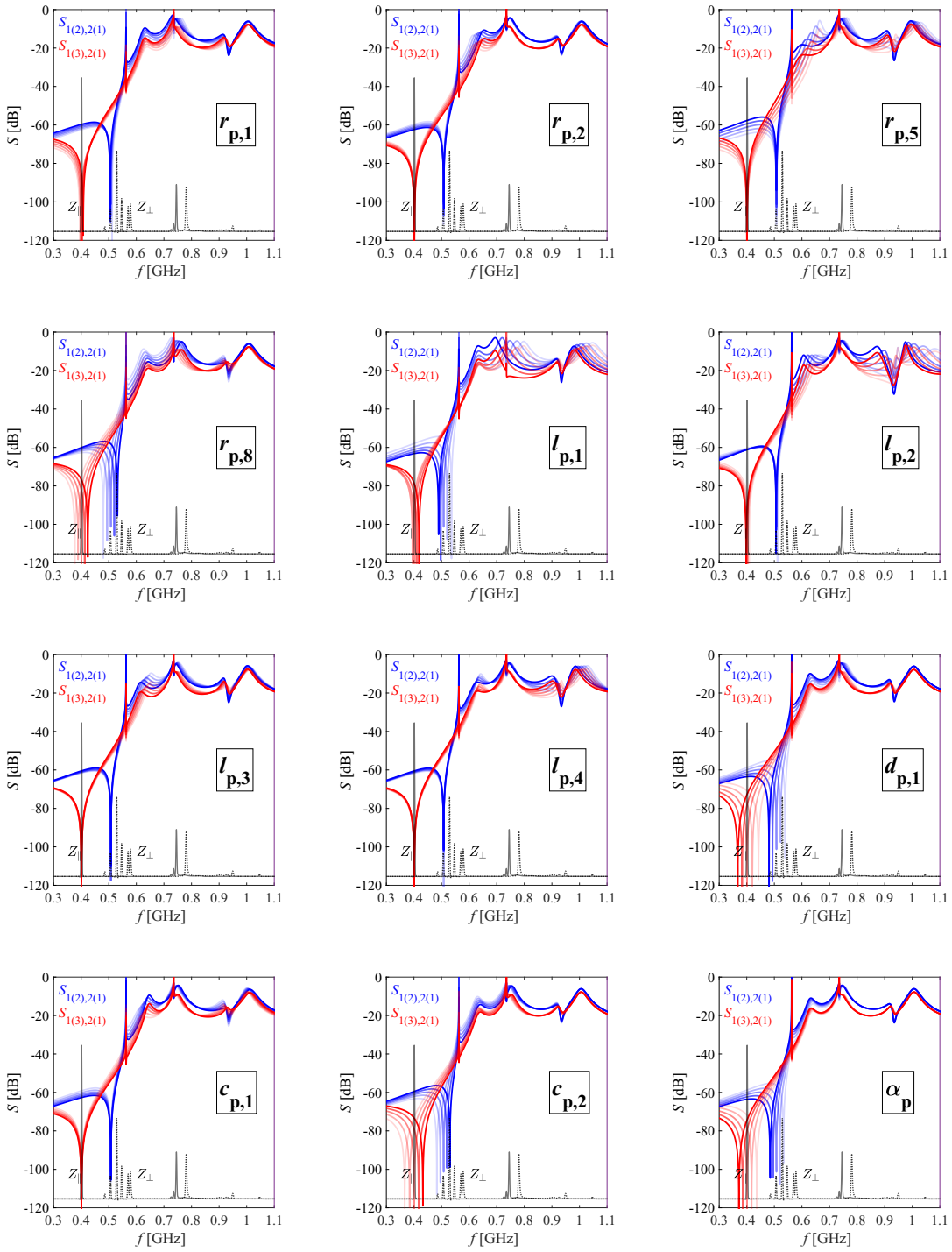

Figure 5.12: Dependency of the S-parameters on the geometrical parameters of the probe-type coupler as depicted in Figure 5.11. The geometrical parameters are varied from −20% (light color) to 20% (dark color) around the nominal values given in Table 5.2. The longitudinal and transversal impedance of the four-cell cavity are shown as black curves for reference.

5.2.3 DQW HOM coupler

The DQW HOM coupler is designed for the HOM damping of the crab cavities used in the HL-LHC project [123, 128]. The coupler has a right angle due to the height restrictions imposed on the design. A parameterized model of the coupler is shown in Figure 5.13. The hook resembles an *LC* circuit that is connected to the capacitive jacket with the small transmission line $l_{\mathrm{d},2}$. The notch effect of the coupler is tuned via the *LC* effect of a cylindrical jacket that is located above the hook and is connected to the central rod with a stub. A transmission line ($l_{\mathrm{d},3}$) follows the capacitive jacket and is coupled to the rest of the coupler via the inductive effect of $l_{\mathrm{d},4}$. In the following optimization the hook of the coupler is oriented perpendicular to the magnetic field of TM_{01} of the beam pipe. This orientation has shown to improve the damping of the monopole modes.

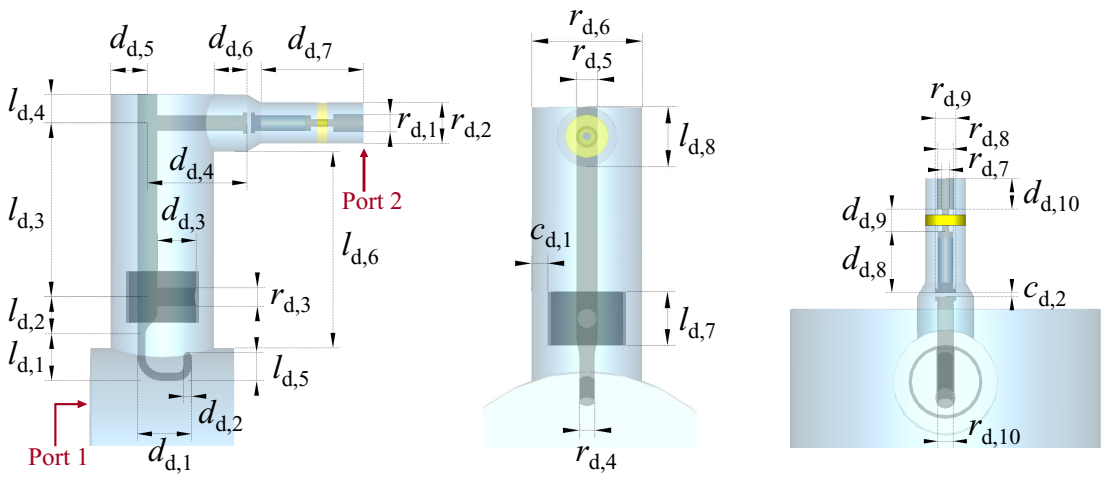

Figure 5.13: Parametrization of the DQW HOM coupler. A circuit model of the coupler is given in [129].

The sensitivity of the S-parameters with respect to the geometrical parameters is shown in Figures 5.14 and 5.15. The sensitivity analysis is carried out around the values given in Table 5.3. In the first step of the geometry optimization, the parameters that have global influence on the S-parameters, such as $d_{\mathrm{d},1}$, $d_{\mathrm{d},4}$, $d_{\mathrm{d},5}$ and $l_{\mathrm{d},3}$, are tuned. The value of $l_{\mathrm{d},3}$ significantly influences the location of the second peak of $S_{1(3),2(1)}$. Since a heavy damping of monopole modes at 745 MHz is aimed for, the value of $l_{\mathrm{d},3}$ is increased to bring the second peak of $S_{1(3),2(1)}$ to 745 MHz. This results in a longer coupler in comparison to the original design used for crab cavities. In the next step, the parameters with local effects, such as $c_{\mathrm{d},2}$, $l_{\mathrm{d},4}$, $l_{\mathrm{d},5}$, $l_{\mathrm{d},8}$ and $r_{\mathrm{d},10}$, are varied to fine-tune the design at the first dipole band. In this respect, the capacitive behavior induced by $c_{\mathrm{d},2}$ (and $r_{\mathrm{d},9}$) is of particular importance, as it significantly changes the shape and location of the peaks of $S_{1(2),2(1)}$

at the first dipole band. The values of $c_{\mathrm{d},1}$, $l_{\mathrm{d},7}$ and $r_{\mathrm{d},3}$ are changed to tune the notch at 400.79 MHz. The parameter $r_{\mathrm{d},3}$ changes the inductive effect of the notch, $l_{\mathrm{d},7}$ changes the capacitive effect, and $c_{\mathrm{d},1}$ changes both the capacitive and the inductive effects. For a fixed jacket thickness and a fixed tube radius, a smaller $c_{\mathrm{d},1}$ demands a larger $d_{\mathrm{d},3}$, which in turn increases the inductive effect of $d_{\mathrm{d},3}$, and both contribute to the lowering of the notch frequency in accordance with (5.1).

The ratio of $r_{\mathrm{d},2}$ to $r_{\mathrm{d},1}$ has to yield a 50 Ω line impedance. The value of $d_{\mathrm{d},10}$ has no significant influence on the S-parameters. The reason is that port 2 is matched to an impedance of 50 Ω, emulating an infinitely long transmission line. The parameter $l_{\mathrm{d},6}$ determines the penetration depth of the coupler into the beam pipe. Larger penetration depth (smaller $l_{\mathrm{d},6}$) results in a stronger damping. However, it gives rise to higher surface losses on the coupler at the FM frequency, and also to a higher transverse kick applied by the coupler to the beam.

One advantage of the DQW HOM coupler is that it can simultaneously provide a good damping of the first higher order monopole and dipole passband, whereas two different types of HOM couplers were needed in the LHC couplers, i.e. the probe-type and the hook-type coupler. The list of parameters of the optimized DQW HOM coupler is given in Table 5.3.

Table 5.3: Geometrical parameters of the optimized DQW coupler as shown in Figure 5.13.

Parameter	$d_{\mathrm{d},1}$	$d_{\mathrm{d},2}$	$d_{\mathrm{d},3}$	$d_{\mathrm{d},4}$	$d_{\mathrm{d},5}$	$d_{\mathrm{d},6}$	$d_{\mathrm{d},7}$	$d_{\mathrm{d},8}$	$d_{\mathrm{d},9}$	$d_{\mathrm{d},10}$
Value [mm]	54.0	8.0	38.5	99.5	36.5	33.0	102.0	60.0	22.0	30.0
Parameter	$l_{\mathrm{d},1}$	$l_{\mathrm{d},2}$	$l_{\mathrm{d},3}$	$l_{\mathrm{d},4}$	$l_{\mathrm{d},5}$	$l_{\mathrm{d},6}$	$l_{\mathrm{d},7}$	$l_{\mathrm{d},8}$	$c_{\mathrm{d},1}$	$c_{\mathrm{d},2}$
Value [mm]	46.0	36.0	170.0	28.0	28.0	192.0	50.4	56.0	15.0	2.0
Parameter	$r_{\mathrm{d},1}$	$r_{\mathrm{d},2}$	$r_{\mathrm{d},3}$	$r_{\mathrm{d},4}$	$r_{\mathrm{d},5}$	$r_{\mathrm{d},6}$	$r_{\mathrm{d},7}$	$r_{\mathrm{d},8}$	$r_{\mathrm{d},9}$	$r_{\mathrm{d},10}$
Value [mm]	17.4	40.0	18.0	14.4	20.0	103.0	7.2	15.2	15.2	15.2

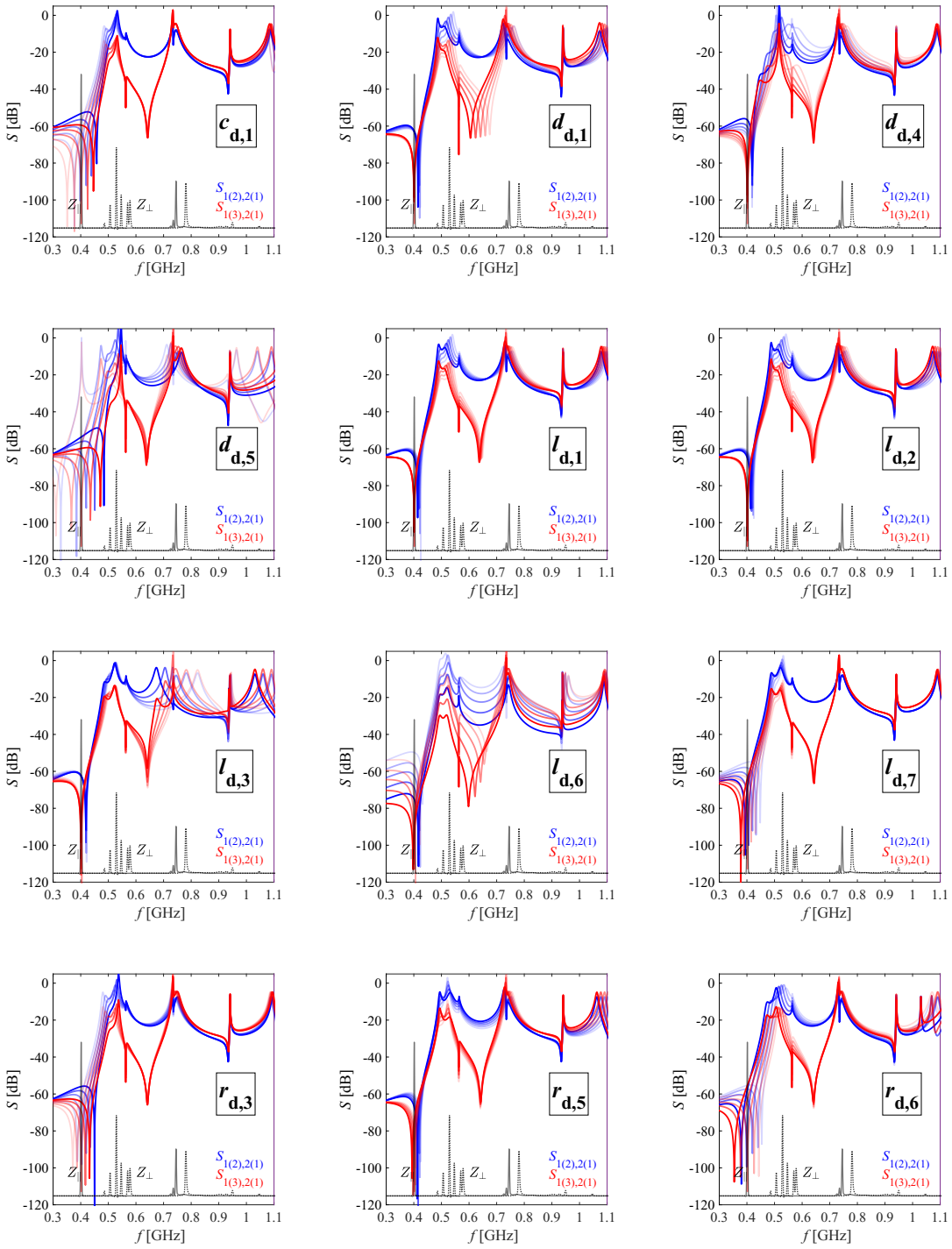

Figure 5.14: Dependency of the S-parameters on the geometrical parameters of the DQW coupler as parameterized in Figure 5.13. All of the geometrical parameters (except $r_{d,6}$) are varied from −20% (light color) to 20% (dark color) around the nominal values given in Table 5.1. The parameter $r_{d,6}$ is varied from −10% to 10%, and the value of $d_{d,3}$ is changed in parallel to maintain the same capacitive distance $c_{d,1}$. The longitudinal and transversal impedance of the four-cell cavity are shown as black curves for reference.

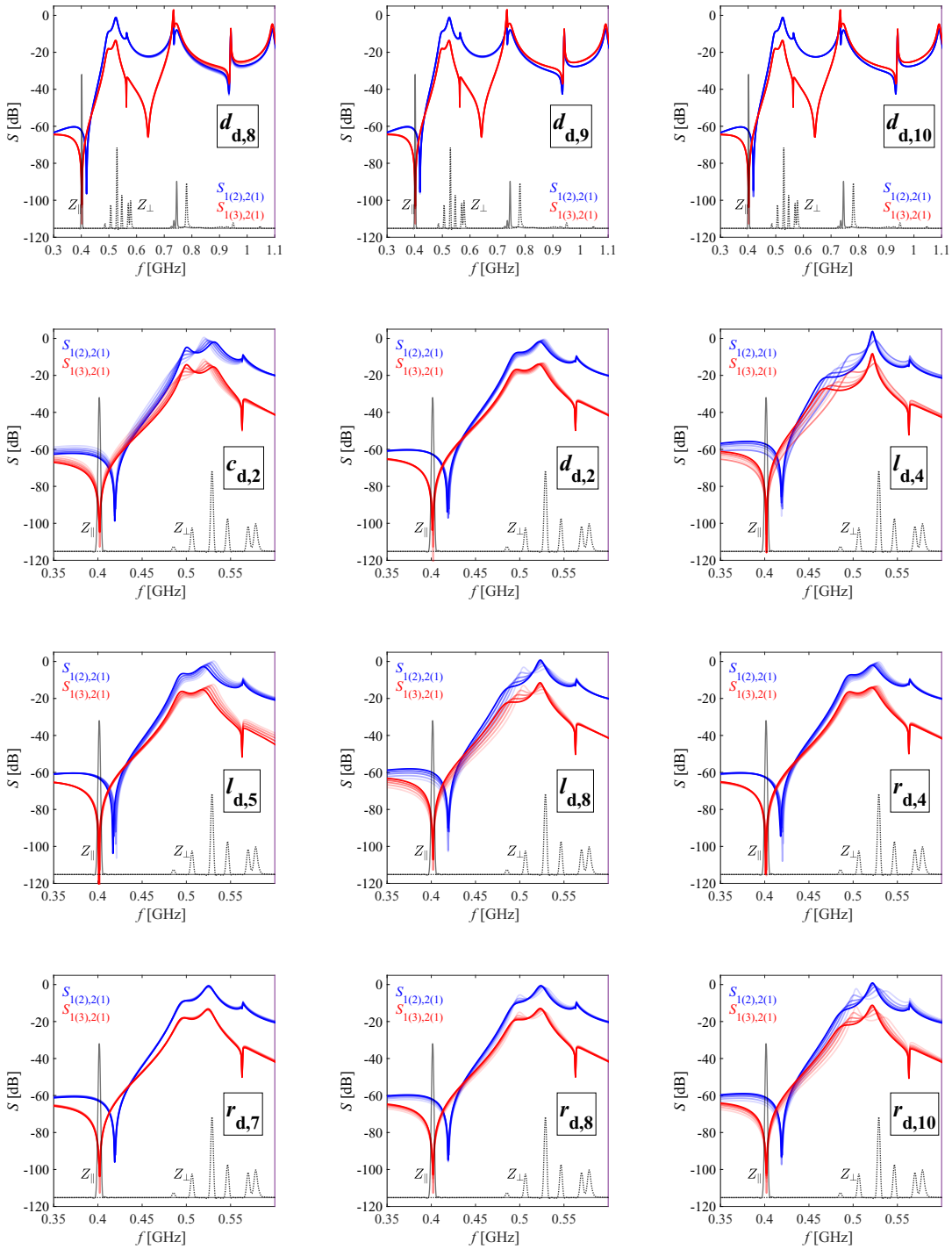

Figure 5.15: Dependency of the S-parameters on the geometrical parameters of the DQW coupler as parameterized in Figure 5.13. All the geometrical parameters (except $l_{d,4}$) are varied from -20% (light color) to 20% (dark color) around the nominal value given in Table 5.1. The parameter $l_{d,4}$ is varied from 0% to 40%. The longitudinal and transversal impedance of the four-cell cavity are shown as black curves for reference.

5.2.4 Waveguide HOM coupler

The dimensions of the waveguide HOM coupler are usually determined such that the fundamental cutoff frequency of the waveguide is larger than the frequency of the FM of the cavity and smaller than the frequency of the HOMs. The cutoff frequency of the TE_{mn} and the TM_{mn} modes of a rectangular waveguide (RWG) with the dimensions a_{wg} and b_{wg} (assuming $b_{wg} \leq a_{wg}$) are calculated by [130, p. 113]

$$f_{cut} = \frac{1}{2\pi\sqrt{\varepsilon\mu}}\sqrt{\left(\frac{m\pi}{a_{wg}}\right)^2 + \left(\frac{n\pi}{b_{wg}}\right)^2}, \tag{5.2}$$

where m is the number of half-wavelength variations in the a_{wg} direction, n is the number of half-wavelength variations in the b_{wg} direction, ε is the electric permittivity and μ is the magnetic permeability inside the waveguide. For the TE_{mn} modes, m and n can be any non-negative integer number ($m = 0, 1, 2, \ldots$ and $n = 0, 1, 2, \ldots$) but both cannot be simultaneously zero, i.e. TE_{00} does not exist. The parameters m and n are positive integers for the TM_{mn} modes, i.e. $m = 1, 2, \ldots$ and $n = 1, 2, \ldots$. The TE_{10} mode ($m = 1$ and $n = 0$) has the lowest cutoff frequency and is called the dominant mode of the RWG. At any given operating frequency, only modes with a cutoff frequency smaller than the working frequency can propagate into the waveguide and the modes with a higher cutoff frequency exponentially decay in the waveguide [130, p. 113].

The cutoff frequencies of the first few modes of a RWG with respect to the side dimension a_{wg} (assuming $b_{wg} = a_{wg}/2$) are plotted in Figure 5.16 (a). The cutoff frequency of the TE_{10} and TE_{20} modes do not depend on b_{wg}, therefore, for a fixed value of a_{wg}, the distance between these two cutoff frequencies determines the maximum achievable bandwidth for the single-mode operation. For large values of b_{wg} ($b_{wg} > a_{wg}/2$), the single-mode bandwidth is limited by the frequency of the TE_{01} mode. In many standard waveguides an aspect ratio of 2:1 is selected ($b_{wg} = a_{wg}/2$) to obtain the maximum bandwidth for the single-mode operation. For a larger aspect ratio ($b_{wg} < a_{wg}/2$) the bandwidth remains the same but the power that can propagate into the waveguide is decreased due to the reduced cross-section size.

The waveguides could be used as HOM couplers in the accelerating cavities. In such an application, the waveguide is overmoded, and all modes excited by the beam traversing the cavity, except the FM, have to propagate into the waveguide. As previously stated, the modes in the first dipole passband of the cavity couple to the TE_{11} mode of the beam pipe as shown in Figure 5.7 (a-b). If a waveguide with an aspect ratio of 2:1 connects to a beam pipe (e.g., Figure 5.19 (a)), the damping of the degenerate TE_{11} mode excited in the beam pipe will depend on its polarization angle. Normally, one polarization of the TE_{11} mode in the beam pipe couples to the TE_{10} mode of the waveguide and propagates to it. The other polarization, on the other hand, couples very weakly to the waveguide's TE_{10} mode, and can only

propagate into the waveguide at frequencies above the cutoff frequency of the TE_{01} mode. Therefore, several waveguides with different mounting angles are usually attached to the beam pipe to efficiently damp different polarizations of the HOMs, and also to increase the extracted HOM power. Another solution is to lower the cutoff frequency of the TE_{01} mode by increasing the width b_{wg} of the RWG. For an aspect ratio of 1:1 ($a_{wg} = b_{wg}$), the cutoff frequencies of the TE_{10} and TE_{01} modes become equal, as shown in Figure 5.16 (b). However, this type of square-shaped waveguide is very bulky and occupies a large space in the module, especially at low frequencies. Furthermore, the large width of the waveguide can result in the trapping of modes between the waveguide and beam pipe with a frequency close to the waveguide cutoff frequency.

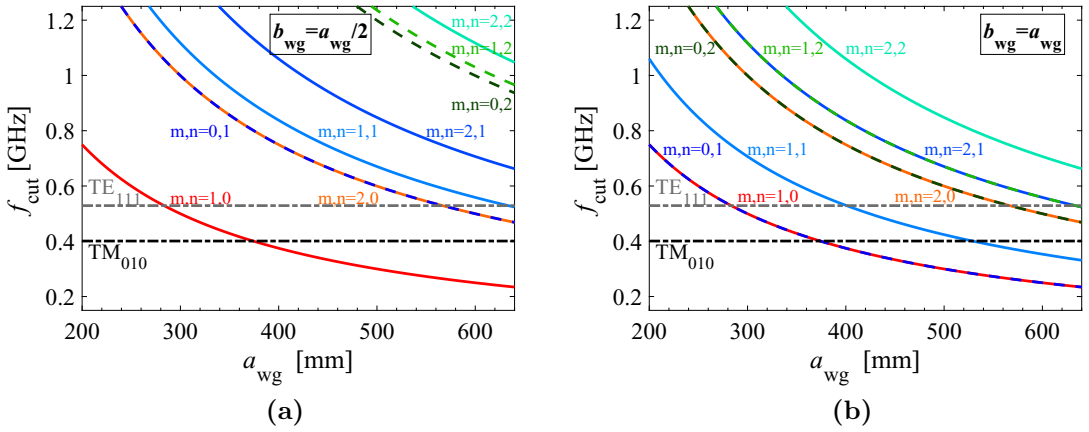

Figure 5.16: Cutoff frequencies of the lowest modes of a RWG with a 2:1 aspect ratio (a) and a 1:1 aspect ratio (b).

For a fixed value of a_{wg} and b_{wg}, the cutoff frequency of the FM of the RWG could be reduced by adding ridges to the waveguide [131, 132]. In single-mode applications, ridges are added to the longer side of the waveguide to enhance the bandwidth of the FM. The ridges could also be added to the shorter side of the waveguide to decrease the cutoff frequency of the second mode. If ridges are added to both short and long sides of the waveguide, a quad-ridged waveguide (QRWG) is formed, and the cutoff frequencies of both the FM and the second mode could be lowered substantially. This enables us to design a more compact waveguide HOM coupler with low cutoff frequencies.

The parametrization of a QRWG is shown in Figure 5.17 (a). The geometrical dimensions of this QRWG are determined such that the cutoff frequencies of the first two modes are reduced to below 500 MHz. In the first step, the cutoff frequency of the second mode is decreased by enlarging r_{bh}. Increasing r_{bh} also decreases the cutoff frequency of the third mode, and has a minor influence on the cutoff frequency

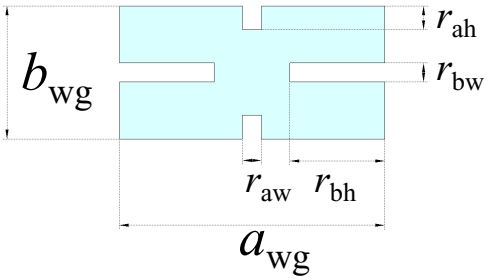

(a) Parametrization of the QRWG

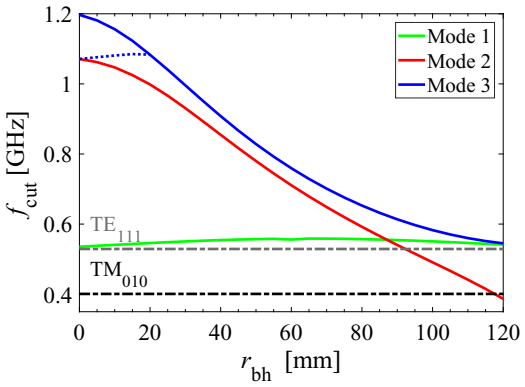

(b) $a_{wg} = 2b_{wg} = 280$ mm, $r_{ah} = 0$ mm and $r_{bw} = 20$ mm

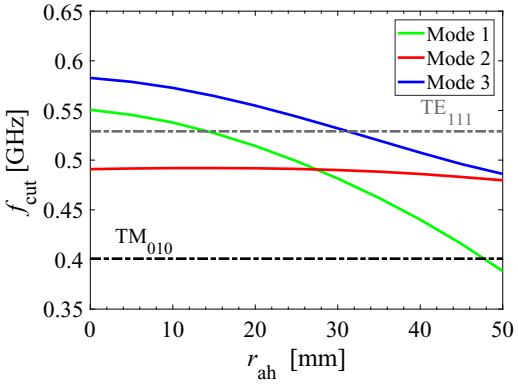

(c) $a_{wg} = 2b_{wg} = 280$ mm, $r_{bh} = 100$ mm and $r_{aw} = r_{bw} = 20$ mm

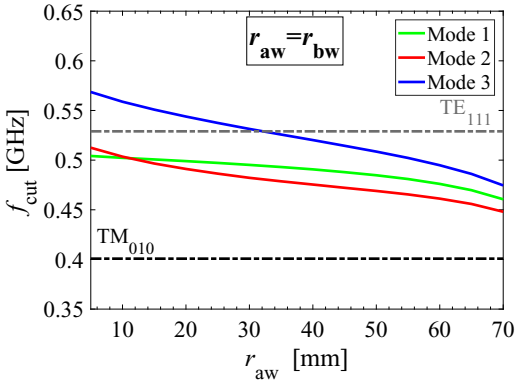

(d) $a_{wg} = 2b_{wg} = 280$ mm, $r_{bh} = 100$ mm and $r_{ah} = 25$ mm

Figure 5.17: QRWG parametrization (a) and the cutoff frequencies of the first three modes plotted with respect to the ridge dimensions (b-d). The field distribution of modes 1, 2 and 3 corresponds to the TE_{10}, TE_{01} and TE_{11} modes of a RWG, respectively. For small values of r_{bh} in (b), the TE_{20} mode is the third smallest mode (indicated by the dotted blue line). The frequency of the FM and the first dipole mode of the single-cell cavity are shown in dashed horizontal lines.

of the first mode. In the next step, the cutoff frequency of the first mode is reduced by increasing r_{ah}. Finally, a value is selected for the width of the ridges. Large values of r_{aw} and r_{bw} have no significant impact on the cutoff frequency of the first three modes, but they decrease the cross-section area of the waveguide and they thus reduce the amount of power that can propagate into the waveguide. It is therefore preferable to select a small value for the width of ridges.

Figure 5.18 shows the first four modes of a RWG with the dimensions $a_{wg} = 2b_{wg} = 280\,\text{mm}$, and a QRWG with the dimensions $a_{wg} = 2b_{wg} = 280\,\text{mm}$, $r_{bh} = 100\,\text{mm}$,

$r_{ah} = 25\,\text{mm}$ and $r_{aw} = r_{bw} = 20\,\text{mm}$. The field patterns of the first few modes of the QRWG are similar to those of the RWG, but with a different order. In Figure 5.18, the field distribution of mode (e) in a QRWG corresponds to mode (b) in a RWG, mode (f) corresponds to mode (a), mode (g) corresponds to mode (d) and mode (h) corresponds to mode (c). The cutoff frequency of the first four modes of the RWG are 0.535 GHz, 1.071 GHz, 1.071 GHz and 1.197 GHz, and they are reduced to 0.491 GHz, 0.499 GHz, 0.544 GHz and 1.06 GHz for the QRWG.

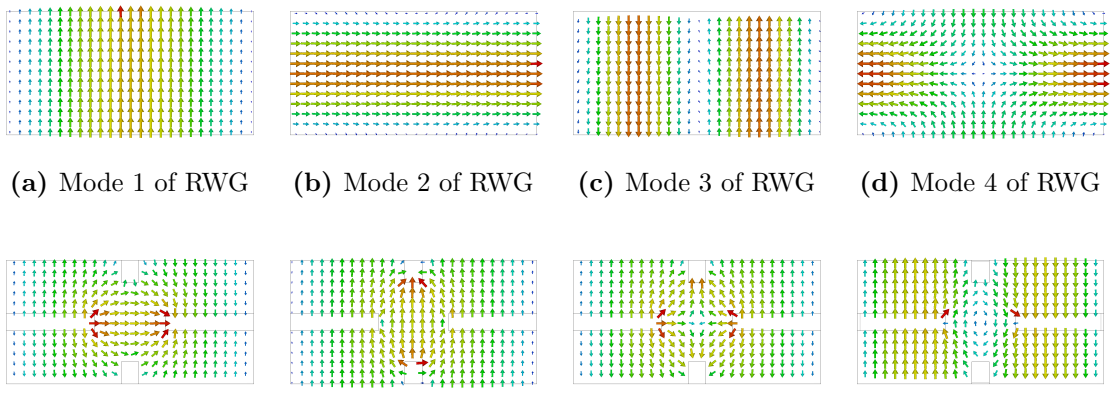

(a) Mode 1 of RWG **(b)** Mode 2 of RWG **(c)** Mode 3 of RWG **(d)** Mode 4 of RWG

(e) Mode 1 of QRWG **(f)** Mode 2 of QRWG **(g)** Mode 3 of QRWG **(h)** Mode 4 of QRWG

Figure 5.18: The first four modes of the RWG and the QRWG. Depending on the dimensions of the ridges, the order and the field pattern of the modes change when transforming the RWG into the QRWG.

The scattering properties of the QRWG and the RWG when connected to a circular beam pipe are shown in Figure 5.19. As indicated in Figure 5.19 (b-c), only the vertical polarization of the TE_{11} mode of the beam pipe propagates into the RWG at low frequencies. The other polarization is transmitted at frequencies above 1.071 GHz, which is the cutoff frequency of the TE_{01} mode of the RWG. In contrast, both polarizations of the TE_{11} mode of the beam pipe can propagate to the QRWG at low frequencies. The TE_{21} mode of the beam pipe port is a quadrupole mode that has two polarizations. Both polarizations of this mode are transmitted to the QRWG at low frequencies, while the transmission for each polarization in the RWG starts at a different frequency, as shown in Figure 5.19 (e-f). Both waveguide couplers show a similar behavior in transmitting the TM_{01} mode, which couples to some monopole modes including the FM and the first higher order monopole passband in the cavity. The length of the waveguide coupler has to be determined such that the field of the FM attenuates enough before reaching the absorbers placed at the end of the waveguide. For the dimensions given above, a length of 600 mm for the QRWG is sufficient to attenuate the power of the FM to below 10^{-5} before reaching the absorbers placed at the end of the waveguide.

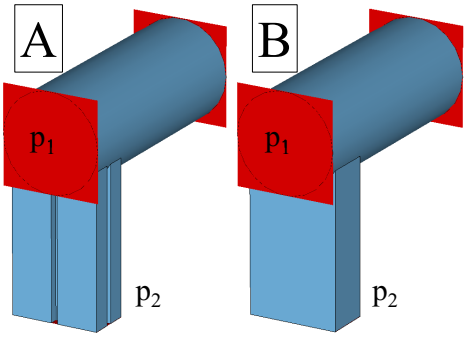

(a) QRWG vs. RWG

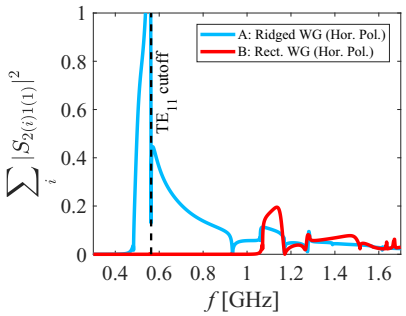

(b) Coupling of the first TE_{11} mode of P1 to P2

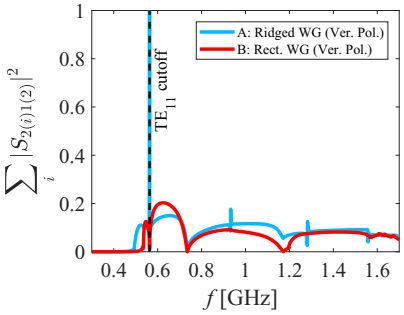

(c) Coupling of the second TE_{11} mode of P1 to P2

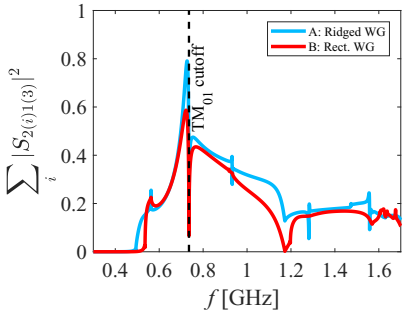

(d) Coupling of the TM_{01} mode of P1 to P2

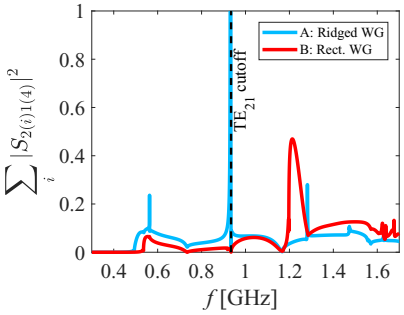

(e) Coupling of the first TE_{21} mode of P1 to P2

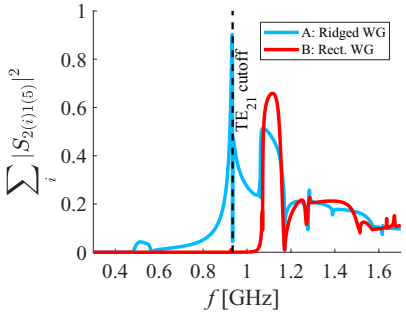

(f) Coupling of the second TE_{21} mode of P1 to P2

Figure 5.19: RWG and QRWG connected in a 90° angle to a circular beam pipe. The value of $\sum_i \left|S_{2(i)1(j)}\right|^2$ is calculated as a measure of power transmitted from mode j of port 1 to port 2. All ports are terminated with a matched impedance to minimize reflection. The dashed vertical lines represent the cutoff frequency of the circular beam pipe for the considered port mode (at port P1). The singularity of the complex-valued reference impedance at the cutoff frequencies creates a singularity in the scattering parameters. The TE_{11} and TE_{21} modes are degenerated and have two polarizations.

6 Survey of HOM-damped cavities

In this chapter, the cavities and HOM couplers that were designed in the previous chapters are combined, and the performance of the cavities and HOM couplers are evaluated. For this purpose, the longitudinal and transversal impedance of the HOM-damped cavities are compared to the impedance limits set by synchrotron radiation. The aim is to choose an appropriate HOM damping scheme to reduce the longitudinal and transversal impedance to below this threshold. Furthermore, the HOM power delivered to the cavities by the beam is estimated.

6.1 Numerical methods for the calculation of quantities of interest

6.1.1 Impedance calculation

Each bunch passing the cavity interacts with the surrounding enclosure and induces surface currents and charges on the walls of the structure. This interaction is described by wakefields in the time domain or impedances in the frequency domain. Wakefields arise from geometrical or material variations of the cavity along the beam path, and may cause undesirable effects such as energy loss or beam instability. Based on the interaction time-scale of the wakefield with the beam, the effects of the wakefield could be classified either as short-range or long-range wakefield effects [133, p. 13]. The short-range wakefields affect the driving bunch and could give rise to single-bunch instabilities. In long-range wakefields, the energy of the excited EM field remains in the structure for a long time until the next bunch arrives. This phenomenon typically occurs when a resonant mode of the cavity is repeatedly excited by the beam. The long-range wakefield generally corresponds to the high impedance peaks in the frequency domain and can drive coupled-bunch instability issues. A common approach to mitigate coupled-bunch instability is to extract the energy of HOMs as fast as possible by decreasing Q_{L} of the resonant modes [24, p. 345].

The motion of a bunch in a storage ring is typically modeled by a simple harmonic resonator where the wakefield effects could act as a driving force to the equation of motion [134]. The equation of motion includes a damping coefficient, which is a measure of how quickly the oscillations decay or grow in time. Some physical phenomena, such as synchrotron radiation or wakefield effects, determine the damping

coefficient. Synchrotron radiation typically provides a natural damping in storage rings, while the real part of the beam impedance affects the growth rate of oscillations [135, p. 30]. In addition, a multi-bunch feedback system is usually employed to add a damping term to the equation of motion and thus to stabilize the bunch motion.

A crucial parameter for the evaluation of the impedance of a cavity is a comparison with the coupled-bunch instability-limit. The impedance threshold is the impedance at which the growth rate of the instability equals the damping rate of the instability. The longitudinal and transversal impedance thresholds for each cavity are calculated from [74, p. 27; 135, p. 79]:

$$Z_{\parallel}^{\mathrm{th}} = \frac{2(E_0/q_e)\nu_s}{N_{\mathrm{cav}} f I_0 \alpha_c \tau_{\mathrm{z}}}, \tag{6.1}$$

$$Z_{\perp}^{\mathrm{th}} = \frac{2(E_0/q_e)}{N_{\mathrm{cav}} f_{\mathrm{rev}} I_0 \beta_{\mathrm{xy}} \tau_{\mathrm{xy}}}. \tag{6.2}$$

The description of the parameters is given in Table 6.1.

The longitudinal impedance threshold has an inverse relationship with the resonance frequency, whereas the transverse impedance threshold is independent of it. Both the longitudinal and the transversal impedance thresholds scale inversely with the revolution frequency f_{rev} (note that $\nu_{\mathrm{s}} = f_{\mathrm{s}}/f_{\mathrm{rev}}$ where f_{s} is synchrotron frequency). This is caused by the fact that the particle passes through the cavity more frequently at a higher f_{rev}, and thus the impedance of the cavity has to be smaller to maintain the beam stability. The impedance thresholds also scale linearly with the beam energy (due to the beam rigidity) and inversely with the beam current. Thus, in FCC-ee, the Z option has the smallest and $\mathrm{t\bar{t}_2}$ has the largest impedance thresholds.

To find the impedance threshold for each cavity, the impedance thresholds are normalized to the number of cavities based on the assumption that all cavities have an identical impedance spectrum. However, it is a conservative threshold as, in practice, there is a small geometrical difference between the cavities that might arise from the manufacturing tolerances or operating conditions. This may cause a spread between the frequency of HOMs of all cavities. A frequency spread between the cavities with a standard deviation of 0.5 MHz can increase the impedance threshold by $1 \sim 2$ orders of magnitude [136, 137]. Nonetheless, a conservative threshold for the impedances is assumed in the following analysis, i.e. the frequency spread between the cavities and the effect of the multi-bunch feedback system on the damping times are not considered.

Table 6.1: Some of the FCC-ee parameters [21] required for the calculation of beam-stability threshold-impedance. The beta function in the cavity (β_{xy}) is assumed to be 50 m for all options.

Parameters	Description	Z	W	H	$t\bar{t}_2$
E_0 [GeV]	Energy	45.6	80	120	182.5
ν_s	Synchrotron oscillation tune	0.025	0.0506	0.036	0.087
I_0 [mA]	Beam current	1390	147	29	$5.4\times2^*$
α_c [10^{-5}]	Momentum compaction factor	1.48	1.48	0.73	0.73
τ_z [ms]	Longitudinal damping time	424.6	78.7	23.4	6.8
τ_{xy} [ms]	Transverse damping time	849.2	157.4	46.8	13.6
f_{rev} [kHz]	Revolution frequency	3.07	3.07	3.07	3.07
N_{cav}	Number of cavities per beam	52	52	136	584^{**}
$Z_{\parallel}^{th}$ [kΩ]	Longitudinal impedance limit	$\frac{5.0}{f[\mathrm{GHz}]}$	$\frac{909}{f[\mathrm{GHz}]}$	$\frac{12797}{f[\mathrm{GHz}]}$	$\frac{101588}{f[\mathrm{GHz}]}$
$Z_{\perp}^{th}$ [kΩ/m]	Transverse impedance limit	9.7	867	8621	27731

* Both beams are assumed to be accelerated by the same RF system for $t\bar{t}_2$.
** Total number of cavities required for $t\bar{t}_2$ at 800 MHz.

6.1.1.1 Wake impedance

In order to analyze the motion of particles in an accelerator, the integrated interaction of the particles with the wakefield is usually of higher interest than the details of the wakefield. For this reason, the wake function is defined as the integrated EM field experienced by a test charge at a transverse offset $\mathbf{r}$ from the longitudinal axis and a distance s behind an exciting point charge q with delta-function distribution. The wake function is calculated on the basis of the following formula [138, p. 8]

$$\mathbf{w}(\mathbf{r},s) = \frac{1}{q}\int_{-\infty}^{\infty} [\mathbf{E}(\mathbf{r},z,t) + \underbrace{c\hat{\mathbf{z}}}_{\mathbf{v}} \times \mathbf{B}(\mathbf{r},z,t)]_{t=(s+z)/c}\, \mathrm{d}z, \tag{6.3}$$

where it is assumed that the particles move in the longitudinal direction (z-axis) with a velocity $\mathbf{v}$ close to the speed of light. The wake function is a vector with three components, one in the longitudinal and two in the transversal directions. Since $\hat{\mathbf{z}} \times \mathbf{B}$ has no component in the z direction (longitudinal direction), the calculation of the longitudinal wake function is reduced to

$$w_{||}(\mathbf{r},s) = \frac{1}{q}\int_{-\infty}^{\infty} E_z(\mathbf{r},z,(s+z)/c)\mathrm{d}z. \tag{6.4}$$

If the wakefield is excited by a bunch with an arbitrary shape, wake potentials are used to describe the interaction of the particles with the field. Since the wake

function is obtained for a point charge with delta function distribution, it can be considered as the Green's function of the problem. Thus, the wake potential could be derived from the convolution of the wake function with the charge distribution

$$\mathbf{W}(\mathbf{r}, s) = \int_0^\infty \lambda_\mathrm{c}(s - s')\mathbf{w}(\mathbf{r}, s')\mathrm{d}s' \tag{6.5}$$

where λ_c is the charge distribution. For a Gaussian bunch with a longitudinal bunch length of σ_z centered at z_0, λ_c in the longitudinal direction is defined as

$$\lambda_\mathrm{c}(z) = \frac{1}{\sigma_z\sqrt{2\pi}}\mathrm{e}^{(-\frac{(z-z_0)^2}{2\sigma_z^2})}. \tag{6.6}$$

The coupling impedance relates the total voltage induced along the beam trajectory to the beam current in the frequency domain. The impedance spectrum of the cavity could be obtained by taking the Fourier transform of the wake function in both longitudinal and transversal directions [138, p. 16-17]

$$Z_{||}(\mathbf{r}, \omega) = \frac{1}{c}\int_{-\infty}^{\infty} w_{||}(\mathbf{r}, s)\mathrm{e}^{-\frac{j\omega s}{c}}\mathrm{d}s, \tag{6.7}$$

$$\mathbf{Z}_\perp(\mathbf{r}, \omega) = \frac{-j}{c}\int_{-\infty}^{\infty} \mathbf{w}_\perp(\mathbf{r}, s)\mathrm{e}^{-\frac{j\omega s}{c}}\mathrm{d}s. \tag{6.8}$$

The unit of longitudinal and transversal impedance defined as above is Ω. Near the axis of symmetry, the dipole modes are the main source of deflection, and their field increases in proportion with the transverse offset of the driving beam. To achieve a definition that is independent of the transverse displacement, it is very common to normalize the transverse impedance ($\mathbf{Z}_\perp$) to the beam offset distance, which in turn changes the unit of transverse impedance to Ω/m [139, p. 25]. There is a relationship between the longitudinal and transversal wake function formulated by the Panofsky-Wenzel theorem. In the frequency domain, the Panofsky-Wenzel theorem states [33, p. 90]

$$\mathbf{Z}_\perp(\mathbf{r}, \omega) = \frac{c}{\omega}\nabla_\perp Z_{||}(\mathbf{r}, \omega) \tag{6.9}$$

where $\nabla_\perp$ acts only on the transverse coordinates.

Wakefields could be calculated by time domain solvers such as ABCI [62] for 2D axisymmetric geometries, or CST Studio Suite® [51] for 3D geometries. In such solvers, the structure is excited by a bunch with an arbitrary shape (usually Gaussian-shaped bunch), and wakefield effects such as wake potential, wake impedance or loss factors are calculated. Depending on how the beam passes the cavity, modes of different polar order and polarization could be excited. If the cavity is excited by an on-axis beam in an axisymmetric structure, only TM-like monopole modes are excited in the cavity. In contrast, an off-axis beam could excite modes

with higher polar orders. As shown in Figure 6.1, different excitation schemes could be exploited to excite modes of a certain polar order and polarization, and suppress the other modes of the cavity [140]. In accelerating cavities, the monopole and dipole modes have the biggest impact on the motion of particles, as they have a strong field near the longitudinal axis. To excite the TM-like monopole modes, only one beam has to pass through the center of the cavity. If the cavity is symmetric with respect to a symmetry plane, a PMC boundary condition could be used to reduce the simulation domain and thus the simulation time (see Figure 6.1).

The following procedure could be used to compute the impedance of the dipole modes: two beams with an opposite charge and with equal offsets from the center have to pass through the cavity to excite the dipole modes. The superposition of the fields of the two beams preserves the dipole modes and suppresses the modes with different polar order. As depicted in Figure 6.1, a horizontal beam offset excites the dipole modes with horizontal polarization, and a vertical beam offset excites the dipole modes with vertical polarization. Since the two beams simultaneously excite the dipole modes, the bunch charge of each beam is set to $q/2$ so that the superposition effect corresponds to a particle-beam with the charge q. In CST Studio Suite®, the wake impedance of each particle beam is calculated by normalizing the Fourier transform of the wake-potential to the charge distribution. For a two-beam excitation scheme, the wake-potential is a superposition of the fields of the two beams, while it is normalized to the charge distribution of one beam. Thus, for any arbitrary q, a normalization to two is required.

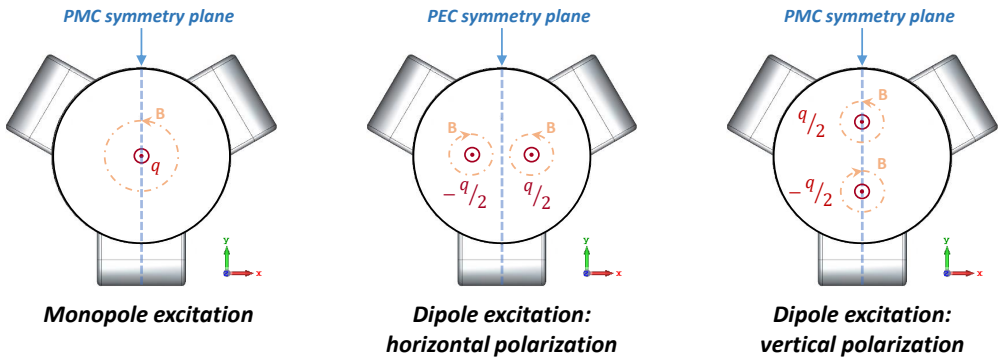

Figure 6.1: Monopole and dipole excitation schemes in 3D wakefield solvers [140]. If the cavity is symmetric with respect to a symmetry plane (indicated by the blue vertical dashed lines), appropriate boundary conditions on the symmetry plane could be used to reduce the simulation domain and thus the simulation time.

Impedance peaks in the wake impedance correspond to the modes with high external quality factor. After excitation by the beam, the energy of these modes remain in the cavity for a long time. To accurately resolve the impedance peaks of such modes, we have to calculate the wake potential for a large distance behind

the driving bunch (a large value of the wakelength). The amplitude and energy of a mode excited by a traversing charged particle in the cavity decay by $e^{-t/\tau}$ and $e^{-2t/\tau}$, respectively, where τ is the time constant of that mode which depends on the loaded quality factor via

$$\tau = 2Q_{\mathrm{L}}/\omega_n. \tag{6.10}$$

For a mode at 1 GHz frequency with a loaded quality factor of $Q_{\mathrm{L}} = 10^6$, the wakelength needed to decrease the amplitude to 1/e of its initial value is $c \cdot \tau \approx 95\,\mathrm{km}$, which requires a very long computation time. The wake potential is usually truncated after several hundreds of meters. In this case, the impedance peaks of the truncated wake potential may not be accurately resolved. An extrapolation scheme is proposed in [140, 141] which approximates the final impedance from two wake potentials truncated at different wakelengths, e.g. truncated after $c \cdot t_1$ and $c \cdot 2t_1$. This approach allows us to approximate the impedance spectrum using a shorter wakelength, and thus saving computation time.

6.1.1.2 Eigenmode impedance

If the energy of a mode slowly decays in the cavity (due to high Q_{ext}), the required wakelength for accurately calculating the beam impedance is very large, and thus the computational time is prohibitive. The impedance of the cavity around the resonance frequency of such modes could be modeled as a simple harmonic oscillator by an RLC circuit. The longitudinal and transversal impedance of such modes around the resonance frequency are approximated by (2.46) and (2.47); thus, the modal analysis of the cavity is required for the calculation of the relevant parameters such as R/Q, Q_{ext} and the resonance frequency. Modal information of the cavity is obtained by solving an eigenvalue problem that arises from the discretization of the Helmholtz equation by numerical methods such as FEM or FIT. The eigenvalues of the eigenvalue problem determine the resonance frequency of the modes, and the eigenvectors correspond to the field distribution of the modes, as was explained in Section 2.3.

In the presence of losses, such as the energy loss via waveguide ports or surface losses, the problem turns into a complex nonlinear eigenvalue problem [142]. In a case like this, the system matrices of the eigenvalue problem depend on the frequency of the modes which themselves are solutions of the eigenvalue problem. The eigenvalues of this problem are complex numbers that contain information about the resonant frequency of the modes and their external quality factor.

In the literature, several methods are proposed for the challenging task of calculating the external quality factor Q_{ext} of modes in the cavities. The pole fitting method is an approach for the calculation of quality factors from the S-parameters [143, 144]. In this method, the S-parameters are approximated with a summation over complex rational functions the poles of which contain information of the loaded frequency and the quality factor of the modes. The drawback of the pole-fitting method is that the

field distribution of each mode is not calculated, and that the field-dependent values, such as R/Q, cannot be calculated. This method may also deliver non-physical modes by over-fitting the S-parameters. Another method is to terminate the external ports with a dissipative material to account for a reflection-free boundary (matched condition) at the ports [145]. The advantage of this method is that the field distribution of the damped modes can be observed. However, this method sometimes yields non-physical modes around the lossy material and might not always converge.

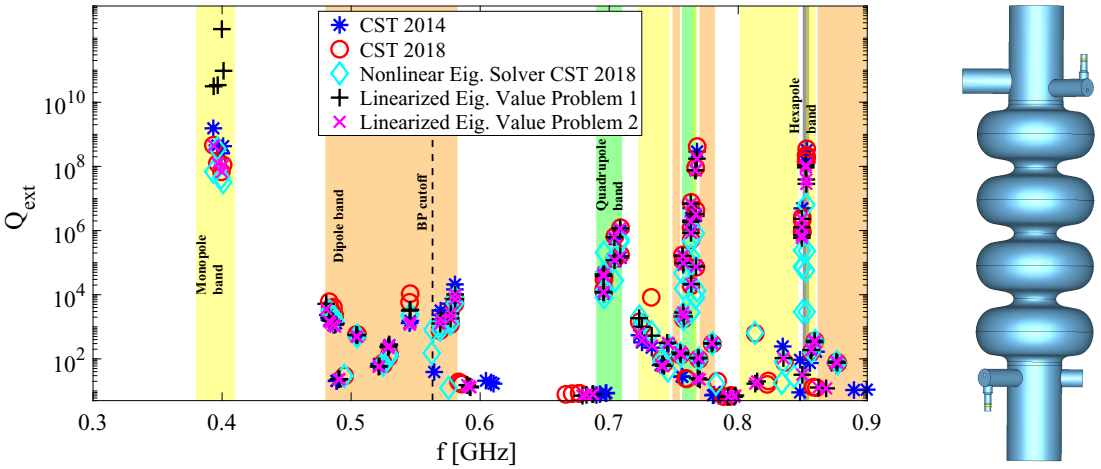

Figure 6.2: This plot shows the Q_{ext} of some passbands of a four-cell cavity with two DQW HOM couplers computed with different approaches. In the linearized case, the SSC method is applied to the system matrices that are exported from CST Studio Suite® 2014. In the first linearized case, the complex wave impedance and in the second linearized case, the absolute value of the wave impedance is considered at the port boundaries. In CST 2014, CST 2018 and the nonlinear eigenmode solver of CST 2018, a tetrahedral mesh is used, and in the linearized cases (in the SSC method) a hexahedral mesh is employed.

The standard method for the calculation of the external quality factor is to terminate ports with a matched boundary condition via waveguide ports. This boundary condition emulates a situation where no energy is reflected back into the structure. In this method, the impedance of each 2D port mode is replaced by the frequency-dependent complex-valued wave impedance of the respective mode. Therefore, a complex nonlinear eigenvalue problem is obtained. The eigenvalues of the resulting nonlinear eigenvalue problem contain information about the resonant frequency and external quality factor of the modes. This will be explained further in Subsection 6.1.4.

Figure 6.2 shows a comparison of some solvers for the calculation of Q_{ext} of the modes of a four-cell cavity with two DQW HOM couplers. Three simulations are carried out with the eigenmode solver of CST Studio Suite® using a tetrahedral

mesh, i.e. with CST 2014, CST 2018 and the prototype of the nonlinear eigenmode solver of CST 2018. Two simulations are also done with the SSC method, which exploits the hexahedral mesh cells created in CST Studio Suite® and applies a model order reduction on the obtained system matrices (this method will be explained in more detail in Section 6.1.4). The resulting nonlinear eigenvalue problem is then linearized at equal frequency intervals (e.g. every 100 MHz). In the first linearized case, the ports are terminated with complex-valued wave impedances (see (6.26) in Section 6.1.4). For this reason, modes that are below the cutoff frequency of the beam pipes, like the FM passband, are not damped by the beam pipes and are only damped by weak coupling to the HOM dampers (the energy does not leave the structure via the beam pipes). In the second linearized case, the absolute value of the wave impedance is considered at the beam pipes. In this case, modes that are below the cutoff frequency of the beam pipe can still weakly couple to the waveguide ports, and their Q_{ext} is thus reduced. The results of the nonlinear eigenmode solver are not accurate for many modes. The other approaches deliver close results, while a difference is expected for some modes.

6.1.2 HOM power in the damped cavities

In case of the resonant excitation of a mode by the beam, the resulting HOM power can be approximated from [146]

$$P_{\mathrm{HOM,n}} = I_0 \frac{2k_{\parallel,n}Q_{\mathrm{b}}}{\mathrm{e}^{t_{\mathrm{b}}/\tau}-1} + k_{\parallel,n}Q_{\mathrm{b}}I_0 = \frac{(R/Q_{\parallel,n})\omega_n Q_{\mathrm{b}}^2}{4t_{\mathrm{b}}}\left(\frac{\mathrm{e}^{t_{\mathrm{b}}/\tau}+1}{\mathrm{e}^{t_{\mathrm{b}}/\tau}-1}\right), \tag{6.11}$$

where ω_n is the resonant angular frequency of mode n, Q_{b} is the bunch charge, t_{b} is the average bunch spacing ($I_0 = Q_{\mathrm{b}}/t_{\mathrm{b}}$), $R/Q_{\parallel,n}$ is the longitudinal shunt impedance defined according to (2.41), τ is the decay time of the HOM field ($\tau = 2Q_{\mathrm{ext},n}/\omega_n$) and $k_{||,n}$ is the loss factor of the resonant mode n. This formula represents the general case of HOM excitation. The energy deposited in the cavity by a bunch partly arises from the interaction of the bunch with the surrounding structure, and partly through the interaction of the bunch with the voltage induced by the preceding bunches. If the next bunch arrives before the HOM field damps down, i.e. $t_{\mathrm{b}} \ll \tau$, a multi-bunch resonance excitation occurs and equation (6.11) could be written as

$$P_{\mathrm{HOM,n}} \approx \frac{(R/Q_{\parallel,n})\omega_n Q_{\mathrm{b}}^2}{4t_{\mathrm{b}}}\left(\frac{1+t_{\mathrm{b}}/\tau+1}{1+t_{\mathrm{b}}/\tau-1}\right) = \frac{(R/Q_{\parallel,n})\omega_n Q_{\mathrm{b}}^2}{4t_{\mathrm{b}}}\left(\frac{2\tau}{t_{\mathrm{b}}}+1\right), \tag{6.12}$$

where $\mathrm{e}^{t_{\mathrm{b}}/\tau}$ is replaced with the first two terms of its Taylor series expansion around zero. Assuming $t_{\mathrm{b}} \ll \tau$, $I_0 = Q_{\mathrm{b}}/t_{\mathrm{b}}$ and $\tau = 2Q_{\mathrm{ext},n}/\omega_n$, equation (6.12) could be further simplified to

$$P_{\mathrm{HOM,n}} \approx \frac{(R/Q_{\parallel,n})\omega_n Q_{\mathrm{b}}^2}{4t_{\mathrm{b}}}\left(\frac{2\tau}{t_{\mathrm{b}}}\right) = R/Q_{\parallel,n} \cdot Q_{\mathrm{ext},n} \cdot I_0^2. \tag{6.13}$$

This equation will be used in the rest of this thesis to approximate the HOM power of the modes with high longitudinal impedance.

If the HOM field damps down before the next bunch arrives i.e. $t_\mathrm{b} \gg \tau$, a non-resonant single-bunch excitation occurs, and equation (6.11) is reduced to $P_{\mathrm{HOM,n}} \approx k_{||,n} Q_\mathrm{b} I_0$. In the case of non-resonant excitation, the HOM powers deposited by the Z, W, H, and $\mathrm{t\bar{t}}$ beams into the single-cell, four-cell, and five-cell cavities (that were designed in Chapter 4) are given in Table 6.2. For the sake of completeness, the HOM power is calculated for both cases of a beams on collision scenario (BS) and a no-collision scenario (SR). In practice, however, the bunches are kept in collision and are dumped otherwise. The high HOM power of the Z-pole scenario reaffirms the choice of a single-cell cavity for it.

Table 6.2: The HOM power of the single-cell, four-cell, and five-cell cavity at different operating scenarios of FCC-ee. It is assumed that the field of the previous bunch is decayed when the next bunch arrives, i.e. the case of non-resonant excitation.

	Z	W	H	$\mathrm{t\bar{t}_2}$
Single-cell cavity at 400 MHz				
Bunch length [mm]	P_HOM [kW]	P_HOM [kW]	P_HOM [kW]	P_HOM [kW]
SR (3.5, 3.0, 3.15, 1.97)	6.86	0.71	0.16	0.11
BS (12.1, 6.0, 5.3, 2.54)	2.53	0.43	0.11	0.09
Four-cell cavity at 400 MHz				
Bunch length [mm]	P_HOM [kW]	P_HOM [kW]	P_HOM [kW]	P_HOM [kW]
SR (3.5, 3.0, 3.15, 1.97)	47.95	5.09	1.16	0.81
BS (12.1, 6.0, 5.3, 2.54)	17.34	2.89	0.76	0.66
Five-cell cavity at 800 MHz				
Bunch length [mm]	P_HOM [kW]	P_HOM [kW]	P_HOM [kW]	P_HOM [kW]
SR (3.5, 3.0, 3.15, 1.97)	66.11	6.94	1.59	1.09
BS (12.1, 6.0, 5.3, 2.54)	23.91	4.09	1.06	0.90

Equation (6.11) is suitable for cases where eigenmode properties of each mode are available. Eigenmode calculation for large frequency ranges is a time-consuming procedure. Therefore, eigenmodes are usually calculated up to 3 to 4 times the frequency of the FM. In order to investigate the impedance of the cavity in a broader frequency range, the wakefield analysis is utilized. In the wakefield solvers, the structure is excited by a beam in the time domain, and the wake potential is then calculated behind the traversing beam. The wake impedance could be calculated by taking the Fourier transform of the wake potential. The total HOM power deposited into the cavity could be calculated from the wake impedance by

$$P_\mathrm{HOM} = I_0^2 \sum_{n=-\infty}^{n=\infty} |\hat{I}_n|^2 \Re[Z_{||}(n f_\mathrm{rev})], \tag{6.14}$$

where I_0 is the average beam current, n the revolution harmonic number, $Z_{||}$ the longitudinal impedance of the cavity, and $\hat{I}_n$ the normalized Fourier spectrum of the beam current at revolution harmonics [147]. Depending on the beam filling scheme, which determines $\hat{I}_n$, different modes could be excited by the beam.

6.1.3 Power propagated into the ports

In the HOM power calculation, the total power released into the cavity by the beam is usually calculated. However, this does not determine the amount of power absorbed by each HOM coupler. For the proper optimization of the HOM couplers, the contribution of each HOM coupler to the absorption of the HOM power has to be determined.

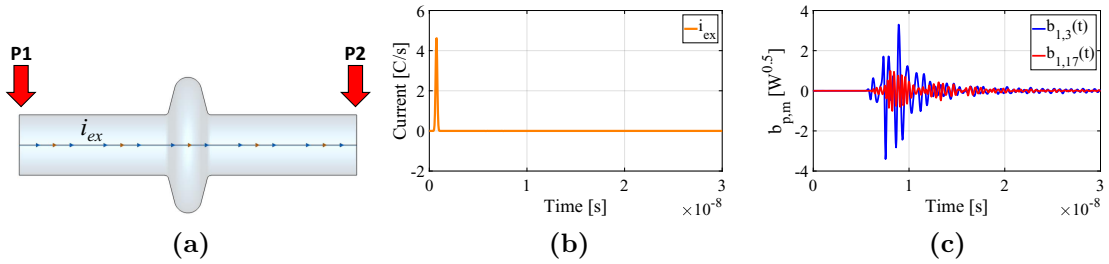

(a) **(b)** **(c)**

Figure 6.3: A single-cell cavity with two waveguide ports (a), excited by a particle beam with the bunch length of 25 mm and the bunch charge of 1 nC (b). Two signals excited into mode 3 and 17 of port 1 are depicted in (c).

In order to find out how the HOM energy leaves the cavity, the couplers (power coupler and HOM couplers) and the beam pipes are terminated with multi-mode ports. Then the cavity is excited by a single bunch, and the port signal for each mode of the ports is calculated. In Figure 6.3 (a), a cavity with two waveguide ports at its beam pipes is depicted. The wakefield solver of CST Studio Suite® is then used to excite the cavity with a beam, and to calculate the signals scattered into different modes of each port (see Figure 6.3 (b-c)). The resulting port signals correspond to a single bunch excitation of the cavity. The amount of power scattered into the ports could differ subject to the beam filling scheme. In order to account for different beam filling schemes, the spectral weighting method [148, 149] is exploited. This method is a post-processing technique applied to the results obtained from the wakefield solver of CST Studio Suite®. First, the Fourier transforms of the signals excited in the ports are obtained and normalized to the Fourier transform of the exciting single bunch as follows

$$\underline{F}_{p,m}(\omega_n) = \frac{\mathrm{FFT}[b_{p,m}(t)]}{\mathrm{FFT}[i_{\mathrm{ex}}(t)]}, \tag{6.15}$$

where $b_{p,m}$ is the time-dependent signal excited into the mode m of port p, i_{ex} is the exciting beam, $\underline{F}_{p,m}$ is the complex-valued weighting transfer function of mode m of port p, and ω_n is the angular frequency of the nth harmonic number. Then the scattered signals for an arbitrary beam filling scheme are calculated by multiplying the weighting transfer function with the beam spectrum in the frequency domain via

$$\underline{b}_{p,m}(\omega_n) = \underline{F}_{p,m}(\omega_n) \cdot \underline{I}_{\mathrm{fcc}}(\omega_n), \tag{6.16}$$

where $\underline{I}_{\mathrm{fcc}}$ is the beam spectrum of the FCC-ee at different beam energies. The beam spectra of the Z, W, H, and $\mathrm{t\bar{t}}_2$ working points for a simplistic case where the bunches are uniformly distributed in the ring are shown in Figure 6.4 (for the BS bunch length). Since the beam spectrum is symmetric in the frequency domain, only its positive side is shown. For the calculation of power in this thesis, only the positive frequencies are considered, and the final result is multiplied by two to account for both sides of the spectrum.

Finally, the power propagated into a port due to the beam current excitation is calculated by summing up over all harmonics and all modes via

$$P_p = \sum_{n=1}^{N_{\mathrm{h}}} \sum_{m=1}^{M_p} \mid \underline{b}_{p,m}(\omega_n) \mid^2, \tag{6.17}$$

where M_p is the maximum number of modes of port p, and N_{h} is the maximum considered harmonic number.

The following part of this section closely follows [150]. Due to a rather small bunch length of the FCC-ee options, the beam has high spectral contributions up to tens of GHz, e.g. up to approximately 12 GHz for the Z-pole option. The numerical determination of the impedance and HOM power of the cavity up to this frequency is computationally costly. According to (6.14), the HOM power is directly proportional to the square of the beam current. As an approximation, the problem could be simplified by calculating the power up to a certain frequency and estimating the rest. For this purpose, the spectrum is divided into three parts: low, middle, and high-frequency ranges, as shown in Figure 6.4. Normally, the trapped modes with high narrow-band impedance peaks are located roughly below three to four times the FM frequency. Above that, the impedance spectrum has a rather broadband behavior. Therefore, the HOM power in the middle-frequency range is used as a benchmark for the calculation of the power in the high-frequency range. Based on the spectrum of the Z-pole beam current squared, 53.3% of the power is located between 0 GHz and 2 GHz (denoted by $P_{\mathrm{L-Z}}$), 32.7% between 2 GHz and 4.1 GHz (denoted by $P_{\mathrm{M-Z}}$) and 14.0% is located above 4.1 GHz (denoted by $P_{\mathrm{H-Z}}$). Thus the total HOM power for the Z-pole option is approximated by

$$P_{\mathrm{tot-Z}} \approx P_{\mathrm{L-Z}} + P_{\mathrm{M-Z}} + \frac{14.0}{32.7} P_{\mathrm{M-Z}}. \tag{6.18}$$

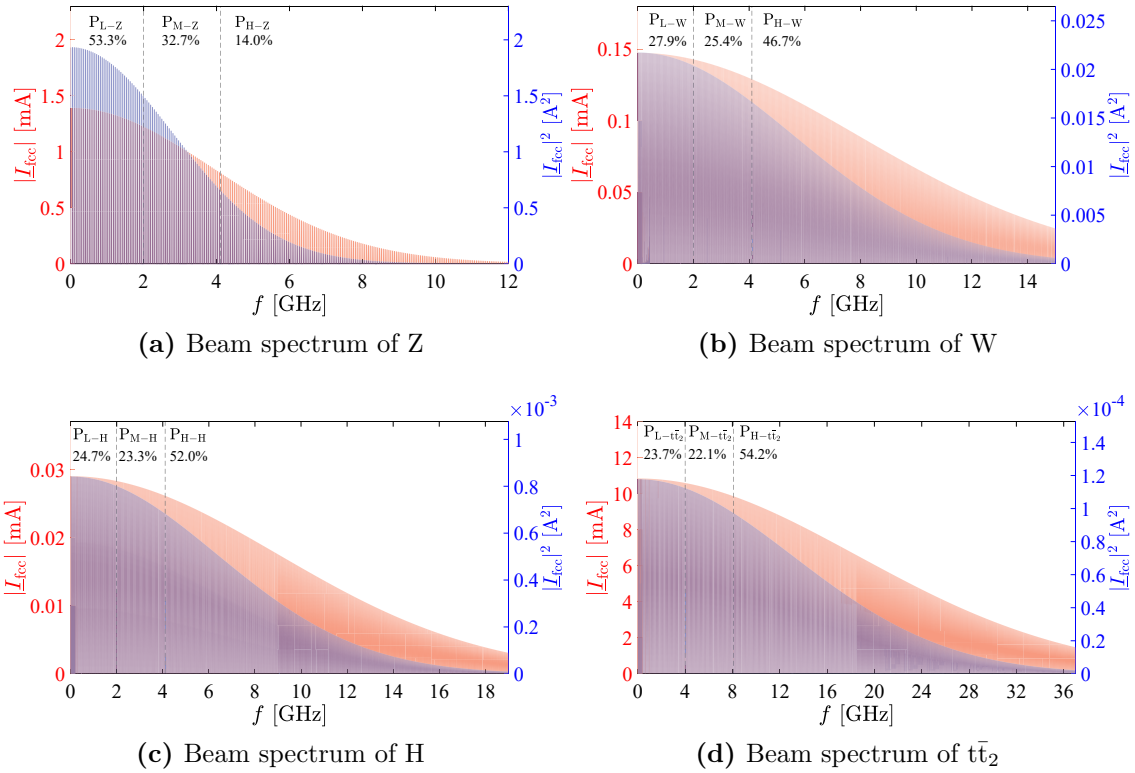

(a) Beam spectrum of Z

(b) Beam spectrum of W

(c) Beam spectrum of H

(d) Beam spectrum of $\mathrm{t\bar{t}_2}$

Figure 6.4: Beam spectra of different operating scenarios of FCC-ee using the parameters of Table 1.1. The spectra correspond to a simple beam filling scheme, assuming that all the bunches are uniformly distributed in the ring. Note that the beam spectra are symmetric around $f = 0$, and here the positive frequency side of the spectra are shown. The distances between the spectral lines are 51 MHz, 6.1 MHz, 1 MHz, and 294 kHz for the Z, W, H, and $\mathrm{t\bar{t}_2}$ working points, respectively (due to the condensed spectral lines, the spectra seem continuous). The current is doubled for the $\mathrm{t\bar{t}_2}$ running, assuming that the same RF structure accelerates both beams.

Similarly, the total HOM power for the W, H, and $\mathrm{t\bar{t}_2}$ working points are, respectively, approximated from

$$P_{\mathrm{tot-W}} \approx P_{\mathrm{L-W}} + P_{\mathrm{M-W}} + \frac{46.7}{25.4} P_{\mathrm{M-W}}, \tag{6.19}$$

$$P_{\mathrm{tot-H}} \approx P_{\mathrm{L-H}} + P_{\mathrm{M-H}} + \frac{52.0}{23.3} P_{\mathrm{M-H}}, \tag{6.20}$$

and

$$P_{\mathrm{tot-t\bar{t}_2}} \approx P_{\mathrm{L-t\bar{t}_2}} + P_{\mathrm{M-t\bar{t}_2}} + \frac{54.2}{22.1} P_{\mathrm{M-t\bar{t}_2}}, \tag{6.21}$$

where for the $t\bar{t}_2$ running, $P_{L-t\bar{t}_2}$ and $P_{M-t\bar{t}_2}$ correspond to the power between 0 GHz and 4.0 GHz and to the power between 4.0 GHz and 8.1 GHz, respectively.

6.1.4 Coupling of modes to the waveguide ports in the State Space Concatenation method

In the design and optimization of SRF resonators such as SRF cavities, the knowledge of the electromagnetic field inside the resonator plays a crucial role. The external quality factor Q_{ext} is an important parameter that describes the energy loss of a particular mode through the waveguide ports. As stated before, the computation of Q_{ext} generally leads to a nonlinear eigenvalue problem whose complex eigenvalues contain information about Q_{ext}. The Q_{ext} of a multi-port structure, however, does not describe the coupling of the resonant mode to each waveguide port. The coupling of the resonant mode to each port is crucial, for example, in the design of HOM couplers for SRF cavities as it can indicate the relative flux of HOM power through each coupler. It should be noted that due to the non-linearity of the problem, the coupling of a mode with one port cannot be simply obtained by closing all other ports.

In this section, eigenvectors of the nonlinear eigenvalue problem are exploited, and a technique to calculate the coupling of the resonant mode to each waveguide port in a multi-port structure is proposed. This approach is explained here within the framework of the SSC method; however, it is equivalently applicable to any state-space model of the RF system. The SSC method is a numerical approach developed by Flisgen at the University of Rostock [151] for simulating large complex RF structures. The nomenclature of this section closely follows [151, 152]. For further information on the SSC method, refer to [151, 152, 153, 154, 155].

The SSC method decomposes a large structure into several non-overlapping segments, and terminates the segments at the cutting planes with waveguide ports. The RF properties of each segment are then represented in state-space form, i.e. a set of differential equations of the inputs, outputs, and state variables obtained from the numerical discretization methods such as FIT. Model order reduction (MOR) techniques are then applied to the state-space models to reduce the degrees of freedom of the respective segments. Due to the continuity of the electric and magnetic field at the cutting planes, algebraic continuity constraints are applied to concatenate the segments and create a state-space model of the full structure. The size of the arising state-space model of the concatenated structure is again reduced with MOR, so that a compact model of the full structure is obtained. The resulting compact state-space model has several orders of magnitude fewer degrees of freedom than the original problem.

The state-space representation of the full structure arising from the discretization of the wave equation with excitation can be expressed in a first-order state-space

model as follows

$$\begin{aligned} \frac{\mathrm{d}}{\mathrm{d}t}\mathbf{x}_\mathrm{f}(t) &= \mathbf{A}_\mathrm{f}\mathbf{x}_\mathrm{f}(t) + \mathbf{B}_\mathrm{f}\mathbf{i}_\mathrm{ext}(t), \\ \mathbf{v}_\mathrm{ext}(t) &= \mathbf{B}_\mathrm{f}^\mathrm{T}\mathbf{x}_\mathrm{f}(t) \end{aligned} \tag{6.22}$$

where $\mathbf{x}_\mathrm{f}(t) \in \mathbb{R}^{N_\mathrm{f}}$ is the time-dependent state vector, $\mathbf{A}_\mathrm{f} \in \mathbb{R}^{N_\mathrm{f}\times N_\mathrm{f}}$ the state matrix, $\mathbf{B}_\mathrm{f} \in \mathbb{R}^{N_\mathrm{f}\times N_\mathrm{ext}}$ the input matrix, $\mathbf{i}_\mathrm{ext}(t) \in \mathbb{R}^{N_\mathrm{ext}}$ the time-dependent input vector, $\mathbf{v}_\mathrm{ext}(t) \in \mathbb{R}^{N_\mathrm{ext}}$ the time-dependent output vector, N_f the number of degrees of freedom and N_ext the total number of external terminals (i.e. all external port modes). In the SSC method, after the MOR and concatenation, a similar first-order state space model of the full structure is obtained, but with a significantly smaller number of degrees of freedom [151, p. 74].

In this thesis, the investigated structures by the SSC method are discretized with hexahedral mesh using CST Studio Suite®. The resulting FIT-based system matrices (given in Table 2.1) are then imported into MATLAB, and the matrices $\mathbf{A}_\mathrm{f}$ and $\mathbf{B}_\mathrm{f}$ are created from them [151, p. 50]. Matrix $\mathbf{A}_\mathrm{f}$ comprises the information of the grid, the averaged material parameters, and the discrete representation of the curl operator. Matrix $\mathbf{B}_\mathrm{f}$ contains information about the grid, the averaged material parameters, and the electric field distribution of the 2D port modes [152]. The input vector $\mathbf{i}_\mathrm{ext}(t)$ contains information about the modal port currents, i.e. the coefficients of the respective 2D magnetic field distribution at the external ports, as follows

$$\mathbf{i}_\mathrm{ext}(t) = \left[i_{\mathrm{ext},1,1}(t), \ldots, i_{\mathrm{ext},1,M_1}(t) \ldots, i_{\mathrm{ext},p,1}(t), \ldots, i_{\mathrm{ext},p,M_p}(t)\right]^\mathrm{T}, \tag{6.23}$$

where p is the port number index and M_p is the maximum number of 2D modes at port p. Similarly, the output vector $\mathbf{v}_\mathrm{ext}(t)$ contains information about the modal port voltages, i.e. the coefficients of the respective 2D electric field distribution at the external ports, as follows

$$\mathbf{v}_\mathrm{ext}(t) = \left[v_{\mathrm{ext},1,1}(t), \ldots, v_{\mathrm{ext},1,M_1}(t), \ldots, v_{\mathrm{ext},p,1}(t), \ldots, v_{\mathrm{ext},p,M_p}(t)\right]^\mathrm{T}. \tag{6.24}$$

The lossless eigenmodes of the structure could be calculated by assuming $\mathbf{i}_\mathrm{ext}(t) = \mathbf{0}$. This assumes a zero tangential magnetic field at the port boundaries, which, according to Poynting's theorem, leads to zero energy flux through the port surfaces. In order to account for a reflection-free energy flux through the waveguide ports, a matched impedance condition is assumed for the port boundaries. In the frequency domain, this reads as follows

$$\underline{\mathbf{i}}_\mathrm{ext} = -\underline{\mathbf{D}}_Z^{-1}(j\underline{\omega})\underline{\mathbf{v}}_\mathrm{ext}, \tag{6.25}$$

where $\underline{\mathbf{D}}_Z(j\underline{\omega})$ is a diagonal complex-valued matrix which contains information of the wave impedances (for TE and TM modes) and line impedances (for TEM modes) of the 2D port modes [151, p.83] as follows

$$\underline{\mathbf{D}}_Z(j\underline{\omega}) = \mathrm{diag}(\underline{Z}_{1,1}(j\underline{\omega}), \ldots, \underline{Z}_{1,M_1}(j\underline{\omega}), \ldots, \underline{Z}_{p,1}(j\underline{\omega}), \ldots, \underline{Z}_{p,M_p}(j\underline{\omega})). \tag{6.26}$$

The wave impedances of the 2D port modes depend non-linearly on the frequency and are given for TE and TM modes, respectively, by

$$\underline{Z}_{\mathrm{wave}}^{\mathrm{TE}}(j\underline{\omega}) = Z_0 \frac{j\underline{\omega}}{\sqrt{(j\underline{\omega})^2 + \omega_{\mathrm{cut}}^2}}, \tag{6.27}$$

$$\underline{Z}_{\mathrm{wave}}^{\mathrm{TM}}(j\underline{\omega}) = Z_0 \frac{\sqrt{(j\underline{\omega})^2 + \omega_{\mathrm{cut}}^2}}{j\underline{\omega}}, \tag{6.28}$$

where ω_{cut} is the cutoff angular frequency of the respective 2D mode, and Z_0 is the impedance of free space ($Z_0 \approx 376.73\ \Omega$).

Combining (6.25) with (6.22) in the frequency domain results in the following nonlinear eigenvalue problem

$$(\mathbf{A}_{\mathrm{f}} - \mathbf{B}_{\mathrm{f}}\underline{\mathbf{D}}_Z^{-1}(\underbrace{j\underline{\omega}}_{\underline{\lambda}})\mathbf{B}_{\mathrm{f}}^{\mathrm{T}})\underline{\mathbf{x}}_{\mathrm{f}} = \underbrace{j\underline{\omega}}_{\underline{\lambda}}\,\underline{\mathbf{x}}_{\mathrm{f}}, \tag{6.29}$$

where $\underline{\lambda}$ and $\underline{\mathbf{x}}_{\mathrm{f}}$ denote the complex-valued eigenvalues and eigenvectors, respectively. A comprehensive study of the numerical methods to solve the nonlinear eigenvalue problem is presented in [142, 155, 156]. The eigenvalues of (6.29) are then used to calculate the resonant frequency and the external quality factor of the lossy modes

$$f_n = \frac{\Im\{\underline{\lambda}_n\}}{2\pi}, \quad Q_{\mathrm{ext},n} = -\frac{\Im\{\underline{\lambda}_n\}}{2\Re\{\underline{\lambda}_n\}}. \tag{6.30}$$

The eigenvectors of (6.29) contain information about the field distribution of the lossy eigenmodes. This information could be exploited to compute the relative energy flux of the eigenmodes through the waveguide ports. The elementwise multiplication of the modal currents and modal voltages of the port modes yields the total external power as follows

$$\begin{aligned} P_{\mathrm{ext},n} &= P_{1,1,n} + \cdots + P_{1,M_1,n} + \cdots + P_{p,1,n} + \cdots + P_{p,M_p,n} \\ &= \Re\{\underline{\mathbf{i}}_{\mathrm{ext},n}^{*}\underline{\mathbf{v}}_{\mathrm{ext},n}\} = \Re\{-\underline{\mathbf{x}}_{\mathrm{f},n}^{*}\mathbf{B}_{\mathrm{f}}\underline{\mathbf{D}}_Z^{-1}(j\underline{\omega}_n)\mathbf{B}_{\mathrm{f}}^{\mathrm{T}}\underline{\mathbf{x}}_{\mathrm{f},n}\}, \end{aligned} \tag{6.31}$$

where $P_{p,M_p,n}$ denotes the power flow of the mode n through the mode M_p of port p, and $\underline{\mathbf{i}}_{\mathrm{ext},n}^{*}$ is the transpose conjugate of $\underline{\mathbf{i}}_{\mathrm{ext},n}$. A quality factor could be defined to account for the coupling of the resonant mode to each waveguide port mode as follows

$$\frac{1}{Q_{\mathrm{ext},n}} = \frac{P_{\mathrm{ext},n}}{\omega_n U_n} = \underbrace{\frac{P_{1,1,n}}{\omega_n U_n}}_{\frac{1}{Q_{\mathrm{ext},1,1,n}}} + \cdots + \underbrace{\frac{P_{1,M_1,n}}{\omega_n U_n}}_{\frac{1}{Q_{\mathrm{ext},1,M_1,n}}} + \cdots + \underbrace{\frac{P_{p,1,n}}{\omega_n U_n}}_{\frac{1}{Q_{\mathrm{ext},p,1,n}}} + \cdots + \underbrace{\frac{P_{p,M_p,n}}{\omega_n U_n}}_{\frac{1}{Q_{\mathrm{ext},p,M_p,n}}}. \tag{6.32}$$

The external quality factor corresponding to the port p is subsequently defined as

$$\frac{1}{Q_{\mathrm{ext},p,n}} = \sum_{m=1}^{M_p} \frac{1}{Q_{\mathrm{ext},p,m,n}}. \tag{6.33}$$

The external quality factor obtained by (6.33) provides a measure to determine the contribution of port p to the damping of mode n.

6.2 Single-cell cavity at 400.79 MHz

In this section, the HOM couplers that were optimized in Chapter 5 are applied to the single-cell cavity designed in Chapter 4. As demonstrated in Figure 5.5, the modes in the first dipole passband are trapped in the single-cell cavity and require strong damping. As shown in Table 6.1, the transverse impedance threshold for the Z-pole option is around 9.7 kΩ/m. The $R/Q_\perp$ of the TM_{110} mode in the single-cell cavity is 27.8 Ω. Therefore, in order to reduce the impedance of the cavity to below the synchrotron radiation threshold according to (2.47), Q_{ext} of the TM_{110} modes should be below 63. This requires a very strong damping of the modes in the first dipole band. In order to fulfill this aim, several hook-type couplers as optimized in Section 5.2.1 are attached to the single-cell cavity, and the Q_{ext} of the modes in the first dipole band are computed. As shown in Figure 6.5 (a), each new coupler is added with a different mounting angle to capture different polarizations of the dipole modes. When two hook-type couplers are added to one side of the cavity, the field of some of the dipole modes is pushed toward the opposite side of the cavity and is not damped properly. Thus, two hook-type couplers on each side of the cavity are required to strongly damp different polarizations of the dipole modes that are tilted to either side of the cavity. As demonstrated in Figure 6.5 (b), at least four hook-type couplers are required to reduce the Q_{ext} of the dipole modes to below 63.

Based on the above results, six damping schemes are devised, as shown in Figure 6.6. The results shown in this section were partially presented in [150]. In the first damping scheme, four hook-type couplers (denoted by 4H) are connected to the cavity. The studies are conducted on a single-cavity module, a four-cavity module and a four-cavity module with tapering. The tapers at the end of the module connect the large beam-pipe radius inside the module (here 156 mm) to the smaller beam-pipe radius outside the module (assumed to be 50 mm). A transition length of 300 mm is considered for the tapers. For more information about the tapers, refer to [147].

LHC-type HOM couplers that consist of two probe-type and two hook-type HOM couplers are used in the second damping scheme (denoted by 2H2P). The hook-type couplers are optimized for strong coupling to the first dipole band (refer to

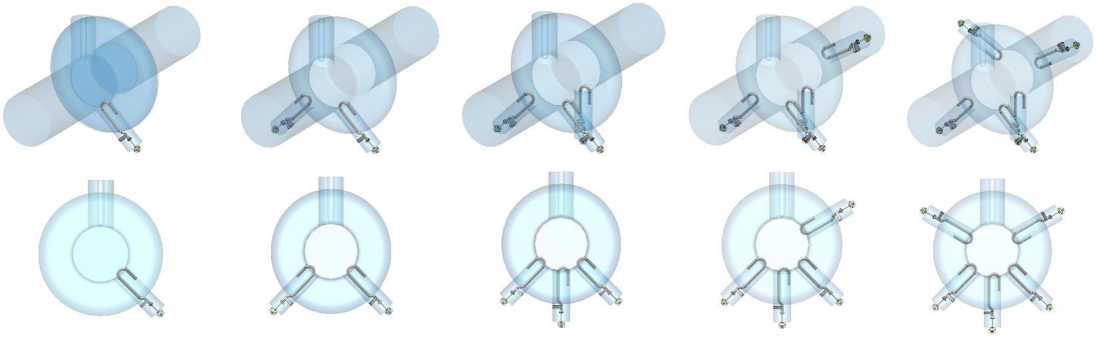

(a) HOM damping schemes using the hook-type HOM coupler

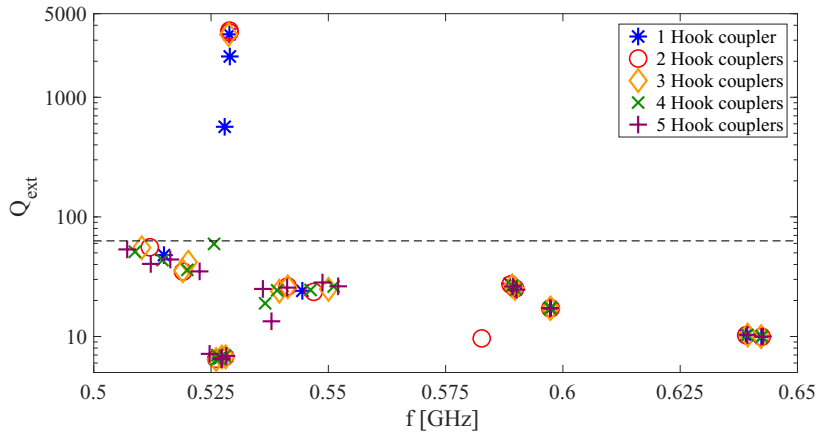

(b) Q_{ext} of the modes around the first dipole passband of the single-cell cavity

Figure 6.5: Different numbers of hook-type couplers are connected to the single-cell cavity to reduce the Q_{ext} of the modes in the first dipole passband to below 63 (indicated by the horizontal dashed line).

Section 5.2.1) while the probe-type couplers are exploited for the damping of high-frequency HOMs (refer to Section 5.2.2).

Five rectangular waveguide couplers with dimensions of 292.1 mm × 146.05 mm are used in the third damping scheme (referred to as 5RWG). The cutoff frequency of the TE_{10} mode of the WG is 513 MHz, which is below the frequency of the first HOM of the cavity (around 529 MHz). WG couplers have a broadband transmission at high frequencies, but show a rather low efficiency in the damping of the first dipole passband. Thus, a WG HOM coupler (for damping high-frequency modes) and three hook-type couplers (for damping the first dipole passband) are combined in the fourth damping scheme (referred to as 3H1RWG). The dimensions of the WG coupler are set to 280 mm × 140 mm, which results in a cutoff frequency of 535 MHz and 1071 MHz for the TE_{10} and TE_{01} modes, respectively.

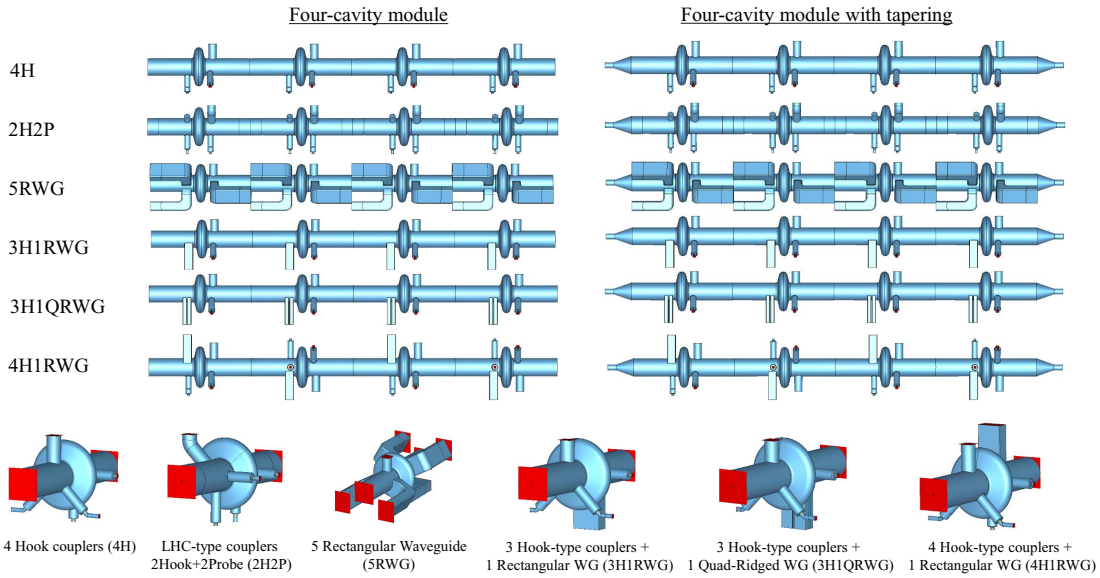

Figure 6.6: Various HOM damping schemes are applied to the single-cavity module, the four-cavity module and the four-cavity module with tapering. The tapers at the end of the module connect the large beam-pipe radius inside the module (here 156 mm) to the smaller beam-pipe radius outside the module (assumed to be 50 mm). A transition length of 300 mm is considered for the tapers.

By introducing ridges to the WG, the cutoff frequency of the WG modes could be reduced. Thus, in the fifth damping scheme, a QRWG is combined with three hook-type couplers (referred to as 3H1QRWG). The dimensions of the QRWG are set to $a_{\mathrm{wg}} = 2b_{\mathrm{wg}} = 280\,\mathrm{mm}$, $r_{\mathrm{aw}} = r_{\mathrm{bw}} = 20\,\mathrm{mm}$, $r_{\mathrm{ah}} = 25\,\mathrm{mm}$ and $r_{\mathrm{bh}} = 100\,\mathrm{mm}$ (see Figure 5.17). The resulting cutoff frequencies of the first two modes of the QRWG (TE_{10} and TE_{01}-like modes), with 3 mm blending of the ridge edges, are 494 MHz and 502 MHz, respectively. For this reason, the QRWG can couple to two polarizations of the TE_{11} mode in the beam pipe (which generally couple to the TM_{110} and TE_{111} modes of the cavity).

A combination of a WG and four hook-type couplers is used in the sixth scheme (denoted by 4H1RWG). The dimensions of the WG coupler are similar to those of the 3H1RWG scheme. The couplers are added alternately in opposite directions in the module to study the influence on the reduction of the transverse kick applied by the input couplers to the beam at FM frequency.

Next, the propagation of the HOM power into the couplers is studied. For this purpose, the fundamental power coupler (FPC), HOM couplers, and beam pipes (BP) are terminated with WG ports in each setup. The cutoff frequency of the last port mode has to be above 4.1 GHz (which is the assumed upper bound for $P_{\text{M-Z}}$ in Figure 6.4 (a)). The number of port modes in each damping schemes is presented in

Table 6.3. The wakefield solver of CST Studio Suite® is used to excite the structure with a single Gaussian-shaped bunch with a length of 12.1 mm at a 5 mm offset from the center of the cavity. The relatively short bunch length of 12.1 mm demands a very fine mesh for accurately resolving fields up to around 8.4 GHz (at which the beam spectral lines reach -20 dB of their peak value). However, since we aim to calculate the RF properties of the cavity only up to 4.1 GHz and rather approximate the HOM power at higher frequencies, a coarser mesh was used. With around 176 M hexahedral mesh cells, a time step width of 0.76 ps and a minimum mesh step of 0.9 mm, the 4H1RWG damping scheme (the case of the four-cavity module with tapering with a total length of 7.884 m) represents the most computationally demanding setup. For a wakelength of 100 m the total computational time was around 122 h on a PC with Intel(R) Xeon(R) CPU E5-2643 v3, 3.4 GHz processor frequency and 64 GB RAM. The signals scattered into different modes of each port were then collected, and the spectral weighting method (as explained in Section 6.1.3) was exploited to account for the Z-pole beam filling scheme.

Table 6.3: The number of modes considered for each waveguide port in the set-up of the simulation models shown in Figure 6.6. The cutoff frequency of the last port mode has to be above 4.1 GHz (to allow coupling to the modes in the $P_{\text{M-Z}}$ range, see Figure 6.4 (a)).

	BP*	FPC	Hook	Probe	RWG	QRWG
4H	100 / 12	20	5	-	-	-
2H2P	100 / 12	20	5	5	-	-
5RWG	100 / 12	20	-	-	60	-
3H1RWG	100 / 12	20	5	-	80	-
3H1QRWG	100 / 12	20	5	-	-	45
4H1RWG	100 / 12	20	5	-	80	-

* For modules without tapering 100 port modes are considered at the beam pipes, and 12 port modes are considered for modules with tapering.

The longitudinal and transversal impedance of the cavities are shown in Figure 6.7 and 6.8, respectively. As shown in Figure 6.7, no dangerous longitudinal mode is trapped in the cavities and modules (due to the large beam-pipe radius), and the longitudinal impedance of each damping scheme is below the impedance limit set by synchrotron radiation. The transversal impedance of the 3H1QRWG and 4H1RWG schemes are below the transversal stability threshold. The other schemes have at least one mode that passes the transversal stability threshold. There is also a large transversal kick at the FM generated by the input coupler (in order to achieve a low loaded quality factor, the input coupler is inserted deep into the cavity). This problem could be overcome by installing couplers in the opposite direction in the module, as shown for the 4H1RWG scheme.

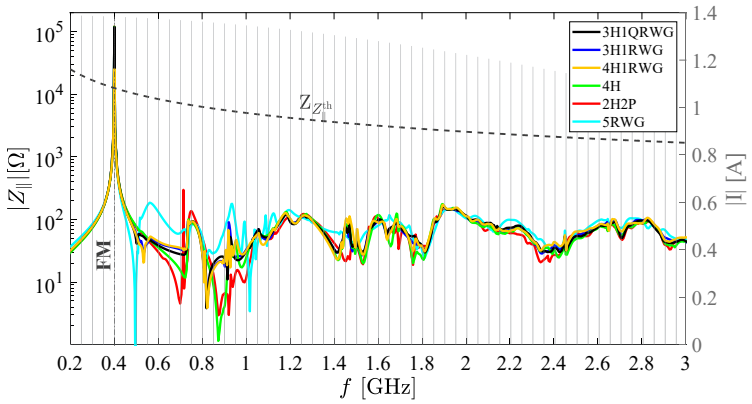

(a) Longitudinal impedance of the single-cavity module

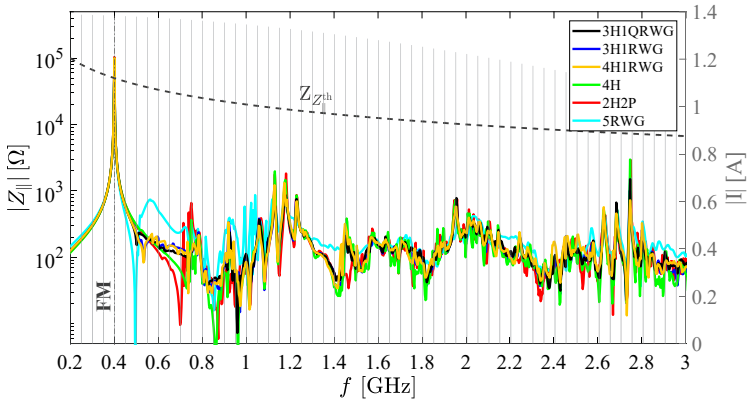

(b) Longitudinal impedance of the four-cavity module

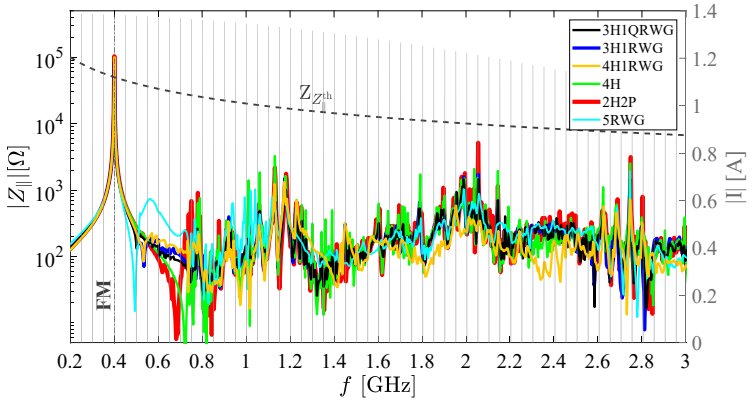

(c) Longitudinal impedance of the four-cavity module with tapering

Figure 6.7: Longitudinal impedance of the cavities with different HOM damping schemes (as shown in Figure 6.6). The wake impedance is calculated from a wakelength of 100 m excited by a beam with 5 mm offset from the center of the cavity (at (x, y) = (3.54 mm, 3.54 mm)). The impedance threshold dictated by the synchrotron radiation is normalized to the number of cavities (or modules) required for the Z-pole. The spectrum of the beam is shown on the right-side y-axis in gray color.

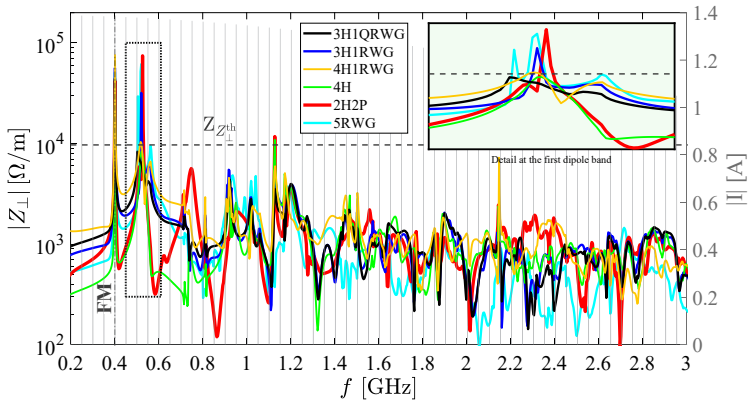

(a) Transversal impedance of the single-cavity module

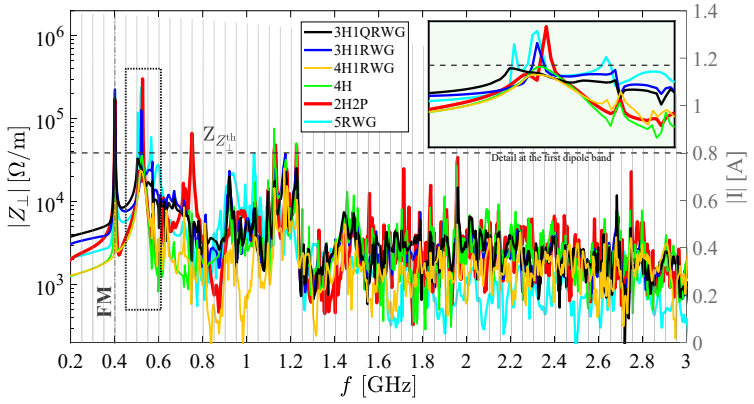

(b) Transversal impedance of the four-cavity module

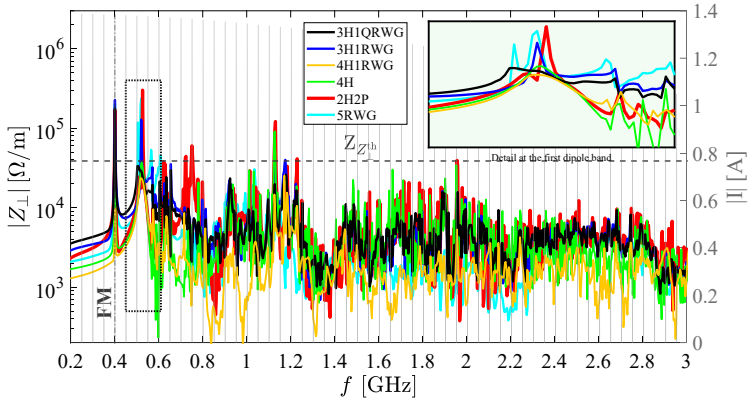

(c) Transversal impedance of the four-cavity module with tapering

Figure 6.8: Transversal impedance of the cavities using different HOM damping schemes as shown in Figure 6.6. The wake impedance is calculated from a wakelength of 100 m excited by a beam with 5 mm offset from the center of cavity (at (x, y) = (3.54 mm, 3.54 mm)). The impedance threshold dictated by the synchrotron radiation is normalized to the number of cavities (or modules) required for the Z-pole. The spectrum of the beam is shown on the right-side y-axis in gray color.

The total HOM power $P_{\mathrm{tot-Z}}$ as well as $P_{\mathrm{L-Z}}$, $P_{\mathrm{M-Z}}$ and the percentage of power absorbed by each type of coupler are given in Table 6.4. On average, the damping schemes with WGs, either in the single-cavity module or the four-cavity module, have a larger HOM power. There are two possible explanations for this difference. The first explanation is that the HOM powers of the other damping schemes are underestimated. In other words, during the considered time period, most of the HOM power propagates out of the ports in the damping schemes with WGs, while in the other damping schemes, a large part of the HOM energy remains in the cavity. Subsequently, the HOM power of such schemes is underestimated. In order to verify this explanation, the energy remaining in the four-cavity modules is investigated, as shown in Figure 6.9. In both the four-cavity module and the four-cavity module with tapering, the remaining energy has reached a stable value after 350 ns. Since there is no large longitudinal HOM trapped in the cavities (see Figure 6.7), the remaining energy in the cavities mostly corresponds to the FM. This implies that the HOM power in the considered damping schemes is not underestimated, as almost all HOM energy has left the cavity in all studied damping schemes.

The second explanation is that the traversing beam deposits more HOM power into the cavities with WGs. The interaction of the large beam current with the cross section variations in the surrounding structure created by the WGs gives rise to a stronger wakefield and subsequently to more HOM power. To asses this claim, the loss factors of the six damping schemes are calculated for the case of the single-cavity module and presented in Table 6.5. A higher loss factor in the damping schemes with WGs affirms that the beam deposits more energy into such damping schemes. In comparison with the 4H scheme, more HOM power is also deposited into the 2H2P scheme because an additional cylinder was considered in the beam pipe for the pick-up probes in this scheme.

The HOM power in the modules with tapering is much larger than that in the modules without tapering. The reason is that the tapers add more discontinuities along the path of the beam, which subsequently increase the total loss factor. Furthermore, due to the narrower end beam pipes, the HOM field remains in the module for a longer time before being damped by the HOM couplers. Such fields have more time to interact with the subsequent bunches and produce more HOM power.

A large portion of the HOM power propagates out of the cavities and modules through the end beam pipes, e.g. around 8 kW for the damping schemes with one WG in a four-cavity module without tapering. Therefore, HOM absorbers at the end of the module are needed. WG HOM couplers, despite producing additional HOM power, have a much higher ratio of power absorption in comparison to coaxial HOM couplers. The WGs in the 3H1RWG, 3H1QRWG, and 4H1RWG schemes absorb around half of the HOM power in the module, while coaxial hook-type couplers absorb a few percent. The amount of power absorbed by the QRWGs is in the same order of that for the RWGs, but a QRWG has the advantage of coupling to two polarizations of the modes in the first dipole band at the cost of a more complicated

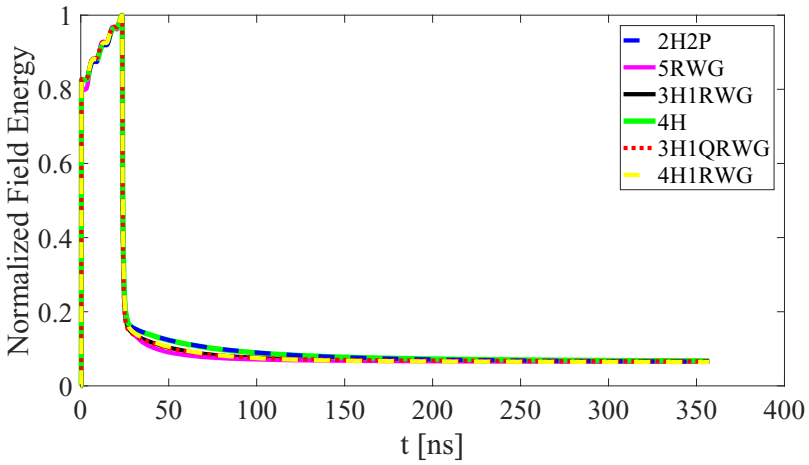

(a) Energy in the four-cavity module

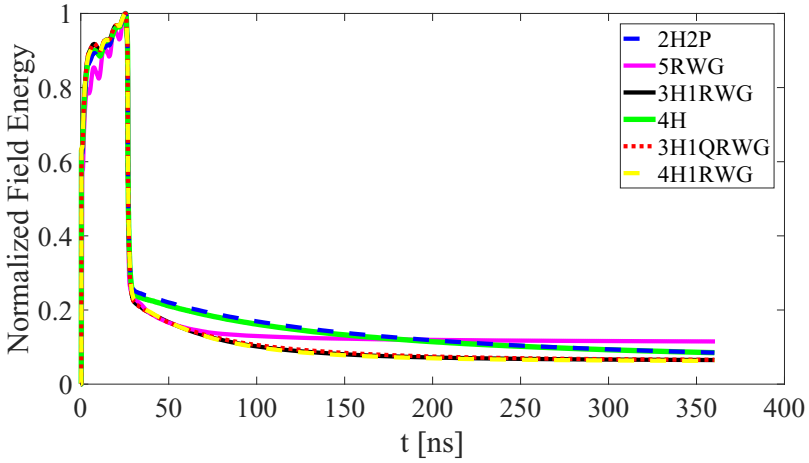

(b) Energy in the four-cavity module with tapering

Figure 6.9: Remaining energy in the four-cavity module after excitation by a relativistic Gaussian beam with a length of 12.1 mm and charge of 1 nC. The energy is computed from the wakefield calculation with a simulated wakelength of 100 m.

geometry. Altogether, the 3H1QRWG and 4H1RWG setups showed promising results in damping the transverse impedance below the stability limit and, at the same time, absorbing a significant amount of HOM power. Multipacting, complexity of fabrication, availability of high power HOM loads, cooling requirements, and robustness against perturbations are some other criteria for choosing an HOM damping scheme. These analyses are outside the scope of this thesis and remain to be studied for the decision on a final design.

Table 6.4: HOM power propagating through each coupler in various HOM damping schemes for the beam spectrum shown in Figure 6.4 (a) (Z option).

	$P_{\mathrm{L-Z}}{}^{*}$	$P_{\mathrm{M-Z}}{}^{*}$	$P_{\mathrm{tot-Z}}{}^{*}$	BP	FPC	Hook	Probe	RWG	QRWG
	[kW]	[kW]	[kW]	[%]	[%]	[%]	[%]	[%]	[%]
Single-cavity module									
4H	2.08	1.59	4.35	86.83	8.74	4.43	-	-	-
2H2P	2.50	1.73	4.97	86.35	8.24	1.82	3.59	-	-
5RWG	5.39	2.05	8.33	36.20	4.54	-	-	59.26	-
3H1RWG	3.10	1.69	5.51	62.51	6.51	1.53	-	29.45	-
3H1QRWG	3.24	1.74	5.72	59.84	6.04	1.63	-	-	32.49
4H1RWG	3.67	1.87	6.34	60.26	7.11	3.05	-	29.58	-
Four-cavity module									
4H	5.93	7.93	17.25	61.78	29.65	8.57	-	-	-
2H2P	7.55	10.20	22.13	55.57	30.23	3.05	11.15	-	-
5RWG	20.31	10.78	35.71	14.98	5.52	-	-	79.50	-
3H1RWG	10.28	8.89	22.98	33.59	14.62	2.6	-	49.19	-
3H1QRWG	10.76	9.54	24.38	33.18	14.80	2.48	-	-	49.54
4H1RWG	12.49	9.68	26.32	32.58	16.02	3.89	-	47.51	-
Four-cavity module with tapering									
4H	10.42	18.44	36.76	21.44	64.87	13.69	-	-	-
2H2P	10.39	18.28	36.49	19.46	64.57	6.22	9.75	-	-
5RWG	21.50	18.22	47.52	8.95	7.35	-	-	83.70	-
3H1RWG	13.80	18.65	40.43	13.55	27.64	3.11	-	55.70	-
3H1QRWG	15.22	20.37	44.31	12.80	27.88	2.85	-	-	56.47
4H1RWG	16.41	20.68	45.94	15.40	26.78	4.05	-	53.77	-

[*] $P_{\mathrm{L-Z}}$ is the HOM power deposited up to 2.0 GHz (not including the FM), whereas $P_{\mathrm{M-Z}}$ corresponds to the power between 2.0 GHz - 4.1 GHz and $P_{\mathrm{tot-Z}}$ is the total HOM power approximated for the whole spectrum using (6.18). This power is approximated from the wakefield calculation with a simulated wakelength of 100 m.

Table 6.5: The loss factor of the single-cavity modules shown in Figure 6.6 for a bunch length of 12.1 mm. In the wakefield calculation, "indirect interfaces" is considered as the wake integration method, and 10 lines per sigma are considered for the longitudinal mesh refinement of the particle beam (see Appendix A.1). The resulting number of hexahedral mesh cells were between 230 M to 290 M, depending on the damping schemes.

	4H	2H2P	5RWG	3H1RWG	3H1QRWG	4H1RWG
$k_{\parallel}$ [V/pC]	0.150	0.161	0.227	0.165	0.169	0.178

6.3 Four-cell cavity at 400.79 MHz

Five damping schemes, as depicted in Figure 6.10, are studied for the damping of HOMs in the four-cell 400 MHz cavities. In the first damping scheme, the cavity is equipped with two DQW HOM couplers, as optimized in Section 5.2.3 and denoted by 2DQW. In order to capture different polarizations of the dipole modes, the couplers are rotated by 90° with respect to each other and attached to the beam pipe. In the second damping scheme, two DQW couplers and one QRWG are used (denoted by 2DQW1QRWG). The dimensions of the QRWG are again set to $a_{\mathrm{wg}} = 2b_{\mathrm{wg}} = 280\,\mathrm{mm}$, $r_{\mathrm{aw}} = r_{\mathrm{bw}} = 20\,\mathrm{mm}$, $r_{\mathrm{ah}} = 25\,\mathrm{mm}$ and $r_{\mathrm{bh}} = 100\,\mathrm{mm}$ (see Figure 5.17), with a 3 mm blending of the ridge edges. The resulting cutoff frequencies of the first two TE_{10} and TE_{01}-like modes are 494 MHz and 502 MHz, respectively. In the third and fourth damping schemes, a combination of one rectangular WG with two DQW HOM couplers is employed. The dimensions of the WGs are set to 280 mm × 140 mm, which yields a cutoff frequency of 535 MHz and 1071 MHz for the first two modes of the WG, respectively. In comparison to the third damping scheme, the orientation of the WG is varied by 45° in the fourth scheme to study the influence of the mounting angle of the WG on the damping of HOMs. These two damping schemes are denoted by 2DQW1RWG(a) and 2DQW1RWG(b), respectively. In the fifth damping scheme, the LHC-type couplers (two hook-type and two probe-type, denoted by 2H2P) are studied. The studies are conducted on a single four-cell-cavity module and a four four-cell-cavity module.

In order to calculate the HOM power for each scheme, couplers and beam pipes were terminated with WG ports. The number of 2D modes of the ports attached to the beam pipes, input couplers, coaxial HOM couplers, and WGs were set to 100, 20, 5, and 50, respectively. The structure was then excited by a Gaussian bunch with a length of 25 mm at a 5 mm offset from the center of the cavity, and the wakefield solver was run for a simulated wakelength of 100 m. The most computationally demanding simulation was the four-cavity module of 2DQW1QRWG setup with around 125 M hexahedral mesh cells, a time step width of 1.2 ps and a minimum mesh step of 1.0 mm, which took around 68 h on a PC with Intel(R) Xeon(R) CPU E5-2687W v2, 3.4 GHz processor frequency and 256 GB RAM. The port signals were then collected and normalized to the Fourier transform of the exciting beam.

The HOM power and the percentage of power absorbed by each coupler for the W beam is given in Table 6.6, and for the H beam in Table 6.7. In the single four-cell-cavity module, more than 70% of the HOM power propagates out of the beam pipes in all of the considered damping schemes. In the four-cavity module, this number decreases to around 30% for the damping schemes with one WG. Similar to the case of the Z-pole, around half of the HOM power is absorbed by the WG couplers in the four cavity module. The HOM power for the H beam is around 1 kW for the single four-cell-cavity module and around 4 kW for the four-cavity module. This power is distributed among the ports, i.e. among eight DQW couplers, four WG

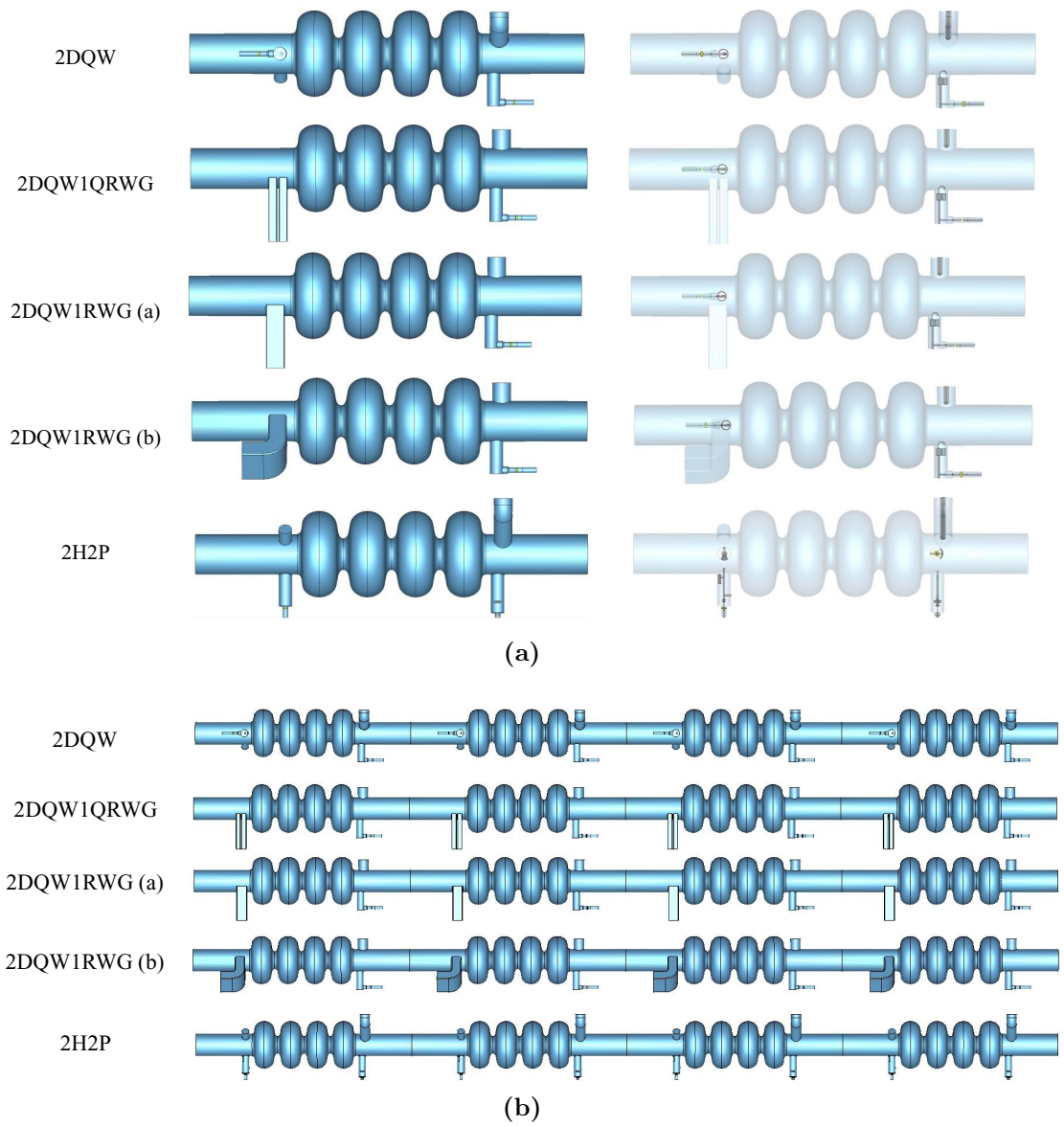

Figure 6.10: Layout of the five damping schemes considered for the four-cell 400 MHz cavities in a single four-cell-cavity module (a) and a four four-cell-cavity module (b).

couplers, four FPC, and two BPs in the four-cavity modules with WGs. The HOM power per each coaxial HOM coupler is below the 1 kW limit, which was assumed for the design of the HOM couplers in the LEP and LHC due to connectors and cable limitations [157].

The HOM power corresponding to the W beam lies in a more critical range. In the single four-cell-cavity module, there is a small difference between the HOM power of different damping schemes. However, for all of the studied schemes, the HOM

power is above 2.89 kW, which was obtained for the bare cavity (see Table 6.2). The extra HOM power is to some extent created by the geometrical variations along the beam path introduced to the structure by the HOM couplers. Thus, the damping schemes with a higher number of HOM couplers produce additional HOM power.

In the case of the four-cavity module, there is a significant difference between the HOM power of the damping schemes with WG and the damping schemes without WG. The energy remaining in the cavities and modules when applying a simulated wakelength of 100 m is shown in Figure 6.11. As shown in Figure 6.11 (b), a considerable amount of energy remains in the module 333 ns (which corresponds to a 100 m wakelength) after the beam has left the cavity. The slowly decaying energy indicates that in addition to the FM (which has a Q_{L} of around 10^6), there are highly resonating longitudinal modes whose energy has not left the cavity in the considered time interval. Therefore, the calculated HOM power is an underestimate of the actual HOM power, as the energies of such trapped modes are not taken into account. Such trapped modes can impose a severe restriction on the operation of the cavities, as their field might interact with the subsequent bunches and produce substantial HOM power. In order to fully account for the contribution of such modes, depending on their Q_{ext}, the wakefield solver should be run for a much larger wakelength. For a mode with a Q_{ext} of 5×10^3 at 1 GHz, we need a wakelength of 1.1 km to decrease the amplitude and energy of the field to 10% and 1% of their initial values, respectively. Yet, the HOM power of such trapped modes could be approximated from (6.11) by using the eigenmodes of the cavity, which provide information about the Q_{ext} and R/Q of the HOMs.

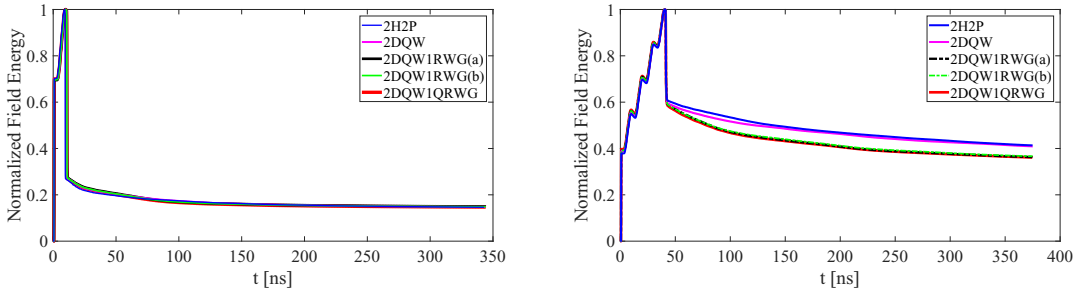

(a) Energy in the single four-cell-cavity module **(b)** Energy in the four four-cell-cavity module

Figure 6.11: The remaining energy in the cavities (shown in Figure 6.10) after excitation by a relativistic Gaussian beam with a length of 25 mm and a charge of 1 nC. The energy is computed from the wakefield calculation with a simulated wakelength of 100 m.

The calculation of the eigenmodes of the four-cavity module is computationally expensive. Therefore, the SSC method was exploited to calculate the eigenmodes of the cavities up to 1.25 GHz. In order to simulate modules with the SSC method, each module was divided into 17 segments, as shown in Figure 6.13. PEC was

assumed as the boundary condition on the walls made of superconducting niobium. The coaxial HOM couplers, input couplers, WGs, and beam pipes were terminated with WG ports. The SSC method was then used to calculate the HOMs and the associated parameters such as frequency, Q_{ext}, $R/Q_{\parallel}$, and $R/Q_{\perp}$ of the eigenmodes.

The longitudinal and transversal impedance of the single four-cell-cavity module are shown in Figure 6.12 for various damping schemes. The wakefield computations were carried out for a wakelength of 1000 m. The impedances were extrapolated as explained in [140, 141] to better resolve the impedance peaks. The lossy eigenmode impedance for the 2DQW1RWG(a) damping scheme (single four-cell-cavity module) was also computed on the basis of equations (2.46)-(2.47) using the SSC method to demonstrate consistency between the two approaches. The external quality factors of modes in the four four-cell-cavity module with different damping schemes are shown in Figure 6.14. The field of the lossy eigenmodes is used to calculate $R/Q_{\parallel}$ and $R/Q_{\perp}$, and subsequently the longitudinal and transversal impedance of the modes of the four four-cell-cavity modules.

The longitudinal impedances of all of the studied damping schemes lie below the stability threshold of the H and W beam, while only the transversal impedances of the schemes with a WG are marginally below the stability threshold of the W beam. Some detrimental HOMs resonate primarily in the beam pipes, e.g. the modes between 0.8-0.84 GHz. Such modes have a relatively high Q_{ext} in the damping schemes that only use coaxial HOM couplers. The energy of these modes can be efficiently extracted from the module by connecting a WG coupler to the beam pipes in proper orientation, i.e. 2DQW1QRWG and 2DQW1RWG(b) schemes. The modes in the hexapole, octopole, and decapole passbands have large values of Q_{ext}. However, such modes are not performance-limiting as they have a negligible value of the EM field at the center of the cavity, and thus their beam coupling impedance is typically small. Similarly, the TE monopole mode has a zero value of the electric field at the center of the cavity, and its magnetic field direction is parallel to the vector velocity of the particles. Therefore, it applies no force to the traversing particles.

The longitudinal impedance of the modes in the four-cavity module is then used to approximate the power loss in case of resonant HOM excitation. As a worst-case scenario, the mode with the highest longitudinal impedance is considered for each damping scheme. The contribution of each HOM coupler to the damping of this dangerous mode is also calculated using (6.32). The resonant power loss of these HOMs with regard to the W and H beam are shown in the third section of Tables 6.6 and 6.7, respectively. Considering the H beam, the resonant power is below 1 kW for all of the studied damping schemes. For the W beam, however, the resonant excitation power can vary between 7 kW to 18 kW in the four four-cell-cavity module, depending on the chosen damping scheme. This imposes a severe restriction on the use of a four-cell cavity for the W option. Therefore, hitting a beam spectral line at frequencies with very large longitudinal impedance should be avoided

e.g. by optimizing the beam filling scheme. Altogether, a combination of WG (or QRWG) with the DQW coaxial couplers is more effective at reducing the impedance to below the stability threshold and simultaneously absorbing a significant amount of HOM power.

Table 6.6: HOM power propagating through each coupler in various HOM damping schemes for the beam spectrum shown in Figure 6.4 (b) (W option). The third section of the table shows the power deposited into the module if an HOM with large longitudinal impedance comes into resonance with the W beam (as a worst-case scenario).

	$P_{\mathrm{L-W}}$ * [kW]	$P_{\mathrm{M-W}}$ * [kW]	$P_{\mathrm{tot-W}}$ * [kW]	BP [%]	FPC [%]	Hook [%]	Probe [%]	DQW [%]	WG [%]
Single four-cell-cavity module									
2DQW	0.94	0.79	3.2	88.8	3.8	-	-	7.4	-
2DQW1QRWG	1.13	0.82	3.5	73.8	4.2	-	-	4.9	17.1
2DQW1RWG(a)	1.14	0.82	3.5	74.0	4.2	-	-	4.8	17.0
2DQW1RWG(b)	1.17	0.89	3.7	73.9	4.2	-	-	4.8	17.1
2H2P	0.82	0.87	3.3	92.6	3.6	1.0	2.8	-	-
Four four-cell-cavity module									
2DQW	3.25	2.78	11.1	54.4	30.8	-	-	14.8	-
2DQW1QRWG	5.39	3.30	14.7	29.9	13.6	-	-	8.9	47.6
2DQW1RWG(a)	5.57	3.46	15.4	28.5	13.0	-	-	9.2	49.3
2DQW1RWG(b)	6.27	3.69	16.7	27.2	12.0	-	-	8.6	52.2
2H2P	3.08	3.05	11.7	51.8	34.1	4.7	9.4	-	-
	f_n [MHz]	$Q_{\mathrm{ext},n}$ [$\times 10^3$]	$P_{\mathrm{HOM},n}$ ** [kW]	BP [%]	FPC [%]	Hook [%]	Probe [%]	DQW [%]	WG [%]
Resonant power loss in the four four-cell-cavity module									
2DQW	746.0	2.98	11.3	32.9	2.3	-	-	64.8	-
2DQW1QRWG	1178.5	5.25	7.8	52.1	21.8	-	-	1.2	24.9
2DQW1RWG(a)	1178.5	5.41	7.8	50.5	28.7	-	-	1.4	19.4
2DQW1RWG(b)	1178.5	5.46	8.1	40.7	28.8	-	-	2.2	28.3
2H2P	802.1	45.7	18.0	14.2	12.1	0.7	73.0	-	-

* $P_{\mathrm{L-W}}$ is the HOM power deposited up to 2.0 GHz (not including the FM), whereas $P_{\mathrm{M-W}}$ corresponds to the power between 2.0 GHz - 4.1 GHz and $P_{\mathrm{tot-W}}$ is the total HOM power approximated for the whole spectrum from (6.19). This power is approximated from the wakefield calculation with a simulated wakelength of 100 m.

** Resonant power loss of the HOM with the highest longitudinal impedance (calculated from $P_{\mathrm{HOM},n} \approx R/Q_{\parallel,n} \cdot Q_{\mathrm{ext},n} \cdot I_0^2$).

Table 6.7: HOM power propagating through each coupler in various HOM damping schemes for the beam spectrum shown in Figure 6.4 (c) (H option). The third section of the table shows the power deposited into the module if an HOM with large longitudinal impedance comes into resonance with the H beam (as a worst-case scenario).

	$P_{\mathrm{L-H}}$ * [kW]	$P_{\mathrm{M-H}}$ * [kW]	$P_{\mathrm{tot-H}}$ * [kW]	BP [%]	FPC [%]	Hook [%]	Probe [%]	DQW [%]	WG [%]
Single four-cell-cavity module									
2DQW	0.19	0.19	0.81	91.3	3.7	-	-	5.0	-
2DQW1QRWG	0.25	0.20	0.90	76.3	4.1	-	-	3.6	16.0
2DQW1RWG(a)	0.25	0.20	0.90	75.3	4.3	-	-	3.9	16.5
2DQW1RWG(b)	0.26	0.22	0.96	76.3	4.0	-	-	3.6	16.1
2H2P	0.19	0.21	0.87	93.1	3.5	1.0	2.4	-	-
Four four-cell-cavity module									
2DQW	0.64	0.68	2.83	56.2	32.5	-	-	11.3	-
2DQW1QRWG	1.03	0.82	3.66	32.2	14.4	-	-	6.4	47.0
2DQW1RWG(a)	1.07	0.85	3.80	30.6	13.7	-	-	6.5	49.2
2DQW1RWG(b)	1.14	0.90	4.04	29.9	13.0	-	-	6.1	51.0
2H2P	0.69	0.73	3.06	52.8	33.8	4.6	8.8	-	-
	f_n [MHz]	$Q_{\mathrm{ext},n}$ [$\times 10^3$]	$P_{\mathrm{HOM},n}$ ** [kW]	BP [%]	FPC [%]	Hook [%]	Probe [%]	DQW [%]	WG [%]
Resonant power loss in the four four-cell-cavity module									
2DQW	746.0	2.98	0.4	32.9	2.3	-	-	64.8	-
2DQW1QRWG	1178.5	5.25	0.3	52.1	21.8	-	-	1.2	24.9
2DQW1RWG(a)	1178.5	5.41	0.3	50.5	28.7	-	-	1.4	19.4
2DQW1RWG(b)	1178.5	5.46	0.3	40.7	28.8	-	-	2.2	28.3
2H2P	802.1	45.7	0.7	14.2	12.1	0.7	73.0	-	-

* $P_{\mathrm{L-H}}$ is the HOM power deposited up to 2.0 GHz (not including the FM), whereas $P_{\mathrm{M-H}}$ corresponds to the power between 2.0 GHz - 4.1 GHz and $P_{\mathrm{tot-H}}$ is the total HOM power approximated for the whole spectrum from (6.20).

** Resonant power loss of the HOM with the highest longitudinal impedance (calculated from $P_{\mathrm{HOM},n} \approx R/Q_{\parallel,n} \cdot Q_{\mathrm{ext},n} \cdot I_0^2$).

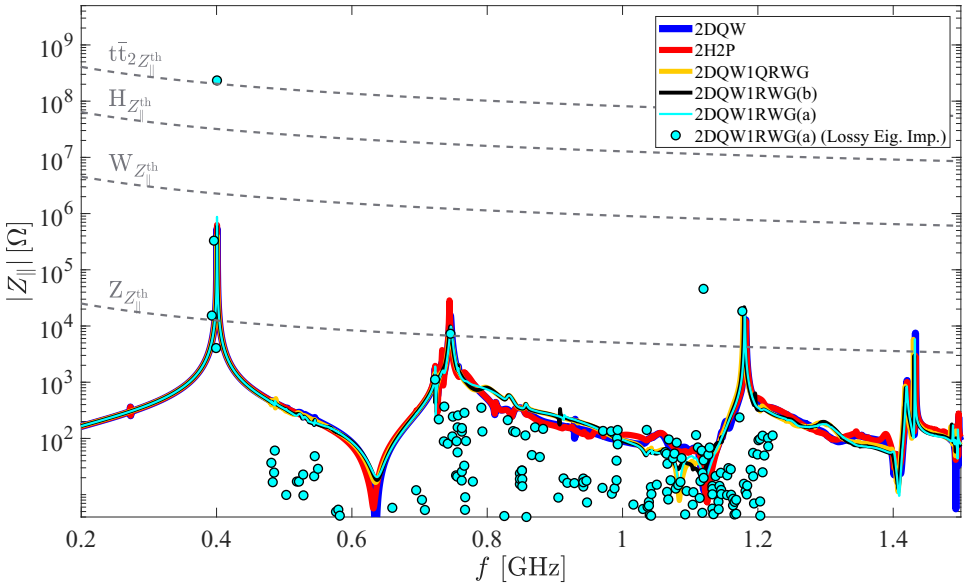

(a) Longitudinal impedance

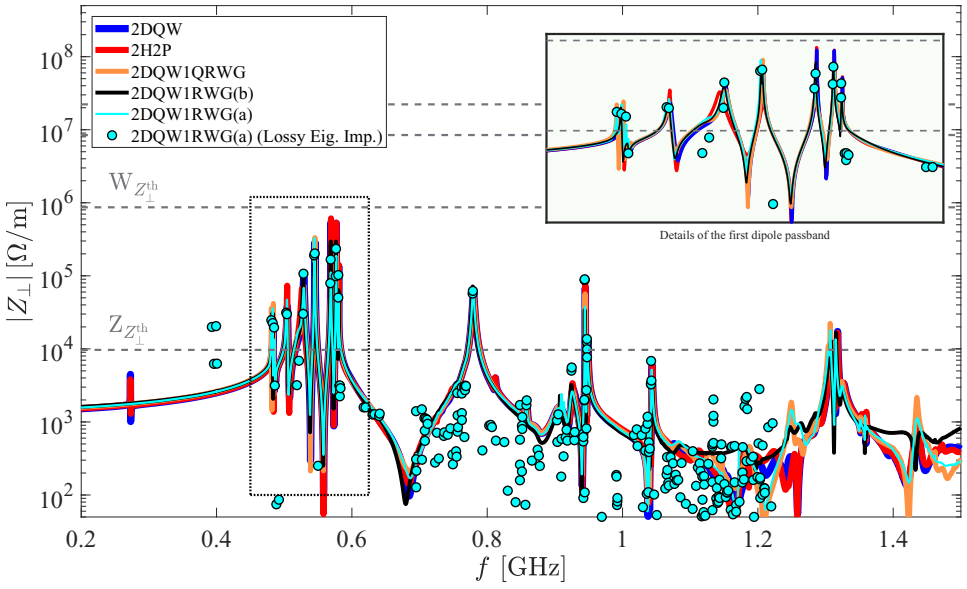

(b) Transversal impedance

Figure 6.12: Longitudinal impedance (a) and transversal impedance (b) of the single four-cell-cavity module. The wake impedances (solid lines) are calculated from the wake potentials with a wakelength of 1000 m. The markers correspond to the lossy eigenmodes calculated with the SSC method. The mode with high longitudinal impedance at 1.12 GHz is an octopole mode with $Q_{\text{ext}} = 2.2 \times 10^8$ and $R/Q_\parallel = 5.0 \times 10^{-4}$.

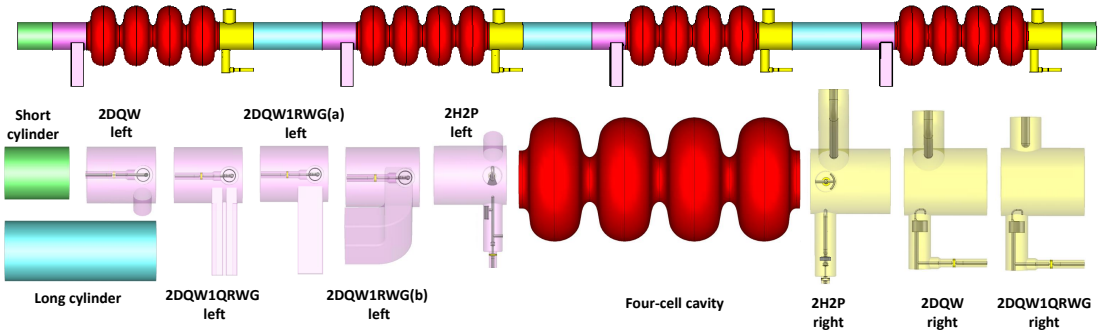

Figure 6.13: In the SSC method, the module is divided into 17 subsections. The top picture shows the complete module, while the bottom pictures show the different segments from which the whole modules shown in Figure 6.10 can be composed. The mesh density and the number of port modes for each segment are given in Appendix A.2.

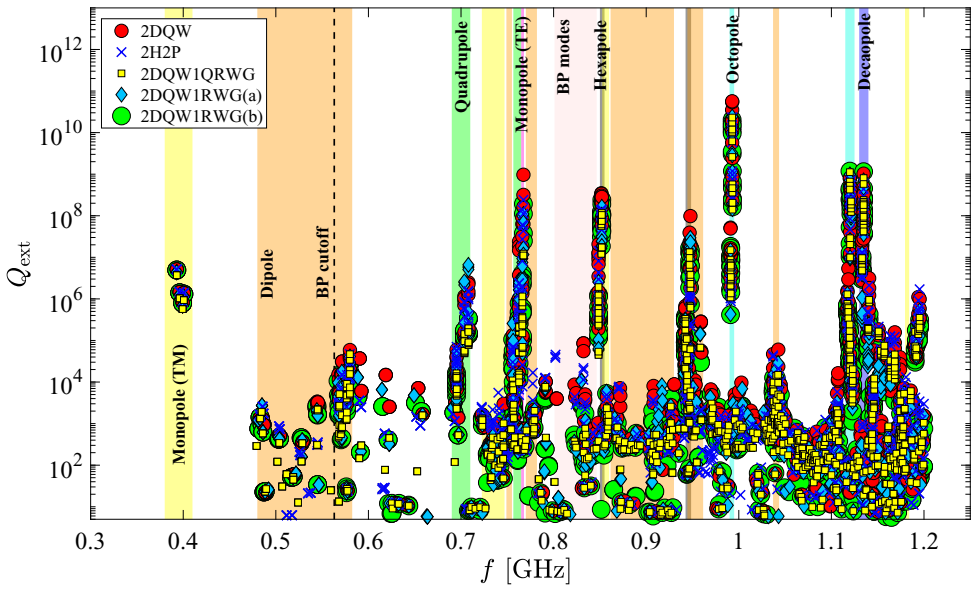

Figure 6.14: Q_{ext} of the modes in the four four-cell-cavity modules shown in Figure 6.10.

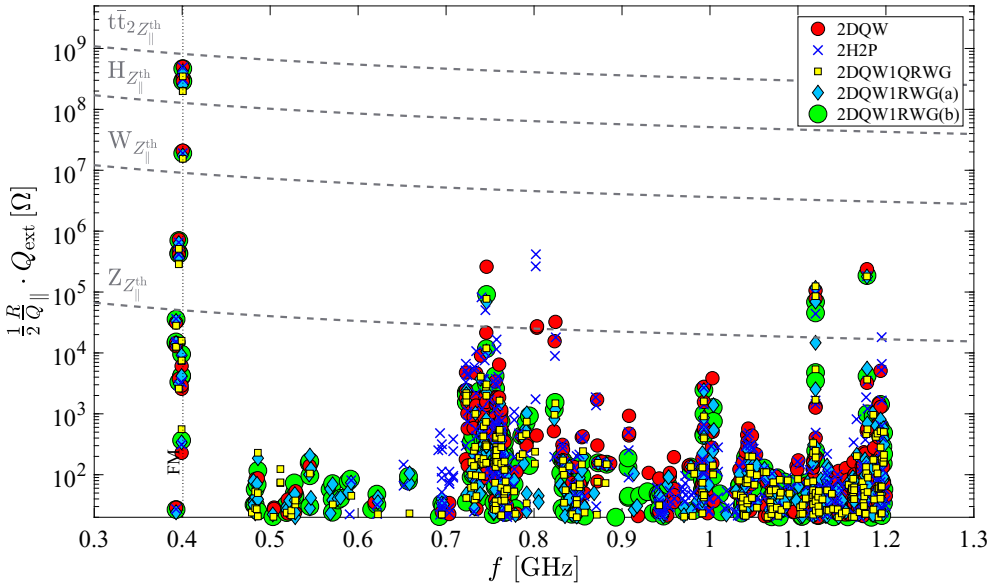

(a) Longitudinal impedance

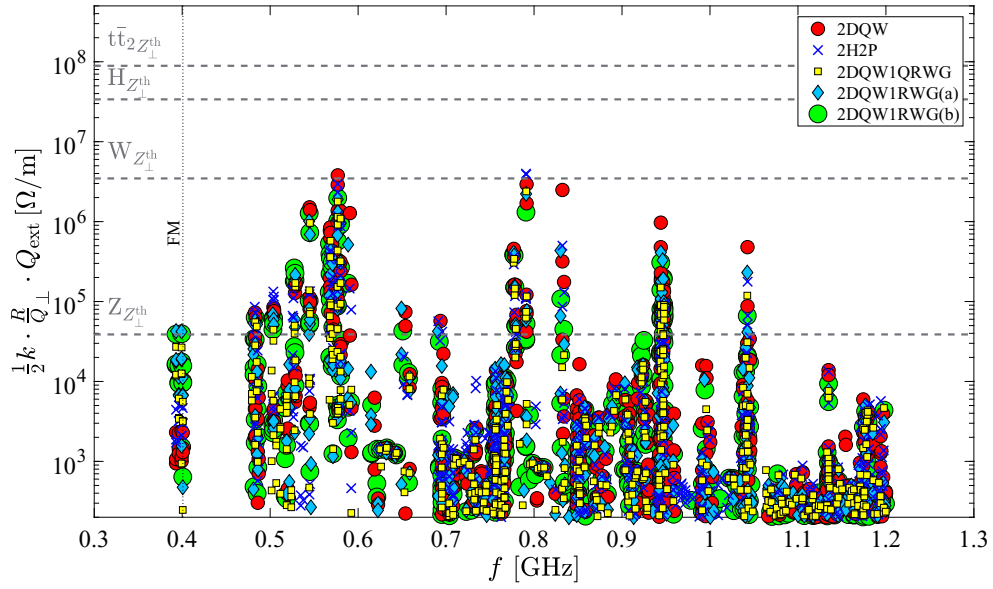

(b) Transversal impedance

Figure 6.15: Longitudinal and transversal impedance of the four four-cell-cavity modules shown in Figure 6.10. The impedances are calculated from the lossy eigenmodes computed with the SSC method using (2.46) and (2.47). The impedance thresholds are normalized to the number of modules required for each energy option.

6.4 Five-cell cavity at 801.58 MHz

In this section, the five damping schemes shown in Figure 6.16 are applied to the five-cell 800 MHz cavity that was designed in Section 4.3.2. In the first damping scheme, the cavities are equipped with two DQW HOM couplers (denoted as 2DQW). As indicated earlier, the WG couplers have a broadband transmission at high frequencies in comparison to the coaxial HOM couplers, whereas the coaxial couplers achieve better results for the modes in the first dipole passband. For this reason, a combination of a single WG for high-frequency modes with coaxial dampers targeted at low-frequency HOMs is used in the second as well as the third scheme. The WG couplers also provide additional damping of the modes that might get trapped in the beam pipes connecting the cavities. In the second damping scheme, a combination of two DQW HOM couplers with a QRWG is used and referred to as 2DQW1QRWG. The dimensions of the QRWG are set to $a_{\mathrm{wg}} = 2b_{\mathrm{wg}} = 140\,\mathrm{mm}$, $r_{\mathrm{aw}} = r_{\mathrm{bw}} = 10\,\mathrm{mm}$, $r_{\mathrm{ah}} = 12.5\,\mathrm{mm}$ and $r_{\mathrm{bh}} = 50\,\mathrm{mm}$ (see Figure 5.17) with a 1.5 mm blending of the ridge edges. The cutoff frequencies of the first two modes of the QRWG are 0.989 GHz and 1.004 GHz, respectively. Similarly, in the third damping scheme, two DQW couplers are combined with a rectangular WG coupler with the dimensions $135 \times 67.5\,\mathrm{mm}$, which yields a cutoff frequency of 1.11 GHz and 2.22 GHz for the TE_{10} and TE_{01} modes, respectively. This damping scheme is denoted as 2DQW1RWG.

Three rectangular waveguide couplers are used in the fourth scheme (denoted as 3RWG). The dimensions of the WGs are set to $165.1 \times 82.55\,\mathrm{mm}$, which gives rise to a cutoff frequency of 908 MHz for the first WG mode while the frequencies of modes in the first dipole passband of the cavity are above 960 MHz. In the fifth damping scheme, LHC-type couplers composed of two hook-type and two probe-type couplers are used (denoted as 2H2P).

Similar to the previous section, WG ports are applied to those surfaces where the field energy can leave the structure. In order to ensure that modes with a frequency up to 8.1 GHz can propagate out of the ports, the number of modes at WG ports is set to 20, 5, 50, and 100 for the input couplers, coaxial HOM couplers, WG couplers, and beam pipes, respectively. Due to the larger cross-section of the WGs in the 3RWG damping scheme, the number of WG port modes for this damping scheme is set to 65. When using the hexahedral mesh in CST Studio Suite®, the ports have to be aligned with the Cartesian planes. Therefore, the coaxial part at the end of the input coupler is extended, bent and aligned with the Cartesian planes in the 2DQW and 2H2P damping schemes. The wakefield solver of CST Studio Suite® is then used to excite the cavity with a Gaussian beam with a length of 12.5 mm at a 5 mm offset from the center of the cavity. The most computationally demanding simulation corresponds to the four-cavity module of the 2DQW1QRWG scheme with 126 M hexahedral mesh cells, a minimum mesh step of 0.54 mm and a time step width of 0.64 ps. Running the simulation took around 124 h for a simulated

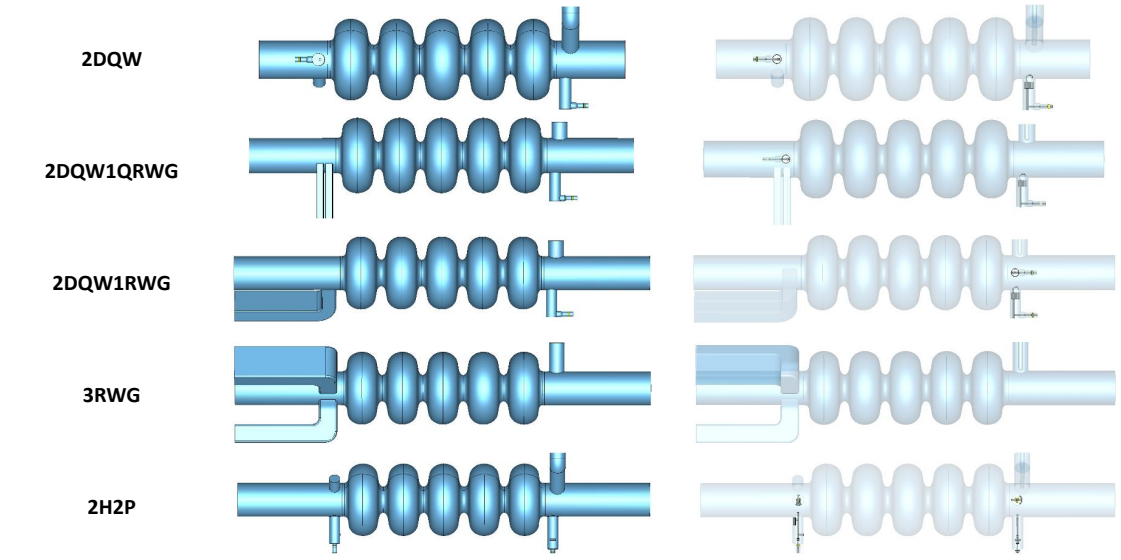

(a)

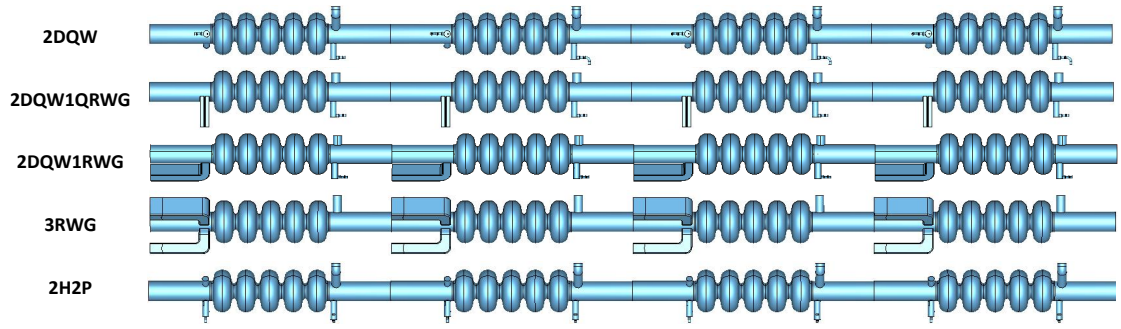

(b)

Figure 6.16: Layout of the five damping schemes considered for the five-cell 800 MHz cavities in a single five-cell-cavity module (a) and a four five-cell-cavity module (b).

wakelength of 100 m on a PC with Intel(R) Xeon(R) CPU E5-2687W v2, 3.4 GHz processor frequency and 256 GB RAM. Port signals were then collected and the equations (6.15), (6.16), (6.17) and (6.21) were used to approximate the HOM power and the percentage of power absorbed by each HOM coupler. The results are given in Table 6.8. Table 6.9 presents the HOM power deposited into a module composed of a different number of bare cavities (without any coupler) using (3.13).

A comparison between the HOM power of the single five-cell-cavity module with HOM couplers (see Table 6.8) and without HOM couplers (see Table 6.9) indicates that the HOM power approximated from the method proposed in Section 6.1.3 is slightly larger than the HOM power corresponding to the non-resonant excitation of the bare cavities calculated from (3.13). The main contributors to this difference

Table 6.8: HOM power propagating through each coupler in various HOM damping schemes for the beam spectrum shown in Figure 6.4 (d) ($t\bar{t}_2$ option). The third section of the table shows the power deposited into the module if an HOM with large longitudinal impedance comes into resonance with the $t\bar{t}_2$ beam (as a worst-case scenario).

	$P_{\mathrm{L}-t\bar{t}_2}$ * [kW]	$P_{\mathrm{M}-t\bar{t}_2}$ * [kW]	$P_{\mathrm{tot}-t\bar{t}_2}$ * [kW]	BP [%]	FPC [%]	Hook [%]	Probe [%]	DQW [%]	WG [%]
Single five-cell-cavity module									
2DQW	0.23	0.23	1.01	90.7	4.1	-	-	5.2	-
2DQW1QRWG	0.30	0.24	1.12	76.7	4.6	-	-	3.7	15.1
2DQW1RWG	0.32	0.23	1.12	76.8	2.0	-	-	6.3	14.9
3RWG	0.27	0.24	1.09	67.5	3.9	-	-	-	28.6
2H2P	0.23	0.25	1.10	92.7	3.6	1.0	2.7	-	-
Four five-cell-cavity module									
2DQW	1.02	0.98	4.41	50.1	36.5	-	-	13.4	-
2DQW1QRWG	1.31	1.01	4.78	31.6	14.9	-	-	6.3	47.2
2DQW1RWG	1.41	0.92	4.58	33.3	14.0	-	-	6.2	46.5
3RWG	1.31	0.96	4.61	23.6	8.3	-	-	-	68.1
2H2P	0.94	0.88	3.99	53.4	32.5	5.5	8.6	-	-
	f_n [MHz]	$Q_{\mathrm{ext},n}$ [$\times 10^3$]	$P_{\mathrm{HOM},n}$ ** [kW]	BP [%]	FPC [%]	Hook [%]	Probe [%]	DQW [%]	WG [%]
Resonance in the four five-cell-cavity module									
2DQW	2357.9	28.5	0.2	88.5	10.9	-	-	0.6	-
2DQW1QRWG	2357.9	16.1	0.1	47.3	14.5	-	-	0.9	37.3
2DQW1RWG	2357.9	29.0	0.2	65.6	30.7	-	-	1.5	2.2
3RWG	2357.8	9.9	0.07	24.2	1.9	-	-	-	73.9
2H2P	1566.2	75.9	0.4	1.8	30.3	14.1	53.8	-	-

* $P_{\mathrm{L}-t\bar{t}_2}$ is the HOM power up to 4.0 GHz (not including the FM), $P_{\mathrm{M}-t\bar{t}_2}$ corresponds to the power between 4.0 GHz - 8.1 GHz and $P_{\mathrm{tot}-t\bar{t}_2}$ is the total HOM power approximated for the whole spectrum from (6.21). This power is approximated from the wakefield calculation with a simulated wakelength of 100 m.

** Resonant power loss of the HOM with the highest longitudinal impedance (calculated from $P_{\mathrm{HOM},n} \approx R/Q_{\parallel,n} \cdot Q_{\mathrm{ext},n} \cdot I_0^2$).

are the additional losses created by the cross-section variations introduced by the HOM couplers. Due to the rather low beam current of the $t\bar{t}_2$ running, the resonant excitation of the beam with a longitudinal mode with a relatively high quality factor is not so critical. For example, the resonant excitation of the $t\bar{t}_2$ beam with a mode with $R/Q_{\parallel} = 1\Omega$ and $Q_{\mathrm{ext}} = 10^4$ gives rise to an HOM power of around 1 W. This value is negligible compared to the total HOM power of $t\bar{t}_2$.

The HOM power of the four-cavity module is around 4.5 kW. As indicated in Figure 6.17 (b), the energy of the field has not reached a stable value at a simulated

Table 6.9: The HOM power of the bare five-cell cavities (without any coupler) approximated from the loss factor considering the $t\bar{t}_2$ beam using (3.14) (assuming non-resonant single bunch excitation). Note that it is assumed that both beams are accelerated by the same RF structure for $t\bar{t}_2$; thus, the beam current is multiplied by a factor of two.

	1 cavity	2 cavities	3 cavities	4 cavities	5 cavities	6 cavities
$k_{\parallel}$ [V/pC] ($\sigma_z = 2.54\,\text{mm}$)	2.91	5.91	8.94	11.97	15.00	18.03
HOM power for $t\bar{t}_2$ beam [kW]	0.90	1.83	2.78	3.72	4.67	5.61

wakelength of 100 m. Therefore, in the calculation of the HOM power, the energy of some modes is not fully taken into account. Similar to the previous section, instead of running the wakefield solver for a very long wakelength, the contribution of such trapped modes can be computed by calculating the eigenmodes of the structure. The modules are thus broken down into several segments, as shown in Figure 6.18, and the SSC method is used to calculate the eigenmodes and the corresponding secondary parameters such as $R/Q_{\parallel}$, $R/Q_{\perp}$ and Q_{ext} of the four-cavity module. In order to show the consistency between the two approaches regarding the calculation of the impedance of modes with large Q_{ext}, the impedance of the single five-cell cavity for the 3RWG damping scheme is calculated using a large wakelength and compared to the results obtained from the eigenmode solution (see Figure 6.19).

The longitudinal and transversal impedance of the modes in the four-cavity module equipped with different HOM couplers are given in Figure 6.20. The respective Q_{ext} of the modes are shown in Figure 6.21. The Q_{ext} of the dipole modes that are below the beam pipe's cutoff frequency are relatively large for the 3RWG scheme. This leads to a large value of transversal impedance at the first dipole passband, as shown in Figure 6.20 (b). However, in all of the studied damping schemes, the longitudinal and transversal impedances are below the stability threshold of the $t\bar{t}_2$ option for the single five-cell cavity and the four five-cell-cavity modules, as shown in Figures 6.19 and 6.20, respectively. The modes trapped in the beam pipes in the frequency range of 1.6-1.7 GHz are not strongly damped by the coaxial couplers. The energy of such modes could be more efficiently extracted by the damping schemes with at least one WG HOM coupler.

For each damping scheme, the HOM with maximum longitudinal impedance is selected as a worst-case scenario, and the power loss corresponding to the resonant HOM excitation of this mode with the $t\bar{t}_2$ beam is calculated. The results are shown in the third section of Table 6.8. The maximum and minimum resonant HOM power are found in the 2H2P and 3RWG damping schemes with 0.4 kW and 0.07 kW HOM power, respectively. The performance-limiting longitudinal mode corresponds to the trapped modes in the beam pipes of the 2H2P damping scheme, while it is the TM_{012}

mode for the other damping schemes. However, the resulting resonant HOM power is within an acceptable level in all of the studied damping schemes. The damping scheme composed of two DQW couplers with one WG has the advantage of providing a larger margin for an increase of the beam intensity in potential machine updates or the utilization of the five-cell cavity for the H working point.

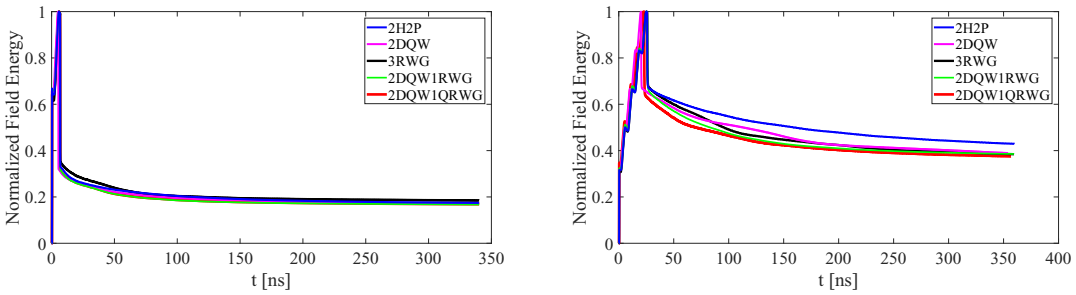

(a) Energy in the single five-cell-cavity module **(b)** Energy in the four five-cell-cavity module

Figure 6.17: Energy remaining in the cavities (as shown in Figure 6.16) after excitation by a relativistic Gaussian beam with a length of 12.5 mm and a charge of 1 nC. The energy is computed from the wakefield calculation with a simulated wakelength of 100 m.

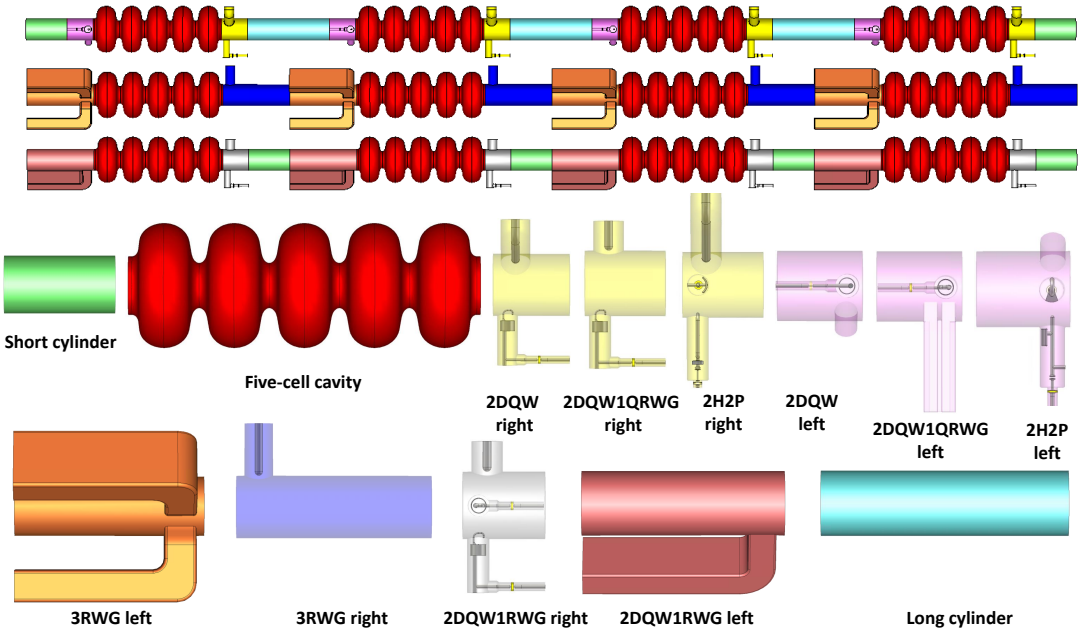

Figure 6.18: In the SSC method, the module is divided into several subsections. The first three pictures display the complete modules, while the last two rows show the different segments from which the whole modules shown in Figure 6.16 can be composed. The mesh density and the number of port modes for each segment are given in Appendix A.2.

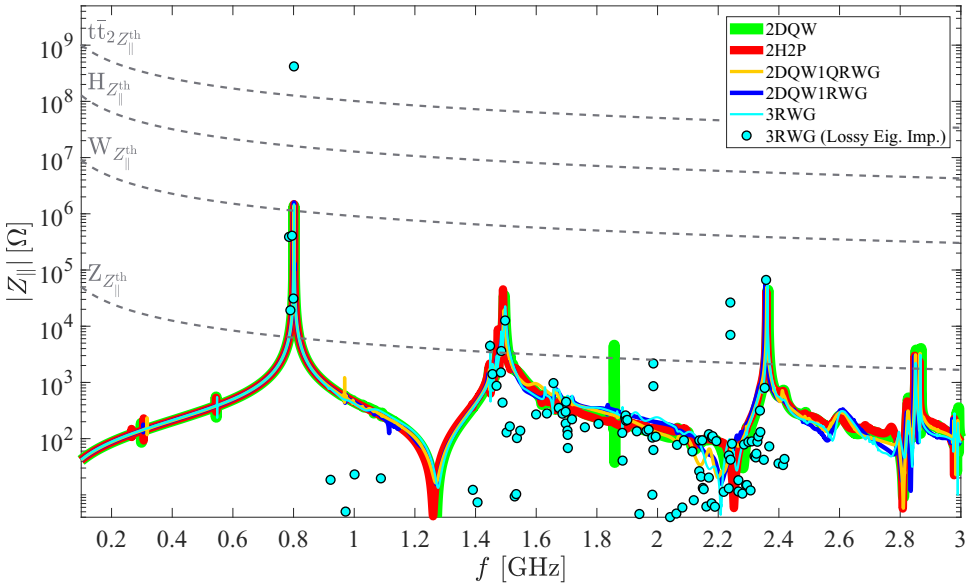

(a) Longitudinal impedance

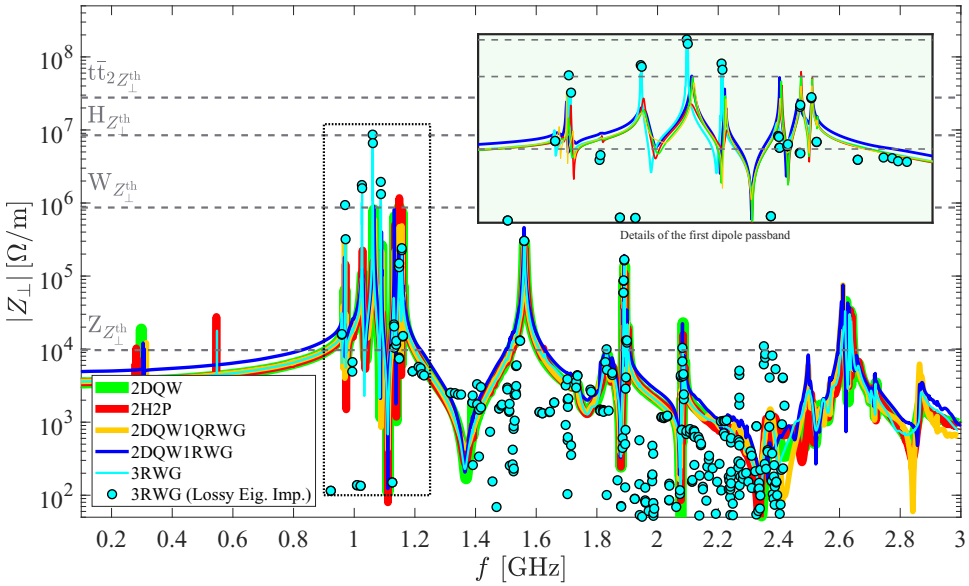

(b) Transversal impedance

Figure 6.19: Longitudinal impedance (a) and transversal impedance (b) of the single five-cell-cavity module. The wake impedances (solid lines) are calculated and extrapolated from the wake potentials with a wakelength of 1000 m. The markers correspond to the lossy eigenmodes calculated with the SSC method. The impedance thresholds are normalized to the number of cavities required for each energy option. The mode with high longitudinal impedance at 2.24 GHz is an octopole mode with $Q_{\text{ext}} = 1.4 \times 10^8$ and $R/Q_{\parallel} = 3.6 \times 10^{-4}$.

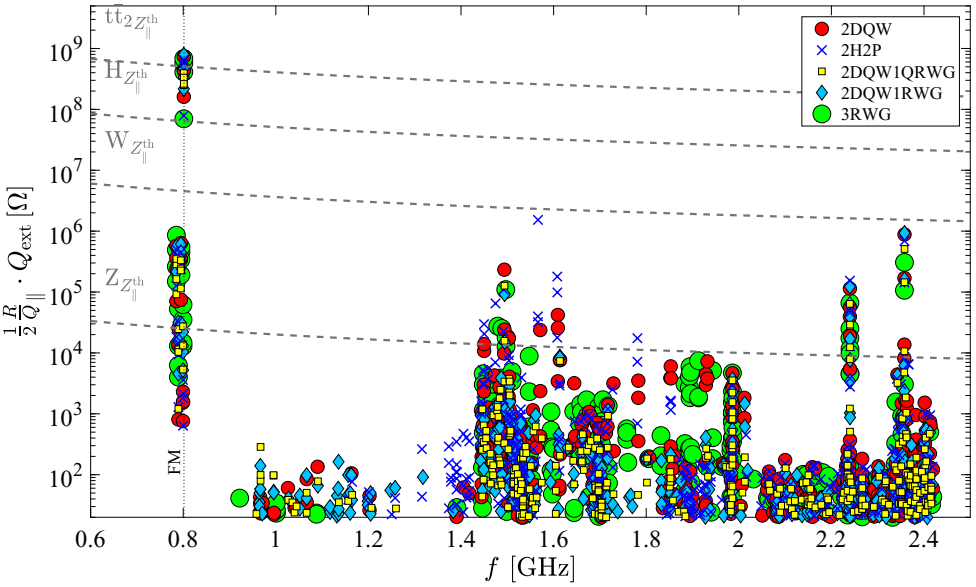

(a) Longitudinal impedance

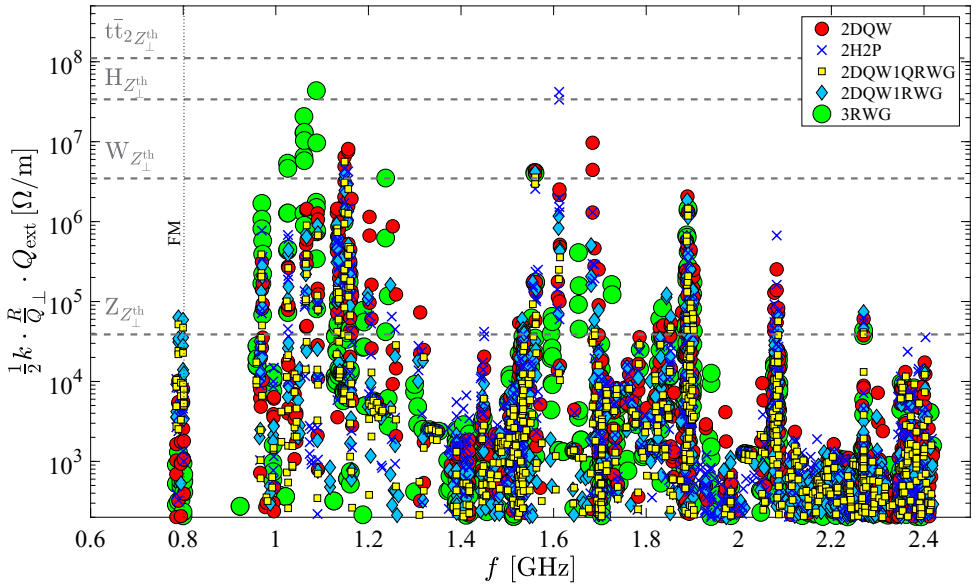

(b) Transversal impedance

Figure 6.20: Longitudinal and transversal impedance of the four five-cell-cavity modules shown in Figure 6.16. The impedances are calculated from the lossy eigenmodes computed with the SSC method using (2.46) and (2.47). The impedance thresholds are normalized to the number of modules required for each energy option.

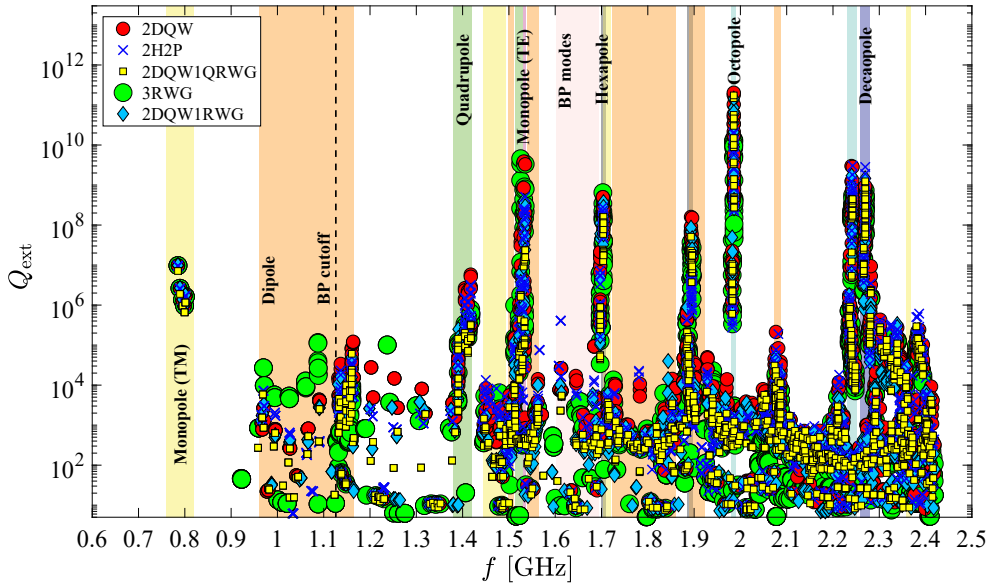

Figure 6.21: Q_{ext} of the four five-cell-cavity modules shown in Figure 6.16.

7 Summary and conclusion

The FCC design study considers a lepton collider as a possible intermediate step towards the 100 TeV hadron collider. The FCC-ee aims to conduct precise measurements of the heaviest known particles, i.e. Z, W, and H bosons, as well as the top quark. The SRF system of the FCC-ee shall accelerate particles to beam energies ranging from 45.6 GeV to 182.5 GeV. Challenges for the SRF cavity design result from its operation at different RF voltages and beam currents. The objective of this thesis was to propose a cavity and HOM coupler design for the large and costly RF system of the FCC-ee. Special focus was given to four areas: the general RF layout of the FCC-ee (Chapter 3), the SRF cavity design (Chapter 4), the HOM coupler design (Chapter 5), and the assessment of the HOM damped cavities using various numerical techniques (Chapter 6).

The thesis started with an introduction to the FCC project and the parameters that determine the machine layout. The two limiting working points of the FCC-ee are the Z-pole characterized by low voltage and a current of 1.39 A, and the $t\bar{t}_2$ working point which requires a high RF voltage of 10.93 GV. Some factors that are of importance in the RF layout design are the dissipated power in the cryogenic temperature, the required input power per cavity, the HOM power, and the beam stability restrictions.

Due to the low RF voltage, the cryogenic losses for the Z running are low. The value of accelerating gradient (E_{acc}) in the Z cavities is limited by the input power per cavity (cf. equations (3.12) and (3.4)). Assuming an upper limit of 1 MW at 400 MHz and of 500 kW at 800 MHz on the input power, and also considering the total SR loss of 50 MW per beam, operating the Z cavities at 400 MHz is more efficient than at 800 MHz. The number of cavities required for the Z running is 52 cavities per beam at 400 MHz (assuming the cavities are grouped in four-cavity modules). This requires an RF voltage of around 1.9 MV per cavity. A lower frequency also helps to reduce the HOM power and it relaxes the beam instability constraints of the Z running. A multi-cell cavity for the Z running was excluded because of the input power limitations, and due to the significantly high HOM power and beam impedance of multi-cell cavities. Therefore, a single-cell Nb/Cu cavity at 400 MHz, similar to that of the LHC, was considered for the Z running. This design can also be used for the FCC-hh.

In order to enhance efficiency, multi-cell cavities were considered for the W, H, and $t\bar{t}$ running. A similar cavity design was considered for the W and H options. In order to re-use a large part of the hardware and RF infrastructure used for the Z

energy, 400 MHz was also considered as the RF frequency for the W and H running. This low frequency also helps to decrease the HOM power and improves the beam impedance limits, which are of high importance particularly for the W beam. Two to four cells per cavity are the possible design options for the W and H cavities. Higher number of cells are not considered due to the bulky shape of the cavity at 400 MHz. A two-cell cavity is preferred for the W option because it puts less constraints on the HOM power, the beam impedance, and the input power per cavity. Due to the smaller beam current, the H option favors a higher number of cells per cavity to increase efficiency and reduce the RF installations. In this thesis, a four-cell Nb/Cu cavity at 400 MHz was considered for the W and H working points, and the pros and cons were studied. Since several hundreds of cavities are required for the $t\bar{t}$ running, which results in a very large RF section in the ring, 800 MHz cavities were considered for the $t\bar{t}$ option. The low beam current of the $t\bar{t}$ running permits the use of a higher number of cells per cavity; thus, five-cell Nb cavities at 800 MHz were considered for $t\bar{t}$. The low beam loading of $t\bar{t}$ also allows the possibility for beams to pass through the same RF structure by aligning the cavities of both beams. For this reason, $t\bar{t}$ requires a double frequency system, i.e. up to 4.0 GV from by the four-cell 400 MHz cavities used for the W and H options and the rest will be provided by the five-cell cavities at 800 MHz.

In Chapter 4 multi-cell cavities were designed for the W, H, and $t\bar{t}$ working points, and a single-cell cavity was designed for the Z option. The middle cells and the end cells of the multi-cell cavities were designed separately. The middle cells were optimized to lower peak fields and losses on the surface of the cavity, which are crucial for the reduction of the total cryogenic power for big machines such as H and $t\bar{t}$. In the end cell design, the coupling of the cavity to the beam pipe and the untrapping of certain HOMs were taken into account in addition to the peak surface fields. The optimized middle cells and end cells were then combined, and a four-cell cavity at 400 MHz and a five-cell cavity at 800 MHz were realized. In the design of the single-cell cavity for the Z energy, special focus was given to the dangerous HOMs of the cavity in addition to the fundamental mode. The beam-pipe radius of the cavity was increased to push the frequency of the higher order monopole modes above the cutoff frequency of the beam pipe and to thus untrap them. However, the same principle is not practical for the first dipole passband. For this reason, the cavity shape was optimized taking into account the properties of the first dipole passband and the fundamental mode simultaneously. The resulting multi-objective optimization problem was then solved using the genetic algorithm method.

Several HOM couplers, including coaxial and waveguide HOM couplers, were optimized to damp the HOMs of the designed cavities. The hook-type coupler, probe-type coupler, and double-quarter-wave coupler were carefully parameterized, and the parameters with high impact on the damping capabilities of the couplers were determined. Figures (5.9), (5.12), (5.14) and (5.15) also provide a good guideline for future use and the optimization of these couplers in other projects. The double-

quarter-wave coupler showed good damping in the first higher order monopole and dipole passbands in comparison to the LHC-type HOM couplers (hook-type and probe-type couplers combined).

A new concept to combine the use of waveguides to absorb the high frequency part of the HOM spectrum alleviating the power capabilities of the coaxial couplers was introduced. Bringing the cutoff frequency of a waveguide coupler below the first HOM frequency of the cavity typically requires a large cross-sectional area. By adding ridges to the waveguide, its cutoff frequency could be reduced without increasing its outer dimensions. This helps us to damp both polarizations of the first dipole passband with one quad-ridged waveguide, while at least two conventional rectangular waveguides are required to damp different polarizations of the modes in the first dipole passband. Additionally, the quad-ridged waveguide also enables us to design a more compact HOM coupler that occupies a smaller space in the cryomodule with a low cutoff frequency at the cost of a more complicated design.

In Chapter 6, the HOM power and the beam impedance of the cavities were studied using different HOM damping schemes. Wakefield solvers were used to calculate the impedance from the time-domain analysis, and the state-space-concatenation method was used to approximate the impedance from the eigenmode analysis of the modules. Methods to calculate the power propagated into each port using time-domain and eigenmode analyses were presented. Presenting a numerical method to calculate the coupling of the eigenmodes to the waveguide ports is also one of the contributions of this thesis.

The longitudinal impedance of the Z cavities was below the stability threshold in all considered damping schemes. The transversal impedance was below the impedance threshold for the 3H1QRWG and 4H1RWG damping schemes (cf. Figure 6.8). The hook-type couplers are mainly used to damp the first dipole passband. However, if the beam-filling scheme is optimized to avoid the excitation of such modes, the use of the hook-type couplers would no longer be necessary. Around 20-30 kW of HOM power is expected in a four-cavity module (without tapering at beam pipe ends). The power absorption rate of the coaxial HOM couplers amounted to a few percent in the four-cavity module, while the waveguide HOM couplers could absorb around half of the HOM power (or above depending on the HOM damping scheme, cf. Table 6.4). The very choice of the HOM damping scheme affects the total HOM power deposited into the cavities, e.g. more HOM power is created in the damping schemes with waveguides (cf. Table 6.5). For this reason, the number of HOM couplers should be limited to avoid the generation of additional HOM power by the HOM couplers, e.g. one waveguide combined with coaxial couplers showed promising results. A large portion of the HOM power propagates out of the module through the beam pipes; as a result, beam-pipe absorbers are also required at the end of the module.

The impedance stays below the threshold for all of the studied damping schemes for the H and $t\bar{t}$ beam, whereas it is close to the transversal impedance threshold

of W (cf. Figure 6.15 (b)). The resonant power loss (hitting a beam spectral line) for the W beam is critical, e.g. for a four-cavity module, depending on the chosen damping scheme, it can reach up to 18 kW (cf. Table 6.6). This should be avoided for the W beam, e.g. by optimizing the beam filling scheme, while for the H beam the resonant power loss is below 1 kW in a four-cavity module (cf. Table 6.7) and below 0.5 kW for the $t\bar{t}_2$ beam (cf. Table 6.8). For the W, H and $t\bar{t}$ working points, the damping schemes with two double-quarter-wave coaxial couplers and one waveguide coupler showed good performance for the damping of the trapped modes and the absorption of a significant amount of HOM power. Further aspects such as the complexity of fabrication, availability of high power absorbers, multipacting, and mechanical analyses exceeded the scope of this thesis and remain to be studied for a decision on a final design.

A Convergence Studies

Two types of simulations were carried out in this thesis: time domain and frequency domain calculations. The time domain calculations were done with the ABCI software for 2D axisymmetric structures, and with the wakefield solver of CST Studio Suite® for 3D geometries. In the frequency domain, the SuperLANS code was used for the 2D axisymmetric geometries investigated in Chapter 4, and the frequency domain solver of CST Studio Suite® was used for the 3D geometries studied in Chapter 5. In the calculation of the eigenmodes by the SSC method, hexahedral mesh cells created by CST Studio Suite® were used to generate the system matrices. This chapter presents convergence studies, such as mesh refinement studies, on some simulations carried out in this thesis.

A.1 Time domain calculations

In this thesis, the loss factors and beam impedances of 2D axisymmetric structures were calculated by the ABCI software, e.g. Table 6.9. The mesh-cell size could be controlled by defining the mesh sizes in the radial and longitudinal directions in the ABCI. Figure A.1 shows the dependency of the loss factor of the five-cell cavity on the mesh-cell size, considering an equal mesh size in the r and z directions. With a mesh-cell size of one-tenth of the bunch length, the relative error in the loss factor is below 1%. For other calculations with the ABCI, the considered mesh-cell size is maximally one-tenth of the bunch length.

The wakefield solver of CST Studio Suite® was used for the calculation of power propagated into the waveguide ports as explained in Section 6.1.3. In Table A.1, a mesh-convergence study is carried out on the 2DQW damping scheme for the single-cavity shown in Figure 6.10. The exciting particle beam in the simulation had a length of 25 mm with Gaussian distribution. This beam current distribution was also used in the denominator of equation (6.15). The weighting transfer function is then scaled with the beam spectrum of the H option using equation (6.16). The results indicate that the distribution of the HOM power among the couplers could be accurately approximated with a rather coarse mesh. Therefore, for the calculation of power propagated into the ports, at least 10 cells per wavelength are considered in the simulations of Chapter 6.

In addition to the mesh grid, the wake integration method has to be properly specified in the wake potential calculation of non-axisymmetric 3D geometries in

CST Studio Suite®. This is especially important for the calculation of the loss factor and the broad-band part of the beam impedance. In Table A.2 a convergence study is carried out on the 2DQW single-cavity damping scheme shown in Figure 6.10. The results are also graphically depicted in Figure A.2. The results indicate that the loss factor converges faster by using the "indirect interfaces" integration method with a refined mesh along the beam path. Accordingly, this simulation setup was used in the calculation of loss factors in Table 6.5.

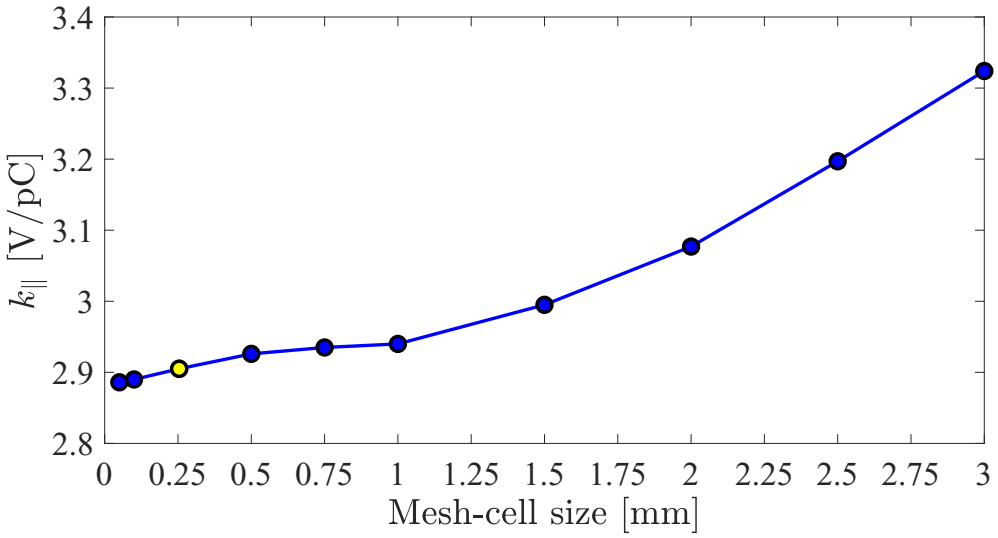

Figure A.1: Mesh convergence study for the loss factor of the five-cell cavity considering the BS bunch length of $t\bar{t}_2$ using the ABCI software. The x-axis shows the mesh sizes in the r and z directions. The mesh-cell size of the yellow marker equals one-tenth of the bunch length. This mesh-cell size was used in the calculation of loss factors in Table 6.9.

Table A.1: Mesh convergence study for the power propagated into the ports of the 2DQW single-cavity damping scheme shown in Figure 6.10 considering the H beam.

Cells per wavelength	Mesh cells	BP upstream [%]	DQW upstream [%]	DQW downstream [%]	FPC [%]	BP downstream [%]	Power [W]
4	3852040	44.2	2.0	3.0	3.6	47.2	751
6	10928172	44.1	1.9	3.1	3.7	47.2	784
8	24860880	44.3	1.9	3.1	3.7	47.1	805
10	45629584	44.2	1.9	3.1	3.7	47.1	811
12	71140200	44.2	1.9	3.1	3.7	47.1	816
14	116864664	44.2	1.9	3.1	3.7	47.0	818

Table A.2: Mesh convergence study for the loss factor calculation of the 2DQW single-cavity damping scheme shown in Figure 6.10. A Gaussian beam with a length of 25 mm is considered in the definition of the particle beam. Different wake integration methods are used in the wakefield calculations. A graphical representation of the numbers of this table is shown in Figure A.2.

Wake integration method	Direct					
Cells per wavelength	4	6	8	10	12	14
Mesh cells	3852040	10928172	24860880	45629584	71140200	116864664
$k_{\parallel}$ [V/pC]	0.416	0.465	0.490	0.503	0.510	0.514
Wake integration method	Indirect interfaces					
Cells per wavelength	4	6	8	10	12	14
Mesh cells	3852040	10928172	24860880	45629584	71140200	116864664
$k_{\parallel}$ [V/pC]	0.406	0.451	0.471	0.481	0.486	0.489
Wake integration method	Indirect interfaces Lines per sigma is ticked in beam mesh setting					
Cells per wavelength	4	6	8	10	12	14
Lines per sigma	4	6	8	10	12	14
Mesh cells	6277850	18656654	42825420	77846076	124099200	207061428
$k_{\parallel}$ [V/pC]	0.476	0.489	0.492	0.494	0.495	0.495

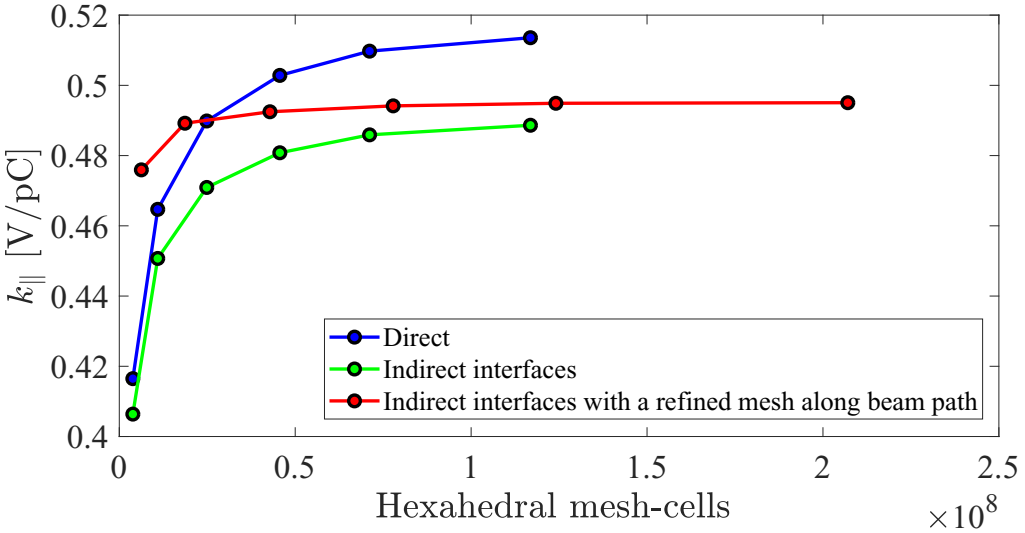

Figure A.2: Mesh convergence study for the loss factor calculation of the 2DQW single-cavity damping scheme shown in Figure 6.10. A Gaussian beam with a length of 25 mm is considered in the definition of the particle beam. Different wake integration methods are used in the wakefield calculations. In general, the "direct method" is less accurate than the indirect methods [51]. A detailed description of the graph is given in Table A.2.

A.2 Frequency domain calculations

The calculations in Chapter 4 were carried out using SuperLANS. The number of mesh cells in 2D-axisymmetric codes could be increased easily without using the computational resources that are typically required by 3D codes. In Figure A.3 (a) a mesh convergence study is carried out on the calculation of $R/Q_{\parallel,0}$ of the four-cell cavity given in Table 4.3. An absolute error below 0.4 Ω and a relative error below 10^{-3} (compared with the finest mesh) could be obtained by using more than 10000 mesh cells. The total time required for the simulation on a PC with Intel(R) Xeon(R) CPU E5-2643 v3, 3.4 GHz processor frequency and 64 GB RAM is shown in Figure A.3 (b).

The built-in adaptive mesh refinement feature of CST Studio Suite® was used for the frequency domain calculations in Chapter 5, which is why the respective convergence studies are not presented here.

The proper calculation of the eigenmodes with the SSC method requires the performance of convergence studies on the mesh cells of each segment and on the number of internal port modes connecting different segments. The fields at the intersections are constructed from the superposition of the 2D port modes. Generally, all the modes with a cutoff frequency below the maximum frequency of interest should be considered for the determination of the number of port modes. Additionally, several evanescent modes should be taken into account. A low number of port modes decreases the accuracy of the results, especially if there are couplers near the intersections. A large number of 2D port modes, on the other hand, increases the computational time in MOR. Therefore, a compromise needs to be sought in order to determine the number of port modes in SSC. As a test case, the impedance of the 2DQW damping scheme of the single-cavity (see Figure 6.10) is calculated with different numbers of port modes and is shown in Figure A.4. A list of 2D port modes with their respective cutoff frequency is given in Table A.3. Twelve port modes are not sufficient for an accurate calculation of the eigenmodes as shown in Figure A.4. The impedances of the most critical HOMs do not change significantly by using 17 or more port modes. As a conservative choice, 26 port modes are considered for the SSC calculations in this thesis.

In the next step, mesh convergence studies are carried out on the segments used in the SSC method. First, a reasonable mesh is chosen for the "four-cell cavity" (see Figure 6.13). Due to the simplicity of the structure, a mesh density with 20 lines per wavelength is chosen as a conservative choice for the "short cylinder" and "long cylinder" segments. The mesh density of the "four-cell cavity" segment varied from 9 to 17 lines per wavelength. The longitudinal and transversal shunt impedances of the bare cavity for different numbers of mesh-cells are shown in Figure A.5. The modes with high shunt impedance could be calculated accurately even with a coarse mesh in the "four-cell cavity" segment. There is a mode at 1.18 GHz whose transversal shunt impedance did not converge. However, this mode is not crucial as its quality

factor is low. As a conservative choice, 17 lines per wavelength are chosen in the mesh setting of the "four-cell cavity" (and also the "five-cell cavity") in the SSC method.

In the next step, a mesh convergence study is carried out on the segments with HOM couplers as shown in Figure A.6. The mesh density of the "short cylinder" and "four-cell cavity" segments are kept fixed, and the mesh density of the "2DQW left" and "2DQW right" segments are varied from 11 to 17 lines per wavelength. As shown in Figure A.6 (b)-(c), the most critical modes that have the highest longitudinal and transversal impedance are resolved with a 15 lines per wavelength mesh setting. For other segments in the SSC method, a mesh setting with at least 15 lines per wavelength is used (considering a maximum frequency three times higher than the FM frequency). The details of the segments used in the SSC method are given in Tables A.4 and A.5.

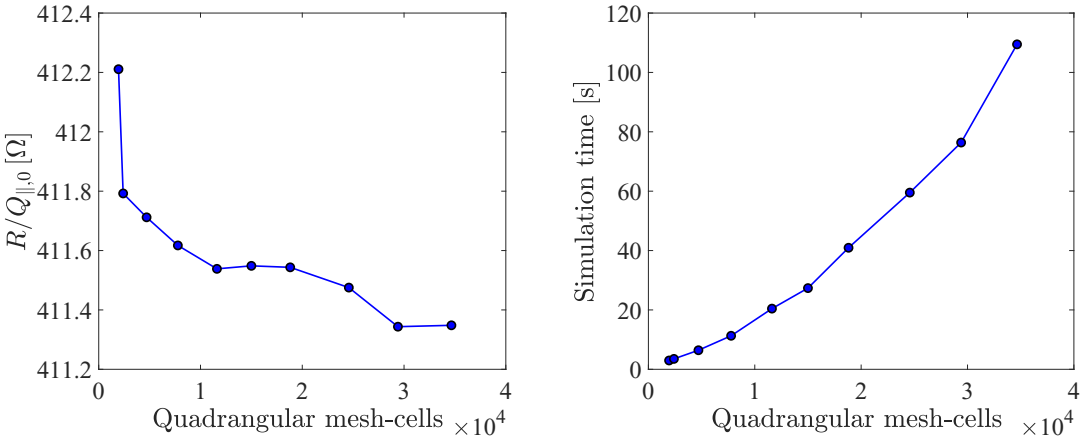

(a) Geometric shunt impedance of FM

(b) Total simulation time

Figure A.3: Mesh convergence study for the calculation of $R/Q_{\parallel,0}$ of the four-cell cavity given in Table 4.3 using SuperLANS. The simulation time represents the total time required to calculate four modes in the first monopole passband.

Table A.3: The first forty 2D port modes of a circular waveguide with the radius 156 mm.

Index	1	2	3	4	5	6	7	8	9	10
Mode type	TE_{11}	TE_{11}	TM_{01}	TE_{21}	TE_{21}	TM_{11}	TM_{11}	TE_{01}	TE_{31}	TE_{31}
f_{cut} [GHz]	0.563	0.563	0.736	0.934	0.934	1.172	1.172	1.172	1.285	1.285
Index	11	12	13	14	15	16	17	18	19	20
Mode type	TM_{21}	TM_{21}	TE_{41}	TE_{41}	TE_{12}	TE_{12}	TM_{02}	TM_{31}	TM_{31}	TE_{51}
f_{cut} [GHz]	1.571	1.571	1.626	1.626	1.631	1.631	1.688	1.951	1.951	1.962
Index	21	22	23	24	25	26	27	28	29	30
Mode type	TE_{51}	TE_{22}	TE_{22}	TM_{12}	TM_{12}	TE_{02}	TE_{61}	TE_{61}	TM_{41}	TM_{41}
f_{cut} [GHz]	1.962	2.051	2.051	2.146	2.146	2.146	2.294	2.294	2.321	2.321
Index	31	32	33	34	35	36	37	38	39	40
Mode type	TE_{32}	TE_{32}	TM_{22}	TM_{22}	TE_{13}	TE_{13}	TE_{71}	TE_{71}	TM_{03}	TM_{51}
f_{cut} [GHz]	2.452	2.452	2.574	2.574	2.611	2.611	2.624	2.624	2.647	2.683

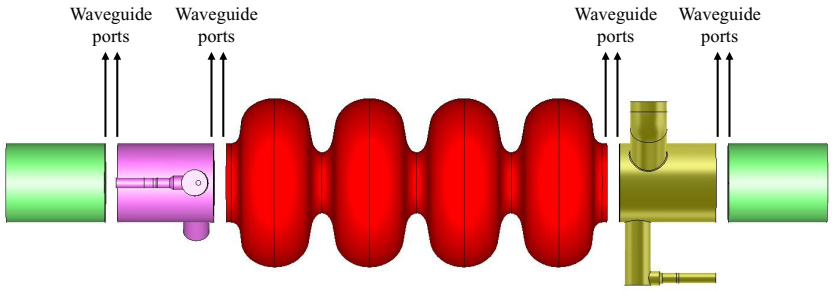

(a) Segments of the 2DQW damping scheme used by the SSC method

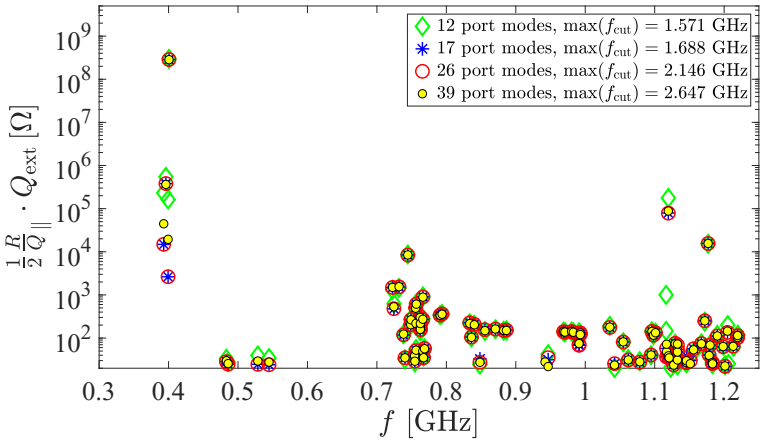

(b) Longitudinal impedance

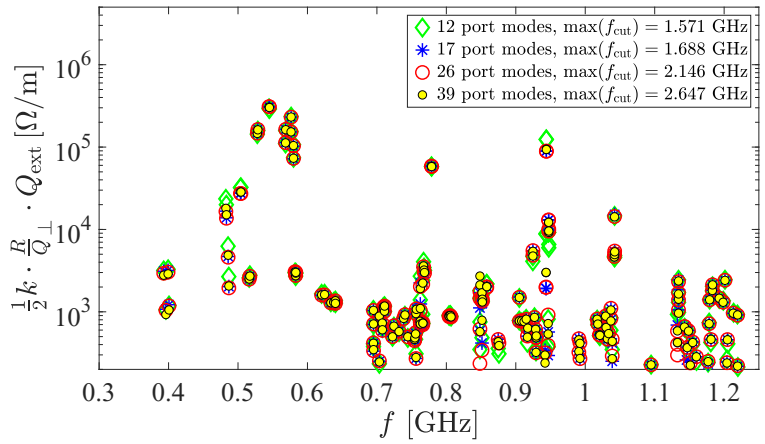

(c) Transversal impedance

Figure A.4: Study of the number of internal port modes between different segments in the SSC method. The value of max(f_{cut}) shows the maximum cutoff frequency of the considered port modes. The port mode information is presented in Table A.3.

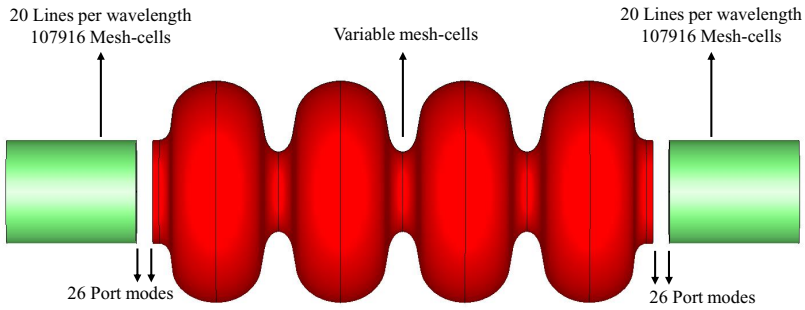

(a) Segments of the bare cavity used by the SSC method

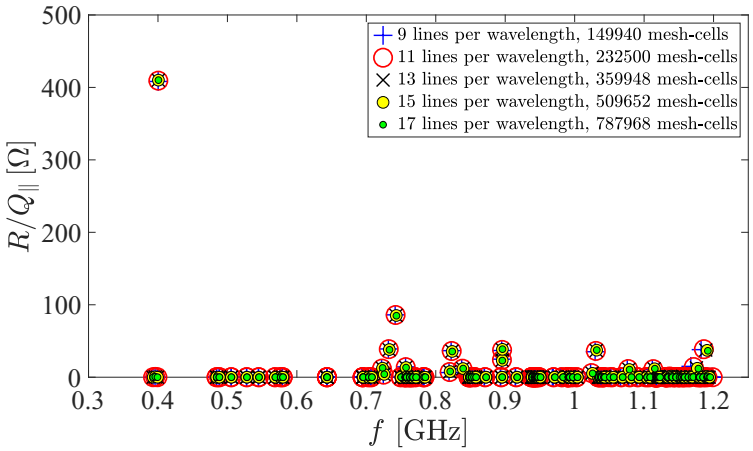

(b) Longitudinal shunt impedance

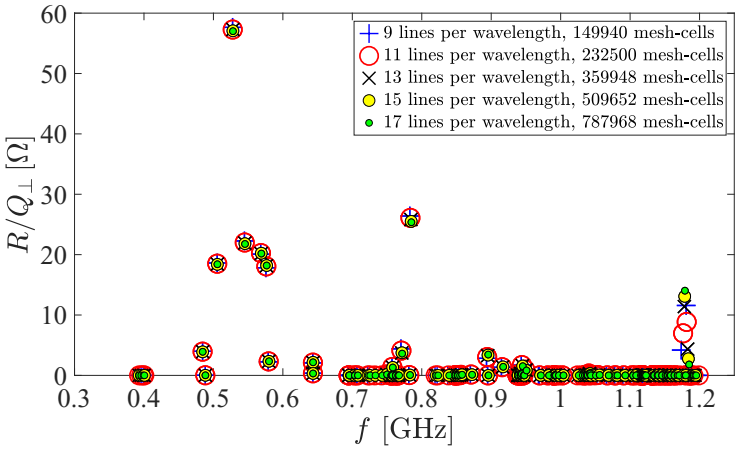

(c) Transversal shunt impedance

Figure A.5: Mesh convergence study of the "four-cell cavity" in the SSC method. A relatively fine mesh is considered for the "short cylinder" with 20 lines per wavelength. In the SSC method, 26 port modes are considered for the internal waveguide ports.

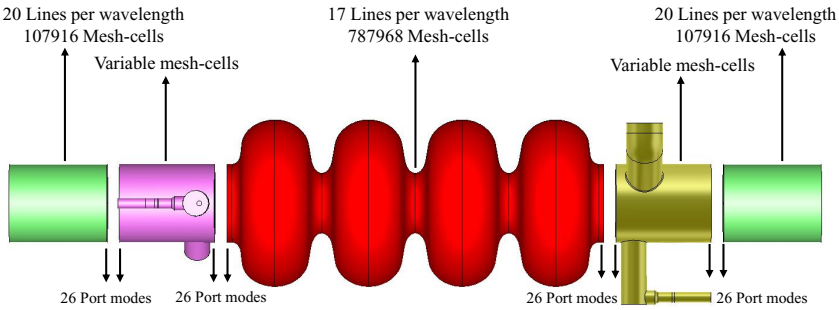

(a) Segments of the 2DQW damping scheme used by the SSC method

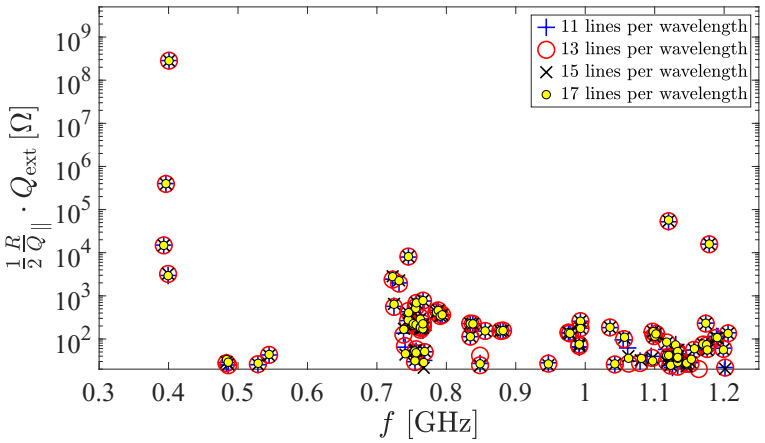

(b) Longitudinal impedance

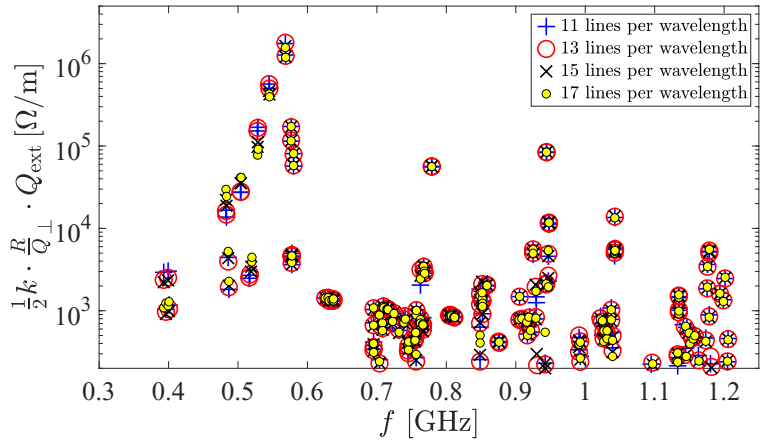

(c) Transversal impedance

Figure A.6: Mesh convergence study of the "2DQW left" and "2DQW right" segments in the 2DQW damping scheme. The number of mesh cells of the "short cylinder" and "four-cell cavity" segments are fixed. The 11, 13, 15 and 17 lines per wavelength yield 783510, 915936, 1016736 and 1181862 mesh cells for the "2DQW left" segment, respectively, and 843660, 1081920, 1205738 and 1395345 mesh cells for the "2DQW right" segment. In the SSC method, 26 port modes are considered for the internal waveguide ports. The maximum frequency considered in the mesh generation is 1.2 GHz.

Table A.4: Data of segments shown in Figure 6.13. The 2D port-mode column shows the number of port modes assigned to the waveguide ports in each segment. 26 port-modes are considered for the waveguide ports on the beam pipes connecting different segments, one port mode on coaxial HOM couplers, three modes on the FPC, seven modes on the QRWG and ten modes on the RWG.

Structure name	Hexahedral mesh cells	2D Port mode
Short cylinder	107916	[26,26]
Long cylinder	133584	[26,26]
Four-cell cavity	787968	[26,26]
2DQW left	1181862	[26,1,26]
2DQW1QRWG left	1319670	[26,1,7,26]
2DQW1RWG(a) left	1554402	[26,1,10,26]
2DQW1RWG(b) left	1416800	[26,1,10,26]
2H2P left	1110444	[26,1,1,26]
2H2P right	1330352	[26,1,1,3,26]
2DQW right	1395345	[26,3,1,26]
2DQW1QRWG right	875336	[26,3,1,26]

Table A.5: Data of segments shown in Figure 6.18. The 2D port-mode column shows the number of port modes assigned to the waveguide ports in each segment. 26 port modes are considered for the waveguide ports on the beam pipes connecting different segments, one port mode on coaxial HOM couplers, three modes on the FPC and the rest correspond to the WG HOM couplers.

Structure name	Hexahedral mesh cells	2D Port mode
Short cylinder	84800	[26,26]
Long cylinder	161600	[26,26]
Five-cell cavity	725200	[26,26]
2DQW left	1145946	[26,1,26]
2DQW1QRWG left	1284020	[26,1,7,26]
2H2P left	1039740	[26,1,1,26]
2DQW1RWG left	1050291	[26,8,26]
3RWG left	1340480	[26,10,10,10,26]
2DQW1QRWG right	1057472	[26,3,1,26]
2DQW right	1484230	[26,1,3,26]
2H2P right	1200960	[26,3,1,1,26]
3RWG right	254540	[26,3,26]
2DQW1RWG right	1427090	[26,3,1,1,26]

Bibliography

[1] ATLAS Collaboration. Observation of a new particle in the search for the Standard Model Higgs boson with the ATLAS detector at the LHC. *Physics Letters B*, 716(1):1 – 29, 2012. ISSN 0370-2693. doi: 10.1016/j.physletb.2012.08.020.

[2] The CMS Collaboration. Observation of a new boson with mass near 125 GeV in pp collisions at $\sqrt{s}$=7 and 8 TeV. *Journal of High Energy Physics*, 2013. doi: 10.1007/JHEP06(2013)081.

[3] G. Apollinari, I. Béjar Alonso, O. Brüning, M. Lamont, and L. Rossi. High-Luminosity Large Hadron Collider (HL-LHC): Preliminary Design Report. Technical report, Geneva, 2015.

[4] The European Strategy for Particle Physics Update 2013, 2013. CERN-Council-S/106.

[5] `https://home.cern/science/accelerators/future-circular-collider`.

[6] G. Velev, G. Ambrosio, E. Barzi, V. V. Kashikhin, S. Krave, V. Lombardo, I. Novitski, S. Stoynev, D. Turrioni, X. Xu, and A. V. Zlobin. Fermilab Superconducting Nb_3Sn High Field Magnet R&D Program. In *Proceedings, 10th International Particle Accelerator Conference (IPAC2019): Melbourne, Australia, May 19-24, 2019*. doi: 10.18429/JACoW-IPAC2019-THPTS099.

[7] D. Tommasini et al. The 16 T Dipole Development Program for FCC. *IEEE Transactions on Applied Superconductivity*, 27(4):1–5, 2017. doi: 10.1109/TASC.2016.2634600.

[8] A. Chancé, D. Boutin, B. Dalena, B. Holzer, A. Langner, and D. Schulte. Updates on the Optics of the Future Hadron-Hadron Collider FCC-hh. In *Proceedings, 8th International Particle Accelerator Conference (IPAC 2017): Copenhagen, Denmark, May 14-19, 2017*, page TUPVA002. doi: 10.18429/JACoW-IPAC2017-TUPVA002.

[9] Future Circular Collider Study. Volume 1: Physics Opportunities. Conceptual Design Report, preprint edited by M. Mangano et al. CERN accelerator reports, CERN-ACC-2018-0056, Geneva, December 2018. Published in Eur. Phys. J. C.

[10] Future Circular Collider Study. Volume 2: The Lepton Collider (FCC-ee) Conceptual Design Report, preprint edited by M. Benedikt et al. CERN accelerator reports, CERN-ACC-2018-0057, Geneva, December 2018. Published in Eur. Phys. J. ST.

[11] Future Circular Collider Study. Volume 3: The Hadron Collider (FCC-hh) Conceptual Design Report, preprint edited by M. Benedikt et al. CERN accelerator reports, CERN-ACC-2018-0058, Geneva, December 2018. Published in Eur. Phys. J. ST.

[12] W. Herr and B. Muratori. Concept of luminosity. 2006. doi: 10.5170/CERN-2006-002.361.

[13] D. d'Enterria. Physics at the FCC-ee. In *Proceedings, 17th Lomonosov Conference on Elementary Particle Physics: Moscow, Russia, August 20-26, 2015*, pages 182–191, 2017. doi: 10.1142/9789813224568_0028.

[14] R. W. Assmann. LEP luminosity revisited: Design and reality. In *Particle accelerator. Proceedings, 2nd Asian Conference, APAC'01, Beijing, P.R. China, September 17-21. 2001*, pages 74–78, 2001.

[15] The CEPC Study Group. CEPC Conceptual Design Report: Volume 1 - Accelerator, 2018. arXiv:1809.00285.

[16] T. Behnke, J. E. Brau, B. Foster, J. Fuster, M. Harrison, J. M. Paterson, M. Peskin, M. Stanitzki, N. Walker, and H. Yamamoto. The International Linear Collider Technical Design Report - Volume 1: Executive Summary, 2013. arXiv:1306.6327.

[17] The CLIC and CLICdp collaborations. The Compact Linear Collider (CLIC) - 2018 Summary Report, 2018. arXiv:1812.06018.

[18] A. Robson and P. Roloff. Updated CLIC luminosity staging baseline and Higgs coupling prospects, 2018. arXiv:1812.01644.

[19] H. Winick. *Synchrotron Radiation Sources: A Primer*. Series on synchrotron radiation techniques and applications. World Scientific, 1995. ISBN 9789810224240.

[20] H. Wiedemann. *Introduction to Accelerator Physics*. Springer, Cham, 4 edition, 2015. doi: 10.1007/978-3-319-18317-6_1.

[21] K. Oide. *FCC-ee Optics Update*. FCC week 2018, Amsterdam, 2018. `https://indico.cern.ch/event/656491/contributions/2939185/attachments/1628880/2597276/FCCee_Optics_Oide_180411.pdf`.

[22] A. Facco. Tutorial on low beta cavity design. In *Proceedings of the 12th International Workshop on RF Superconductivity*, Cornell University, Ithaca, NY, USA, 2005.

[23] S. Belomestnykh and V. Shemelin. High-β cavity design - A tutorial. In *12^{th} International Workshop on RF Superconductivity*, Ithaca, NY, USA, 2005.

[24] H. Padamsee, J. Knobloch, and T. Hays. *RF Superconductivity for Accelerators*. Wiley, New york, 1998.

[25] F. Gerigk. Status and Future Strategy for Advanced High Power Microwave Sources for Accelerators. In *Proceedings of IPAC2018*, Vancouver, BC, Canada, 2018. doi: 10.18429/JACoW-IPAC2018-MOYGB1.

[26] J. C. Maxwell. *A Treatise on Electricity and Magnetism*, volume 1. Cambridge University Press, 2010. doi: 10.1017/CBO9780511709333.002.

[27] U. van Rienen. *Numerical methods in computational electrodynamics: Linear systems in practical applications*. Berlin, Germany: Springer, 2001.

[28] D. K. Cheng. *Field and Wave Electromagnetics, Second Edition*. Addison-Wesley Publishing Company, 1989.

[29] C. A. Balanis. *Advanced Engineering Electromagnetics, 2nd Edition*. John Wiley & Sons, 2012.

[30] E. Jensen. RF Cavity Design. (arXiv:1601.05230):25 p, 2014. doi: 10.5170/CERN-2014-009.405.

[31] N. Juntong. *Investigation of optimised electromagnetic fields in SRF cavities for the ILC*. PhD thesis, University of Manchester, 2011.

[32] W. K. H. Panofsky and W. A. Wenzel. Some considerations concerning the transverse deflection of charged particles in radio-frequency fields. *American Institute of Physics*, 1956. doi: 10.1063/1.1715427.

[33] B.W. Zotter and S.A. Kheifets. *Impedances and Wakes in High Energy Particle Accelerators*. World Scientific, 1998.

[34] Y. Yang, A. Nassiri, G. Waldschmidt, D. Li, and H. Chen. Wakefield characterization in an asymmetric superconducting deflecting cavity. *Physical Review Accelerators and Beams*, 17(3), 2014. doi: 10.1103/PhysRevSTAB.17.032001.

[35] M. Dohlus and V. Kaljuzhny. Relative Nonuniformity in the Amplitude of the Accelerating Field Along the M x N-cell TESLA Supercavities. TESLA Report, Hamburg, Germany, 1998.

[36] D. E. Nagle, E. A. Knapp, and B. C. Knapp. Coupled Resonator Model for Standing Wave Accelerator Tanks. *Review of Scientific Instruments*, 38(11), 1967. doi: 10.1063/1.1720608.

[37] J. Sekutowicz, M. Ferrario, and Ch. Tang. Superconducting superstructure for the TESLA collider: A concept. *Physical Review Special Topics - Accelerators and Beams*, 2(6), 1999. doi: 10.1103/PhysRevSTAB.2.062001.

[38] A. Yamamoto. The Future of Superconducting Technology for Accelerators. In *Proceedings of IPAC2017*, Copenhagen, Denmark, 2017. doi: 10.18429/JACoW-IPAC2017-MOYBA1.

[39] C. L. Zekios, P. C. Allilomes, and G. A. Kyriacou. Eigenanalysis of Electromagnetic Structures Based on the Finite Element Method. *Applied Mathematics*, 2013. doi: 10.4236/am.2013.47138.

[40] H. Podlech. Superconducting versus normal conducting cavities. *CERN Yellow Report CERN-2013-001, pp.151-170*, 2013. doi: 10.5170/CERN-2013-001.151.

[41] K. K. G. Yan. *Numerical Estimation of Discretization Error on Unstructured Meshes*. PhD thesis, The University of British Columbia, 2018.

[42] T. Rylander, A. Bondeson, and P. Ingelström. *Computational Electromagnetics*. Springer, 2 edition, 2012. doi: 10.1007/978-1-4614-5351-2.

[43] K. Brackebusch. *Perturbative Methods for the Computation of Resonant Cavity Eigenmodes Subject to Geometric Variations*. PhD thesis, Universität Rostock, 2016.

[44] S. Gorgizadeh, T. Flisgen, and U. van Rienen. Eigenmode computation of cavities with perturbed geometry using matrix perturbation methods applied on generalized eigenvalue problems. *Journal of Computational Physics*, 364, 2018. doi: 10.1016/j.jcp.2018.03.012.

[45] R. B. Lehoucq, D. C. Sorensen, and C. Yang. ARPACK Users' Guide: Solution of Large Scale Eigenvalue Problems with Implicitly Restarted Arnoldi Methods, Oct 1997.

[46] T. Weiland. A discretization model for the solution of Maxwell's equations for six-component fields. *Electronics and Communications AEUE*, 31:116–120, 1977.

[47] U. Niedermayer. *Determination of Beam Coupling Impedance in the Frequency Domain*. PhD thesis, TU Darmstadt, 2015.

[48] R. Schuhmann and T. Weiland. Conservation of discrete energy and related laws in the finite integration technique. *Progress In Electromagnetics Research, PIER*, 32:301–316, January 2001. doi: 10.2528/PIER00080112.

[49] R. Courant, K. Friedrichs, and H. Lewy. On the partial difference equations of mathematical physics. *IBM Journal of Research and Development*, 11:215–234, March 1967. doi: 10.1147/rd.112.0215.

[50] T. Weiland. Time domain electromagnetic field computation with finite difference methods. *International Journal of Numerical Modeling: Electronic Networks, Devices and Fields*, 9:295–319, July 1996.

[51] Computer Simulation Technology, CST Studio Suite 2018. https://www.3ds.com/products-services/simulia/products/cst-studio-suite/.

[52] N. R. Chevalier, T. Junquera, J. Thermeau, L. M. Romão, and D. Vandeplassche. Cryogenic system for the MYRRHA superconducting linear accelerator. In *AIP Conference Proceedings*, Anchorage, USA, 2013.

[53] F. Zimmermann et al. Electrical power budget for FCC-ee. In *Proceedings of IPAC2016*, pages 3828 – 3831, Busan, Korea, 2016.

[54] E. Chojnacki, E. Smith, R. Ehrlich, V. Veshcherevich, and S. Chapman. Cryogenic heat load of the Cornell ERL main LINAC cryomodule. In *Proceedings of the International Conference on RF Superconductivity 2003*, pages 638 – 642, Berlin, Germany, 2009.

[55] S. Aull, O. Brunner, A. Butterworth, and N. Schwerg. Material options for the superconducting RF system of the Future Circular Collider. Technical Report CERN-ACC-2018-0019, CERN, Geneva, Jun 2018.

[56] W. J. Schneider, P. Kneisel, C. H. Rode, and Jefferson Lab SRF Staff. Gradient optimization for SC CW accelerators. In *Proceedings of the 2003 Particle Accelerator Conference*, Portland, USA, 2003.

[57] C. H. Rode and D. Proch. Cryogenic optimization for cavity systems. In *Proceedings of the IEEE Particle Accelerator Conference*, 1989.

[58] S. Posen and M. Liepe. RF test results of the first Nb_3Sn cavities coated at Cornell. In *Proceedings of SRF2013*, Paris, France, 2013.

[59] S. Posen and D.L. Hall. Nb_3Sn superconducting radiofrequency cavities: fabrication, results, properties, and prospects. *Superconductor Science and Technology*, 30, January 2017. doi: 10.1088/1361-6668/30/3/033004.

[60] O. Brunner. Private communication, February 2016.

[61] T. Schilcher. *Vector sum control of pulsed accelerating fields in Lorentz force detuned superconducting cavities*. PhD thesis, Universität Hamburg, 1998.

[62] Y.H. Chin. Advances and Applications of ABCI. In *International Particle Accelerator Conference*, Washington, D.C, USA, 1993.

[63] Z. Hongjuan, G. Jie, and L. Zhenchao. Cavity and HOM Coupler Design for CEPC. *Chinese Physics C*, 40(5), 2016.

[64] S. Gorgi Zadeh, R. Calaga, F. Gerigk, and U. van Rienen. FCC-ee hybrid RF scheme. In *9th International Particle Accelerator Conference, IPAC2018*, Vancouver, BC, Canada, 2018. doi: 10.18429/JACoW-IPAC2018-MOPMF036.

[65] B. Aune et al. Superconducting TESLA cavities. *Physical Review Accelerators and Beams*, 3(9), 2000. doi: 10.1103/PhysRevSTAB.3.092001.

[66] G. Taylor. *HEP and Collider Activities in Asia*. FCC week 2018, Amsterdam, 2018. `https://indico.cern.ch/event/656491/contributions/2908935/attachments/1629181/2596218/2018_April_AsiaCollider_FCC_Taylor_v4.pdf`.

[67] O. Brüning. *Scaling options and cost estimate for the LHeC ERL*. Electrons for the LHC, LHeC/FCCeh and PERLE workshop, LAL-Orsay, France, 2018. `https://indico.cern.ch/event/698368/attachments/1676680/2692124/Cost-Scaling-V2.pdf`.

[68] W. Singer, A. Brinkmann, R. Brinkmann, J. Iversen, A. Matheisen, W.-D. Moeller, A. Navitski, D. Reschke, J. Schaffran, A. Sulimov, N. Walker, H. Weise, P. Michelato, L. Monaco, C. Pagani, and M. Wiencek. Production of superconducting 1.3-GHz cavities for the European X-ray Free Electron Laser. *Physical Review Accelerators and Beams*, 19(9), 2016. doi: 10.1103/PhysRevAccelBeams.19.092001.

[69] E. Montesinos. *RF power & LLRF*. LLRF 2017 Workshop, Barcelona, Oct 2017. `https://public.cells.es/workshops/www.llrf2017.org/pdf/Orales/PL-05.pdf`.

[70] M. L. Mangano. *CERN roadmap and FCC*. International Workshop on High Energy Circular Electron Positron Collider, Beijing, 2017. `https://indico.ihep.ac.cn/event/6618/session/2/contribution/31/material/slides/0.pdf`.

[71] E. Montesinos. *RF fundamental power couplers*. FCC week 2017, Berlin, 2017. `https://indico.cern.ch/event/556692/contributions/2484366/attachments/1466409/2269379/20170530_FCC_week_FPC.pdf`.

[72] E. Jensen. *Developments Towards Higher Efficiency of RF Systems*. FCC week 2016, Rome, 2016. https://indico.cern.ch/event/438866/contributions/1085177/attachments/1255575/1853613/RFSystems16to9.pdf.

[73] S. Aull. *SRF Material Options for FCC*. FCC week 2017, Berlin, 2017. https://indico.cern.ch/event/556692/contributions/2484364/attachments/1467340/2268917/2017-05-30_FCCweek_SKA.pdf.

[74] F. Marhauser. Next generation HOM-damping. *Superconductor Science and Technology*, 30(6), 2017. doi: 10.1088/1361-6668/aa6b8d.

[75] K. Hübner. Designing and building LEP. *Physics Reports*, 403-404, 2004. doi: 10.1016/j.physrep.2004.09.004.

[76] E. Jensen, C. Bracco, O. Brüning, R. Calaga, N. Catalan-Lasheras, B. Goddard, M. Klein, and A. Torres-Sanchez, R .and Valloni. Design study of an ERL Test Facility at CERN. In *5th International Particle Accelerator Conference*, Dresden, Germany, 2014. doi: 10.18429/JACoW-IPAC2014-TUOBA02.

[77] F. Marhauser, S. Castagnola, W.A. Clemens, P. Dhakal J.G. Dail, F. Fors, J. Henry, R.A. Rimmerpresenter, L. Turlington, R.S. Williams, R. Calaga, K.M. Dr. Schirm, and E. Jensen. 802 MHz ERL Cavity Design and Development. In *Proceedings of IPAC2018*, Vancouver, BC, Canada, 2018. doi: 10.18429/JACoW-IPAC2018-THPAL146.

[78] D. Angal-Kalinin et al. PERLE Powerful Energy Recovery Linac for Experiments. Conceptual Design Report, 2017.

[79] R. Calaga. A design for an 802 MHz ERL Cavity. CERN-Acc-Note-2014-xxx ACC, CERN, Geneva, Switzerland, 2014.

[80] S. Belomestnykh. Review of High Power CW Couplers for Superconducting Cavities. In *Presented at the Workshop on High-Power Couplers for Superconducting Accelerators*, Jefferson Lab, USA, 2002.

[81] H. P. Kindermann and M. Stirbet. The variable power coupler for the LHC superconducting cavity. In *Accelerator Technology for the 21st Century: Proceedings, 9th Workshop on RF Superconductivity (SRF 1999): Santa Fe, New Mexico, November 1-5, 1999*.

[82] W. Wolski. *Beam Dynamics In High Energy Particle Accelerators*. Imperial College Press, London, 2014.

[83] J. M. Byrd and M. Georgsson. Lifetime increase using passive harmonic cavities in synchrotron light sources. *Physical Review Special Topics - Accelerators and Beams*, 4(3), 2001. doi: 10.1103/PhysRevSTAB.4.030701.

[84] S. Ogur et al. Overall Injection Strategy for FCC-ee. In *Proceedings, 62nd ICFA Advanced Beam Dynamics Workshop on High Luminosity Circular e^+e^- Colliders (eeFACT2018): Hong Kong, China, September 24-27, 2018*, page TUPAB03. doi: 10.18429/JACoW-eeFACT2018-TUPAB03.

[85] O. Brunner, A. Butterworth, I. Karpov, S. Aull, and N. Schwerg. Proposed RF Staging Scenario for FCC-ee. *Beam Dynamics Newsletter No. 72*, December 2017.

[86] M. Kranjčević, S. Gorgi Zadeh, A. Adelmann, P. Arbenz, and U. van Rienen. Constrained multi-objective shape optimization of superconducting RF cavities considering robustness against geometric perturbations. *Physical Review Accelerators and Beams*, 22(12), 2019. doi: 10.1103/PhysRevAccelBeams.22.122001.

[87] J. C. Slater. Microwave Electronics. *Reviews of Modern Physics*, 18(4), 1946. doi: 10.1103/RevModPhys.18.441.

[88] J. Sekutowicz. New Geometries: Elliptical Cavities. In *Proceedings of the Workshop on Pushing the Limits of RF Superconductivity*, pages 3 – 10, Argonne, Illinois, USA, 2005.

[89] V. Shemelin, H. Padamsee, and R. L. Geng. Optimal cells for TESLA accelerating structure. *Nuclear Instruments and Methods in Physics Research*, 496 (1), 2003. doi: 10.1016/S0168-9002(02)01620-0.

[90] V. Shemelin. Reentrant cavities have highest gradient and minimal losses simultaneously. Cornell University LEPP Report SRF 051010-09, 2005.

[91] T. P. Wangler. *RF Linear Accelerators*. Wiley, New york, 2008.

[92] V. Shemelin, R.L. Geng, J. Kirchgessner, H. Padamsee, and J. Sears. An optimized shape cavity for TESLA: concept and fabrication. In *Proceedings of the 2003 Particle Accelerator Conference*, Portland, Oregon, USA, 2003.

[93] V. Shemelin. Optimal choice of cell geometry for a multicell superconducting cavity. *Physical Review Special Topics - Accelerators and Beams*, 12(11), 2009. doi: 10.1103/PhysRevSTAB.12.114701.

[94] V. Shemelin. Low loss and high gradient SC cavities with different wall slope angles. In *Proceedings of PAC07*, New Mexico, USA, 2007. doi: 10.1109/PAC.2007.4441247.

[95] V. Shemelin, S. Gorgi Zadeh, J. Heller, and U. van Rienen. Systematical study on superconducting radio frequency elliptic cavity shapes applicable to future high energy accelerators and energy recovery linacs. *Physical Review Special Topics - Accelerators and Beams*, 19(10), 2016. doi: 10.1103/PhysRevAccelBeams.19.102002.

[96] D. G. Myakishev and V. P. Yakovlev. The new possibilities of SuperLANS code for evaluation of axisymmetric cavities. In *Proceedings of Particle Accelerator Conference*, Dallas, TX, USA, 1995. doi: 10.1109/PAC.1995.505548.

[97] `https://www.euclidtechlabs.com/superlans`.

[98] V. Shemelin. High-gradient and low-loss SC cavities with different wall slope angles. Cornell University LEPP Report Nr. SRF 070614-02, Cornell, New York, USA, 2007.

[99] T. Homem de Mello and G. Bayraksan. Monte carlo sampling-based methods for stochastic optimization. *Surveys in Operations Research and Management Science*, 19(1):56 – 85, 2014. ISSN 1876-7354. doi: 10.1016/j.sorms.2014.05.001.

[100] MATLAB. *Version R2017b*. The MathWorks, Inc., Natick, Massachusetts, USA, 2017.

[101] N. J. Higham. *Accuracy and Stability of Numerical Algorithms*. SIAM, Philadelphia, USA, 2 edition, 2002.

[102] F. Furuta and K. Saito. Field flatness degradation problems and cure. In *Proceedings of SRF2009*, Berlin, Germany, 2009.

[103] K. Deb. *Multi-Objective Optimization Using Evolutionary Algorithms*. John Wiley & Sons, Chichester, England, 2001.

[104] H. Padamsee, P. Barnes, C. Chen, W. Hartung, M. Hiller, J. Kirchgessner, D. Moffat, R. Ringrose, D. Rubin, Y. Samed, D. Saraniti, J. Sears, Q. S. Shu, and M. Tigner. Accelerating cavity development for the Cornell B-factory, CESR-B. In *Conference Record of the 1991 IEEE Particle Accelerator Conference*, volume 2, pages 786–788, May 1991. doi: 10.1109/PAC.1991.164441.

[105] T. Roggen, P. Baudrenghien, and R. Calaga. A higher harmonic cavity at 800 MHz for HL-LHC. In *Proceedings of SRF2015*, Whistler, BC, Canada, 2015. doi: 10.18429/JACoW-SRF2015-THPB017.

[106] R. Calaga. Private communication, June 2019.

[107] E. Haebel. Couplers, tutorial and update. In *Particle Accelerators, 1992, Vol. 40, pp.141-159*, 1992.

[108] S. Wang, J. Guo, R. Rimmer, and H. Wang. JLEIC SRF cavity RF design. In *Proceedings of IPAC2016*, Busan, Korea, 2016.

[109] E. Chojnacki and W. J. Alton. Beamline RF load development at Cornell. In *Proceedings of the 1999 Particle Accelerator Conference*, New York, USA, 1999.

[110] K. Akai et al. RF systems for the KEK B-Factory. *Nuclear Instruments and Methods in Physics Research*, 499(1), 2003. doi: 10.1016/S0168-9002(02)01773-4.

[111] Ya. V. Shashkov, N. P. Sobenin, and M. M. Zobov. Comparison of high order modes damping techniques for 800 MHz single cell superconducting cavities. In *Proceedings of IPAC2014*, Dresden, Germany, 2014.

[112] Ya. V. Shashkov, N. P. Sobenin, and M. M. Zobov. Suppression of higher oder modes in an array of cavities using waveguides. In *Proceedings of IPAC2015*, Richmond, VA, USA, 2015. doi: 10.18429/JACoW-IPAC2015-WEPMN047.

[113] S. Belomestnykh. HOM damper hardware considerations for future energy frontier circular colliders. In *HF2014*, Beijing, China, 2014.

[114] F. Marhauser, T.S. Elliott, A.T. Wu, E. Chojnacki, and E. Savrun. Absorber materials at room and cryogenic temperatures. In *Proceedings of IPAC2011*, San Sebastian, Spain, 2011.

[115] G. Biallas, P. Brindza, H. Larry Phillips, and J. Kirschgessner. The CEBAF cavity cryostat. In *Proceedings of the 1986 International Linac Conference*, Stanford, California, USA, 1986.

[116] C. E. Reece. Continuous wave superconducting radio frequency electron linac for nuclear physics research. *Physical Review Accelerators and Beams*, 19(12), 2016. doi: 10.1103/PhysRevAccelBeams.19.124801.

[117] R. A. Rimmer, R. Bundy, G. Cheng, G. Ciovati, E. F. Daly, R. Getz, J. Henry, W. R. Hicks, P. Kneisel, S. Manning, R. Manus, F.Marhauser, K. Smith, M. Stirbet, L. Turlington, L. Vogel, H. Wang, and K. M. Wilson. JLAB high-current CW cryomodules for ERL and FEL applications. In *Proceedings of PAC2007*, New Mexico, USA, 2007. doi: 10.1109/PAC.2007.4441294.

[118] R. Rimmer et al. *Waveguide HOM damping studies at JLab.* Workshop on Higher-Order-Mode Damping Superconducting RF Cavities, Ithaca, USA, 2010.

[119] D. Boussard and T. Linnecar. The LHC superconducting RF system. LHC Project Report 316, CERN, Geneva, Switzerland, 1999.

[120] S. Papadopoulos. Higher Order Mode Couplers Optimization for the 800 MHz Harmonic System for HL-LHC. Aug 2014. `https://cds.cern.ch/record/1751451`.

[121] J. Sekutowicz. Higher order mode coupler for TESLA. In *Proceedings of the Sixth Workshop on RF Superconductivity*, Newport News, Virginia, USA, 1993.

[122] K. Papke, F. Gerigk, and U. van Rienen. Comparison of coaxial higher order mode couplers for the CERN Superconducting Proton Linac study. *Physical Review Accelerators and Beams*, 20(6), 2017. doi: 10.1103/PhysRevAccelBeams.20.060401.

[123] J. A. Mitchell, G. Burt, N. Shipman, B. Xiao, S. Verdú-Andrés, Q. Wu, and R. Calaga. HOM coupler alterations for the LHC DQW crab cavity. In *18th International Conference on RF Superconductivity*, Lanzhou, China, 2017. doi: 10.18429/JACoW-SRF2017-MOPB079.

[124] F. Gerigk. *Design of Higher-Order Mode Dampers for the 400 MHz LHC Superconducting Cavities*. Studienarbeit, CERN, 1997.

[125] P. Sotirios. Higher Order Mode Couplers Optimization for the 800 MHz Harmonic System for HL-LHC. CERN-STUDENTS-Note-2014-114, CERN, Geneva, Switzerland, 2014.

[126] E. Häbel, V. Rödel, F. Gerigk, and Z. T. Zhao. The Higher-Order Mode Dampers of the 400 MHz Superconducting LHC Cavities. In *8th Workshop on RF Superconductivity*, Abano-Terme, Italy, 1997.

[127] F. Caspers. RF engineering basic concepts: S-parameters. *CERN Yellow Report CERN-2011-007, pp. 67-93*, 2012. doi: arXiv:1201.2346.

[128] J. A. Mitchell, G. Burt, S. Verdú-Andrés, B. Xiao, and R. Calaga. DQW HOM coupler design for the HL-LHC. In *9th International Particle Accelerator Conference, IPAC2018*, Vancouver, BC, Canada, 2018. doi: 10.18429/JACoW-IPAC2018-THPAL018.

[129] J. Mitchell. HL-LHC DWQ HOM coupler design and SPS measurements. In *ICFA Mini Workshop on Higher Order Modes in Superconducting Cavities (HOMSC2018).*, Ithaca, NY, USA, October 2018. https://indico.classe.cornell.edu/event/185/contributions/545/.

[130] D. M. Pozar. *Microwave Engineerng, 4th edition*. Wiley, 2011.

[131] S. B. Cohen. Properties of ridge wave guide. *Proceedings of the IRE*, 35(8), 1947. doi: 10.1109/JRPROC.1947.226277.

[132] T. N. Anderson. Rectangular and ridge waveguide. *IRE Transactions on Microwave Theory and Techniques*, 4(4), 1956. doi: 10.1109/TMTT.1956.1125063.

[133] P. Craievich. *Short-range longitudinal and transverse wakefield effects in FERMI@Elettra FEL project*. PhD thesis, Technische Universiteit Eindhoven, 2010.

[134] M. Lonza and H. Schmickler. Multi-bunch Feedback Systems. *CERN Yellow Report CERN-2014-009, pp.503-546*, 2016. doi: 10.5170/CERN-2014-009.503.

[135] M. Ruprecht. *Calculation of Coupled Bunch Effects in the Synchrotron Light Source BESSY VSR*. PhD thesis, Humboldt-Universität zu Berlin, 2016.

[136] H. Zheng, J. Zhai, and J. Gao. *HOM Analysis and HOM Coupler Preliminary Design for CEPC*. International ICFA Mini-Workshop on High Order Modes in SC Cavities, Warnemünde, Germany, 2016.

[137] H. J. Zheng, F. B. Meng, and J. Y. Zhai. HOM coupler design for CEPC cavities. In *Proceedings of SRF2017*, Lanzhou, China, 2017.

[138] T. Weiland and R. Wanzenberg. *Wake Fields and Impedances*. DESY M-91-06, 1991.

[139] L. Palumbo, V. G. Vaccaro, and M. Zobov. *Wake Fields and Impedance*. Laboratori Nationali di Frascati, 1994.

[140] F. Marhauser, R. Rimmer, and H. Wang. *Narrowband and Broadband Impedance Budget of the 1497 MHz HOM-Damped Five Cell High Current Cavity*. Jefferson Laboratory, 2008.

[141] F. Marhauser, R.A. Rimmer, K. Tian, and H. Wang. Enhanced method for cavity impedance calculations. In *Proceedings of PAC09*, pages 4523–4525, Vancouver, BC, Canada, 2009.

[142] H. W. Pommerenke, J. D. Heller, S. Gorgi Zadeh, and U. van Rienen. Computation of lossy higher order modes in complex SRF cavities using Beyn's and Newton's methods on reduced order models. *International Journal of Modern Physics A*, 34(36):1942037, 2019. doi: 10.1142/S0217751X19420375.

[143] T. Galek, T. Flisgen, U. van Rienen, B. Riemann, and A. Neumann. Traveling poles elimination scheme and calculations of external quality factors of HOMs in SC cavities. In *Proceedings of ICAP2012*, pages 152 – 154, Rostock-Warnemünde, Germany, 2012.

[144] H. W.Glock, T.Galek, G. Pöplau, and U. van Rienen. HOM spectrum and Q-factor estimations of the high-beta CERN-SPL-cavities. In *Proceedings of IPAC'10*, pages 2905 – 2907, Kyoto, Japan, 2010.

[145] F. Marhauser. Calculations for RF cavities with dissipative material. In *Proceedings of SRF2015*, pages 1056 – 1060, Whistler, BC, Canada, 2015.

[146] A. Lunin, T. Khabiboulline, N. Solyak, A. Sukhanov, and V. Yakovlev. Resonant excitation of high order modes in the 3.9 GHz cavity of the Linac Coherent Light Source. *Physical Review Accelerators and Beams*, 21(2), 2018. doi: 10.1103/PhysRevAccelBeams.21.022001.

[147] I. Karpov, R. Calaga, and E. Shaposhnikova. HOM power in FCC-ee cavities. CERN-ACC-NOTE-2018-0005, CERN, Geneva, Switzerland, 2018.

[148] A. Tsakanian, H.-W. Glock, A. Velez, and J. Knobloch. Study on HOM power levels in the BESSY VSR module. In *Proceedings of IPAC2017*, pages 982 – 985, Copenhagen, Denmark, 2017. doi: 10.18429/JACoW-IPAC2017-MOPVA052.

[149] T. Flisgen, H.-W. Glock, and A. Tsakanian. Estimation of dielectric losses in the BESSY VSR warm beam pipe absorbers. In *Proceedings of IPAC2018*, pages 3185 – 3188, Vancouver, BC, Canada, 2018. doi: 10.18429/JACoW-IPAC2018-THPAF085.

[150] S. Gorgi Zadeh, T. Flisgen, R. Calaga, and U. van Rienen. HOM Damping Options for the Z-Pole Operating Scenario of FCC-ee. In *10th International Particle Accelerator Conference, IPAC2019*, Melbourne, Australia, 2019. doi: 10.18429/JACoW-IPAC2019-MOPRB006.

[151] T. Flisgen. *Compact State-Space Models for Complex Superconducting Radio-Frequency Structures Based on Model Order Reduction and Concatenation Methods*. PhD thesis, Universität Rostock, 2015.

[152] T. Flisgen, A. Vélez, J. Heller, S. Gorgi Zadeh, and U. van Rienen. Computation of eigenmodes in the BESSY VSR cavity chain by means of concatenation strategies. In *13th Int. Computational Accelerator Physics Conf.*, pages 253 – 259, Key West, FL, USA, 2018. doi: 10.18429/JACoW-ICAP2018-TUPAG01.

[153] T. Flisgen, J. Heller, T. Galek, L. Shi, N. Joshi, N. Baboi, R. M. Jones, and U. van Rienen. Eigenmode compendium of the third harmonic module of the European X-ray Free Electron Laser. *Physical Review Accelerators and Beams*, 20, 2017. doi: 10.1103/PhysRevAccelBeams.20.042002.

[154] T. Flisgen, H. Glock, and U. van Rienen. Compact time-domain models of complex rf structures based on the real eigenmodes of segments. *IEEE Transactions on Microwave Theory and Techniques*, 61(6):2282–2294, June 2013. ISSN 0018-9480. doi: 10.1109/TMTT.2013.2260765.

[155] J. Heller. *Numerical simulation of electromagnetic fields in complex multicavity superconducting radio frequency resonators*. PhD thesis, Universität Rostock, 2018.

[156] R. Van Beeumen. *Rational Krylov methods for nonlinear eigenvalue problems*. PhD thesis, KU Leuven, 2015.

[157] Z.T. Zhao, V. Rödel, and E. Haebel. Estimation of the Higher-order Mode Power in the 400 MHz Superconducting Cavities of the LHC. CERN-SL-Note-97-10-RF, CERN, Geneva, Switzerland, 1997.

Selbstständigkeitserklärung

Hiermit erkläre ich, dass ich die vorliegende Dissertation mit dem Titel "Accelerating cavity and higher order mode coupler design for the Future Circular Collider" selbstständig und ohne fremde Hilfe und nur unter Verwendung der von mir angegebenen Quellen und Hilfsmittel verfasst habe.

Rostock,

Shahnam Gorgi Zadeh